



UNIVERSITÀ  
DEGLI STUDI  
DI PADOVA

Università degli Studi di Padova

Dipartimento di Scienze Chimiche

**SCUOLA DI DOTTORATO DI RICERCA IN SCIENZA E INGEGNERIA DEI  
MATERIALI - INDIRIZZO COMUNE**

CICLO XXVIII

**LASER ABLATION SYNTHESIS IN SOLUTION AND  
CHARACTERIZATION OF MAGNETIC-PLASMONIC  
ALLOY NANOPARTICLES**

**Direttore della Scuola:** Ch.mo Prof. Gaetano Granozzi

**Supervisore:** Ch.mo Prof. Vincenzo Amendola

**Dottorando:** Stefano Scaramuzza





# Abstract

---

In the history of nanoparticle synthesis, combining the properties of different elements in a single nanostructure has always been an important objective. In particular, alloy nanoparticles (NPs) are attracting a great research interest from the scientific community, since alloying is a way for combining different properties in a single nano-object, and obtaining peculiar structures such as NPs with magnetic and plasmonic response. Besides, by acting on alloy composition, it becomes possible to finely tune a given physical or chemical property, such as intensity and position of the surface plasmon resonance in Ag-Au NPs, or the efficiency of hydrogenation of nitro-substituted aromatics with Ni-Pd nanoalloys.

The most frequent approach for the synthesis of metal alloy NPs relies on wet-chemistry methods. There are many available reactions, such as the one used to obtain in one step Ag-Au alloy NPs by co-reduction of  $\text{HAuCl}_4$  and  $\text{AgNO}_3$ , and they depend on the type of metal precursors and solvents employed. Other chemical methods have also been used, such as radiolysis, electrochemistry, sonochemistry and biosynthesis. All these methods run in thermodynamic or near-to-thermodynamic equilibrium conditions, thus limiting the type and composition of achievable nanoalloys.

Physical methods such as ion implantation and molecular beams can also produce metastable nanoalloys, but are less frequently employed because of the limitations in the scalability and use of final products. With these methods, NPs are produced inside a solid matrix or on a substrate where they often undergo irreversible agglomeration.

A different and more promising physical method for the production of both thermodynamically stable and metastable alloy NPs consists in Laser Ablation Synthesis in Solution (LASiS). LASiS employs a pulsed laser focused on the surface of a bulk metal target for the generation of a colloidal solution of NPs. Following laser absorption by the bulk target, the ablation process takes place through the generation of a plasma plume and the formation of a cavitation bubble, where NPs form. The structure and composition of the NPs are determined by a number of ablation parameters, like laser power, pulse duration, solvent, target, and molecules available in the solvent. In recent years, LASiS has been employed to create metal alloy NPs such as Au-Ag, Pt-Au, Pt-Ir.



In this PhD work, the synthesis of alloy nanoparticles by LASiS was investigated, considering in particular the Au-Fe and Ag-Fe systems.

Au-Fe alloy nanoparticles were obtained by laser ablation of a bulk Au<sub>73</sub>Fe<sub>27</sub> target. Different solvents were used to obtain more insight about the influence of the ablation liquid environment on the structure and composition of the nanoparticles.

The plasmonic and magnetic properties of the nanoparticles were also studied in detail and, taking advantage from their coexistence, these nanoalloys were optimized as multimodal contrast agents for Magnetic Resonance Imaging, x-ray absorption computerized tomography, and surface enhanced Raman scattering (SERS) imaging. In-vitro and in-vivo tests of their biocompatibility and functionality as multimodal contrast agents were also carried out.

Ag-Fe nanoparticles were synthesized in water and ethanol from targets with different composition. The nanoparticles were studied for their plasmonic and magnetic properties, and in-depth understanding of their complex structure required the use of various complementary techniques of analysis. Due to their magnetic properties, these nanoparticles were used to create customizable arrays for SERS analysis. Various nanoparticles parameters were studied to optimize the SERS efficiency of these arrays, such as surface coating with thiolated ligands or nanoparticles concentration. As a last step, the possibility of reusing these arrays was investigated.

In summary, the application of LASiS to the synthesis of magnetic-plasmonic alloy NPs, which has been attempted in this thesis for the first time, opens several fascinating opportunities for the development of new multifunctional tools in various fields ranging from nanophotonics to nanomedicine.

# Riassunto

---

Nella storia della sintesi delle nanoparticelle, unire le proprietà di differenti elementi in una singola nanostruttura è sempre stato un obiettivo molto importante. Le nanoparticelle di lega metallica attraggono molto l'attenzione dalla comunità scientifica interessata proprio perché creare una lega è un interessante modo di combinare molteplici proprietà in un singolo oggetto, ottenendo ad esempio nanoparticelle con proprietà magnetiche e plasmoniche. Con queste nanostrutture è inoltre possibile effettuare una messa a punto precisa ed accurata di una determinata proprietà fisica o chimica, come ad esempio la posizione del picco di risonanza plasmonico nelle particelle di lega Au-Ag, o l'efficienza dell'idrogenazione di molecole aromatiche nitro-sostituite con leghe Ni-Pd.

L'approccio più frequentemente utilizzato per la sintesi di nanoparticelle in lega metallica sfrutta la sintesi chimica in fase liquida. Molteplici procedure sono state utilizzate in questo ambito, come ad esempio la co-riduzione in singolo stadio di  $\text{HAuCl}_4$  e  $\text{AgNO}_3$ . Altri metodi chimici possibili sono la radiolisi, la sintesi elettrochimica e anche la biosintesi. Tutti questi metodi lavorano in condizioni di equilibrio termodinamico, e questo induce delle severe limitazioni alla varietà di struttura e composizione ottenibili per le nanoleghe.

Metodi fisici come l'impianto ionico o l'epitassia con raggi molecolari possono produrre nanoleghe metastabili, ma sono usate più raramente a causa dei limiti insiti nella scalabilità della produzione di nanoparticelle e nella difficoltà di utilizzo quando le particelle sono inglobate in matrici solide o sono aggregate (spesso irreversibilmente) su un substrato.

Un metodo differente e promettente per la produzione di nanoparticelle in lega è denominato Laser Ablation Synthesis in Solution (LASiS), ovvero ablazione laser in soluzione. Questo metodo prevede l'utilizzo di un laser ad impulsi focalizzato sulla superficie di un bersaglio metallico per generare nanoparticelle in soluzione. Dopo l'assorbimento dell'energia dell'impulso laser da parte del bersaglio metallico, il processo di ablazione avviene mediante la generazione di un plasma e, successivamente, di una bolla di cavitazione, nella quale le nanoparticelle si formano per essere poi raccolte sotto forma di soluzione colloidale nel liquido circostante. La struttura e la composizione delle nanoparticelle sono determinate da numerosi parametri, come la potenza del laser, la durata dell'impulso, il solvente impiegato, la presenza di eventuali molecole in soluzione. Recentemente, la tecnica LASiS è stata

impiegata per creare nanoparticelle in lega metallica, come oro-argento, platino-oro, o platino-iridio.

In questa tesi di dottorato è stata affrontata la sintesi mediante LASiS di nanoparticelle in lega metallica a base di Au-Fe ed Ag-Fe, la cui composizione è metastabile.

Nanoparticelle in lega Au-Fe sono state ottenute ablando un target  $Au_{73}Fe_{27}$ . Differenti solventi sono stati impiegati per ottenere una comprensione più approfondita dell'effetto della soluzione liquida sulla struttura e composizione delle nanoleghe ottenute mediante LASiS.

Le proprietà plasmoniche e magnetiche di queste nanoleghe sono state studiate in dettaglio dal punto di vista sperimentale e con il supporto di modelli teorici. Inoltre, le nanoparticelle di Au-Fe sono state ingegnerizzate per un'applicazione specifica, quella di agenti di contrasto multimodali per imaging mediante risonanza magnetica nucleare, tomografia computerizzata da assorbimento di raggi x, e Raman amplificato tramite l'effetto di Surface Enhanced Raman Scattering (SERS).

Nanoparticelle di Ag-Fe sono state ottenute mediante LASiS partendo da target bimetallici immersi in etanolo. Le proprietà magnetiche e plasmoniche delle nanoparticelle sono state studiate e messe in relazione con la complessa struttura cristallina, che ha richiesto l'utilizzo di numerose tecniche di indagine strutturale per essere compresa appieno. Grazie alle apprezzabili proprietà magnetiche, le nanoparticelle di Ag-Fe sono state utilizzate per realizzare arrays auto-assemblanti utili come substrati per analisi SERS.

In conclusione, la LASiS si è rivelata essere uno strumento molto potente per sintetizzare nanoleghe multifunzionali. In particolare, le nanoparticelle magneto-plasmoniche, qui sintetizzate, studiate ed utilizzate per la prima volta, aprono affascinanti prospettive nella creazione di nuovi strumenti multifunzionali di interesse per vari campi, dalla nanofotonica alla nanomedicina.

# Table of Contents

## **1. An introduction to nanoalloys**

1.1	Introduction	11
1.2	The structure of nanoalloys	17
1.3	Synthesis of nanoalloys	19
1.4	Characterization of nanoalloys	25
1.5	Application of nanoalloys	39
1.6	Bibliography	44

## **2. Optical properties of plasmonic intermetallic nanoparticles and nanoalloys**

2.1	Plasmons	49
2.2	Models for the SPR	52
2.3	SPR Dynamics	57
2.4	Surface-Enhanced Raman Scattering	58
2.5	Plasmonic properties of alloys	62
2.6	Bibliography	67

## **3. Laser Ablation Synthesis of Nanoparticles in Liquid Solution**

3.1	Introduction	71
3.2	Dynamics of Laser Ablation	72
3.3	Investigation Techniques	83
3.4	Parameters of Laser Ablation	87
3.5	Bibliography	96

#### **4. Gold-Iron alloy nanoparticles**

4.1	Abstract	101
4.2	Nanoparticle Synthesis	102
4.3	Nanoparticle Characterization	105
4.4	Optical Properties	109
4.5	Effect of solution on LASiS of Au-Fe Nanoalloys	115
4.6	Magnetic Properties	122
4.7	Au-Fe NPs as Multimodal Contrast Agents	125
4.8	Ablation of multilayer targets	129
4.9	Magnetic-Plasmonic NPs by LASiS and chemical reduction synthesis	134
4.10	Bibliography	136

#### **5. Iron-doped Ag nanoparticles**

5.1	Abstract	139
5.2	Nanoparticle Synthesis	139
5.3	Nanoparticle Characterization	142
5.4	Magnetic properties	149
5.5	Magnetic amplification of optical properties	150
5.6	Reusability of arrays	155
5.7	Bibliography	158

<b>Conclusions</b>	159
--------------------	-----

<b>Publication</b>	161
--------------------	-----

<b>Acknowledgements</b>	162
-------------------------	-----

# Chapter 1

## An introduction to Nanoalloys

### 1.1 Introduction

The Oxford Advanced Learner's Dictionary's entry for the term "nanoparticle", reads

*"A piece of matter less than 100 nm long"*

We know that it is nothing more than a doorplate that adorns the entry to the world of nanoparticles. This category comprises very different objects, from gold nanoparticles used in spectroscopy, to iron oxide nanoparticles used for catalysis and sensors, just to cite a few examples. We can have differences in shape, composition, dimensions and each difference can alter significantly the properties of the nanoparticle. In order to show why nanoparticles are studied so extensively, one can refer to two remarkable examples of monometallic nanoparticles (respectively, gold and iron) and to the related gamut of different phenomena achievable from them.

*The example of gold: Plasmonic nanoparticles.* Gold nanoparticles are probably the type of nanomaterial used since the longest time. Considering the historical fascination of men with the bright colours and durability of noble metals, it is no surprise that gold nanoparticles were appreciated by unaware people already in 4<sup>th</sup>-5<sup>th</sup> century BC in China or Egypt. The most famous use of these nanoparticles as decoration is probably the Lycurgus cup, with its striking double coloration. The cup, when observed under normal illumination conditions, is green. However, when the light is coming from inside the cup, the glass becomes red due

## 1. An introduction to Nanoalloys

to the peculiar absorption of the gold nanoparticles contained in the glass, as can be seen in Figure 1.1.

The first testimony of the employment of these nanoparticles in medicine comes instead from XVII century, when the ancient physician Francisci Antonii published a book detailing the medical uses of colloidal gold<sup>1</sup> (figure 1.1).

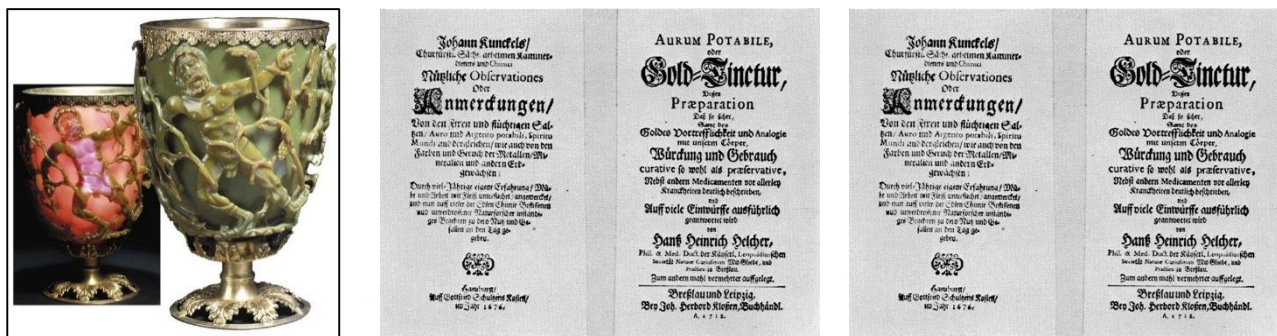


Figure 1.1 – (Left) The Lycurgus Cup (British Museum) (Middle) Panacea Aurea-Auro Potabile, from reference<sup>2</sup>. (Right) Nützliche Observaciones oder Anmerkungen von Auro und Argentio Potabili. From reference<sup>3</sup>.

The optical properties of the gold nanoparticles were already linked to their small dimensions since in 1676 (even if without the in-depth analysis of the following centuries), when the German author Johann Kunckels wrote “gold must be present in such a degree of communion that it is not visible to the human eye”<sup>3</sup> (figure 1.1). In the following centuries, more studies followed, investigating in growing detail the optical properties of gold<sup>2</sup>.

The first true cornerstone of the topic is without doubt the 1857 work of Faraday. He studied the preparation of a colloidal solution of gold, and the optical properties of the solution, such as the reversible colour change visible in dried films obtained from colloidal solutions of gold when subjected to mechanical compression<sup>4</sup>.

In 1908 Gustav Mie authored a publication explaining the optical properties of gold nanoparticles attributing them to the Surface Plasmon Absorption (SPA)<sup>5</sup>. This phenomenon is a broad absorption band visible around 520 nm, due to the collective oscillation of the electron cloud when excited by the electromagnetic field of incoming light. By using Mie's theory, it is possible to calculate the total surface plasmon absorption and scattering cross sections, by considering all the contribution due to the magnetic and electric oscillations. It is also possible to describe the resonances by solving the Maxwell equations for spherical particles, considering the correct boundary conditions. Further studies, carried out in recent years have confirmed Mie's theory that is now considered a cornerstone in the study of gold nanoparticles (see chapter 2 for a more in-depth treatment of the SPA).

The interest for Au NPs greatly increased after the setup of simple and reproducible synthetic methods by Turkevich<sup>6</sup> and Brust et al.<sup>7</sup>, which have made much easier for scientist to obtain nanoparticles with well controlled characteristics. This allowed a larger number of studies on the properties of gold nanoparticles to be performed in multiple fields.



Figure 1.2 - Gold nanoparticles in aqueous solution. The red colour of the solution is linked to the SPA, and the variations are linked to the dimensions of the nanoparticles.

Indeed gold nanoparticles have many applications due to their many interesting characteristics. The SPA allows gold nanoparticles to act like probes for their surrounding environment. Just to cite some examples, it is possible to use the position of the SPA to see changes in the refractive index surrounding the nanoparticles<sup>8</sup>. A frequently used strategy is to functionalize the nanoparticles with specific receptors for the target molecules. When the molecule is bound to the nanoparticle, the refractive index of the nanoparticle's surroundings is investigated by studying the nanoparticle absorption spectra<sup>9</sup>. Another interesting use of gold nanoparticles in this field is their application as molecular rulers<sup>10</sup>. Since the plasmon coupling is so sensitive to the distance between two nanoparticles, it is possible to monitor very fine processes such as DNA hybridization and folding<sup>11</sup>.

Another very interesting application is linked to the local field enhancement. This enhancement is due to the collective oscillation of conduction electrons, and depends on particles size and the assembly of the nanoparticles. As discussed further in Chapter 2, the local field between two gold nanoparticles in optimal conditions can be amplified by many orders of magnitude. The gap between nanoparticles, where this enhancement is available, are called hot spots. It is possible to use this phenomenon to obtain up to 14 orders of magnitude improvement in spectroscopic signals of nearby molecules<sup>12</sup>. The applications of this phenomenon are many, from ultrasensitive detection of multiple analytes<sup>11, 12</sup> to in-vivo labelling of cells<sup>13</sup>.

The chemical properties of the gold nanoparticles are strongly defined by the gold-thiol bond. Nanoparticles obtained with an alkenthiolate coating layer can use ligand exchange reactions without affecting the nanoparticle itself. The dynamics of this exchange reaction



## 1. An introduction to Nanoalloys

depend from many parameters, from the chain length of the ligand<sup>14</sup> to the steric bulk of the leaving and incoming thiols<sup>15, 16</sup>. This technique is very interesting because it allows the introduction of many functional ligands to the surface of the nanoparticle, from electroactive<sup>17-24</sup> and photoactive groups<sup>23-32</sup>, to spin labels<sup>33</sup> and catalysts<sup>34, 35</sup>, as well as simple groups such as halides, nitriles, alkenes, and sulfonates<sup>36-38</sup>. These reagents can be useful by themselves, or they can allow the creation of complex structures after reactions, like the hollow-sphere capsules formed by ring-opening metathesis polymerization of gold nanoparticles functionalized with a tripod ligand exchange<sup>39</sup>.

A different approach available is to use supramolecular chemistry to obtain complex structures such as quasi monodimensional arrays of nanoparticles immobilized into hydrophilic interlayers of dispersed lamellar structures, obtained by mixing bilayer membranes and quaternary cationic ammonium-stabilized AuNPs<sup>39</sup>.

Gold nanoparticles have many uses in catalysis, regardless of the popular knowledge of gold as a chemically inert metal. In CO oxidation different mechanisms<sup>40, 41</sup> were proposed as explanation for the oxidation even at sub-ambient temperature<sup>42</sup>. It is very interesting to note that the geometrical form of the nanoparticles has been shown as important in catalytic activity<sup>43</sup>. Other reactions were reported in literature, such as the electro-oxidation of CO<sup>44</sup> and CH<sub>3</sub>OH<sup>45, 46</sup> or hydrogenation of unsaturated substrates<sup>47</sup>. An alternative approach, using thiolate ligands for catalysis, has been shown to accelerate an already known process, cleavage of 2,4-dinitrophenyl acetate, by more than an order of magnitude<sup>35</sup>.

*The example of iron: iron-based magnetic nanoparticles:* Iron-based magnetic nanoparticles are studied in detail for their many possible applications, from catalysis<sup>48, 49</sup> to biotechnology<sup>50</sup>, to magnetic resonance imaging<sup>51, 52</sup>, to data storage<sup>53</sup> and environmental uses<sup>54, 55</sup>.

The magnetic properties of these nanoparticles are dominated by two contributions: finite-size and surface effects.

The two effects related to the finite size are the single-domain limit, and the superparamagnetic limit. The first defines the maximum dimension to have a single domain uniformly magnetized with all the spins aligned in the same direction<sup>56</sup>. The second is a magnetic behaviour that occurs in small (single-domain, 1-20 nm) *ferro*- or *ferr*i-magnetic particles, that can be simply approximated considering them as with a single giant magnetic moment, derived from the sum of all the magnetic moments of the atoms composing the nanostructure<sup>57</sup>.

Surface effects, on the other hand, can be associated to a series of heterogeneous behaviours, such as the change of magnetization in comparison to bulk values<sup>58, 59</sup>, and/or the enhancement of magnetic anisotropy with decreasing particle size<sup>59, 60</sup>, just to name a few.

A host of possible composition is available for iron-based magnetic nanoparticles, from iron oxides such as  $\text{Fe}_3\text{O}_4$  and  $\gamma\text{-Fe}_2\text{O}_3$ <sup>61-63</sup> to pure metals such as  $\text{Fe}$ <sup>64</sup>. The synthesis methods vary from coprecipitation (particularly used to obtain iron oxides)<sup>65</sup>, to thermal decomposition<sup>66</sup> and other chemical methods. Table 1.1 shows a short resume of the methods available and their peculiarities<sup>67</sup>:

Synthetic method	Synthesis	Reaction temp. [°C]	Reaction period	Solvent	Surface-capping agents	Size distribution	Shape control	Yield
Coprecipitation	Very simple, ambient conditions	20–90	Minutes	Water	Added during or after reaction	Relatively narrow	Not good	High, scalable
Thermal decomposition	Complicated, inert atmosphere	100–320	Hours or days	Organic compound	Added during reaction	Very narrow	Very good	High, scalable
Microemulsion	Complicated, ambient conditions	20–50	Hours	Organic compound	Added during reaction	Relatively narrow	Good	Low
Hydrothermal synthesis	Simple, high pressure	220	Hours or days	Water-ethanol	Added during reaction	Very narrow	Very good	Medium

Table 1.1 – Summary comparison of the synthetic methods. From reference 67.

It is often necessary to protect the surface of these nanoparticles to avoid agglomeration or precipitation, since stability is a fundamental requirement for almost every application of the magnetic nanoparticles. Another crucial issue, especially for pure metal nanoparticles, arises from their sensitivity to oxidation: for very small nanoparticles even mono- or bi-layers of oxide constitute a significant fraction of the atoms, influencing heavily the properties of the nanoparticles. It is interesting to note that almost all of the protection strategies result in a core-shell structure, with an outer layer impervious to oxidation protecting the inner nanoparticles from further modification. What changes is the way this result is achieved: we can have an outer organic shell created with surfactants or polymers<sup>68-72</sup> or an inorganic shell, obtained by silica<sup>73</sup>, carbon<sup>74</sup>, precious metals<sup>75, 76</sup>, or oxides created from the metal of the nanoparticle or additionally deposited<sup>77</sup>. If an organic shell is chosen, it is possible to

## 1. An introduction to Nanoalloys

further functionalize the nanoparticle, obtaining nanosystems useful for drug-delivery, catalysis or sensing.

The biological applications of these nanoparticles are many, from imaging to drug delivery, to magnetic separation. When used for imaging, these nanoparticles mainly serve for magnetic resonance imaging (MRI). This technique studies the relaxation times of protons subjected to a static magnetic field when irradiated with a transversal pulsed radiofrequency field. The two imaging modes available concerns the longitudinal re-alignment of the magnetization vector with the static field (T1) or the transverse re-alignment (T2). Magnetic nanoparticles serve mainly as T2 contrast agents, and are often based on superparamagnetic iron oxides (SPIOs) of mixed maghemite-magnetite composition with dimensions ranging from 3 to 10 nm, covered with hydrophilic molecules such as dextran or polyethylenglicol<sup>78</sup>. A more advanced approach is to target specific molecules by functionalizing the contrast agents with adequate receptors, such as what Boutry et al. carried out by selectively targeting the endothelial inflammatory molecule E-selectin in in-vivo and in-vitro models of inflammation<sup>79</sup>.

When used for magnetic separation, these nanoparticles can capture specific protein or biomolecules. An example of these structures are magnetic iron oxide nanoparticles grafted with dopamine for protein separation<sup>80, 81</sup>. Another important use is for gene separation, like the genomagnetic nanocapturer (GMNC) system created by Tan et al.<sup>82</sup> from a magnetic nanoparticle covered with a silica shell for biocompatibility and protection, with a further layer of avidin-biotin molecules as linkers for bio-conjugating a molecular beacon as the DNA probe.

When used for drug-delivery, iron oxide nanoparticles are generally biocompatible, but their specific behaviour depends greatly from the size of the nanoparticles, since for example NPs with size greater than 200nm are easily removed from the bloodstream by the spleen, while NPs with dimensions smaller than 10 nm are removed through extravasations and renal clearance<sup>83</sup>. When nanoparticles with the correct dimensions (10-100 nm) are used, promising results have been obtained, such as those reported by Alexiou et al. using SPIOs covered with mitoxantrone accumulated at the tumour location with the help of a strong magnetic field<sup>84</sup>. Similar results were obtained by Kohler et al. with biostable methotrexate-immobilized SPIOs nanoparticles that may potentially be used for real-time monitoring by MRI of drug-delivery<sup>85</sup>.

*Merging properties and structures.* The two examples about gold and iron-based nanoparticles are related to mono-element structures, showing multiple and useful properties. The peculiar properties of these nanoparticles can be modified to a certain extent by changing their final shape, structure, size, or surface functionalization. However, there is an intrinsic limit brought by the immutable composition, which makes impossible the introduction of plasmonic response in iron nanoparticles and of appreciable superparamagnetic character in gold nanoparticles.

One solution to this problem is the creation of multielement alloy nanoparticles. By using this approach we can have structures that show more than one property, such as plasmonic and magnetic response, but also new chemical and physical properties of relevance for photonics<sup>86</sup>, catalysis<sup>87</sup>, and nanobiotechnology<sup>88</sup>.

## 1.2 The structure of Nanoalloys

An alloy can be defined as the mixture of two or more metals. One might pursue the realization of nanoalloys to obtain new properties, to combine already existing features in a single structure, or to enhance significantly the already existing ones due to synergistic effects<sup>89</sup>.

The general structure of a binary alloy is defined as  $A_mB_n$ , where  $m$  and  $n$  describe both the size (defined as the number of atoms  $m+n$ ) and composition ( $m/n$ ). These parameters do not give all the information about the nanoparticles, because details about the crystalline order of the nanoalloy, as well as about the occurrence of elements segregation or presence of amorphous domains are not specified. Indeed, on the nanoscale, one can access structures that are normally not available in bulk alloys. This happens because surface effects and size effects become relevant for nanometric objects.

When studying the energy that comes from having different elements in a single structure, it becomes clear that nanoalloys introduce a new problem compared to single element nanoparticles: when atoms from different elements coexist inside a nanostructure, the total energy is not only determined by its crystalline characteristics (such as cell type and parameters) but also to the relative arrangement of the atoms one to another, on the short and on the long distance.

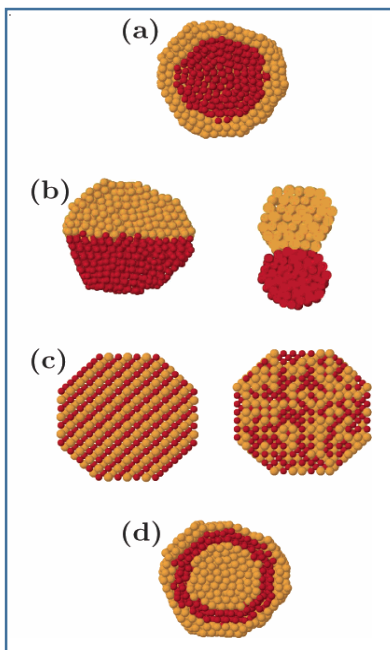
A good way to study the scale of the problem is to see the sheer possible number of “homotops”, defined as alloy clusters with composition  $A_mB_n$ , number of atoms  $m+n$  and composition given by the ratio  $m/n$ , as expressed in equation 1.1:

## 1. An introduction to Nanoalloys

$${}^N P_{A,B} = \frac{N!}{N_A! N_B!} = \frac{N!}{N_A! (N - N_A!)} \quad (1.1)$$

In this equation,  $N=m+n$ ,  $N_A$  is the number  $m$  of atoms of species A, and  $N_B$  is the number  $n$  of atoms of species B<sup>90</sup>. It is immediately clear that the number of possible combinations is very high. If we consider a 25 atoms cluster, with  $m=10$  and  $n=15$ , we already reach 3268760 possible combinations, while if we consider a 100 atoms cluster with  $m=35$  and  $n=65$  we reach  $1.1 \cdot 10^{27}$  possible combinations, without considering point group symmetry.

Nonetheless, the way two elements can arrange in a nanoalloy, i.e. the mixing pattern, can be grouped into four main models (figure 1.3):



A. Core-shell segregated nanoalloys, that comprise clusters where one set of atoms A, is enveloped by the other set of atoms, B; there may be a limited extent of mixing at the interface. This kind of structure is conventionally described as A@B.

B. Segregated nanoalloys, where the atoms remain mainly separated one from the other. Mixing at the interface is theoretically possible.

C. Mixed structures, possible in either their ordered and unordered form.

D. Multishell structures, composed from onion-like structures where the elements alternate, in patterns like A-B-A.

Figure 1.3: Representations of possible mixing patterns (from reference 89)

A number of geometric structures are available in nanoalloys, called “geometric patterns”. In the same way of what happens with bulk structures, the nanoalloys can assume crystalline shapes or non-crystalline shapes. Usually the choice for non-crystalline shapes is made because they allow a better packing of the atoms, even if this comes at the expense of a certain amount of internal strain. It is important to remember that this kind of strain is proportional to the cell volume, therefore it is relevant mainly for big structures, but it becomes sustainable at the nanoscale due to the contribution of surfaces and interfaces, and this explains why non-crystalline structures are often found in nanoparticles<sup>91</sup>. In those cases where the size mismatch between the different atomic species is large, the smaller one can locate inside the crystalline scaffold of the bigger to reduce the structural strain<sup>92</sup>.

The reasons behind the propensity of a nanoalloy for a structure or another is linked to the interaction energies of the atomic species between them and with the environment. In particular, one observes the following general behaviour

- The relative bond strength influences mixing, since if the A-B bond is stronger than A-A and B-B bonds there will be a tendency to observe mixing.
- The surface energies of the single species dictate what atoms will migrate to the surface. The atoms with the lowest surface energy will move to the surface.
- The dimensions influence what atom will occupy the positions closest to the core of the nanoparticle, since in the alloys this part is usually more compressed and benefits greatly from the reduced strain.
- If charge transfer between the two elements occurs, mixing of the elements will be favoured.
- The strength of the bond of the atomic species to surface ligands influences what is the atomic species that will more probably be taken to the surface.
- Magnetic and electronic effects can give further stability to specific configuration, for example by electronic shell structure (as in the jellium model) or electron-spin interaction.

## 1.3 Synthesis of nanoalloys

Materials scientists have several options to obtain new materials with well defined structure and controlled composition, with two or even more different elements. This flexibility arises from the many available methods that can be used to obtain the desired nanoalloy, from physical methods such as ion beam implantation to chemical ones like co-precipitation.

*Chemical reduction of metal salts.* Metal salts are dissolved in an organic solvent, and reduced by appropriate reagents, such as hydrazine hydrate and tri-sodium citrate<sup>93</sup>. By using stabilizing molecules tailored to the surface characteristics of the nanoparticles it becomes possible to stabilize the obtained nanoparticles<sup>94</sup>. These approaches can be in a single phase, in two phases, or can use inverted micelles synthesis.

Many single phase methods can be retraced to the example set by the gold nanoparticles synthesis set up by Turkevich in 1951<sup>95</sup>.

A good example of single-phase synthesis used to obtain alloy nanoparticles is the one used by Mallin et al. to obtain gold-silver alloy nanoparticles by reduction of varying mole fractions of H<sub>2</sub>AuCl<sub>4</sub> and AgNO<sub>3</sub> in water, obtained by using sodium borohydride as a reducing agent

## 1. An introduction to Nanoalloys

and sodium citrate as a capping agent. This synthesis has been shown to obtain an alloy structure thanks to the direct relation between the shift of the plasmon absorbance peak and the metal salt ratio, and to the lack of any appreciable core-shell structure under TEM study, as reported in figure 1.4<sup>96</sup>.

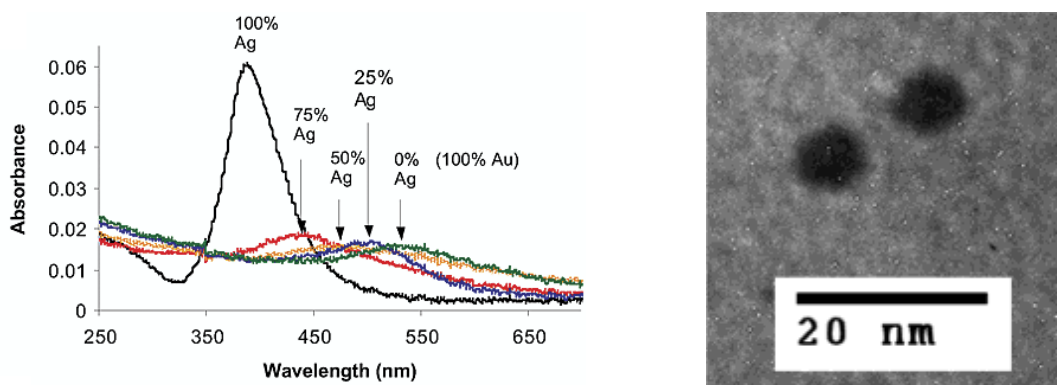


Figure 1.4 - On the left UV-vis absorption spectra of Ag-Au alloy nanoparticles with various molar ratios of Au and Ag. On the right, TEM images of 25% Ag, 75% Au alloy nanoparticles. All particles showed uniform electron density suggesting a non-core-shell structure. From reference 96.

Hostetler et al. used a two-phase synthesis to obtain various noble metals nanoparticles. The metals salts were dissolved in a water-toluene biphasic solution, reduced with the aid of sodium borohydride in the presence of a phase-transfer catalyst (Oct<sub>4</sub>NBr) and a 3-fold excess, in comparison with gold, of either dodecanethiol or didodecyl sulfide. The nanoparticles obtained were gold-silver, gold-copper, gold-silver-copper, gold-platinum, gold-palladium, gold-silver-copper-palladium, and in this study the structures obtained were mainly core-shell type or exhibited at least a partial surface segregation<sup>97</sup>.

The third alternative is using reverse micelles, with the internal side chemically attractive for the metal ions and the external surface soluble in the chosen solvent. In this way, different parameters can be controlled to give the desired result, such as the volume of the solvent, reaction time, relative concentration of the reagents, and temperature<sup>98</sup>.

Weihua et al. obtained platinum-copper alloy nanoparticles of water/cetyltrimethylammonium bromide (CTAB)/isooctane/n-butanol by the co-reduction of H<sub>2</sub>PtCl<sub>6</sub> and CuCl<sub>2</sub> using hydrazine at room temperature. The obtained nanoparticles were studied with multiple methods and had zero-valence and metallic binding energy. Further studies showed that the nanoparticles possessed a lattice spacing consistent with those of a PtCu<sub>3</sub> alloy<sup>99</sup>.

When applying the chemical synthesis to obtain alloys, one main problem is that the nucleation of the two different atomic species must give a single nano-object instead of two distinct nanoparticles composed of different elements. Even in case of formation of bimetallic nanoparticles, usually the metal with the highest redox potential is the first to precipitate,

creating a core where the second metal deposits itself. One can alter this sequence by using a ligand that temporarily binds to the element with the highest redox potential. In this way, the result is an inverse core-shell arrangement. A good example of this procedure is the formation of Ag@Pd clusters: normally when one tries to synthesize an alloy of silver and palladium obtains Pd@Ag nanoparticles, because palladium has a higher redox potential. To obtain the inverse core-shell arrangement, it is necessary to proceed with the synthesis in presence of ammonia: Pd binds more strongly to  $\text{NH}_3$  than Ag, and so the precipitation of silver occurs first, forming the core of the particles, then also palladium is reduced, yielding to the inverse core-shell structure<sup>100</sup>.

We can also create a seed particle of the core material without covering it with a stabilizing ligand and then have it undergo a second reduction with the metal salt of the shell material. Schmid et al used this approach to cover gold nanoparticles without surface protection with platinum or palladium by adding them to a solution of  $\text{H}_2\text{PtCl}_6$  or  $\text{H}_2\text{PdCl}_4$  and  $\text{H}_3\text{NOHCl}$ , and using  $p\text{-H}_2\text{NC}_6\text{H}_4\text{SO}_3\text{Na}$  for stabilization<sup>101</sup>. It is interesting to note that the obtained structure differed significantly, since for the gold-platinum a heterogeneous aggregate was obtained, while the gold-palladium particles showed a well-organized shell of palladium atoms.

Complexes containing both metals are another way of obtaining directly alloy nanoparticles, by decomposition of both metals at the same time. Torigoe et al. obtained silver-palladium colloids by reduction with UV irradiation of Ag(I)bis(Oxalato)palladate(II) in a solution containing PVP. The obtained nanoparticles showed bimetallic nanoparticles, even if their composition was not completely constant<sup>102</sup>.

Mono- and bi-metallic nanoparticles can be synthesized by thermal decomposition of organometallic compounds or salts<sup>103-105</sup>. The best results in terms of size polydispersivity are possible by stabilizing the alloy nanoparticles with a coating molecule, such as polyvinylpyrrolidone<sup>106</sup>.

However, bimetallic nanoparticles with size of the order of few nanometers require particular solutions, such as anchoring the nanoparticles in micropores, by preserving the surface for catalytic applications. Good examples of this technique are the bimetallic RuM (M= Pd, Sn, Pt, Cu, Ag) nanoparticles obtained by Midgley et al. for low-temperature single-step hydrogenation<sup>107</sup>, and shown in Figure 1.5.



## 1. An introduction to Nanoalloys

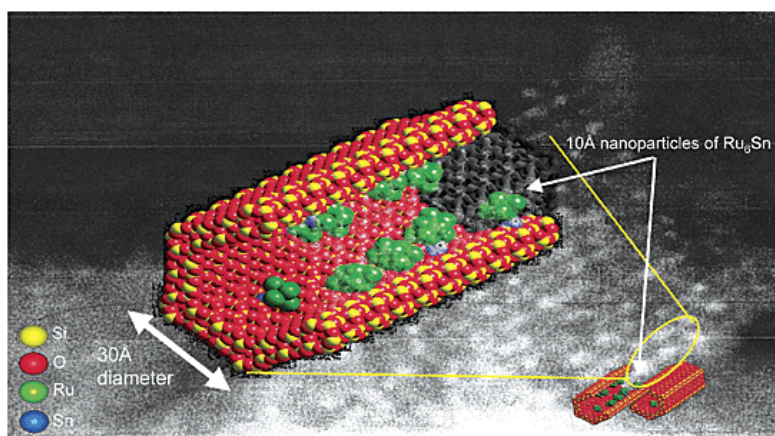


Figure 1.5 - Computer graphic illustration of the Ru<sub>6</sub>Sn nanoparticles superimposed on an enlargement of High-angle annular dark-field (scanning electron transmission) micrograph showing the distribution of anchored Ru<sub>6</sub>Sn nanoparticles within the nanopores of the siliceous host. From reference 107.

**Radiolysis.** Irradiation by nuclear radiation of a solution containing metal ions can induce their co-reduction into bimetallic clusters. In this process,  $\gamma$ -rays are used to generate solvated electrons from water molecules. These electrons are then used to reduce the metal salts<sup>108-111</sup>. Similar to the chemical reduction approach, radiolysis brings to the reduction of the more noble specie first, leading often to the formation of core-shell nanoparticles. However, varying the  $\gamma$ -ray dose is a way to alter the structure of the final product, since higher amounts of  $\gamma$ -rays lead to intra-particle mixing after the formation of the core-shell structure. Various other factors influence the final result, such as the ligands available, the relative metal salts concentration, and in certain circumstances it is still possible to obtain mixed structures without powerful irradiation<sup>112</sup>.

Oh et al. obtained alloy colloids by  $\gamma$ -irradiation with a <sup>60</sup>Co source of a solution containing the dissolved precursors of multiple noble metals and PVP. They obtained mono- and multi-metallic nanoparticles, for example Pd-Ag, Pd-Cu, or Pd-Ni. The obtained nanoparticles were mainly core-shell, but the interactions between the different atoms at the moment of the synthesis brought about varying results (for example silver nanoparticles were formed independently during Pd-Ag synthesis)<sup>113</sup>.

**Electrochemical synthesis.** This method, widely used for mono-element nanoparticles, is indeed very versatile and can be used also to obtain multi-metallic nanoparticles. By using sacrificial bulk metallic anodes, bimetallic nanoparticle such as Fe-Ni, Pd-Ni or Fe-Co were obtained<sup>114</sup>. However, when one would build nanoparticles with ruthenium, rhodium or palladium, it is necessary to reduce their salts at the anodes. By using particular combination of synthesis methods, such as iron and palladium (Fe<sup>2+</sup>/Fe<sup>0</sup> has an E<sup>0</sup> of -0.45 eV, while [PdCl<sub>4</sub>]<sup>2-</sup>/Pd<sup>0</sup> has an E<sup>0</sup> of +0.59 eV) it is possible to obtain core-shell structures (in this particular synthesis, Pd-coated iron nanoparticles)<sup>115</sup>.

An alternative electrochemical approach is the electrodeposition at the interface between two immiscible liquids, particularly appreciated because it allows a smooth reaction surface<sup>116</sup>. An example is shown in Figure 1.6

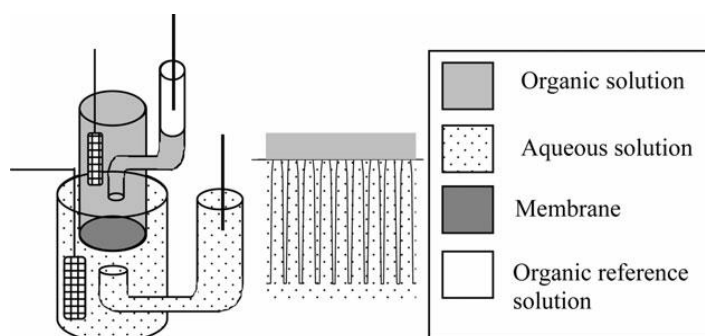


Figure 1.6 - Configuration of the machinery used for electrodeposition at the interface. From reference 117.

This approach allowed Platt et al. to obtain well defined Pd nanoparticles at the mouth of alumina pores of a membrane separating a 1,2-dichloroethane/water interface. By applying a potential difference across the membrane, reduction of aqueous phase tetrachloropalladate to metallic palladium is induced by the potential difference, with butylferrocene in the organic phase employed as an electron donor<sup>117</sup>. Bimetallic nanoparticles can be obtained due to the presence of “seeding” effects from one element promoting the nucleation of the other, as shown by Platt and Dryfe, who used this process to co-deposit platinum and palladium. In this instance the process required specific corrections, such as the use of DMFC as a more facile electron donor. Nucleation of nanoparticles was observed if the aqueous solution contained both metallic ions<sup>118</sup>.

*Sonochemical synthesis.* Ultrasound waves can be used for the synthesis of bimetallic nanoparticles. Mizukoshi et al. obtained gold/palladium bimetallic nanoparticles by irradiating an aqueous solution containing gold(III) and palladium (II) ions with high-intensity ultrasounds, and exploiting the resulting cavitation effects. Sodium dodecyl sulphate was added to the solution to stabilize the obtained nanoparticles, but it was also an important source of reducing species for the metal ions. The obtained nanoparticles showed a gold core-palladium shell structure, with a direct relation on the core-shell ratio from the ions concentrations ratio. It was also suggested that the effects originating from the collapse of the cavitation bubbles, such as effective stirring, microjet stream or shockwaves could have a noticeable effect on the obtained structure<sup>119</sup>. Further studies have shown that successive addition can be an improvement over simultaneous addition of the reagents. Kan et al. for example, have shown that by obtaining Pd nanoclusters from the reduction of  $\text{Pd}(\text{NO}_3)_2$  precursors and then adding  $\text{HAuCl}_4$  it is possible to obtain gold core-palladium shell

## 1. An introduction to Nanoalloys

nanoparticles (instead of the usual palladium core-gold shell) and it is easier to obtain well defined core-shell structures.<sup>120</sup>.

*Biosynthesis.* This approach uses self-assembly by biomolecules to obtain nanostructures<sup>121</sup>. Many systems of biological origin are available for this kind of work, from DNA to polysaccharides.

Senapati et al. reported the synthesis of Au-Ag alloy nanoparticles using fungal biomass, and it was reported that the final composition was influenced by the quantity of cofactor NADH released by the fungi<sup>122</sup>. An alternative approach was used by Zhang et al. to obtain Au-Ag nanoparticles by using extract of *Cacumen platycladi* for the synthesis<sup>123</sup>. In this reaction it was shown that specific functional groups available in the extract (such as C=C, N-H, and -OH) served as reducing agent, while peptides and proteins prevented the aggregation of the obtained nanoparticles<sup>123</sup>.

Another very interesting approach is the biological synthesis of bimetallic nanoparticles. It is already known that a number of microorganisms can reduce metal salts to their metallic state<sup>124, 125</sup>. These particular characteristics allow some strain of bacteria, such as *Spirulina platensis*<sup>126</sup> or various strains of *Lactobacillus*<sup>127</sup> to create gold, silver and gold-silver alloys. An example of what can be obtained by using this synthesis is shown in Figure 1.7.

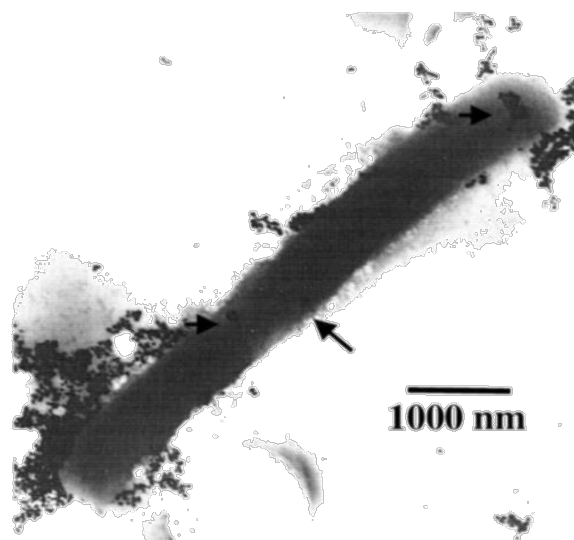


Figure 1.7 - TEM image illustrating coalescence inside the bacteria. The smaller particles of about 25 nm are made outside the bacteria, and they coalesce in larger crystallites inside. From reference 127.

*Ion implantation.* This technique is of particular interest because it allows the creation of metal nanoclusters embedded in insulating matrices, with interesting applications in catalysis<sup>128</sup> and optical switching<sup>129</sup>.

Fernandez et al., in a study concerning Fe-Al implantation in a silica matrix, have shown that an important factor is played by the implantation order<sup>130</sup>. By implanting the aluminium ions first and then the iron ones, they obtained 5-40 nm core-shell nanoparticles with a magnetic behaviour similar to those of bulk iron and lattice parameter similar to those of  $\alpha$ -Fe. If the implantation order was reversed, the obtained core-shell nanoparticles showed diameters ranging from 10 to 15 nanometres, with superparamagnetic behaviour and a bcc iron-based structure with a lattice parameter 2.5% smaller than that of  $\alpha$ -Fe<sup>130</sup>.

*Molecular beams.* With this method, clusters are generated in a specific area, where the metal atoms are vaporized, aggregate, and then coalesce to form clusters. From this area of relatively high pressure, they move through a very narrow nozzle into a vacuum area. At the nozzle exit, we have creation of a high-speed stream of clusters, without significant differences in velocity<sup>131</sup>. An important parameter in this synthesis is the choice of the vaporization/atomization method: we can have laser vaporization, pulsed arc synthesis, ion sputtering, or magnetron sputtering. An example scheme for this method is shown in figure 1.8.

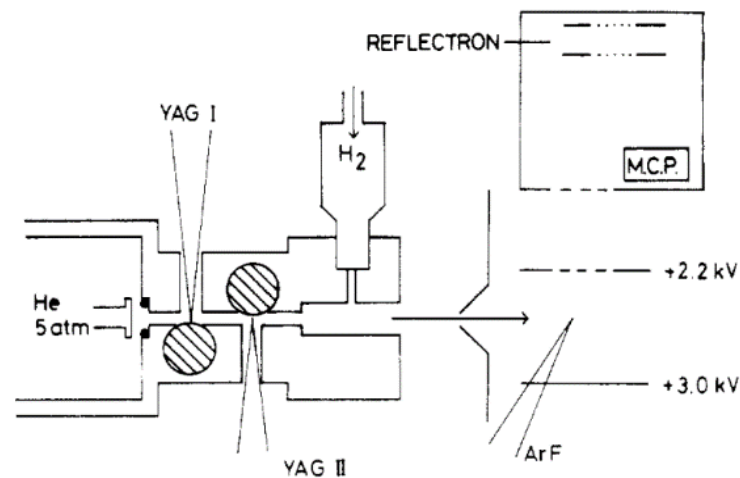


Figure 1.8 - Schematic diagram of the molecular beam apparatus used for creating alloy clusters. From reference 132.

Since in the post-nozzle area the number of impacts among clusters is low, one is forced to the use of alloy targets, mixed metal powders, or two different metal sources. Nonose et al. used this approach to obtain bimetallic vanadium and cobalt clusters from two separate targets<sup>132</sup>.

## 1.4 Characterization of nanoalloys

In addition to all the standard methods routinely exploited for single-element nanoparticles, the characterization of nanoalloys and, in general, of bimetallic nanoparticles, poses the

## 1. An introduction to Nanoalloys

problem of finding further information about how the constitutive components are distributed inside the single nanoparticle, such as the relative positions of the atoms inside the crystalline cells, and how this influences the properties of the nanostructure. A single characterization technique is seldom enough to give a complete picture of the bimetallic nanoparticles structure, and complementary investigation approaches are required.

*Ultraviolet-Visible Spectroscopy.* The optical properties of the nanoparticles are susceptible of change following the variation of composition<sup>133</sup> and ordering<sup>134</sup>. Aggregation is also another parameter that can be monitored by use of this technique<sup>135</sup>.

The UV-visible absorption spectra reported in figure 1.9 show the variation of the surface plasmon absorption peak following the composition change of gold-silver nanoparticles. We can see that moving from the left to right we have a red shift of the plasmon band, from the position of pure silver nanoparticles (400 nm) to the position of pure gold nanoparticles (520 nm). At intermediate composition we see that the plasmon absorption band is moved almost linearly with the composition of the nanoparticles. For example, at around 50%-50% composition we see that the plasmon absorption band is positioned at around 460 nm, a good approximation of the middle position between 400 nm and 520nm<sup>133</sup>.

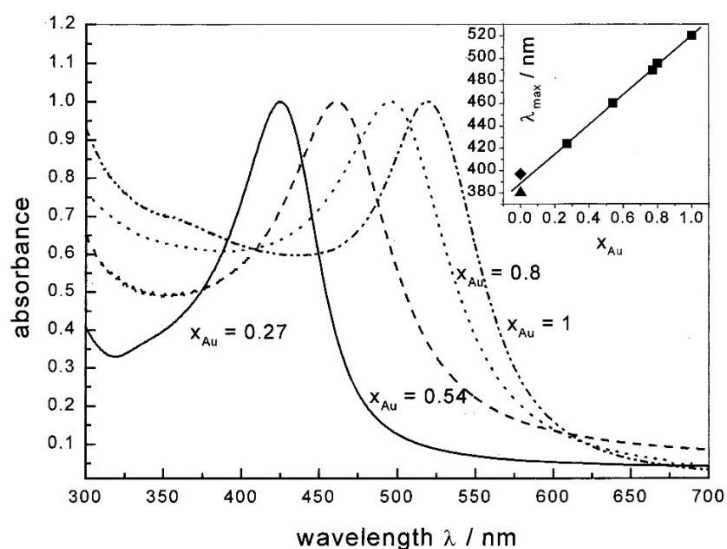


Figure 1.9 - UV-vis absorption spectra of gold and gold-silver alloy nanoparticles with varying gold mole fractions  $x_{Au}$ . The spectra have been normalized at the plasmon absorption maximum. The inset shows how the absorption maximum of the plasmon band depends on the composition. The solid line is a linear fit of the absorption maximum to the gold mole fraction  $x_{Au}$ . The squares correspond to the experimental data while the triangle and diamond are two literature values for pure silver nanoparticles. From reference 133.

We refer to Chapter 2 to show how the SPA can be used to study the structure of bimetallic plasmonic nanoparticles.

*Raman Spectroscopy.* Surface Enhanced Raman Scattering is a method that uses the dramatic increase in the scattering cross sections for molecules positioned at the surface or

in hot spots of the nanoparticles. This method can be used to study the external structure of the nanoparticles, by studying the molecules adsorbed on the surface. Kim et al. have used this method to analyse gold-silver alloy nanoparticles obtained by one-phase synthesis by exploiting pyridine to aggregate the nanoparticles and then studying the obtained Raman spectra. It was shown that the SERS spectra of the alloy nanoparticles were more similar to the one of pure silver nanoparticles, suggesting an enrichment in silver of the surface composition. We will discuss more of the SERS effect in Chapter 2.

*Infrared Spectroscopy.* By using this technique, we can study the vibrational spectrum of small molecules absorbed on the surface of metallic nanoparticles. It can be therefore used to discern the difference in surface composition of the bimetallic nanoparticles from known pure metal ones<sup>87</sup>.

Alayoglu et al. used Fourier-transform infrared spectroscopy to study the differences from a mixture of Pt and Ru nanoparticles and Pt-Ru core-shell nanoparticles obtained by a sequential polyol process. The nanoparticles were dosed with CO and monitored, showing that the IR spectrum closely resembled the IR spectrum of Pt, indicating a platinum-rich surface<sup>136</sup>.

*Mossbauer spectroscopy.* This technique is based on recoil-free absorption and emission of  $\gamma$ -rays from atoms in a lattice. Since the probability of these events is determined by the energy of the  $\gamma$ -ray, this can happen only for certain isotopes that have low-energy transitions available. Examples of atoms that can be used in these studies comprehend <sup>57</sup>Fe, <sup>57</sup>Co, <sup>191</sup>Ir, <sup>197</sup>Au. A certain degree of Doppler-shift is created by accelerating the source at increasing velocities, and when the emitted energy corresponds to the energy levels of the sample, we have an increase in the absorption. The exact position and form of these “peaks” provide information on the environment of the selected isotopes<sup>137</sup>.

The main drawback of this technique is that it is only sensible to the same atoms available in the source.

*Nuclear Magnetic Resonance.* This technique studies the chemical shift and line splitting associated with the local surroundings of nuclei with nonzero magnetic moment. These phenomena are visible due to magnetic coupling to the nuclear spins of magnetic atoms. Extra information may be available when we have quadrupolar nuclei, with  $I > \frac{1}{2}$ , such as <sup>10</sup>B, <sup>17</sup>O and <sup>87</sup>Rb, where the line shape and the number of peaks can give information on the symmetry of the atomic environment.

## 1. An introduction to Nanoalloys

In bimetallic nanoparticles the Knight shift, arising from conduction electrons, can give important information on the metallic nature of the particle<sup>138</sup>.

Properties such as paramagnetism and ferromagnetism can also be analysed with the help of NMR techniques, as can be the structure of adsorbed organic molecules.

Babu et al. studied the differences from the commercial-grade platinum-black and platinum-ruthenium alloy nanoparticles. The NMR peaks of the platinum and alloy nanoparticles showed many differences, since the alloy spectrum is composed from a single Gaussian peak, while the platinum nanoparticles shows a complex "multi-Gaussian" NMR spectrum. Other important differences were found, such as a significant increase in T2 relaxation times of the alloy nanoparticles and a "slow beat" in the spin-echo decay curve of the alloy, suggesting a surface enrichment of Pt atoms in the nanoparticles<sup>139</sup>.

*Magnetic measurements.* Many techniques are available to measure the magnetic properties of a nanoparticle. One of the earliest techniques developed, described by Foner over 40 years ago<sup>140</sup>, is vibrating sample magnetometry. This technique allows the measurement of the magnetic moment of the sample by vibrating it between conducting coils and measuring the resulting alternate current developed at the correct frequency.

Various optical analysis methods are available, exploiting the effect of a magnetic medium on electromagnetic radiation. We can study the magneto-optical Kerr effect, visualizing the effect on polarization and intensity of polarized light when reflected by the surface of a ferromagnetic medium<sup>141</sup>. It is also possible to use circular and linear dichroism measurements in X-ray based spectroscopic techniques<sup>142</sup>. The most common and powerful of these techniques is called X-Ray magnetic circular dichroism in photoabsorption, and in metals studies the differences in L-Edge X-Ray absorption spectra using circularly polarized X-rays with their angular momentum either parallel or antiparallel to the magnetization of the studied sample<sup>143</sup>.

Fundamental data are also acquired by studying the magnetization-magnetic field curves (M-H) that link the magnetic moment of the material with the applied magnetic field<sup>144</sup>. From these curves it is possible to obtain data on retentivity, residual magnetism, coercive force, permeability and reluctance. An instrument that allows the measurement of these curves at different temperatures is called Superconducting Quantum Interference Device<sup>145</sup> (SQUID). Park and Cheon used SQUID to obtain a great deal of data from core-shell and alloy Co-Pt nanoparticles, such as blocking temperature and coercivity. These data showed that the core-shell nanoparticles retain the properties of the cobalt core and are not significantly

influenced by the platinum shell, while on the alloy nanoparticles higher values were obtained, due to increased anisotropy linked to the alloy formation<sup>146</sup>.

Other information about the samples can be obtained by using magnetic force microscopy. This technique is a special mode of noncontact operation of the scanning force microscope that uses a magnetized tip to scan a magnetic sample. The interactions between the sample and the tip give information about the various magnetic characteristics of the sample, such as domain walls and closure domains<sup>147</sup>. Sui et al. used this technique to acquire magnetic and topographic images of FePt clusters obtained by hydrogen reduction of  $\text{Fe}(\text{NO}_3)_3 \cdot 9\text{H}_2\text{O}$  and  $\text{H}_2\text{PtCl}_6 \cdot 6\text{H}_2\text{O}$  mixtures within the pores of alumina<sup>148</sup>.

**Electrochemistry.** The electrochemical behaviour of nanoalloys can be evaluated by techniques such as cyclic voltammetry<sup>46</sup> and scanning electrochemical microscopy<sup>149</sup>. The advantage of these techniques is that they allow the study of nanoalloys in real working conditions for catalytic applications. Fernandez et al. have used scanning electrochemical microscopy to rapidly screen M-Co (M= Pd, Au, Ag) nanoparticles for their oxygen reduction activities, comparing them to the pure-metal ones for their activity in oxygen reduction reaction, as shown in Figure 1.10. For example it was shown that adding cobalt to palladium nanoparticles increased catalytic activity up to 20%, while different composition of gold-cobalt were studied for their electrocatalytic activity<sup>149</sup>.

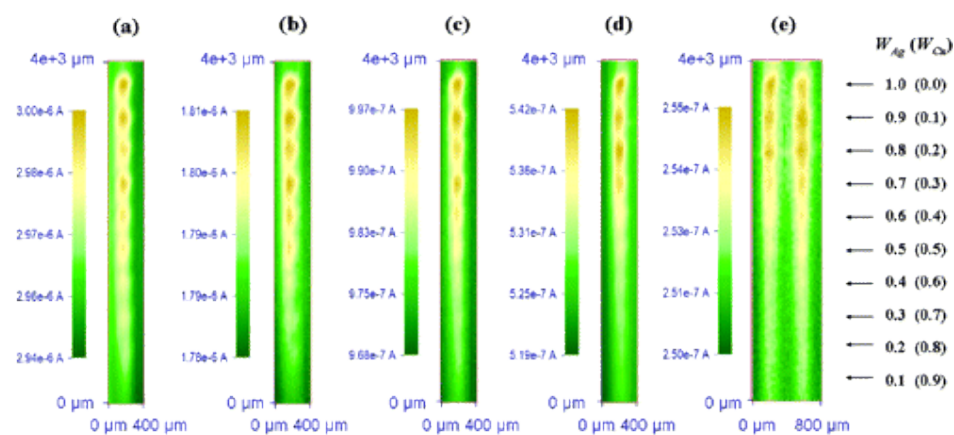


Figure 1.10 - Scanning Electrochemical Microscopy image in Tip generation-substrate collection mode. The data regard oxygen reduction activity measured on binary arrays of Ag-Cu in 0.5M in  $\text{H}_2\text{SO}_4$ . Tip-substrate distance =  $30 \mu\text{m}$ , tip current =  $-160 \text{ nA}$ , scan rate =  $20 \mu\text{m}$  each  $0.017 \text{ s}$ , ES = 0.0 (a), 0.05 (b), 0.1 (c), 0.15 (d), 0.2 (e) V vs HRE. WM is the atomic ratio of metal M in the spot. From reference 149.

**Inductively-Coupled Plasma Assisted - Mass spectroscopy.** With this technique, we have atomization and ionization of the clusters and their subsequent deflection by an electric field, related to their mass/charge ratio. This technique is frequently used to ascertain the composition of bimetallic nanoparticles<sup>150, 151</sup>.



## 1. An introduction to Nanoalloys

*Scanning Electron Microscopy.* Scanning Electron Microscopy (SEM) is a technique that works by giving us an image from secondary electrons emitted from a sample excited by primary electrons from the instrument source. This technique is seldom used in the analysis of alloy nanoparticles because it lacks resolution. It can be used because it allows analysis of bigger samples and because it gives better 3D views of the sample due to its better field of view.

It is possible, with Energy Disperse X-Ray Microanalysis (EDX), to acquire X-rays emitted from the sample when excited with the electrons. These signals are generated in an area deep about 2  $\mu\text{m}$ . By scanning the sample it is possible to acquire an elemental map of selected nanoparticles<sup>152</sup>. An example recorded spectra, acquired with this technique, is shown in Figure 1.11.

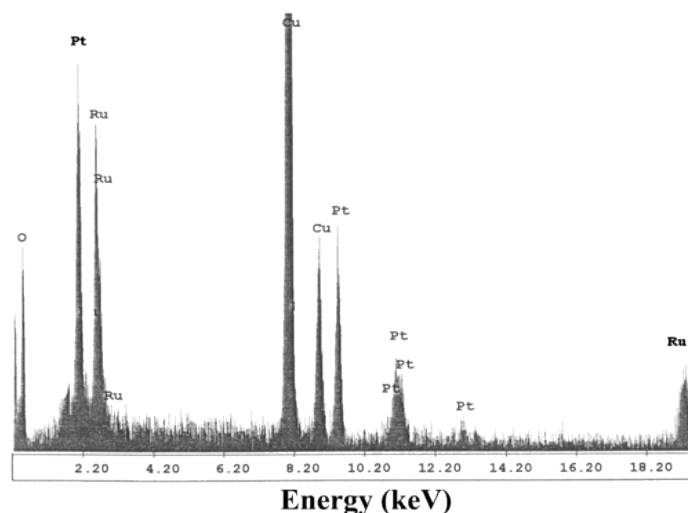


Figure 1.11 - Broad area TEM-EDX spectra of unsupported Pt-Ru nanoparticles. The copper lines are due to substrate grid. From reference 152.

*Transmission Electron Microscopy.* Transmission Electron Microscopy (TEM) is of particular interest in the study of nanoparticles because of its ability to study very small objects<sup>153</sup>. The main principle in this technique is the visualization of the interaction between emitted electrons and the sample while the former pass through the latter. It allows us to see individual nanoparticles with up to sub-nanometric resolution, and they are particularly useful since the contrast between different species with different atomic weight (Z-contrast) is well visible. This helps in discriminating elements with highly different sub-structures, like in the so called “Janus” nanoparticles<sup>154</sup> or in core-shell ones<sup>155</sup>.

High-Resolution Transmission Electron Microscopy (HRTEM) modality allows the analysis in even greater detail of the structure of the bimetallic nanoparticles, obtaining for example

data on atomic packing, crystalline order or defectivity and crystalline interplanar spacings<sup>156</sup>, as shown in Figure 1.12.

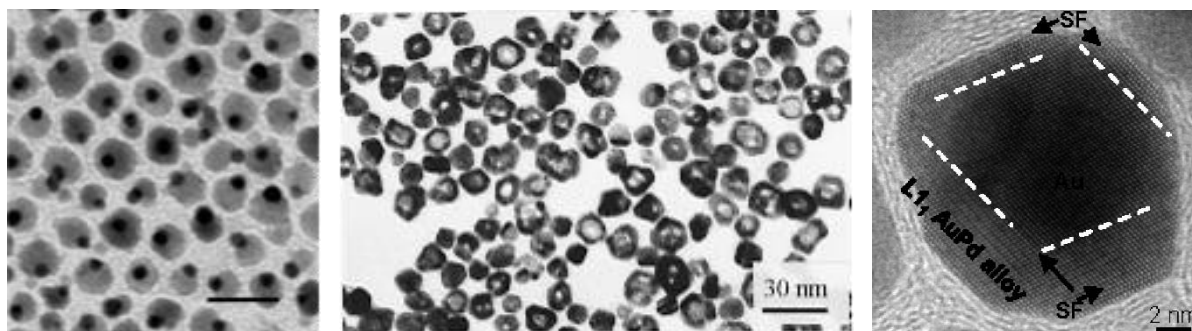


Figure 1.12 – (a) Janus particles consisting of gold (darker spheres) and iron oxide (brighter spheres) [99] (b) TEM images and particle size distributions of silver-iron nanoparticles with Ag/Au-0.4 [100] (c) HRTEM image of AuPd alloy, showing the stacking faults. From reference 156.

Ding et al. have used TEM and HRTEM to analyse the structure of gold core-palladium shell nanoparticles. These methods allowed to see the differences between nanoparticles with very thin shells (<2 nm), that exhibited Shockley partial dislocations (SPD) and stacking faults, and NPs with thicker shells, that exhibit only the stacking faults. The HRTEM allowed to see the diffusion of gold atoms in the Pd shell, that probably allowed the removal of the SPDs from the bigger nanoparticles (visible in figure 1.12 c). A similar process was discovered for small nanoparticles after annealing. This mixing area at the interface between the two materials has been identified as a long range AuPd alloy phase.

Another interesting technique often used in analysis of bimetallic nanoparticles is Scanning Transmission Electron Microscopy (STEM). This technique is similar to a classic TEM, but the electron beam is scanned over the whole surface of the sample and, when used with Z-sensitive imaging techniques such as the high angle annular dark field (HAADF) detector, can give further information about the internal structure of nanoparticles<sup>157</sup>.

Ferrer et al. have used STEM to study the structure of three-layer core-shell nanoparticles of gold and palladium obtained by successive alcoholic reduction of their constituent metal ions. These nanoparticles show a particularly complex structure, with an evenly-alloyed inner core, an Au-rich intermediate layer and a Pd-rich outer shell. The STEM analysis allowed to ascertain the composition of the single layer, and to discover a degree of alloying at the interface between each<sup>157</sup>. An example of the results of this technique when used for the analysis of these multilayer nanoparticles is shown in in figure 1.13.

## 1. An introduction to Nanoalloys

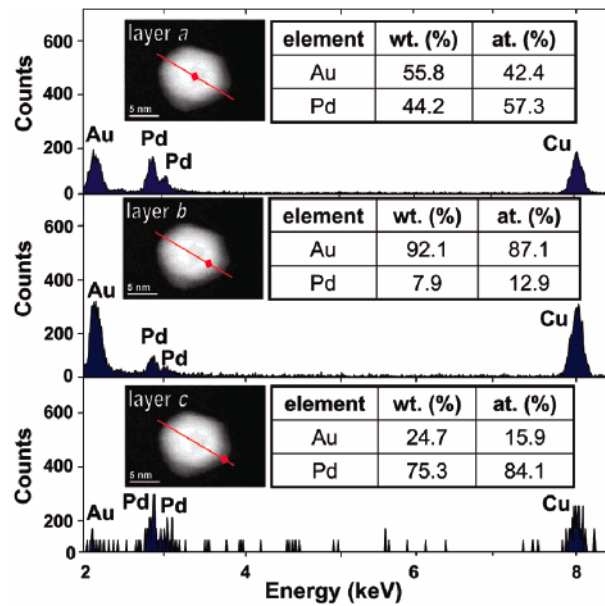


Figure 1.13 – STEM images and results from the analysis of the separate layer of Au-Pd nanoparticles. The first layer is the alloyed core, the second layer the gold-rich shell and the last layer a successive palladium-rich layer. From reference 157.

It is particularly interesting to note that this sensitivity to the Z number can help in discriminating alloy areas in the nanoparticles from same-metal ones, especially in metals that show similar structures like Ag-Au nanoparticles<sup>158</sup>. Li et al. have used the HAADF technique to study the structure of gold-silver nanoparticles of different types, such as core-shell and alloyed, obtained by reverse micelle synthesis. The characteristic of this technique is that the electron scattering is mostly incoherent and the contrast is proportional to nearly the square of the atomic number, so a detailed study of the intensity profile can be used to ascertain the structure of nanoparticles. An example of the energy profiles and the analysis they allow is visible in figure 1.14<sup>158</sup>.

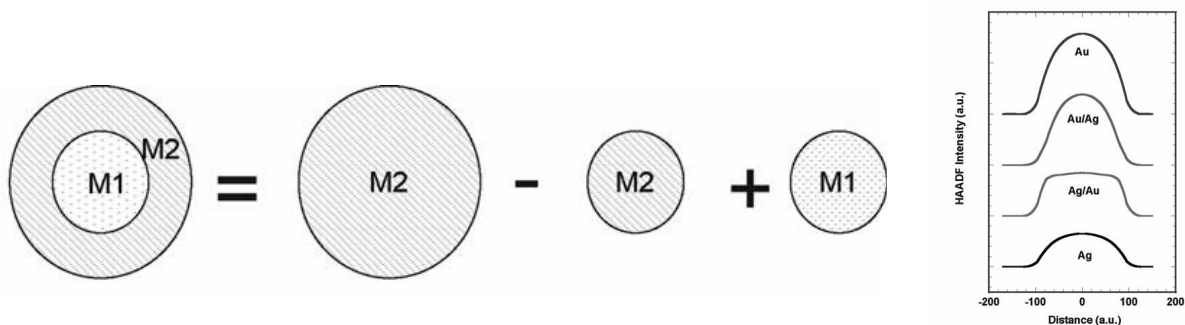


Figure 1.14 – On the left, schematic showing that a core/shell binary nanoparticle is modelled by a simply geometric consideration, where M1 and M2 denote material 1 and material 2, respectively. On the right, simulated HAADF intensity line profiles through the centres of the particles after taking into account the probe size effect. The atomic composition for Au/Ag and Ag/Au is 1 : 1. From reference 158.

TEM also permits the collection of the electron diffraction (ED) patterns, to study the crystal structure and its defects. Compared to X-Ray diffraction, with ED it is possible to probe a much smaller area of the sample down to the single nanoparticles<sup>155</sup>.

*Scanning Probe Microscopy*. This technique uses an atomically-sharp tip to image a surface, sometimes at atomic resolution. The acquired data regard the interaction between the tip and the sample.

If we bring the tip in close proximity to the sample, we can scan the repulsive force between the sample itself and the tip, acquiring data on its topography. This instrument is known as Atomic Force Microscope. This analysis can be carried out in “contact” mode, that is, simply moving the tip on the sample. Another mode of operation is known as “tapping”, where the tip is made to oscillate at its resonant frequency, and by monitoring the decrease in the oscillation amplitude as it reaches the sample, information about the sample is obtained. The last mode of operation is known as “non-contact” mode, carried out again by oscillating the tip at its resonant frequency, but this time the tip is distanced from the sample enough to compensate to keep the frequency constant, and creating an x-y map of the sample, where y is the strength of the interaction. This kind of analysis is often very useful in visualizing the surface of an individual nanoparticles in great detail.

Yang et al. have used this technique to study core-shell gold and silver nanoparticles. The AFM images caught allowed seeing that the average dimensions of the core-shell nanoparticles were compatible with the hypothesis of gold nanoparticles covered by a silver shell. In figure 1.15 are reported the data acquired<sup>159</sup>.

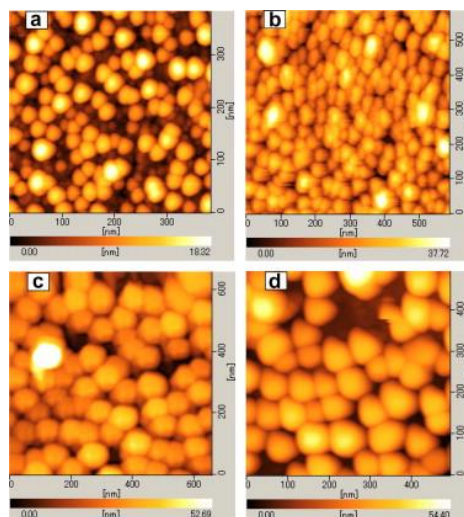


Figure 1.15 - AFM images of (a) pure Au, (b) pure Ag, (c) Au-Ag and (d) Ag-Au monolayer. From reference 159.

A different kind of analysis is carried out using Scanning Tunnelling Microscopy. In this case, a voltage is applied to a circuit composed of the tip and a conductive sample, and the current flow between these two is monitored. We have again different mode of operations: in constant current mode the tip is moved in height over the sample to keep the current constant, while in constant height mode the tip does not move vertically and the flow of the

## 1. An introduction to Nanoalloys

current is monitored. With this technique we can have useful information about electronic structure and topography. Santra et al. have used this analysis method to study the growth kinetics of gold on a clean  $\text{TiO}_2$  and a Ag pre-deposited  $\text{TiO}_2$  surface. With this method, very precise information can be gained, allowing to distinguish that the growth rate on the step-sites is higher than that of the terrace sites. The growth of gold on silver pre-covered substrates seems to suggest that many details of the growth are determined by the availability of empty step-sites. However, it still seems that the pre-deposited silver nanoparticles are determining the growth mode, since it resembles closely that of silver on  $\text{TiO}_2$ . In figure 1.16 are reported some example images acquired with this method<sup>160</sup>.

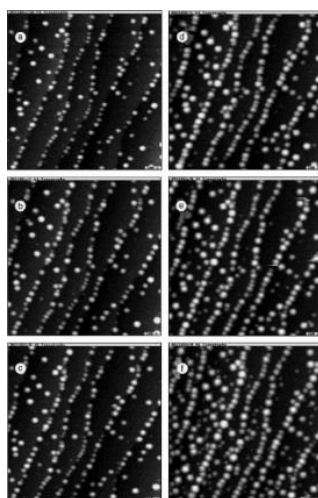


Figure 1.16 - STM images ( $100 \times 100$  nm) during Au deposition on a Ag pre-covered (0.08 ML)  $\text{TiO}_2(1\ 1\ 0)$  surface after deposition of (a) 0.08 ML Ag, (b) 0.17, (c) 0.34, (d) 0.85, (e) 1.53 and (f) 2.04 ML Au. From reference 160.

**X-Ray Absorption Spectroscopy.** This technique studies the absorption of the sample when irradiated with synchrotron X-ray radiation. By studying different areas of the absorption spectrum, we can have information on multiple structural data.

With the analysis of the absorption edge (a technique called Extended X-Ray Absorption Fine Structure, EXAFS), it is possible to obtain information about the atoms that surround the element absorbing the x-rays, such as their atomic number, symmetry and bond length<sup>161</sup>. This information is available because the photoelectrons that result from the absorption event are backscattered from the chemical environment and influence the following absorption events. The effect of this process appears as oscillations in the absorption edge on the high-energy side. This technique is particularly useful in studying nanoalloys because gives information about the reciprocal positions of the atoms even when diffractive techniques fail. Hannemann et al. have used this technique to study gold and gold-silver nanoparticles prepared by flame spray pyrolysis. The data obtained allowed to

ascertain that the nanoparticles are actually mixed nanoparticles, and not core-shell<sup>162</sup>. Some of these results are reported in figure 1.17.

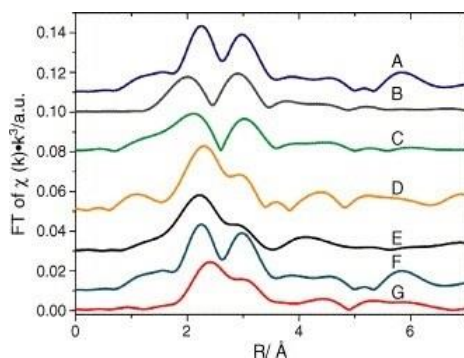


Figure 1.17 - Fourier transformed EXAFS spectra ( $k^3$ -weighted) at the Au  $L_3$ -edge recorded in fluorescence mode of: (A) 1% Au–1% Ag/TiO<sub>2</sub>, (B) 1% Au–1% Ag/SiO<sub>2</sub> and (C) 0.1% Au–0.1% Ag/SiO<sub>2</sub> compared with (D) 1% Au/Fe<sub>2</sub>O<sub>3</sub>/Fe<sub>3</sub>O<sub>4</sub>, (E) 1% Au/SiO<sub>2</sub>, (F) simulated Au–Ag sample and (G) gold foil (transmission mode, scaled down to 40%). From reference 162.

With the Near Edge X-Ray Adsorption Fine Structure (NEXAFS) one obtains information about energy, intensity and symmetry on the bonds between the surface of the nanoparticles and adsorbate molecules. This happens because NEXAFS spectra are heavily influenced by  $\sigma$  and  $\pi$  intramolecular resonances.

Alayoglu et al. used NEXAFS data to study cobalt and platinum-cobalt nanoparticles under reaction conditions during CO<sub>2</sub> hydrogenation. NEXAFS was particularly useful because it allowed to study the oxidation state of the catalyst, discovering that the platinum aids the reduction of cobalt to its metallic state in those conditions. Combined with XPS and TEM analysis, this study allowed the full study of the catalytic dynamics of the nanoparticles under reaction conditions<sup>163</sup>, as is shown in Figure 1.18.

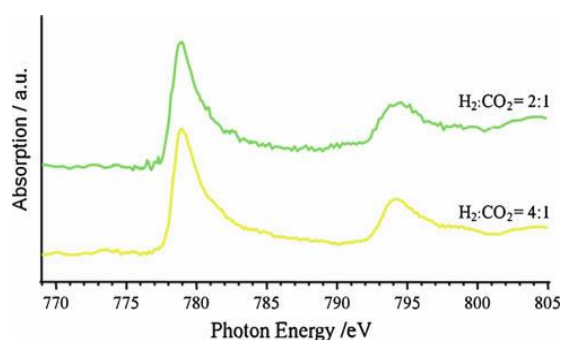


Figure 1.18 - NEXAFS Co  $L$ -edge spectra with Pt50Co50, 4 nm nanoparticles obtained under reactions conditions (1 atmosphere, total pressure 260 Torr, 230 °C with CO<sub>2</sub>:H<sub>2</sub> gas compositions as shown). From reference 163.

Another hot spot of available information is located up to 40 eV from the X-Ray absorption edge. Studying the absorption spectra around this point with the technique called X-Ray Near Edge Absorption (XANES), we can gain further data about the oxidation state of the atom, vacant orbitals, electronic configuration and symmetry of the absorbing atom. Shao

## 1. An introduction to Nanoalloys

et al. used this technique to study the differences between synthesized Co@Pd nanoparticles and a model of palladium foil<sup>164</sup>. The results of the comparison is reported in figure 1.19.

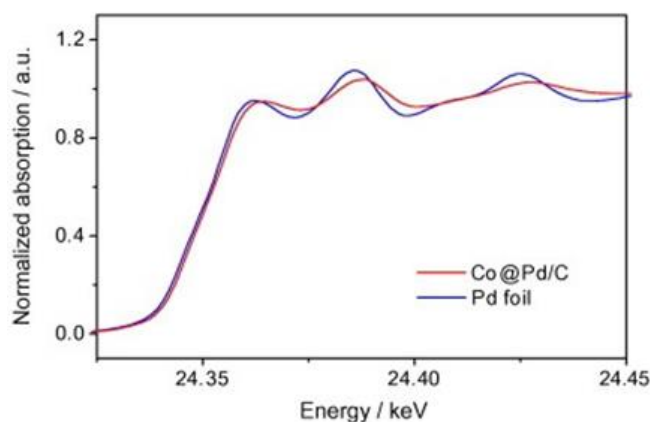


Figure 1.19 – Comparison of XANES spectra of core-shell Co-Pd nanoparticles and Pd foil K-Edge. From reference 164.

**X-Ray Photoelectron Spectroscopy.** In XPS, the sample is irradiated with X-Ray photons, and the photoelectrons emitted from the sample are analysed. We can have emission from core and valence electrons, and thanks to the unique fingerprints of the core electrons we can distinguish the elements present in the sample. Since the peak position and shape are sensitive to multiple parameters, we can also get details about the oxidation state and the formation of chemical bonds<sup>165</sup>.

Jianbo et al. have used this technique to study gold-palladium alloy nanoparticles obtained from organometallic complex precursors. The XPS analysis allowed to see that gold functions as a catalyst for the co-reduction of metal ions in DMF, while monometallic gold and platinum nanoparticles showed different results, especially the lack of evidence of any reduction of platinum to the metallic state, but only to Pt(II)<sup>166</sup>. The results of these studies are reported in figure 1.20.

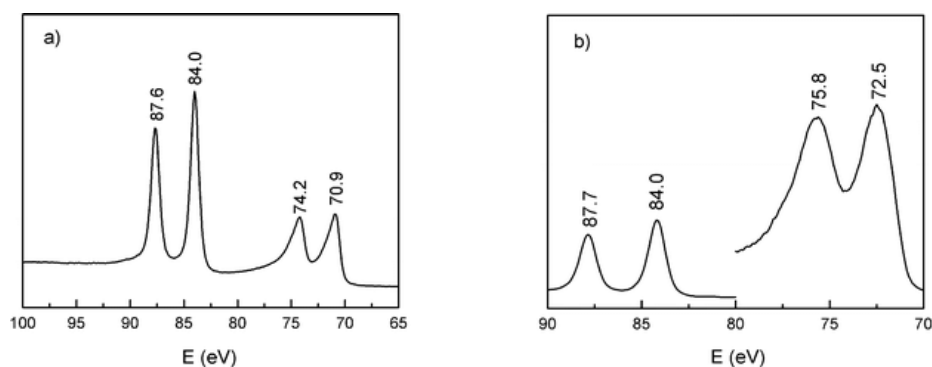


Figure 1.20 - (a) XPS spectra of the AuPt NPs in the Pt 4f and Au 4f regions and (b) XPS spectra for the Au 4f and Pt 4f region of monometallic samples. From reference 166.



The secondary (Auger) electrons emitted from the core also bring information about the composition of the sample<sup>167</sup>.

Stamenkovic et al. used Auger electron spectroscopy to study polycrystalline PtM (M= Co, Ni, Fe) alloys. This technique allowed to find that, due to surface segregation thermodynamics, annealed alloy surfaces form the outermost Pt-skin surface layer, which consists only platinum atoms, while the sputtered surfaces have the bulk ratio of alloying components. After exposure to acidic electrochemical environment the structures exhibited different surface behaviours and led to different activity in oxygen reduction reaction. An example of these information is shown in figure 1.21<sup>168</sup>.

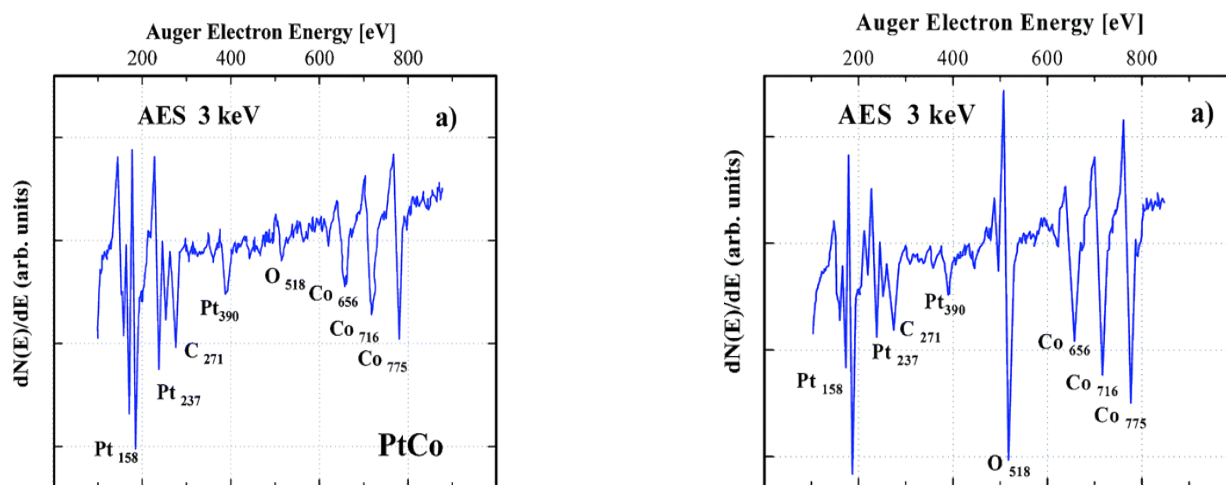


Figure 1.21 – Auger spectrum of PtCo surface after exposure to 0.1M HClO<sub>4</sub> (left), revealing the decrease of Pt content, and H<sub>2</sub>O (right), revealing the formation of stable oxides. From reference 168.

**Ultraviolet photoelectron spectroscopy.** This technique is similar to XPS, but works with vacuum UV radiation (10-45 eV). This radiation is capable of ionising only the valence levels. However, this technique has two main advantages over XPS: the very narrow line width of the radiation and the powerful flux of photons available even from simple sources. The main uses of this technique on nanoparticles concern mainly the study of the electron structures of solids, and the discovery of adsorbate molecules on metals. Stamenkovic et al. used UPS to study Pt<sub>3</sub>M (M= Ni, Co, Fe, Ti, V) sputtered and annealed nanoparticles of interest in oxygen reduction reactions. The technique was used to characterize the surface electronic properties of these nanoparticles, allowing the team to find out that, irrespectively of the 3d element used in conjunction with platinum, the d-band of the annealed surfaces is always downshifted in comparison to that of the sputtered surfaces<sup>169</sup>. The results of these studies are reported in Figure 1.22.



## 1. An introduction to Nanoalloys

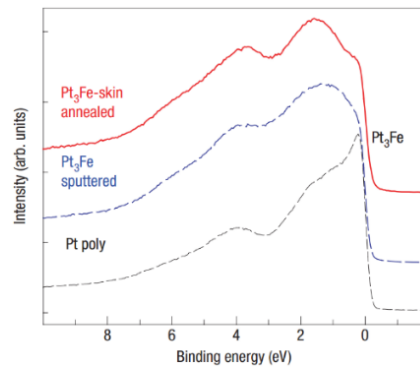


Figure 1.22 – Ultraviolet Photoelectron Spectroscopy (90 eV) of  $Pt_3Fe$ . From reference 169.

**X-Ray Diffraction.** This technique, when applied to nanoparticles, can give us information regarding structure, degree of crystallinity, lattice spacing, particle size and composition. We can also see if any mixing is visible, if the lattice constants of the metals are different enough. Particularly important is Vegard's law, which directly links the lattice parameters of an alloy to the rule of mixture of the single elements' parameters, as can be seen in equation 1.2.

$$a_{A(1-x)Bx} = (1 - x)a_A + xa_B \quad (1.2)$$

In this equation,  $a_{A(1-x)Bx}$  is the lattice parameter of the solution, while  $a_A$  and  $a_B$  are the lattice parameters of the separate elements. And  $x$  is the molar fraction of B in the alloy.

Mehtap et al. used XRD to correlate in detail the annealing process of Pt-Cu alloy nanoparticles, clarifying the roles of temperature and times in the process, and tracing the Vegard structure-composition relationships over a wide temperature range. An interesting result of the study was that the annealing temperature controls the Cu content of the resulting disordered Pt-Cu lattices during heating ramps, while increasing times only allow dimensional increase of the nanoparticles. The ordering happens only during the cooling phase<sup>170</sup>. The results of these studies are shown in figure 1.23.

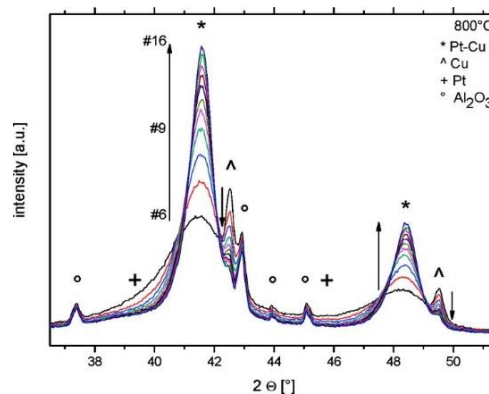


Figure 1.23 - Series of XRD patterns, recorded in a parallel-beam XRD setup during Pt-Cu alloy formation at 800 °C over 9 h. Numbers indicate the first scan (#6,  $t = 0$  h) and final (#16,  $t = 9$  h) at 800 °C. Symbols denote individual crystallographic phases for disordered fcc Pt-Cu alloy, pure Cu, and Pt nanoparticles at 800 °C. From reference 170.

*Ion Scattering Spectroscopy*. In this technique ions are accelerated onto a sample, and the energies and angles of scattered ions are analysed to have information about the sample. One of the strength points of the technique is that by varying the energy of the ions it is possible to probe at variable depth into the sample, even if the intensity of the detected signal decreases. Another interesting application of this technique is that, depending on the energy of the incident ion, surface etching is possible, and so for specific configurations depth profiling of the composition of the nanoparticles is possible. Stamenkovic et al. used this technique to study PtM (M= Co, Ni, Fe) nanoparticles. The technique was used to assess the surface composition of the outermost atomic layer of the nanoparticles, exploiting the calculation of scattering peaks of Pt and M atoms from the classical equation for elastic collisions. The data acquired with this technique are reported in figure 1.24. This technique allowed the detection of different surface compositions depending on the pretreatment<sup>168</sup>.

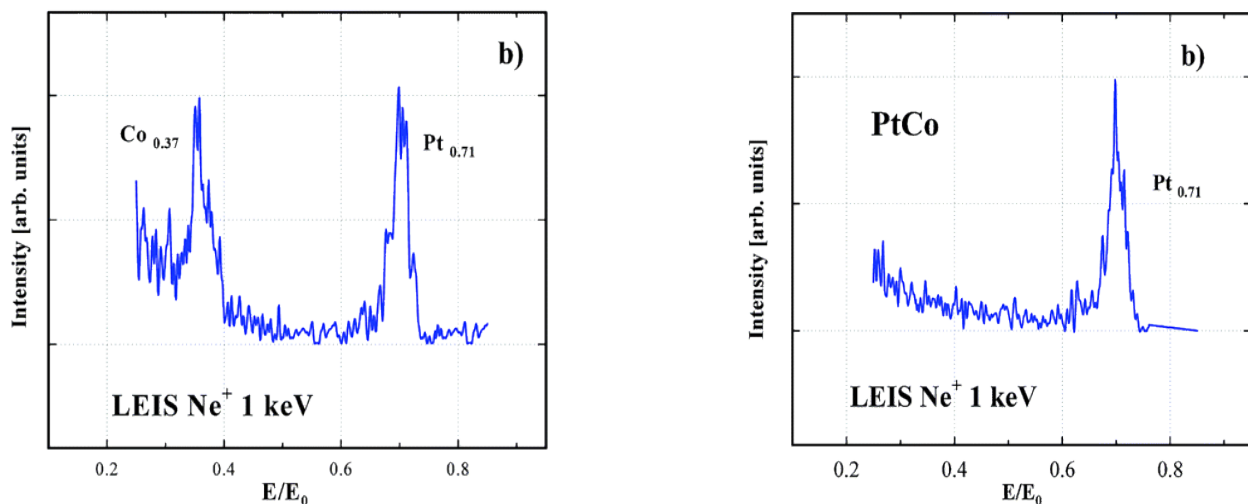


Figure 1.24– Low Energy Ions Spectroscopy spectra of PtCo surface after exposure to 0.1M HClO<sub>4</sub>(left), , and H<sub>2</sub>O (right), showing that only Pt is available on the surface of the nanoparticles in comparison to the pristine nanoparticles. From reference 168.

## 1.5 Applications of nanoalloys

The discovery of nanoalloys opens new opportunities for the application of nanoparticles to solve scientific and technological problems. There are several fields where nanoalloys are being considered with great attention for their new properties and superior performances, such as catalysis, fuel cells, memory devices, optical applications, and nanomedicine.

*Catalysis*. Catalysis is one of the main fields of application of nanoalloys. This is mostly due to the differences in the interactions of neighbouring atoms of different elements compared to single element counterparts, which is exploitable for the realization of catalysts with better properties than those of standard single-element nanoparticles (as we know thanks to the

## 1. An introduction to Nanoalloys

work of Schmid<sup>101</sup>). This is a well-known effect for bulk catalysts<sup>171</sup>, but has been observed also in nanocatalysts<sup>136, 172, 173</sup>. In electrocatalysis there are similar studies carried out from the 1960s<sup>174</sup> and the first examples of this technology employed in commercial products come from the 1970s<sup>175</sup>. This field remains quite strong, especially for oxygen reduction<sup>176, 177</sup>.

Among the many possibilities opened with nanoalloys, it has been shown that alloying of silver nanoparticles with gold improves their selectivity as catalysts for alkene epoxidation<sup>178, 179</sup>.

Pd-Au nanoparticles have been extensively studied for their usefulness in a wide range of catalytic applications. Schmid et al. have shown that core-shell structures of these two materials, supported on titania substrates, can be very useful for the hydrogenation of hex-2-yne to cis-hex-2-ene<sup>180</sup>. The availability of gold inside the nanoparticle dramatically increased the catalytic activity when compared to pure palladium clusters, and the influence of gold was more prominent as the thickness of the shell decreased.

In 2004 Walter et al.<sup>181</sup> discovered that nanorods with a gold-platinum-gold structure displayed autonomous propulsion due to catalytic decomposition of H<sub>2</sub>O<sub>2</sub><sup>182</sup>. Many variations of this structure have been experimented, such as addition of magnetic nickel to provide another control system<sup>183</sup>, the use of different catalysts instead of platinum<sup>184</sup>, or asymmetric deposition of the catalyst to give the object a rotatory acceleration<sup>185</sup>.

Sub-nanometric Ni-Al nanoparticles were obtained by Massicot et al. reducing Ni(OAc)<sub>2</sub> and Al(OAc)<sub>3</sub><sup>186</sup>. These nanoparticles have shown high catalytic activity for the reductive dehalogenation of aliphatic and aromatic halides and polychlorinated arenes.

Ni-Pd nanoparticles show improved catalytic activity in hydrogenation of many nitro-substituted aromatic in mild condition<sup>187</sup> when deposited on silica substrates, while core-shell nanoparticles of these elements show improved activity for Sonogashira coupling reactions, in comparison with pure palladium ones<sup>188</sup>. These structures, obtained by Rothenberg et al. via electrochemical formation of nickel particles followed by reduction of palladium over the obtained seeds, have shown improved activity over many over nanoparticles, as can be seen in figure 1.25<sup>189</sup>.

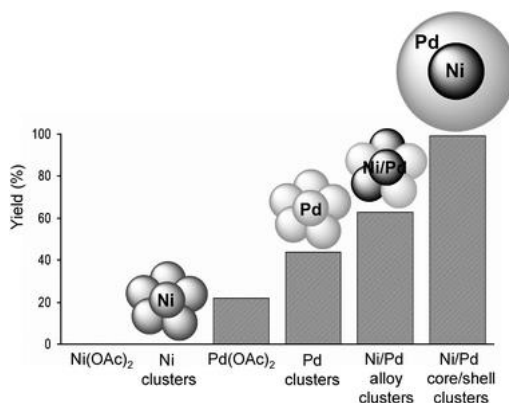


Figure 1.25 - Comparison of catalytic activity for six different systems in the Hiyama cross-coupling of iodotoluene **1b** and trimethoxyphenylsilane **2**: Ni(OAc)<sub>2</sub>, Ni(0) clusters, Pd(OAc)<sub>2</sub>, Pd(0) clusters, Ni(0)/Pd(0) alloy clusters and Ni(0)/Pd(0) core-shell clusters. Reactions were carried out for 24 h in THF at 65 °C. From reference 189.

**Fuel cells.** In fuel cell applications, alloying the platinum electrodes with other metals improves the electro-oxidation currents, especially at lower potentials, and extends the catalyst lifetime. Ru-Pt nanoparticles, supported on carbon, have shown many potential uses in fuel-cells<sup>190, 191</sup> like methanol oxidation in direct methanol fuel cells<sup>192</sup>, and in electrocatalyzed oxidation of methanol<sup>193</sup>. It is also interesting to note that Ru helps in avoiding poisoning of the catalyst by CO<sup>194</sup>. Oxygen reduction reactions appeared promoted when cobalt-platinum nanoparticles deposited on carbon where available<sup>195</sup>.

**Memory devices:** Another avenue of application for the nanoalloys is the creation of more performing memory devices. Park et al. have synthesized Co-Pt nanoparticles by redox transmetalation, and followed their transition from core-shell to intermixed structure with EXAFS measurements. The intermixed structures have shown ferromagnetic properties, and could have useful application as memory devices<sup>196</sup>.

Evans et al. synthesized, with the help of microwave heating, Fe-Pd and Fe-Pt nanoparticles. The Fe-Pt nanoparticles are of special interest, since with this method many monodispersed (2 nm) nanoparticles can be easily synthesized. After heating at moderate temperature (364°C) formation of an ordered phase has been confirmed, with interesting magnetic properties<sup>145, 197</sup>.

Pure-iron nanoparticles are easily oxidized, so coating with a noble metal can allow stabilization and retention of the particular magnetic properties that make them interesting. A good example of this technique was applied by Zhou et al., which synthesized iron core-gold shell nanoparticles with a two-stage process that uses inverse micelles. The magnetic moment of the nanoparticles were found to be similar to those of bulk iron. These nanoparticles were even assembled, with the help of a magnetic field, into monodimensional "nanobands", with length up to 10 μm<sup>198</sup>.

## 1. An introduction to Nanoalloys

An alternative approach has been used by Paulus et al. to coat cobalt nanoparticles with gold, obtaining a structure with strongly reduced magnetic anisotropy (similar to that of bulk cobalt). Structural studies have suggested that this kind of structure might not be a core-shell one, but a mixed structure is more probable<sup>199</sup>.

It is also interesting to note that Fe-Pt and Co-Pt nanoalloys are very interesting for ultrahigh density recording media, since they have high associated magnetic susceptibility and coercivity. Intermixed alloys show ferromagnetic-like behaviour, in comparison with pure cobalt nanoparticles that show superparamagnetic characteristics<sup>200, 201</sup>.

**Biodetection.** Alloy nanoparticles can be used in detection of biological molecules. A good example of these applications is the work carried out by Cao et al., where Ag@Au nanoparticles were functionalized on the surface with alkanethiol-capped oligonucleotides, and used for analysis of DNA by detecting the aggregation caused by DNA-induced assembly<sup>202</sup>. In these applications, sensitivities up to 50 pM were recorded<sup>203</sup>. The use of bimetallic nanoparticles which employs silver shell coated with a gold nanoparticle, can give sensitivities up to 100 aM for the detection of organic molecules<sup>203</sup>. In a similar approach, Cai et al. used Cu@Au nanoparticles to detect *colitoxin* genes, but in this study the hybridization events were monitored by detecting the release of copper atoms anchored on the hybrids via anodic stripping voltammetry<sup>204</sup>.

Zheng et al. used gold-silver alloy nanoshells, synthesized on a silica core, as SERS nanoprobe for the detection of FITC-labeled antihuman IgG molecules. In figure 1.26 we see a short summary of the method used and of the data acquired with this method<sup>205</sup>.

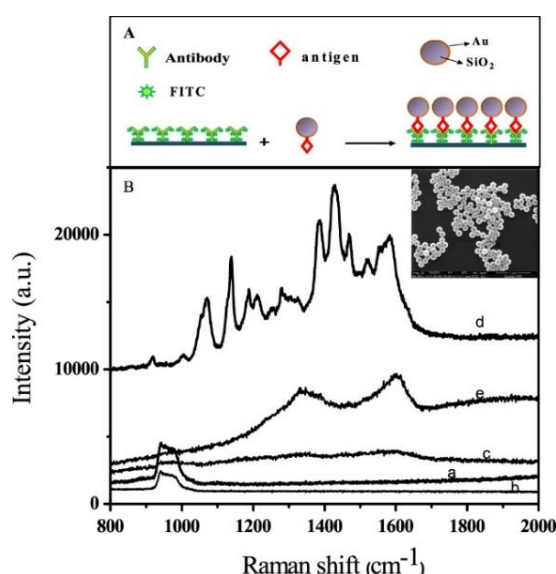


Figure 1.26 - SERS signal of the FITC molecule. The curves (a, b) are corresponding to different proteins (5 nM rat IgG, 5 nM mouse IgG) bound by Au-Ag nanoalloy shells with 0.5 ml HAuCl<sub>4</sub> solution; The curves (c, d, e) correspond to 5 nM human IgG bound by Au/Ag nanoalloy shells with 0.05 ml (c), 0.5 ml (d), 5 ml (e) HAuCl<sub>4</sub> solution. From reference 205.

Alternatively it is possible to use the alloy nanoparticles in conjunction with other structures, as it was carried out by Li et al. by depositing platinum-gold alloy nanoparticles on carbon nanotubes to create a label-free amperometric immunosensor<sup>206</sup>.

*Optical properties:* Nickel can be deposited on gold nanorods, allowing interesting properties such as the alignment of these nanostructures in an external magnetic field<sup>207</sup>. The alignment of nanorods is of interest for further applications because when nanorods composed from coinage metal are aligned with a preferred orientation with respect to light, they show a variation of their optical extinction characteristics on the base of polarization and angle of incidence of the light<sup>208</sup>. Another interesting application of these structures is the creation of barcoded gold-nickel nanorods with the gold end attached to a substrate, that have shown constant velocity circular movements when immersed in a solution containing H<sub>2</sub>O<sub>2</sub> due to the catalytic decomposition of the oxygen at the unattached nickel end of the nanorod<sup>209</sup>.

Jain et al. have synthesized and tested Fe<sub>2</sub>O<sub>3</sub>@Au nanoparticles showing an enhanced optical Faraday rotation peak at 530 nm, not normally visible in maghemite or in gold nanoparticles. This peak is due to a near-field enhancement of the Faraday rotation resulting from the spectral overlap of the surface plasmon resonance in the gold with the electronic transition in maghemite<sup>210</sup>.

Hybrid nanoparticles where one of the components is a compound that can undergo metal-insulator transition (i.e. VO<sub>2</sub>, WO<sub>3</sub>, SmS)<sup>211, 212</sup> in response to different stimuli such as composition, pressure or temperature. A nanoparticle comprising these components will have a section with a variable refractive index, strongly affecting the available plasmon resonance. One example is VO<sub>2</sub>, that has shown two different structures, under 67°C it shows a monoclinic semi-conducting structure VO<sub>2</sub>-M1, while above this temperature the structure switches to tetragonal metallic VO<sub>2</sub>-R. This transformation has a large effect on the conductive and optical properties of these nanoparticles<sup>212-214</sup>, and so this material was combined with gold and silver<sup>215</sup>. The defining properties of these nanoparticles is the drop in optical cross section when they are heated through their phase transition<sup>211</sup>. However, the synthesis methods for these nanoparticles are still in their very early phases<sup>166, 216</sup>.

In silver-iron nanoparticles the shape and position of the plasmon resonance peak vary greatly with the composition and mixing of the two elements<sup>134</sup>. Wilcox and Provencio have shown that these properties could be used as anti-counterfeiting ink<sup>217</sup>.

## 1.6 Bibliography

- 1 F. Antonii, *Panacea Aurea-Auro Potabile*, Bibliopolio Frobeniano, Hamburg, 1618.
- 2 E. A. Hauser, *J. Chem. Educ.*, 1952, **29**, 456.
- 3 J. Kunckels, *Nuetliche Observationes oder Anmerkungen von Auro und Argento Potabili*, Schutzens, Hamburg, 1676.
- 4 M. Faraday, *Philosophical Transactions of the Royal Society of London*, 1857, **147**, 145-181.
- 5 G. Mie, *Annalen der physik*, 1908, **330**, 377-445.
- 6 J. Turkevich, P. C. Stevenson and J. Hillier, *Discuss. Faraday Soc.*, 1951, **11**, 55-75.
- 7 M. Brust, M. Walker, D. Bethell, D. J. Schiffrin and R. Whyman, *J.Chem.Soc., Chem.Commun.*, 1994, , 801-802.
- 8 K. Lee and M. A. El-Sayed, *The Journal of Physical Chemistry B*, 2006, **110**, 19220-19225.
- 9 K. L. Kelly, E. Coronado, L. L. Zhao and G. C. Schatz, *The Journal of Physical Chemistry B*, 2003, **107**, 668-677.
- 10 C. A. Mirkin, R. L. Letsinger, R. C. Mucic and J. J. Storhoff, *Nature*, 1996, **382**, 607-609 (DOI:10.1038/382607a0 [doi]).
- 11 V. M. Shalaev and S. Kawata, *Nanophotonics with surface plasmons*, Elsevier, 2006.
- 12 K. Kneipp, M. Moskovits and H. Kneipp, *Surface-enhanced Raman scattering: physics and applications*, Springer Science & Business Media, 2006.
- 13 X. Qian, X. - Peng, D. O. Ansari, Q. Yin-Goen, G. Z. Chen, D. M. Shin, L. Yang, A. N. Young, M. D. Wang and S. Nie, *Nat. Biotechnol.*, 2008, **26**, 83-90
- 14 A. C. Templeton, W. P. Wuelfing and R. W. Murray, *Acc. Chem. Res.*, 2000, **33**, 27-36.
- 15 M. Montalti, L. Prodi, N. Zaccheroni, R. Baxter, G. Teobaldi and F. Zerbetto, *Langmuir*, 2003, **19**, 5172-5174.
- 16 Y. Song and R. W. Murray, *J. Am. Chem. Soc.*, 2002, **124**, 7096-7102.
- 17 G. Schmid, R. Pfeil, R. Boese, F. Bandermann, S. Meyer, G. Calis and van der Velden, Jan WA, *Chem. Ber.*, 1981, **114**, 3634-3642.
- 18 D. T. Miles and R. W. Murray, *Anal. Chem.*, 2001, **73**, 921-929.
- 19 L. C. Brousseau, Q. Zhao, D. A. Shultz and D. L. Feldheim, *J. Am. Chem. Soc.*, 1998, **120**, 7645-7646.
- 20 H. Nakai, M. Yoshihara and H. Fujihara, *Langmuir*, 1999, **15**, 8574-8576.
- 21 S. Chen and K. Huang, *Langmuir*, 2000, **16**, 2014-2018.
- 22 N. Chandrasekharan and P. V. Kamat, *The Journal of Physical Chemistry B*, 2000, **104**, 10851-10857.
- 23 P. Sudeep, B. I. Ipe, K. G. Thomas, M. George, S. Barazzouk, S. Hotchandani and P. V. Kamat, *Nano Letters*, 2002, **2**, 29-35.
- 24 K. G. Thomas, B. I. Ipe and P. Sudeep, *Pure and Applied Chemistry*, 2002, **74**, 1731-1738.
- 25 P. V. Kamat, *The Journal of Physical Chemistry B*, 2002, **106**, 7729-7744.
- 26 A. Dawson and P. V. Kamat, *The Journal of Physical Chemistry B*, 2001, **105**, 960-966.
- 27 J. Hu, J. Zhang, F. Liu, K. Kittredge, J. K. Whitesell and M. A. Fox, *J. Am. Chem. Soc.*, 2001, **123**, 1464-1470.
- 28 G. Wang, J. Zhang and R. W. Murray, *Anal. Chem.*, 2002, **74**, 4320-4327.
- 29 A. Aguila and R. W. Murray, *Langmuir*, 2000, **16**, 5949-5954.
- 30 B. I. Ipe, K. G. Thomas, S. Barazzouk, S. Hotchandani and P. V. Kamat, *The Journal of Physical Chemistry B*, 2002, **106**, 18-21.
- 31 S. Evans, S. Johnson, H. Ringsdorf, L. Williams and H. Wolf, *Langmuir*, 1998, **14**, 6436-6440.
- 32 H. Imahori, M. Arimura, T. Hanada, Y. Nishimura, I. Yamazaki, Y. Sakata and S. Fukuzumi, *J. Am. Chem. Soc.*, 2001, **123**, 335-336.
- 33 P. Ionita, A. Caragheorghopol, B. C. Gilbert and V. Chechik, *J. Am. Chem. Soc.*, 2002, **124**, 9048-9049.
- 34 H. Li, Y. Luk and M. Mrksich, *Langmuir*, 1999, **15**, 4957-4959.
- 35 L. Pasquato, F. Rancan, P. Scrimin, F. Mancin and C. Frigeri, *Chemical Communications*, 2000, , 2253-2254.
- 36 S. Chen, *Langmuir*, 1999, **15**, 7551-7557.
- 37 S. Chen and R. W. Murray, *Langmuir*, 1999, **15**, 682-689.
- 38 M. G. Warner, S. M. Reed and J. E. Hutchison, *Chemistry of materials*, 2000, **12**, 3316-3320.
- 39 M. Wu, S. A. O'Neill, L. C. Brousseau, W. P. McConnell, D. A. Shultz, R. J. Linderman and D. L. Feldheim, *Chemical Communications*, 2000, , 775-776.
- 40 Y. Yuan, K. Asakura, H. Wan, K. Tsai and Y. Iwasawa, *Chem. Lett.*, 1996, , 755-756.
- 41 A. P. Kozlova, A. I. Kozlov, S. Sugiyama, Y. Matsui, K. Asakura and Y. Iwasawa, *Journal of Catalysis*, 1999, **181**, 37-48.
- 42 M. Haruta, A. Ueda, S. Tsubota and R. T. Sanchez, *Catalysis Today*, 1996, **29**, 443-447.
- 43 T. M. Salama, R. Ohnishi, T. Shido and M. Ichikawa, *Journal of catalysis*, 1996, **162**, 169-178.
- 44 M. M. Maye, Y. Lou and C. Zhong, *Langmuir*, 2000, **16**, 7520-7523.

- 45 J. Luo, M. M. Maye, Y. Lou, L. Han, M. Hepel and C. J. Zhong, *Catalysis today*, 2002, **77**, 127-138.
- 46 Y. Lou, M. M. Maye, L. Han, J. Luo and C. Zhong, *Chemical Communications*, 2001, , 473-474.
- 47 C. Mohr, H. Hofmeister, J. Radnik and P. Claus, *J. Am. Chem. Soc.*, 2003, **125**, 1905-1911.
- 48 A. Lu, W. Schmidt, N. Matoussevitch, H. Bönemann, B. Spliethoff, B. Tesche, E. Bill, W. Kiefer and F. Schüth, *Angewandte Chemie International Edition*, 2004, **43**, 4303-4306
- 49 S. C. Tsang, V. Caps, I. Paraskevas, D. Chadwick and D. Thompsett, *Angewandte Chemie*, 2004, **116**, 5763-5767 (DOI:10.1002/ange.200460552).
- 50 A. K. Gupta and M. Gupta, *Biomaterials*, 2005, **26**, 3995-4021.
- 51 S. Mornet, S. Vasseur, F. Grasset, P. Veverka, G. Goglio, A. Demourgues, J. Portier, E. Pollert and E. Duguet, *Progress in Solid State Chemistry*, 2006, **34**, 237-247
- 52 Z. Li, L. Wei, M. Gao and H. Lei, *Adv Mater*, 2005, **17**, 1001-1005
- 53 T. Hyeon, *Chemical Communications*, 2003, , 927-934.
- 54 D. W. Elliott and W. Zhang, *Environ. Sci. Technol.*, 2001, **35**, 4922-4926.
- 55 M. Takafuji, S. Ide, H. Ihara and Z. Xu, *Chemistry of materials*, 2004, **16**, 1977-1983.
- 56 X. Batlle and A. Labarta, *J. Phys. D*, 2002, **35**, R15.
- 57 M. Benz, *Unpublished manuscript*, 2012, .
- 58 R. Kodama, *J Magn Magn Mater*, 1999, **200**, 359-372.
- 59 M. Respaud, J. Broto, H. Rakoto, A. Fert, L. Thomas, B. Barbara, M. Verelst, E. Snoeck, P. Lecante and A. Mosset, *Physical Review B*, 1998, **57**, 2925.
- 60 F. Bødker, S. Mørup and S. Linderoth, *Phys. Rev. Lett.*, 1994, **72**, 282.
- 61 S. Neveu, A. Bee, M. Robineau and D. Talbot, *J. Colloid Interface Sci.*, 2002, **255**, 293-298.
- 62 F. Grasset, N. Labhsetwar, D. Li, D. Park, N. Saito, H. Haneda, O. Cadot, T. Roisnel, S. Mornet and E. Duguet, *Langmuir*, 2002, **18**, 8209-8216.
- 63 S. Sun and H. Zeng, *J. Am. Chem. Soc.*, 2002, **124**, 8204-8205.
- 64 S. Park, S. Kim, S. Lee, Z. G. Khim, K. Char and T. Hyeon, *J. Am. Chem. Soc.*, 2000, **122**, 8581-8582.
- 65 A. Bee, R. Massart and S. Neveu, *J Magn Magn Mater*, 1995, **149**, 6-9.
- 66 S. Sun, H. Zeng, D. B. Robinson, S. Raoux, P. M. Rice, S. X. Wang and G. Li, *J. Am. Chem. Soc.*, 2004, **126**, 273-279.
- 67 A. Lu, E. e. Salabas and F. Schüth, *Angewandte Chemie International Edition*, 2007, **46**, 1222-1244.
- 68 L. E. Euliss, S. G. Grancharov, S. O'Brien, T. J. Deming, G. D. Stucky, C. Murray and G. Held, *Nano Letters*, 2003, **3**, 1489-1493.
- 69 X. Liu, Y. Guan, Z. Ma and H. Liu, *Langmuir*, 2004, **20**, 10278-10282.
- 70 R. Hong, N. O. Fischer, T. Emrick and V. M. Rotello, *Chemistry of materials*, 2005, **17**, 4617-4621.
- 71 Y. Sahoo, H. Pizem, T. Fried, D. Golodnitsky, L. Burstein, C. N. Sukenik and G. Markovich, *Langmuir*, 2001, **17**, 7907-7911.
- 72 M. Kim, Y. Chen, Y. Liu and X. Peng, *Adv Mater*, 2005, **17**, 1429-1432.
- 73 Y. Kobayashi, M. Horie, M. Konno, B. Rodríguez-González and L. M. Liz-Marzán, *The Journal of Physical Chemistry B*, 2003, **107**, 7420-7425.
- 74 A. Lu, W. Li, N. Matoussevitch, B. Spliethoff, H. Bönemann and F. Schüth, *Chemical communications*, 2005, , 98-100.
- 75 Q. Liu, Z. Xu, J. Finch and R. Egerton, *Chemistry of materials*, 1998, **10**, 3936-3940.
- 76 J. Lin, W. Zhou, A. Kumbhar, J. Wiemann, J. Fang, E. Carpenter and C. O'Connor, *Journal of Solid State Chemistry*, 2001, **159**, 26-31.
- 77 N. O. Núñez, P. Tartaj, M. P. Morales, P. Bonville and C. J. Serna, *Chemistry of materials*, 2004, **16**, 3119-3124.
- 78 R. Qiao, C. Yang and M. Gao, *Journal of Materials Chemistry*, 2009, **19**, 6274-6293.
- 79 S. Boutry, S. Laurent, L. V. Elst and R. N. Muller, *Contrast media & molecular imaging*, 2006, **1**, 15-22.
- 80 C. Xu, K. Xu, H. Gu, R. Zheng, H. Liu, X. Zhang, Z. Guo and B. Xu, *J. Am. Chem. Soc.*, 2004, **126**, 9938-9939.
- 81 L. X. Chen, T. Liu, M. C. Thurnauer, R. Csencsits and T. Rajh, *The Journal of Physical Chemistry B*, 2002, **106**, 8539-8546.
- 82 X. Zhao, R. Tapeç-Dytioco, K. Wang and W. Tan, *Anal. Chem.*, 2003, **75**, 3476-3483.
- 83 S. Laurent, D. Forge, M. Port, A. Roch, C. Robic, L. Vander Elst and R. N. Muller, *Chem. Rev.*, 2008, **108**, 2064-2110.
- 84 C. Alexiou, W. Arnold, P. Hulin, R. J. Klein, H. Renz, F. G. Parak, C. Bergemann and A. S. Lübbe, *J Magn Magn Mater*, 2001, **225**, 187-193.
- 85 N. Kohler, C. Sun, J. Wang and M. Zhang, *Langmuir*, 2005, **21**, 8858-8864.
- 86 G. Armelles, A. Cebollada, A. García-Martín and M. U. González, *Advanced Optical Materials*, 2013, **1**, 10-35.
- 87 N. Toshima and T. Yonezawa, *New Journal of Chemistry*, 1998, **22**, 1179-1201.
- 88 V. Amendola, S. Scaramuzza, L. Litti, M. Meneghetti, G. Zuccolotto, A. Rosato, E. Nicolato, P. Marzola, G. Fracasso and C. Anselmi, *Small*, 2014, .
- 89 R. Ferrando, J. Jellinek and R. L. Johnston, *Chem. Rev.*, 2008, **108**, 845-910.



## 1. An introduction to Nanoalloys

- 90 J. Jellinek and E. B. Krissinel, in *Theory of Atomic and Molecular Clusters*, ed. nonymous, Springer, 1999, p. 277-308.
- 91 F. Baletto and R. Ferrando, *Reviews of modern physics*, 2005, **77**, 371.
- 92 G. Rossi, A. Rapallo, C. Mottet, A. Fortunelli, F. Baletto and R. Ferrando, *Phys. Rev. Lett.*, 2004, **93**, 105503.
- 93 A. Pal, S. Shah and S. Devi, *Colloids Surf. Physicochem. Eng. Aspects*, 2007, **302**, 51-57.
- 94 G. S. Chaubey, C. Barcena, N. Poudyal, C. Rong, J. Gao, S. Sun and J. P. Liu, *J. Am. Chem. Soc.*, 2007, **129**, 7214-7215.
- 95 M. Wuiherschick, A. Birnbaum, S. Witte, M. Sztucki, U. Vainio, N. Pinna, K. Rademann, F. Emmerling, R. Kraehnert and J. Polte, *ACS nano*, 2015, .
- 96 M. P. Mallin and C. J. Murphy, *Nano Letters*, 2002, **2**, 1235-1237.
- 97 M. J. Hostetler, C. Zhong, B. K. Yen, J. Anderegg, S. M. Gross, N. D. Evans, M. Porter and R. W. Murray, *J. Am. Chem. Soc.*, 1998, **120**, 9396-9397.
- 98 A. B. Smetana, J. S. Wang, J. Boeckl, G. J. Brown and C. M. Wai, *Langmuir*, 2007, **23**, 10429-10432.
- 99 W. Weihua, T. Xuelin, C. Kai and C. Gengyu, *Colloids Surf. Physicochem. Eng. Aspects*, 2006, **273**, 35-42.
- 100 D. V. Goia and E. Matijević, *New Journal of Chemistry*, 1998, **22**, 1203-1215.
- 101 G. Schmid, A. Lehnert, J. Malm and J. Bovin, *Angewandte Chemie International Edition in English*, 1991, **30**, 874-876.
- 102 K. Torigoe and K. Esumi, *Langmuir*, 1993, **9**, 1664-1667.
- 103 K. Esumi, T. Tano, K. Torigoe and K. Meguro, *Chemistry of Materials*, 1990, **2**, 564-567.
- 104 P. Braunstein and J. Rose, *Metal Clusters in Chemistry*, 1999, , 616-677.
- 105 H. Bönemann and R. M. Richards, *European Journal of Inorganic Chemistry*, 2001, **2001**, 2455-2480.
- 106 J. S. Bradley, G. H. Via, L. Bonneviot and E. W. Hill, *Chemistry of materials*, 1996, **8**, 1895-1903.
- 107 J. M. Thomas, B. F. Johnson, R. Raja, G. Sankar and P. A. Midgley, *Acc. Chem. Res.*, 2003, **36**, 20-30.
- 108 S. Remita, M. Mostafavi and M. Delcourt, *Radiat. Phys. Chem.*, 1996, **47**, 275-279.
- 109 T. A. Yamamoto, T. Nakagawa, S. Seino and H. Nitani, *Applied Catalysis A: General*, 2010, **387**, 195-202.
- 110 T. Redjala, H. Remita, G. Apostolescu, M. Mostafavi, C. Thomazeau and D. Uzio, *Oil & Gas Science and Technology-Revue de l'IFP*, 2006, **61**, 789-797.
- 111 T. A. Yamamoto, S. Kageyama, S. Seino, H. Nitani, T. Nakagawa, R. Horioka, Y. Honda, K. Ueno and H. Daimon, *Applied Catalysis A: General*, 2011, **396**, 68-75.
- 112 J. Belloni, M. Mostafavi, H. Remita, J. Marignier and M. Delcourt, *New Journal of Chemistry*, 1998, **22**, 1239-1255.
- 113 S. Oh, M. Kim, S. Choi, J. Chun, K. Lee, A. Gopalan, C. Hwang, K. Sang-Ho and O. J. Hoon, *Journal of Industrial and Engineering Chemistry*, 2008, **14**, 687-692.
- 114 M. T. Reetz, W. Helbig and S. A. Quaiser, *Chemistry of materials*, 1995, **7**, 2227-2228.
- 115 C. Wang and W. Zhang, *Environ. Sci. Technol.*, 1997, **31**, 2154-2156.
- 116 Y. Cheng and D. J. Schiffrin, *Journal of the Chemical Society, Faraday Transactions*, 1996, **92**, 3865-3871.
- 117 M. Platt, R. A. Dryfe and E. P. Roberts, *Chemical Communications*, 2002, , 2324-2325.
- 118 M. Platt and R. A. Dryfe, *Physical Chemistry Chemical Physics*, 2005, **7**, 1807-1814.
- 119 Y. Mizukoshi, T. Fujimoto, Y. Nagata, R. Oshima and Y. Maeda, *The Journal of Physical Chemistry B*, 2000, **104**, 6028-6032.
- 120 C. Kan, W. Cai, C. Li, L. Zhang and H. Hofmeister, *J. Phys. D*, 2003, **36**, 1609.
- 121 R. Brayner, T. Coradin, F. Fiévet-Vincent, J. Livage and F. Fiévet, *New journal of chemistry*, 2005, **29**, 681-685.
- 122 S. Senapati, A. Ahmad, M. I. Khan, M. Sastry and R. Kumar, *Small*, 2005, **1**, 517-520.
- 123 G. Zhang, M. Du, Q. Li, X. Li, J. Huang, X. Jiang and D. Sun, *RSC Advances*, 2013, **3**, 1878-1884.
- 124 J. R. Lloyd and D. R. Lovley, *Curr. Opin. Biotechnol.*, 2001, **12**, 248-253.
- 125 J. R. Lloyd, V. A. Sole, C. V. Van Praagh and D. R. Lovley, *Appl. Environ. Microbiol.*, 2000, **66**, 3743-3749.
- 126 K. Govindaraju, S. K. Basha, V. G. Kumar and G. Singaravelu, *J. Mater. Sci.*, 2008, **43**, 5115-5122.
- 127 B. Nair and T. Pradeep, *Crystal Growth & Design*, 2002, **2**, 293-298.
- 128 J. He, I. Ichinose, T. Kunitake, A. Nakao, Y. Shiraishi and N. Toshima, *J. Am. Chem. Soc.*, 2003, **125**, 11034-11040.
- 129 G. Mattei, C. Maurizio, P. Mazzoldi, F. D'Acapito, G. Battaglin, E. Cattaruzza, C. de Julián Fernández and C. Sada, *Physical Review B*, 2005, **71**, 195418.
- 130 C. de Julián Fernández, M. Tagliente, G. Mattei, C. Sada, V. Bello, C. Maurizio, G. Battaglin, C. Sangregorio, D. Gatteschi and L. Tapfer, *Nuclear Instruments and Methods in Physics Research Section B: Beam Interactions with Materials and Atoms*, 2004, **216**, 245-250.
- 131 P. Milani and S. Iannotta, *Cluster beam synthesis of nanostructured materials*, Springer Science & Business Media, 2012.
- 132 S. Nonose, Y. Sone, K. Onodera, S. Sudo and K. Kaya, *J. Phys. Chem.*, 1990, **94**, 2744-2746.
- 133 S. Link, Z. L. Wang and M. El-Sayed, *The Journal of Physical Chemistry B*, 1999, **103**, 3529-3533.

- 134 U. Kreibig and M. Vollmer, in *Optical properties of metal clusters*, ed. anonymous, Springer, 1995, p. 13-201.
- 135 V. Amendola and M. Meneghetti, *The Journal of Physical Chemistry C*, 2009, **113**, 4277-4285.
- 136 S. Alayoglu, A. U. Nilekar, M. Mavrikakis and B. Eichhorn, *Nature materials*, 2008, **7**, 333-338.
- 137 Y. Kobayashi, S. Kiao, M. Seto, H. Takatani, M. Nakanishi and R. Oshima, in *ICAME 2003*, ed. anonymous, Springer, 2004, p. 75-79.
- 138 J. S. Bradley, in *Clusters and colloids: from theory to applications*, ed. G. Schmid, John Wiley & Sons, 2008, p. 459.
- 139 P. K. Babu, H. S. Kim, E. Oldfield and A. Wieckowski, *The Journal of Physical Chemistry B*, 2003, **107**, 7595-7600.
- 140 S. Foner, *Rev. Sci. Instrum.*, 1959, **30**, 548-557.
- 141 C. Petit, S. Rusponi and H. Brune, *J. Appl. Phys.*, 2004, **95**, 4251-4260.
- 142 J. Bansmann, S. Baker, C. Binns, J. Blackman, J. Bucher, J. Dorantes-Dávila, V. Dupuis, L. Favre, D. Kechrakos and A. Kleibert, *Surface Science Reports*, 2005, **56**, 189-275.
- 143 G. Schütz, W. Wagner, W. Wilhelm, P. Kienle, R. Zeller, R. Frahm and G. Materlik, *Phys. Rev. Lett.*, 1987, **58**, 737.
- 144 Q. A. Pankhurst, J. Connolly, S. Jones and J. Dobson, *J. Phys. D*, 2003, **36**, R167.
- 145 H. L. Nguyen, L. E. Howard, S. R. Giblin, B. K. Tanner, I. Terry, A. K. Hughes, I. M. Ross, A. Serres, H. Bürckstümmer and J. S. Evans, *Journal of Materials Chemistry*, 2005, **15**, 5136-5143.
- 146 J. Park and J. Cheon, *J. Am. Chem. Soc.*, 2001, **123**, 5743-5746.
- 147 U. Hartmann, *Annual review of materials science*, 1999, **29**, 53-87.
- 148 Y. Sui, W. Liu, L. Yue, X. Li, J. Zhou, R. Skomski and D. J. Sellmyer, *David Sellmyer Publications*, 2005, , 20.
- 149 J. L. Fernández, D. A. Walsh and A. J. Bard, *J. Am. Chem. Soc.*, 2005, **127**, 357-365.
- 150 A. Marcu, G. Toth, R. Srivastava and P. Strasser, *J. Power Sources*, 2012, **208**, 288-295.
- 151 C. J. Serpell, J. Cookson, D. Ozkaya and P. D. Beer, *Nature chemistry*, 2011, **3**, 478-483.
- 152 X. Zhang and K. Chan, *Chemistry of Materials*, 2003, **15**, 451-459.
- 153 A. Mayer and M. Antonietti, *Colloid Polym. Sci.*, 1998, **276**, 769-779.
- 154 N. Glaser, D. J. Adams, A. Böker and G. Krausch, *Langmuir*, 2006, **22**, 5227-5229.
- 155 I. Srnová-Šloufová, F. Lednický, A. Gemperle and J. Gemperlová, *Langmuir*, 2000, **16**, 9928-9935.
- 156 Y. Ding, F. Fan, Z. Tian and Z. L. Wang, *J. Am. Chem. Soc.*, 2010, **132**, 12480-12486.
- 157 D. Ferrer, A. Torres-Castro, X. Gao, S. Sepulveda-Guzman, U. Ortiz-Mendez and M. Jose-Yacaman, *Nano letters*, 2007, **7**, 1701-1705.
- 158 Z. Li, J. Wilcoxon, F. Yin, Y. Chen, R. Palmer and R. Johnston, *Faraday Discuss.*, 2008, **138**, 363-373.
- 159 Y. Yang, J. Shi, G. Kawamura and M. Nogami, *Scr. Mater.*, 2008, **58**, 862-865.
- 160 A. Santra, F. Yang and D. Goodman, *Surf. Sci.*, 2004, **548**, 324-332.
- 161 A. I. Frenkel, *Journal of synchrotron radiation*, 1999, **6**, 293-295.
- 162 S. Hannemann, J. Grunwaldt, F. Krumeich, P. Kappen and A. Baiker, *Appl. Surf. Sci.*, 2006, **252**, 7862-7873.
- 163 S. Alayoglu, S. K. Beaumont, F. Zheng, V. V. Pushkarev, H. Zheng, V. Iablokov, Z. Liu, J. Guo, N. Kruse and G. A. Somorjai, *Topics in catalysis*, 2011, **54**, 778-785.
- 164 M. Shao, K. Sasaki, N. S. Marinkovic, L. Zhang and R. R. Adzic, *Electrochemistry Communications*, 2007, **9**, 2848-2853.
- 165 S. W. Han, Y. Kim and K. Kim, *J. Colloid Interface Sci.*, 1998, **208**, 272-278.
- 166 J. Xu, T. Zhao, Z. Liang and L. Zhu, *Chemistry of materials*, 2008, **20**, 1688-1690.
- 167 F. Reniers, *Surf. Interface Anal.*, 1995, **23**, 374-380.
- 168 V. R. Stamenkovic, B. S. Mun, K. J. Mayrhofer, P. N. Ross and N. M. Markovic, *J. Am. Chem. Soc.*, 2006, **128**, 8813-8819.
- 169 V. R. Stamenkovic, B. S. Mun, M. Arenz, K. J. Mayrhofer, C. A. Lucas, G. Wang, P. N. Ross and N. M. Markovic, *Nature materials*, 2007, **6**, 241-247.
- 170 M. Oezaslan, F. Hasché and P. Strasser, *Chemistry of Materials*, 2011, **23**, 2159-2165.
- 171 J. Sinfelt, *Journal of Catalysis*, 1973, **29**, 308-315.
- 172 D. Mott, J. Luo, P. N. Njoki, Y. Lin, L. Wang and C. Zhong, *Catalysis today*, 2007, **122**, 378-385.
- 173 M. Shao, K. Sasaki and R. R. Adzic, *J. Am. Chem. Soc.*, 2006, **128**, 3526-3527.
- 174 J. H. Sinfelt, *Bimetallic catalysts: discoveries, concepts, and applications*, Wiley-Interscience, 1983.
- 175 H. Kunz and G. Gruver, *J. Electrochem. Soc.*, 1975, **122**, 1279-1287.
- 176 C. V. Rao, A. L. M. Reddy, Y. Ishikawa and P. M. Ajayan, *Carbon*, 2011, **49**, 931-936.
- 177 H. Yang, W. Vogel, C. Lamy and N. Alonso-Vante, *The Journal of Physical Chemistry B*, 2004, **108**, 11024-11034.
- 178 N. Toreis, X. E. Verykios, S. M. Khalid and G. B. Bunker, *Surf. Sci.*, 1988, **197**, 415-429.
- 179 D. I. Kondarides and X. E. Verykios, *Journal of Catalysis*, 1996, **158**, 363-377.
- 180 G. Schmid, *Metal Clusters in Chemistry*, 1999, , 1325-1341.

## 1. An introduction to Nanoalloys

- 181 W. F. Paxton, K. C. Kistler, C. C. Olmeda, A. Sen, S. K. St. Angelo, Y. Cao, T. E. Mallouk, P. E. Lammert and V. H. Crespi, *J. Am. Chem. Soc.*, 2004, **126**, 13424-13431.
- 182 M. B. Cortie and A. M. McDonagh, *Chem. Rev.*, 2011, **111**, 3713-3735.
- 183 T. R. Kline, W. F. Paxton, T. E. Mallouk and A. Sen, *Angewandte Chemie*, 2005, **117**, 754-756.
- 184 Y. Wang, R. M. Hernandez, D. J. Bartlett, J. M. Bingham, T. R. Kline, A. Sen and T. E. Mallouk, *Langmuir*, 2006, **22**, 10451-10456.
- 185 L. Qin, M. J. Banholzer, X. Xu, L. Huang and C. A. Mirkin, *J. Am. Chem. Soc.*, 2007, **129**, 14870-14871.
- 186 F. Massicot, R. Schneider, Y. Fort, S. Illy-Cherrey and O. Tillement, *Tetrahedron*, 2000, **56**, 4765-4768.
- 187 R. Raja, V. B. Golovko, J. M. Thomas, A. Berenguer-Murcia, W. Zhou, S. Xie and B. F. Johnson, *Chemical communications*, 2005, , 2026-2028.
- 188 S. U. Son, Y. Jang, J. Park, H. B. Na, H. M. Park, H. J. Yun, J. Lee and T. Hyeon, *J. Am. Chem. Soc.*, 2004, **126**, 5026-5027.
- 189 L. D. Pachón, M. B. Thathagar, F. Hartl and G. Rothenberg, *Physical Chemistry Chemical Physics*, 2006, **8**, 151-157.
- 190 C. Burda, X. Chen, R. Narayanan and M. A. El-Sayed, *Chem. Rev.*, 2005, **105**, 1025-1102.
- 191 S. Wasmus and A. Küver, *J Electroanal Chem*, 1999, **461**, 14-31.
- 192 Z. Liu, X. Y. Ling, X. Su and J. Y. Lee, *The Journal of Physical Chemistry B*, 2004, **108**, 8234-8240.
- 193 Y. Takasu, H. Itaya, T. Kawaguchi, W. Sugimoto and Y. Murakami, *Studies in Surface Science and Catalysis*, 2003, **145**, 279-282.
- 194 D. Aberdam, R. Durand, R. Faure, F. Gloaguen, J. Hazemann, E. Herrero, A. Kabbabi and O. Ulrich, *J Electroanal Chem*, 1995, **398**, 43-47.
- 195 U. Paulus, A. Wokaun, G. Scherer, T. Schmidt, V. Stamenkovic, V. Radmilovic, N. Markovic and P. Ross, *The Journal of Physical Chemistry B*, 2002, **106**, 4181-4191.
- 196 J. Park, M. G. Kim, Y. Jun, J. S. Lee, W. Lee and J. Cheon, *J. Am. Chem. Soc.*, 2004, **126**, 9072-9078.
- 197 L. E. Howard, H. L. Nguyen, S. R. Giblin, B. K. Tanner, I. Terry, A. K. Hughes and J. S. Evans, *J. Am. Chem. Soc.*, 2005, **127**, 10140-10141.
- 198 W. Zhou, E. Carpenter, J. Lin, A. Kumbhar, J. Sims and C. O'Connor, *The European Physical Journal D-Atomic, Molecular, Optical and Plasma Physics*, 2001, **16**, 289-292.
- 199 P. Paulus, H. Bönemann, A. Van der Kraan, F. Luis, J. Sinzig and L. De Jongh, *The European Physical Journal D-Atomic, Molecular, Optical and Plasma Physics*, 1999, **9**, 501-504.
- 200 S. Sun, C. B. Murray, D. Weller, L. Folks and A. Moser, *Science*, 2000, **287**, 1989-1992 (DOI:8349 [pii]).
- 201 H. Ebert, S. Bornemann, J. Minár, P. Dederichs, R. Zeller and I. Cabria, *Computational materials science*, 2006, **35**, 279-282.
- 202 Y. Cao, R. Jin and C. A. Mirkin, *J. Am. Chem. Soc.*, 2001, **123**, 7961-7962.
- 203 N. L. Rosi and C. A. Mirkin, *Chem. Rev.*, 2005, **105**, 1547-1562.
- 204 H. Cai, N. Zhu, Y. Jiang, P. He and Y. Fang, *Biosensors and Bioelectronics*, 2003, **18**, 1311-1319.
- 205 Z. Zheng, G. Shan, J. Li, Y. Chen and Y. Liu, *Materials Research Express*, 2014, **1**, 045408.
- 206 Y. Li, R. Yuan, Y. Chai and Z. Song, *Electrochim. Acta*, 2011, **56**, 6715-6721.
- 207 M. Grzelczak, B. Rodríguez-González, J. Pérez-Juste and L. M. Liz-Marzán, *Age*, 2007, **10**, 13.
- 208 M. Cortie, X. Xu and M. Ford, *Physical Chemistry Chemical Physics*, 2006, **8**, 3520-3527.
- 209 S. Fournier-Bidoz, A. C. Arsenault, I. Manners and G. A. Ozin, *Chem. Commun.*, 2005, , 441-443.
- 210 P. K. Jain, Y. Xiao, R. Walsworth and A. E. Cohen, *Nano letters*, 2009, **9**, 1644-1650.
- 211 M. Cortie, A. Dowd, N. Harris and M. Ford, *Physical Review B*, 2007, **75**, 113405.
- 212 N. F. Mott and L. Friedman, *Philosophical Magazine*, 1974, **30**, 389-402.
- 213 F. Morin, *Phys. Rev. Lett.*, 1959, **3**, 34.
- 214 S. Biermann, A. Poteryaev, A. Lichtenstein and A. Georges, *Phys. Rev. Lett.*, 2005, **94**, 026404.
- 215 O. Mikheeva and A. Sidorov, *Technical Physics*, 2003, **48**, 602-606.
- 216 J. Suh, E. Donev, D. Ferrara, K. Tetz, L. Feldman and R. Haglund Jr, *Journal of Optics A: Pure and Applied Optics*, 2008, **10**, 055202.
- 217 J. P. Wilcoxon and P. P. Provencio, *J. Am. Chem. Soc.*, 2004, **126**, 6402-6408.

# Chapter 2

## Optical properties of plasmonic intermetallic nanoparticles and nanoalloys

### 2.1 Plasmons

The elements that appear most often when discussing optical properties in nanoalloys are gold and silver, and this happens for two reasons<sup>1</sup>: the first reason is that nanoparticles composed by these two elements can be easily prepared with various methods, as we have already seen in Chapter 1; the second reason is that Surface Plasmon Resonances (SPRs) are observed in these nanomaterials.

A *plasmon* is the collective oscillation of conduction electrons in metals<sup>2, 3</sup>. According to the Fermi liquid model, plasmons occur when negatively charged electron clouds are displaced from their equilibrium position in relation to a lattice composed of positively charged ions. Normally this kind of excitation is not possible by interaction with the electromagnetic field in bulk materials, but when one includes the surface of the real materials in the problem, new excitation modes called *surface plasmons* appear, that can be excited by electromagnetic waves<sup>2, 3</sup>. Surface plasmon-polaritons are propagating plasmon modes that can exist on the surface of bulk materials and in periodic structures, while in metal nanoparticles we can observe non-propagating collective excitations of conduction electrons

## 2. Optical properties of plasmonic intermetallic nanoparticles and nanoalloys

called localized surface plasmons<sup>2, 3</sup>. When the electric field along the nanoparticle, and so electron cloud polarization, is homogeneous in each point of the material, excitation of dipolar plasmon oscillations is possible. Instead, if the wavelength of the resonant radiation is comparable to the nanoparticle size, the electric field inside the nanoparticle is not uniform and the electron cloud is polarized in a non-homogeneous way, originating multipolar plasmon oscillations<sup>3</sup>.

In single nanoparticles, plasmons can be studied with electron energy loss spectroscopy (EELS)<sup>4</sup>, far field extinction spectroscopy<sup>5</sup>, and cathodoluminescence<sup>6</sup>. For ensembles of nanoparticles, such as colloidal solutions, we can instead use optical absorption spectroscopy<sup>2, 3, 7, 8</sup>.

The intensity of the surface plasmon absorption band is proportional to the number of conduction electrons in the metal nanoparticle, and since each metal atom gives one conduction electron<sup>7</sup>, this explains the very large extinction cross sections.

It is important to remember that the SPR peak in the spectrum is due to both scattering and absorption of photons, and the ratio of one phenomenon to the other is determined by the dimension of the nanoparticle. Scattering is proportional to  $d^6$ , while the absorption is proportional to  $d^3$ , and in practice we have mainly scattering for nanoparticles bigger than 50 nm, while for smaller ones the absorption is the prevailing phenomenon<sup>2, 3</sup>.

There are many factors that may influence the SPR, such as the size of the nanoparticles, their shape, and the surrounding environment.

Nanoparticles size is responsible for extrinsic and intrinsic effects. The extrinsic size effects are due to a retardation linked to the excitation of multipolar plasmon modes while increasing the dimension of the nanoparticles<sup>2, 3</sup>. These effects are appreciable in the absorption spectrum as a broadening and red-shift of the SPR peak, and are especially visible once the size of the nanoparticles exceeds 60 nm, since over this limit the multipolar excitations prevail. In nanoparticles below 25 nm the multipolar excitations are negligible, whereas the dipolar mode prevail<sup>2, 3</sup>. On the other hand, when nanoparticles size gets below 30 nm, additional contributions to the free electron relaxation become relevant and cause a change in the metal optical constants. These are the intrinsic size effects, with the main contribution coming from free electron scattering at the surface when the mean free path of the electrons becomes comparable to the nanoparticles' size (in gold this happens below 40 nm). Since this effect increases the decay rate of the SPR, it is responsible for the almost complete quenching of the SPR when nanoparticle size gets below 2 nm<sup>2, 3</sup>.

## 2. Optical properties of plasmonic intermetallic nanoparticles and nanoalloys

Nanoparticle shape determines number, position and width of the SPR. This happens because in perfectly spherical nanoparticles we have only one SPR, while oblate nanoparticles have two, one at shorter wavelength originated along the shorter axis of the nanorod and the second, at longer wavelengths, originated along the major axis of the rod. In figure 2.1 we can see the effect of varying the spheroid aspect-ratio on the extinction cross-section<sup>8</sup>.

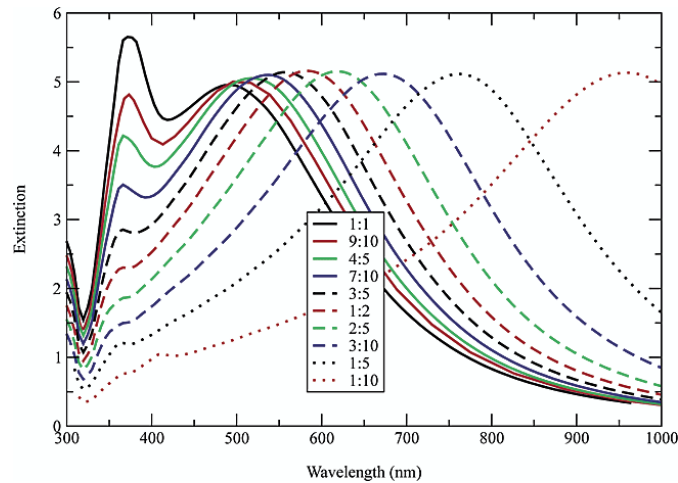


Figure 2.1 – Calculation results of the extinction spectra of spheroids of equivalent volume and increasing aspect ratios. The extinction area is normalized to the area of a sphere with radius equal to the semi-major axis. From reference 8.

The surrounding environment of nanoparticles exerts its own influence on the SPR. The dominating chemical effect is the chemical interface damping, visible in the absorption spectra as a broadening and a red-shift of the SPR if there are adsorbates (either chemisorbed and physisorbed) on the surface of the nanoparticles<sup>9, 10</sup>. The main reason for this effect is the creation of new relaxation pathways for excited electrons, as shown by Perrson<sup>11</sup> model. In this model, the empty LUMOs of the chemisorbed molecules are coupled with the conduction band electrons, and during SPR excitation some electrons can be reversibly transferred in the LUMOs, causing loss of coherence with the other excited electrons and a larger bandwidth. In case of adsorbates which are physisorbed, they cause a change in the dielectric properties of the environment, with a consequent variation of the SPR position and width<sup>3</sup>.

Another possible factor influencing the SPR is the presence of other plasmonic nanoparticles in the surroundings. The plasmon modes in aggregates of spheres interact one with each other, and new hybrid resonances become possible when the nanoparticle separation is small enough<sup>2, 12</sup>. In the simplest case, a dimer, SPR hybridization causes the rise of a second red-shifted SPR peak, but this effect decreases almost exponentially when the interparticle distance increases. In Figure 2.2 are shown the data for the plasmon shift<sup>13</sup>. The experimental data is in greement with the discrete dipole approximation (DDA)

## 2. Optical properties of plasmonic intermetallic nanoparticles and nanoalloys

simulation, a method in which the structure of interest is modelled with a cubic array composed of  $N$  polarizable points (dipoles), without any constrictions on the shape<sup>8, 14-16</sup>, and shows the rapid decay of the red shift of the plasmon with an increase in interparticle distance.

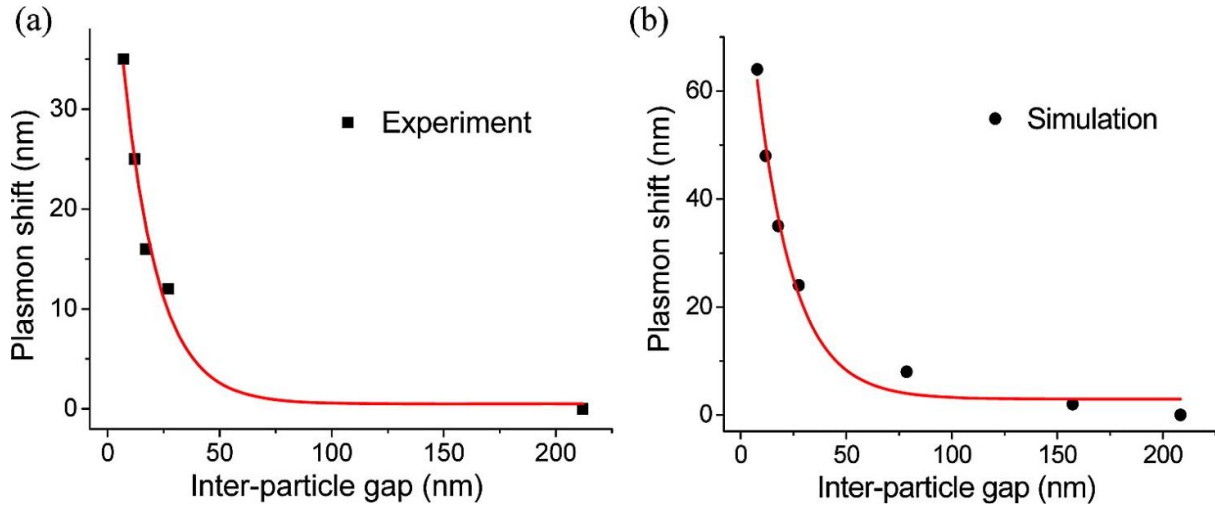


Figure 2.2 – Shift of SPA peak of two Au nanodiscs as a function of the border-to-border separation (a) for experimental data and (b) DDA simulation. From reference 13.

## 2.2 Models for the SPR

We can define a material as a *free-electron metal* when its optical and electronic properties are defined mainly by its conduction electrons. For these metals, with filled valence bands and partially filled conduction bands, the response to visible radiation and the dielectric function  $\epsilon(\omega)$  at visible frequencies are dominated by transitions within the conduction band. For other metals, instead, we have non negligible contributions from interband transition of electrons, typically from lower bands to the conduction bands, or in some cases also from the conduction band to higher unoccupied levels<sup>3</sup>.

For a gas of free electrons, it is possible to write the optical constant  $\epsilon(\omega) = \epsilon_1(\omega) + i\epsilon_2(\omega)$  with the Drude-Lorentz-Sommerfeld model<sup>3</sup> as:

$$\epsilon_D(\omega) = 1 - \frac{\omega_p^2}{\omega^2 + i\Gamma\omega} \quad (2.1)$$

Where the relaxation constant  $\Gamma$ , is linked to the electron mean free path  $\ell$  and the Fermi velocity  $v_F$  by the equation  $\Gamma = v_F/\ell$ , and the *plasma frequency*  $\omega_p$  is a function of electron mass and density that can be written as<sup>3</sup>:

$$\omega_p = \sqrt{\frac{Ne^2}{\epsilon_0 m_e}} \quad (2.2)$$

## 2. Optical properties of plasmonic intermetallic nanoparticles and nanoalloys

In this equation,  $N$  is the conduction electron density,  $e$  is the electron charge,  $m_e$  is the electron mass and  $\epsilon_0$  the vacuum dielectric permittivity. As recalled above, in the bulk it is impossible to excite the plasmons with photons, since the energy dispersion curves of photons and plasmons do not cross each other, as reported in figure 2.3<sup>17</sup>:

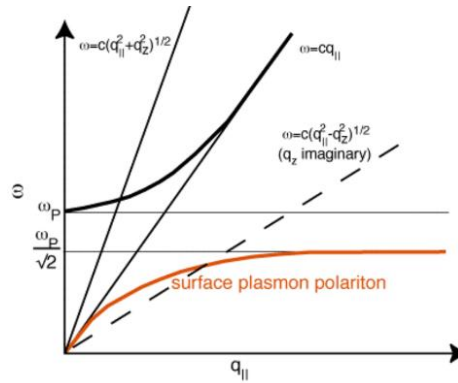


Figure 2.3 – Energy dispersion curves of electromagnetic radiation in vacuum (black continuous line), for the surface plasmon (red line), for the bulk plasmon (black curve), and of the incident excitation radiation (dashed black line). From reference 17.

In nanoparticles, since we have a surface, it is possible to modify the symmetry of the system introducing new boundary conditions. The wave vectors of the new surface confined plasmons are compatible with those of the photons, meaning that it is possible to excite the surface plasmon by annihilation of a photon with the appropriate energy.

The Mie model, first developed in 1908<sup>18</sup>, is the reference point for the study of the surface plasmon in spherical particles. The model derives from the solution to the electromagnetic problem found by applying Maxwell's equations, with the appropriate boundary conditions, in spherical coordinates and using multipolar expansions for the electric and magnetic fields of the incoming light. Born<sup>19</sup> and Stratton<sup>20</sup> applied and refined this model in a way closer to what is usually found in textbooks. One of the ingredients that explains the success of this approach is the possibility of introducing all the material-related aspects in the particle dielectric function.

With the Mie model we can calculate the scattering ( $\sigma_{sca}$ ), absorption ( $\sigma_{abs}$ ) and extinction ( $\sigma_{ext}$ ) cross section of a spherical particle by the following expressions<sup>3</sup>:

$$\sigma_{ext} = \frac{2\pi}{|k|^2} \sum_{L=1}^{\infty} (2L+1) \text{Re}\{a_L + b_L\} \quad (2.3)$$

$$\sigma_{sca} = \frac{2\pi}{|k|^2} \sum_{L=1}^{\infty} (2L+1) (|a_L|^2 + |b_L|^2) \quad (2.4)$$

$$\sigma_{abs} = \sigma_{ext} - \sigma_{sca} \quad (2.5)$$

With



## 2. Optical properties of plasmonic intermetallic nanoparticles and nanoalloys

$$a_L = \frac{m\psi_L(mx)\psi'_L(x) - \psi'_L(mx)\psi_L(x)}{m\psi_L(mx)\eta'_L(x) - \psi'_L(mx)\eta_L(x)} \quad (2.6)$$

$$b_L = \frac{\psi_L(mx)\psi'_L(x) - m\psi'_L(mx)\psi_L(x)}{\psi_L(mx)\eta'_L(x) - m\psi'_L(mx)\eta_L(x)} \quad (2.7)$$

$$m = n/n_m \quad (2.8)$$

In these equations,  $n$  and  $n_m$  are respectively the complex index of refraction of the particle and the real index of refraction of the surrounding medium,  $\mathbf{k}$  is the wavevector,  $x = |\mathbf{k}|R$  the size parameter,  $\psi_L(z)$  and  $\eta_L(z)$  are Riccati-Bessel cylindrical functions. It is important to note that the summation order  $L$  gives the order of the partial wave, and thus it is the order of the spherical multipole excitations in the clusters. For  $L=1$  we have dipole fields, for  $L=2$  we have quadrupolar fields, for  $L=3$  we have octupolar fields, up to the order of our interest<sup>3</sup>.

In the *quasi-static* regime, defined as having  $R \ll \lambda$ , phase retardation and the effects of higher-order multipoles are neglected, and it is possible to simplify the extinction cross-section formula considerably:

$$\sigma_{ext}(\omega) = 9 \frac{\omega}{c} \varepsilon_m^{3/2} V_0 \frac{\varepsilon_2(\omega)}{[\varepsilon_1(\omega) + 2\varepsilon_m]^2 + \varepsilon_2(\omega)^2} \quad (2.9)$$

where  $V_0 = (4\pi/3)R^3$  is the volume of the sphere,  $\varepsilon_m$  is the dielectric function of the surrounding media and  $\varepsilon(\omega)$  the dielectric function of the particle. It is possible to see that the resonance is located where  $[\varepsilon_1(\omega) + 2\varepsilon_m]^2 + \varepsilon_2(\omega)^2$  has a minimum, and this happens (with some simplifications) where  $\varepsilon_1(\omega) = -2\varepsilon_m$ .

It is also very important to keep into consideration the intrinsic size effects by appropriate correction of the optical constant. For this reason, the optical constant  $\varepsilon_{bulk}$  is usually replaced with the size-corrected  $\varepsilon(\omega, R)$  with the following formula:

$$\varepsilon(\omega, R) = \varepsilon_{bulk}(\omega) + \omega_p^2 \left( \frac{1}{\omega^2 + \Gamma_\infty^2} - \frac{1}{\omega^2 + \Gamma(R)^2} \right) + i \frac{\omega_p^2}{\omega} \left( \frac{\Gamma(R)}{\omega^2 + \Gamma(R)^2} - \frac{\Gamma_\infty}{\omega^2 + \Gamma_\infty^2} \right) \quad (2.10)$$

where  $\varepsilon_{bulk}(\omega)$  is a term that includes interband transitions and size independent conduction electron processes,  $\Gamma_\infty$  is the bulk relaxation frequency, while  $\Gamma(R)$  is calculated with the following formula:

$$\Gamma(R) = \Gamma_\infty + A \frac{v_F}{R} \quad (2.11)$$

In the (2.13),  $A$  is a quantity usually close to 1, and  $v_F$  is the Fermi speed.

When dealing with spheroidal nanoparticles, it is possible to model the optical properties in

## 2. Optical properties of plasmonic intermetallic nanoparticles and nanoalloys

the *quasi-static approximation*, as a function of the main parameters which characterize particles geometry: the two axis,  $a$  and  $b$ , the *axial ratio*  $b/a$ , and the *eccentricity*  $e = \sqrt{(a^2 - b^2)}/a$ . First of all it is necessary to define the polarizability along each axis:

$$\alpha_i(\omega) = \varepsilon_0 \frac{\varepsilon(\omega) - \varepsilon_m}{\varepsilon_m + [\varepsilon(\omega) - \varepsilon_m]L_i} V_{cluster} \quad (2.12)$$

Where  $L_i$  are numerical factors depending on the spheroid geometry. The model defined by Gans<sup>21</sup> uses an average over all the orientations of the (2.14), useful if we consider a sample containing multiple arbitrarily oriented spheroids such as in a colloidal dispersion. The average polarizability then becomes:

$$\alpha = \varepsilon_0 \left( \frac{1}{3} \frac{\varepsilon(\omega) - \varepsilon_m}{3\xi[\varepsilon(\omega) - \varepsilon_m] + 3\varepsilon_m} + \frac{2}{3} \frac{\varepsilon(\omega) - \varepsilon_m}{3\xi'[\varepsilon(\omega) - \varepsilon_m] + 3\varepsilon_m} \right) V_{cluster} \quad (2.13)$$

In this equation  $\xi$  is related to the eccentricity as following:

$$\xi = \frac{1-e^2}{e^2} \left[ \frac{1}{2e} \log \left( \frac{1-e}{1+e} \right) - 1 \right] \quad (2.14)$$

$$\xi' = \frac{1-\xi}{2} \quad (2.15)$$

Resonances occur when the denominator in 2.12 is zero, so we have two resonances for spheroids with random orientation in space<sup>3</sup>.

Analytical expressions derived from the Mie theory are available also for spherical core@shell nanoparticles. In this case, if the core has a dielectric function  $\varepsilon(\omega)$  and it is surrounded by a shell of thickness  $d$  and dielectric constant  $\varepsilon_s(\omega)$ , it is possible to calculate the polarizability in a quasi-static regime as:

$$\alpha = \varepsilon_0 \frac{(\varepsilon_s - \varepsilon_m)(\varepsilon + 2\varepsilon_s) + \left(\frac{R}{R+d}\right)^3 (\varepsilon - \varepsilon_s)(\varepsilon_m + 2\varepsilon_s)}{(\varepsilon_s + 2\varepsilon_m)(\varepsilon + 2\varepsilon_s) + \left(\frac{R}{R+d}\right)^3 (\varepsilon - \varepsilon_s)(2\varepsilon_s - \varepsilon_m)} \frac{4\pi}{3} (R + d)^3 \quad (2.16)$$

For a multishell nanoparticle, the solution becomes possible with a recursive calculation, substituting the Mie coefficients  $a_L$  and  $b_L$  with the following expressions:

$$a_L = - \frac{m_z \psi_L(m_z x_z) [\psi'_L(x_z) + T_L^h \chi'_L(x_z)] - \psi'_L(m_z x_z) [\psi_L(x_z) + T_L^h \chi_L(x_z)]}{m_z \xi_L(m_z x_z) [\psi'_L(x_z) + T_L^h \chi'_L(x_z)] - \xi'_L(m_z x_z) [\psi_L(x_z) + T_L^h \chi_L(x_z)]} \quad (2.17)$$

$$b_L = - \frac{\psi_L(m_z x_z) [\psi'_L(x_z) + S_L^h \chi'_L(x_z)] - m_z \psi'_L(m_z x_z) [\psi_L(x_z) + S_L^h \chi_L(x_z)]}{\xi_L(m_z x_z) [\psi'_L(x_z) + S_L^h \chi'_L(x_z)] - m_z \xi'_L(m_z x_z) [\psi_L(x_z) + S_L^h \chi_L(x_z)]} \quad (2.18)$$

In these equations, we have the functions  $T_L^Z$  and  $S_L^Z$  that can be described as:

$$T_L^Z = - \frac{m_z \psi_L(m_z x_z) [\psi'_L(x_z) + T_L^{Z-1} \chi'_L(x_z)] - \psi'_L(m_z x_z) [\psi_L(x_z) + T_L^{Z-1} \chi_L(x_z)]}{m_z \chi_L(m_z x_z) [\psi'_L(x_z) + T_L^{Z-1} \chi'_L(x_z)] - \chi'_L(m_z x_z) [\psi_L(x_z) + T_L^{Z-1} \chi_L(x_z)]} \quad (2.19)$$

## 2. Optical properties of plasmonic intermetallic nanoparticles and nanoalloys

$$S_L^z = -\frac{\psi_L(m_z x_z)[\psi'_L(x_z) + S_L^{z-1} \chi'_L(x_z)] - m_z \psi'_L(m_z x_z)[\psi_L(x_z) + S_L^{z-1} \chi_L(x_z)]}{\chi_L(m_z x_z)[\psi'_L(x_z) + S_L^{z-1} \chi'_L(x_z)] - m_z \chi'_L(m_z x_z)[\psi_L(x_z) + S_L^{z-1} \chi_L(x_z)]} \quad (2.20)$$

The recurrence starts with  $z=1$ . In these equations  $L$  indicates the order of the Riccati-Bessel functions  $\Psi$ ,  $X$ , and  $\xi$ , while  $m_z$  indicates the ratio between the wave vectors  $k_{z+1}/k$ , and  $x_z$  the size parameter  $|\bar{k}_s| R_s$  ( $R_s$  is the radius of the nanostructure considered)<sup>3</sup>.

When analytical models are not available for the calculation of the optical properties of the nanoparticles, it is possible to use the DDA<sup>22</sup>. With DDA, the polarization  $P_j$  of each point with position  $r_j$  and polarizability  $\alpha_j$  can be calculated as<sup>8, 14-16</sup>:

$$\bar{P}_j = \alpha_j \bar{E}_{loc}(\bar{r}_j) \quad (2.21)$$

$\bar{E}_{loc}$  is the local field, resulting from the incoming radiation plus the contributions from all the surrounding dipoles<sup>8, 14-16</sup>:

$$\bar{E}_{loc}(\bar{r}_j) = \bar{E}_0 \exp(i\bar{k} \cdot \bar{r}_j + i\omega t) - \sum_{l \neq j} \bar{A}_{jl} \bar{P}_l \quad (2.22)$$

$\bar{A}_{jl}$  is the interaction matrix, and it is possible to calculate the formula for  $\bar{A}_{jl} \bar{P}_l$  with the following formula:

$$\bar{A}_{jl} \bar{P}_l = \frac{\exp(ik\bar{r}_{jl})}{\bar{r}_{jl}^3} \times \left\{ k^2 \bar{r}_{jl} \times (\bar{r}_{jl} \times \bar{P}_l) + \frac{(1-ik\bar{r}_{jl})}{\bar{r}_{jl}^2} [\bar{r}_{jl}^2 \bar{P}_l - 3\bar{r}_{jl}(\bar{r}_{jl} \cdot \bar{P}_l)] \right\} \quad (2.23)$$

It is extremely important to use a correct expression for the polarizability, and the most commonly adopted solution is the one proposed by Draine and Goodman as correction by the Clausius-Massotti polarizability, that allows a calculation of the desired extinction spectra with an accuracy below 10% when the inter-dipole spacing is small compared to incident wavelength and main features of the nanoparticle.

A different method, considered the recent state of the art for solving Maxwell's equation for complex geometries, is the Finite-difference time domain method (FDTD). The classical method for FDTD uses an orthogonal cubic spatial grid (Yee cell) where each field component is sampled and evaluated at a particular space position, and electrical and magnetic fields are calculated at half the time steps of sampling<sup>23</sup>. The materials are modelled by specifying their characteristics at every point in their grid in homogeneous region, while in interface areas proper boundary conditions need to be specified<sup>23</sup>.

## 2.3 SPR dynamics

It is possible to exploit the plasmon resonance to probe the electron dynamics inside the nanoparticle, exciting the plasmonic material with a laser probe pulse. After plasmon absorption of the laser pulse, conduction electrons (whose temperature is now in the range of thousands of degrees<sup>24, 25</sup>) assume a non-Fermi distribution of energies, known as “nonthermalized distribution” (nTD). In a time scale of 10 fs, the nTD evolves into an “internally thermalized distribution” (iTD) by internal exchange of energy among electrons in the conduction band (i.e. electron-electron scattering)<sup>26, 27</sup>. The iTD still is not a Fermi distribution since the electrons are not yet in equilibrium with the lattice.

When the electron gas in plasmonic nanoparticles is heated, the bleaching of the surface plasmon absorption is observed. This behaviour is due to the promotion of excited electrons in higher energy states: these electrons follow multipolar plasmon modes, which couple with the applied field at higher frequencies, and the plasmon absorption at the standard frequency decreases accordingly<sup>28</sup>. The SPR modification depends on the combination of the bleaching and the absorption of the newly formed excited state, but the overall effect is generally significant since the number of electrons involved can reach up to 30% of the total<sup>28</sup>.

Absorption spectra obtained in pump-probe experiments from gold and gold-silver alloy spherical nanoparticles are reported in figure 2.4<sup>29</sup>. In these figures it is possible to see the experimental evidence of what discussed above, with a strong bleaching of the plasmon absorption immediately after the pump pulse followed by the progressive return to the normal absorption. It is noteworthy to point out that, while we have a blue-shift of the plasmon absorption in the Au-Ag alloy compared to pure Au, the dynamics of the excitation remain the same<sup>29</sup>.

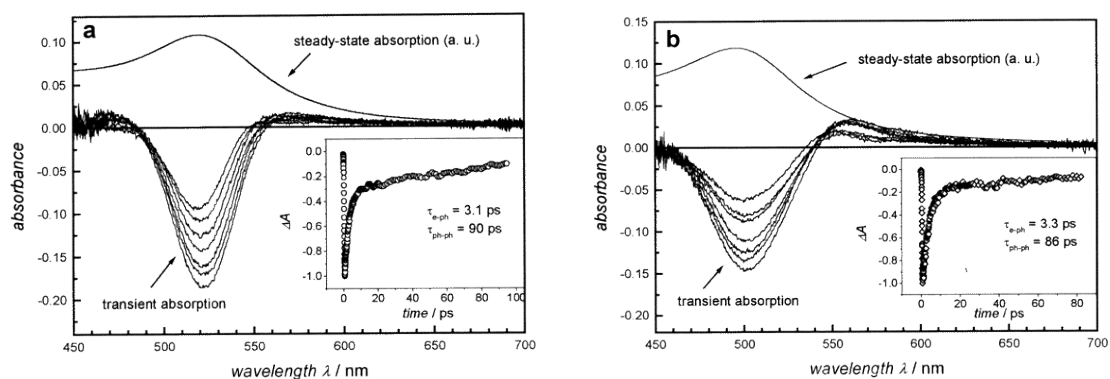


Figure 2.4 – Transient absorption spectra of (a) 15nm gold and (b) 18nm gold-silver alloy spherical nanoparticles, excited with a 400nm, 100 fs, laser. In both insets, we can see the decay of the transient bleach monitored at the bleach maximum of (a) 520nm and (b) 500nm. From reference 29.

## 2. Optical properties of plasmonic intermetallic nanoparticles and nanoalloys

Electron-phonon interactions are required to bring down the temperature of the electron gas up to thermal equilibrium. This process has been studied in detail<sup>30, 31</sup>, and requires a time that is of the order of 1 - 3 ps, as shown in the insets of Figure 2.4<sup>29</sup>, and are comparable in case of gold and gold-silver alloys.

The excess of energy gained by the nanoparticle upon plasmon absorption is then redistributed in the lattice by phonon-phonon coupling and, ultimately, by phononic coupling with the surrounding medium, in a timescale longer than 50ps<sup>32</sup>. This is still visible in the transient absorption spectra of plasmonic nanoparticles, with a slow recovery of the pristine absorbance (see insets of Figure 2.4), and resulted in 86 and 90 ps, respectively for the Au and Ag-Au nanoparticles<sup>29</sup>.

## 2.4 Surface-Enhanced Raman Scattering

The phenomenon called Surface Enhanced Raman Scattering (SERS) is based on the highly localized electromagnetic field generated in proximity of metallic nano-objects to enhance the Raman scattering of nearby molecules.

The Raman effect is an anelastic scattering process between a photon and a molecule. The incoming photon, with an energy  $h\nu_L$ , impacts a molecule in its ground or excited vibrational state. If the molecule was in the ground state, a vibration with energy  $\nu_M$  is excited in the molecule, while the scattered photon loses the corresponding vibrational energy and its new frequency becomes (Stokes scattering)

$$\nu_S = \nu_L - \nu_M \quad (2.24)$$

If the molecule was in a vibrational excited status the photon increases its energy and its frequency becomes (anti-Stokes scattering)<sup>33, 34</sup>:

$$\nu_{AS} = \nu_L + \nu_M \quad (2.25)$$

An example of Raman spectrum is reported in figure 2.5<sup>35</sup>. As shown in this figure, Raman transitions are not usually in resonance with the electronic states of the molecule, contrary to the case of fluorescence, in fact the Raman transition is a scattering event, i.e. there is no absorption or emission of photons, even if the incoming photon is in resonance with an electronic transition (resonant Raman scattering)<sup>2</sup>.

## 2. Optical properties of plasmonic intermetallic nanoparticles and nanoalloys

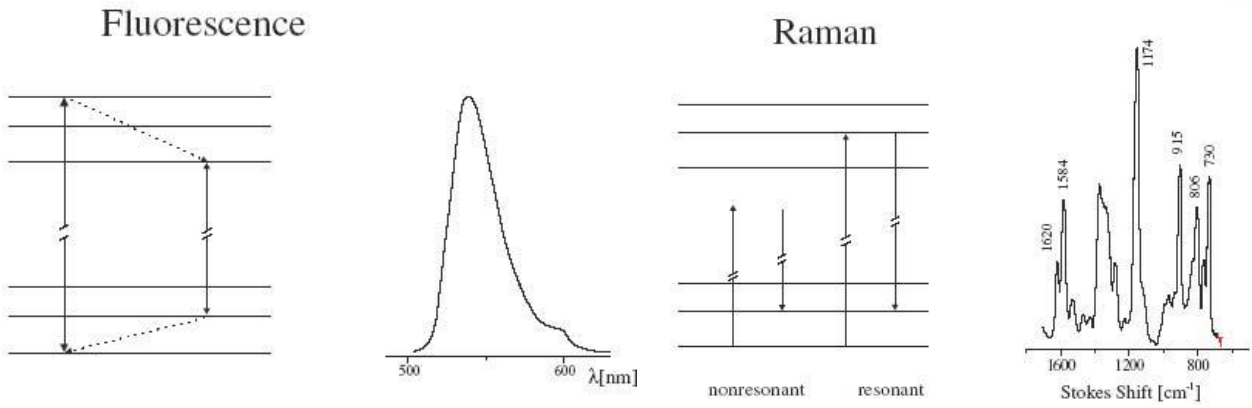


Figure 2.5 – Sample spectra and depiction of fluorescence (left) and Raman (right). From reference 35.

The power of the scattered beam is determined by the following formula<sup>35</sup>:

$$P_S(\nu_S) = N\sigma_{RS}I(\nu_L) \quad (2.26)$$

In this equation  $N$  is the number of scattering molecules under the incident beam,  $\sigma_{RS}$  is the scattering cross section, and  $I$  the intensity of the laser beam<sup>35</sup>. However, the main experimental problem of Raman is the relatively small cross section, for instance when compared to fluorescence, which may vary from  $10^{-31}$  to  $10^{-29}$   $\text{cm}^2/\text{molecule}^2$  in non-resonant conditions. For this reason, SERS is intensively investigated as a way to get signals up to the single molecule level, despite the intrinsically low Raman cross section of the target compound. In SERS, the enhancement in Raman signals requires the placement of the Raman-active molecules in the near-field of a plasmonic nanostructure.

SERS effect is generally attributed to the resultant of two distinct contributions. The first contribution is defined as *chemical enhancement* and is due to the introduction or modification of the electronic transitions of the molecule that brings to an increase of  $\sim 100$  of the molecular cross section  $\sigma_{RS}$ <sup>2</sup>. The second effect, defined *electromagnetic enhancement*, is linked to the increase in the local electric field due to the presence of localized surface plasmon<sup>36-38</sup>. This effect is quantified with the electromagnetic enhancement factor  $L^2$ :

$$L(\nu) = \frac{|E_{loc}(\nu)|}{|E_0|} \quad (2.27)$$

Considering  $L$ , the power of the Raman scattered beam becomes<sup>2, 35</sup>:

$$P_S(\nu_S) = N\sigma_{SERS}|L(\nu_L)|^2|L(\nu_S)|^2I(\nu_L) \quad (2.28)$$

Due to the very small difference between  $\nu_L$  and  $\nu_S$  when compared with the width of the plasmon enhancement, it is possible to observe that this contribution is proportional to  $L^4$ .

## 2. Optical properties of plasmonic intermetallic nanoparticles and nanoalloys

Then, the electromagnetic enhancement becomes<sup>36</sup>:

$$G_{SERS} = L(\nu) = \frac{|E_{loc}|^4}{|E_0|^4} \quad (2.29)$$

According to Maier<sup>2</sup>, it becomes possible to split the electromagnetic enhancement factor  $L$  in two factors: the enhancement due to the surface plasmon,  $L_{SP}$  has a strong dependence on the frequency of the radiation, while the enhancement linked to the lightning rod effect,  $L_{LR}$ , is not affected by this parameter but only by the geometry:

$$L(\nu) = L_{SP}(\nu)L_{LR} \quad (2.30)$$

$L_{SP}$  can be expressed as the polarizability of a metallic nanostructure with a defined shape<sup>2</sup>. For an isolated metal nanosphere with a diameter inferior to the wavelength this means that  $L_{SP}$  can be written as:

$$L_{SP}(\omega) \propto \frac{\varepsilon(\omega)-1}{\varepsilon(\omega)+2} \quad (2.31)$$

For ellipsoidal nanoparticles it becomes necessary to calculate the polarizability along each of the major axes, defined as  $\alpha_1$ ,  $\alpha_2$ ,  $\alpha_3$ , with the help of the following formula, derived by Bohren and Huffman<sup>39</sup>:

$$\alpha_i = 4\pi a_1 a_2 a_3 \frac{\varepsilon(\omega) - \varepsilon_m}{3\varepsilon_m + 3L_i(\varepsilon(\omega) - \varepsilon_m)} \quad (2.32)$$

And  $L_i$  can be expressed as:

$$L_i = \frac{a_1 a_2 a_3}{2} \int_0^\infty \frac{dq}{(a_i^2 + q)f(q)} \quad (2.33)$$

$$f(q) = \sqrt{(q + a_1^2)(q + a_2^2)(q + a_3^2)} \quad (2.34)$$

This expression accounts also for the fact that in ellipsoid particles there is a strong contribution from the lightning rod effect near the tips.

However, in the majority of experimental cases, the enhancement of the Raman scattering is observed as the effect of the interaction between a molecule and an electromagnetic cavity mode<sup>2</sup>, such as the junction (hot spot) between two very near nanoparticles<sup>40</sup>. Following Maier<sup>2</sup>, the characteristics of SERS in the hot spot can be described as the interaction between the molecule and an electromagnetic cavity mode. In this case, we can use two parameters: the quality factor  $Q$ , that describes the energy density of the *spectral* mode and is proportional to the cavity photon lifetime, and the effective mode volume  $V_{eff}$ , that describes the energy density of the *spatial* mode and is proportional to the electric field

## 2. Optical properties of plasmonic intermetallic nanoparticles and nanoalloys

strength per photon<sup>2, 41</sup>. The spontaneous Raman scattering process can be compared to an excitation of a target molecule by an incoming beam with intensity  $|E_i(\omega_0)|^2/2\eta$ , with  $\eta$  the impedance of free space and  $\omega_0$  its frequency. This scattering creates a Stokes photon with an energy  $\omega$ . Since the  $\Delta\omega$  between the incoming and the scattered beam is very small, we can assume  $Q(\omega_0)=Q(\omega)=Q$  and  $V(\omega_0)=V(\omega)=V$ . Therefore, following Maier<sup>2</sup>, it becomes possible to write the enhancement of the incoming radiation in a metallic cavity as:

$$\sqrt{G_{SERS}} = \frac{|E_{loc}|^2}{|E_i|^2} = \frac{\gamma_{rad} A_c}{4\pi^2 c^2 \eta \epsilon_0 \lambda_0} \frac{Q^2}{V_{eff}} \quad (2.35)$$

Where  $\gamma_{rad}$  is the radiation cross section of the incoming radiation,  $\eta$  is the impedance of free space,  $\lambda_0$  is the exciting radiation wavelength, while  $A_c$  corresponds to the radiation cross-section of the resonant cavity mode.

Shubin et al. has obtained an equivalent law for the localization of plasmonic energy of fractal-like aggregates of metal nanoparticles deposited on the surface of metal nanoparticles<sup>42</sup>.

With this information, it becomes possible to calculate the  $G_{SERS}$  for the nanometre-sized hot spot crevice located between two silver nanoparticles, obtaining a value  $G_{SERS} \sim 2.7 \times 10^{10}$ , a value compatible with full-field three dimensional FDTD simulations of similar structures<sup>43</sup>.

Further examples of similar structures, and their enhancement factors, are reported in figure 2.6<sup>40</sup>:

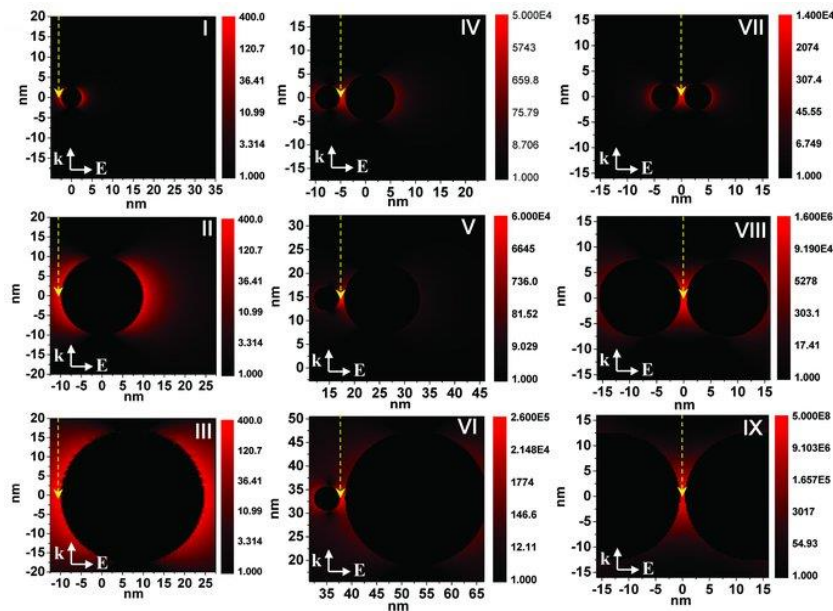


Figure 2.6 – Calculation of the enhancement factor  $G_{SERS}$  for 632.8nm excitation for AuNPs monomers of 5nm (I), 10nm (II), 15nm (III), heterodimers of 5nm (IV), 10nm (V), 15nm (VI), homodimers of 5nm (VII), 15nm (VIII), 25nm (IX). From reference 40.



## 2. Optical properties of plasmonic intermetallic nanoparticles and nanoalloys

In this figure the enhancement factor is reported as  $G_{SERS}$ , accounting for the actual local electric field  $E_{loc}$  probed by each molecule on the surface of the metal nanoparticle. It is possible to see that the highest values of enhancement are reported with dimers, especially homodimers, and that  $G_{SERS}$  increases with the dimensions of the nanoparticles. In figure 2.7 are reported the maximum enhancement factors for the different available structures, and it is possible to see that the best results are available with the homodimers.

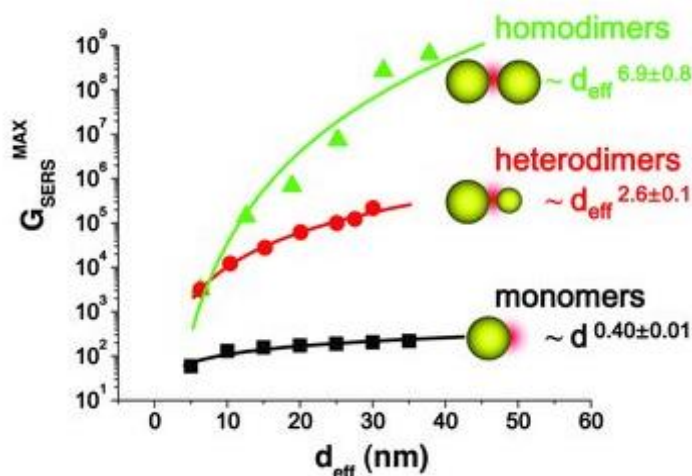


Figure 2.7 – Maximum values of  $G_{SERS}$  for distances of 0.5 nm from the surface of the nanoparticles for monomers (black), heterodimers (red), and homodimers (green).  $D_{eff}$  is the effective size of the dimer. From reference 40.

## 2.5 Plasmonic properties of alloys

An important characteristic of a plasmonic metal is the quality factor of the resonance in a nanosphere or nanoshell, which is proportional to  $-\epsilon_1/\epsilon_2$ , while for an ellipsoid can be approximated to  $(\epsilon_1)^2/\epsilon_2^1$ ,<sup>44</sup>. In Figure 2.8 are shown the dielectric functions of some representative metals with plasmonic response<sup>45</sup>.

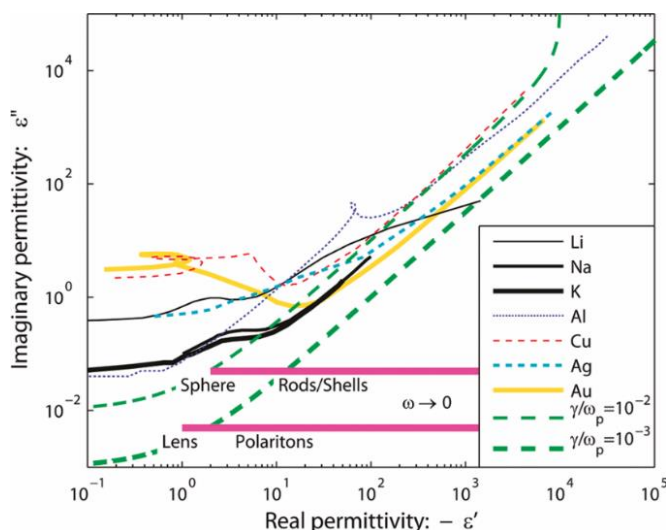


Figure 2.8 – Dielectric functions of various elements that show strong plasmonic responses, and two overlaid plasmonic systems for example. The green lines represent Drude models. From reference 44.

## 2. Optical properties of plasmonic intermetallic nanoparticles and nanoalloys

We can see that K and Al offer better plasmonic responses in some areas of the spectrum, however at lower frequencies of the incident radiation gold and silver become the better choices.

When considering hybrid metal nanoparticles composed by elements with plasmonic properties, three results are possible: we can have both properties still separately available in the hybrid, the properties can merge, or new properties can emerge. This result depends greatly from the resulting structure of the obtained nanoparticle: for example if the plasmon resonance of two metals merge in a single one, it is reasonable to assume that a single-phase alloy has been formed<sup>46-48</sup>, even if small degrees of segregation are visible in the hybrid<sup>46, 49</sup>.

In literature, the optical properties displayed by available examples of hybrid nanoparticles are usually grouped in base at the elements composing the nanoparticles:

*Group 11 Metal Hybrids:* Copper, silver and gold, also known as "coinage" metals, have an electronic configuration of the type  $d^{10}(q+1)s^1$  with  $q=3, 4, 5$  and all have a face centered cubic (fcc) cell. Their characteristic interband absorption allows them to show appreciable absorption from the visible to the near-UV area, especially for gold and copper. The plasmon resonances for spherical nanometric nanoparticles are located at about 600 nm for copper, 400 nm for silver and 520 nm for gold<sup>45</sup>.

Gold-silver hybrids can be easily formed because they are mutually soluble<sup>50</sup>, and this allows a good control of the position of the plasmon resonance simply by changing the composition of the nanoparticles<sup>48, 51-53</sup>. In Figure 2.9 are shown the real and imaginary values for the dielectric constants of gold-silver nanoparticles of different composition, obtained by DDA using a simple rule<sup>54</sup>:

$$\varepsilon_{alloy}(x_{Ag}, \omega) = x_{Ag}\varepsilon_{Ag}(\omega) + (1 - x_{Ag})\varepsilon_{Au}(\omega) \quad (2.36)$$

This equation is similar, at least in concept, to Vegard's law (see Chapter 1), and it is generally accepted, although it disregards the probable modification of the electronic band structure of the alloy and the change in intensity of the interband contribution to the dielectric function<sup>54</sup>.

## 2. Optical properties of plasmonic intermetallic nanoparticles and nanoalloys

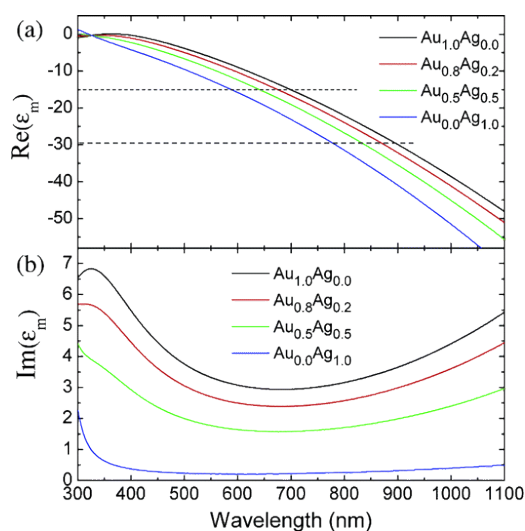


Figure 2.9 – Real and imaginary parts of the dielectric function for different compositions of gold and silver alloys. The dashed lines represent the index change in the surroundings from a low value (upper line) to a higher value (lower line) of the medium dielectric constant in terms of an arbitrary value of  $-Y\epsilon_s$ , with  $Y = (1/L) - 1$ , with  $L$  being the depolarization factor along an axis, and  $\epsilon_s$  it the dielectric constant of the medium. From reference 54

In a core-shell structure, it is important to point out that the core resonance dominates only for thin shell, and it is rapidly masked by the shell resonance. Only in case of silver cores, this behaviour is somehow altered by the superior plasmon resonance of silver<sup>55</sup>, whose plasmon usually shapes the absorption spectra. The examples shown in Figure 2.10 show the effect of the shell in both structures. The starting cores have similar size (20nm Au core, 15nm Ag core), and are covered with a shell of different thickness. The plasmonic absorption of silver is much stronger than the one of gold, and almost always prevails as both core and shell.

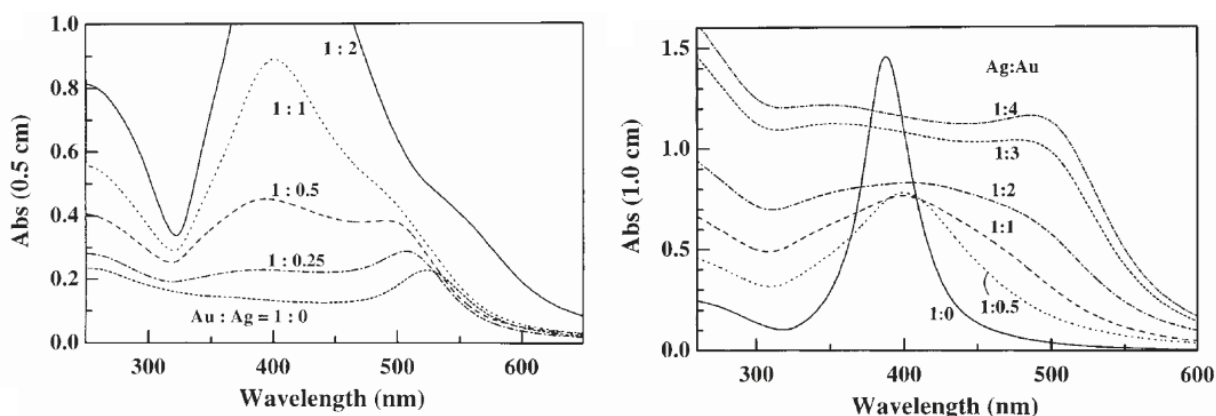


Figure 2.10 – Absorption spectra of Au@Ag (left) and Ag@Au (right) nanoparticles of different composition. From reference 56.

The shell generally dominates the resulting optical properties, up to a point where the identity of the metal core is unimportant so long as it remains metallic<sup>57-59</sup>. In summary, in core@shell systems the plasmon resonance of the resulting nanoparticle can be tuned between those displayed by the single element nanoparticles, but cannot exceed any one of them.

## 2. Optical properties of plasmonic intermetallic nanoparticles and nanoalloys

More exotic structures, such as hollow core-shell nanoparticles made with a shell of gold-silver alloy have been also described in literature, and showed extremely tuneable optical properties, with an SPA that can be shifted from 500 to 1200 nm<sup>60</sup>. This is the combined effect of the variable composition of the shell, as well as of the hollow nature of the nanoparticles, which induces a sensible red shift of the plasmon resonance<sup>61</sup>.

Gold-copper nanoparticles have been obtained, despite the relative complexity of their phase diagrams<sup>50</sup>, but it is still debated if their lattice is ordered or random<sup>46, 62-65</sup>. Their optical properties however, are interesting, because the two structures (ordered and disordered) strongly differ for what concerns the intraband transitions<sup>1</sup>. Consequently, the  $\epsilon_1$  values for these two phases are comparable<sup>66</sup>, but as the wavelength passes 680 nm the  $\epsilon_2$  value of the disordered phase becomes larger than that of the ordered phase<sup>67</sup>. Therefore, the plasmon resonance of the disordered phase is much stronger than that of the ordered phase<sup>66</sup>, and the difference increases the more the plasmon resonance is moved at longer wavelengths.

Silver and copper are scarcely soluble<sup>50</sup> so bimetallic Ag-Cu nanoparticles segregate to form core@shell nanoparticles, with structure depending from the synthesis methods<sup>68-70</sup>. The optical properties of Ag@Cu nanoparticles are similar to those of silver nanoparticles, with only a small peak around 550 nm due to the presence of copper if the core is silver<sup>69, 70</sup>. Conversely, Cu@Ag nanoparticles have an optical spectrum with a single broad peak at 440 nm, expected for a copper core plasmon strongly damped by the silver shell.

### *Platinum group metal hybrids:*

Core@shell structures composed of platinum group metal shell and a coinage metal core show a core plasmon resonance almost completely damped, which reduces their usefulness for purely plasmonic applications. This behaviour is linked to the highly damped plasmon response of the platinum group metals<sup>71</sup>. On the other hand, inversed structures show the typical plasmon response of the coinage metals when the thickness of the shells is large enough, as shown in figure 2.11:

## 2. Optical properties of plasmonic intermetallic nanoparticles and nanoalloys

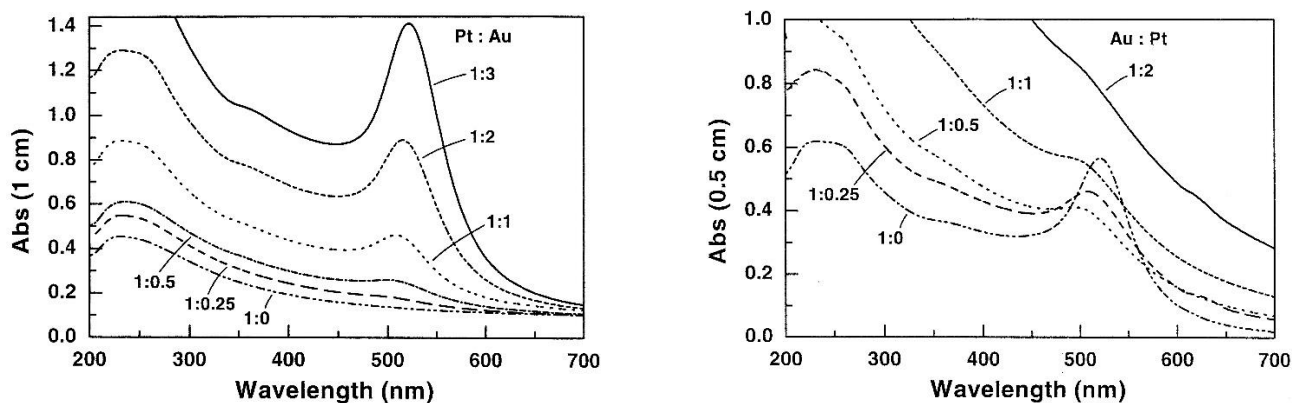


Figure 2.11 – Absorption spectra of Pt@Au (left) and Au@Pt (right) nanoparticles with varying molar ratios. The nanoparticles are all obtained depositing the shell material on a stabile core nanoparticle. From reference 72.

Gold and palladium are readily soluble in their bulk phase<sup>50</sup>, and the catalytic properties displayed by palladium have many promising applications<sup>73</sup>. In many of these nanostructures, the study of the SPA of a gold core is exploited to quickly assess the growth of the Pd shell on the surface of the nanoparticles, since the plasmon resonance of gold was reduced or even completely damped with the increasing amount of palladium in the shell<sup>74</sup>.<sup>75</sup>. This kind of behaviour was observed not only for nanoparticles, but also for nanorods, that exhibited a damping of both their longitudinal and transverse plasmons<sup>76, 77</sup>.

Gold and platinum nanoparticles are formed with greater difficulty, since in bulk these metals are scarcely soluble<sup>50</sup>, and the only intermixed nanoparticles that have been formed are in the 3-6 nm range<sup>78-80</sup>. In the 10-100 nm range, the more interesting for having appreciable resonances, only examples of core-shell nanoparticles are available. Pt@Au nanoparticles have been synthesized, and when the quantity of gold in the nanoparticle is at least half the quantity of platinum, the Au SPA has been observed (see above, figure 2.11)<sup>72</sup>. A particular behaviour was documented when platinum was deposited onto gold nanorods: if the deposition is uniform, damping is observed; however, if the deposition is only on the extremities of the rod, a red-shift of the longitudinal plasmon has been observed<sup>81</sup>, probably due to the increase in local permittivity.

Ag-Pd intermixed alloys have been obtained by radiolytic synthesis of silver and palladium salts, by an approach proposed by Belloni et al.<sup>82</sup>. Data for this experiment is reported in figure 2.12, where one can see the strong dependence of the nanoparticles' SPA peak position from the composition of the salts mixture.

## 2. Optical properties of plasmonic intermetallic nanoparticles and nanoalloys

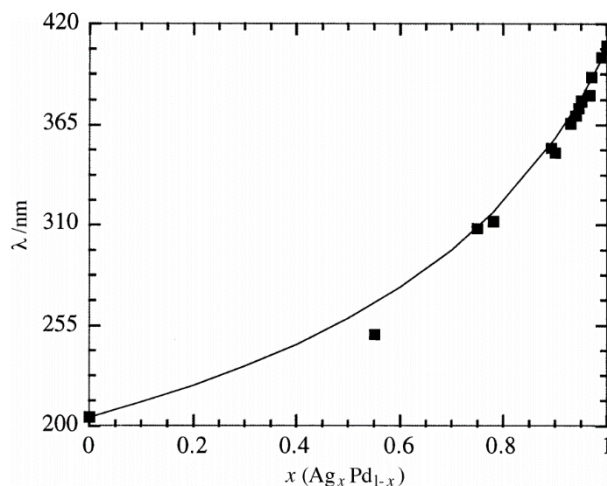


Figure 2.12 – Maximum wavelength of the surface plasmon band of Ag-Pd nanoparticles in relation with the composition of the intermixed solution at complete reduction. From reference 82.

*Hybrids with magnetic metals:* Structures composed of coinage (Au, Ag, Cu) and magnetic (Fe, Co, Ni, Cr) metals are usually obtained as core-shell due to the immiscibility of the typical constitutive elements. If the shell is composed by the coinage metal, we usually see a slightly attenuated and red-shifted plasmon resonance<sup>83</sup>. This behaviour has been attributed to an increase in the surface roughness of the shell, a characteristic that in literature is often associated to the red-shift of the SPA<sup>84, 85</sup>.

In case of Au-Ni, the formed nanoparticles usually have gold shell<sup>86, 87</sup> due to the lower surface energy of this metal compared to nickel<sup>88</sup>: experimental data show that for gold the value is 1.500-1.506 J/m<sup>2</sup>, while for nickel this value is 2.380-2.450 J/m<sup>2</sup><sup>89, 90</sup>.

Gold and iron nanoparticles have been obtained also as a solid solution by ion implantation<sup>91</sup>. In this case, the plasmon resonance of the gold was rapidly damped with the increase of iron content<sup>91</sup>. A similar behaviour is expected for silver and nickel<sup>46</sup> or cobalt<sup>86</sup>.

## 2.6 Bibliography

- 1 M. B. Cortie and A. M. McDonagh, *Chem. Rev.*, 2011, **111**, 3713-3735.
- 2 S. A. Maier, *Plasmonics: fundamentals and applications*, Springer Science & Business Media, 2007.
- 3 U. Kreibig and M. Vollmer, 1995, .
- 4 M. Bosman, V. J. Keast, M. Watanabe, A. I. Maarof and M. B. Cortie, *Nanotechnology*, 2007, **18**, 165505.
- 5 S. A. Maier, M. L. Brongersma, P. G. Kik and H. A. Atwater, *Physical Review B*, 2002, **65**, 193408.
- 6 J. Van Wijngaarden, E. Verhagen, A. Polman, C. Ross, H. Lezec and H. Atwater, *Appl. Phys. Lett.*, 2006, **88**, 221111.
- 7 V. Amendola and M. Meneghetti, *The Journal of Physical Chemistry C*, 2009, **113**, 4277-4285.
- 8 K. L. Kelly, E. Coronado, L. L. Zhao and G. C. Schatz, *The Journal of Physical Chemistry B*, 2003, **107**, 668-677.
- 9 U. Kreibig, M. Gartz and A. Hilger, *Berichte der Bunsengesellschaft für physikalische Chemie*, 1997, **101**, 1593-1604.
- 10 H. Hövel, S. Fritz, A. Hilger, U. Kreibig and M. Vollmer, *Physical Review B*, 1993, **48**, 18178.
- 11 B. Persson, *Surf. Sci.*, 1993, **281**, 153-162.

## 2. Optical properties of plasmonic intermetallic nanoparticles and nanoalloys

- 12 Y. Xia and N. J. Halas, *MRS Bull*, 2005, **30**, 338-348.
- 13 P. K. Jain, W. Huang and M. A. El-Sayed, *Nano Letters*, 2007, **7**, 2080-2088.
- 14 C. Noguez, *The Journal of Physical Chemistry C*, 2007, **111**, 3806-3819.
- 15 B. T. Draine and P. J. Flatau, *JOSA A*, 1994, **11**, 1491-1499.
- 16 A. Gonzalez, C. Noguez, G. Ortiz and G. Rodriguez-Gattorno, *The Journal of Physical Chemistry B*, 2005, **109**, 17512-17517.
- 17 H. Raether, *Surface plasmons on smooth surfaces*, Springer, 1988.
- 18 G. Mie, *Annalen der Physik*, 1908, **330**, 377-445.
- 19 M. Born, *Optik*, Springer-Verlag, Berlin, 1972.
- 20 J. A. Stratton, *Electromagnetic theory.*, McGraw-Hill, New York, 1941.
- 21 R. Gans, *Annalen der Physik*, 1912, **342**, 881-900.
- 22 V. Amendola, O. M. Bakr and F. Stellacci, *Plasmonics*, 2010, **5**, 85-97.
- 23 S. G. Garcia, A. R. Bretones, B. G. Olmedo and R. G. Martin, *Time Domain Techniques in Computational Electromagnetics*, 2003, .
- 24 J. H. Hodak, I. Martini and G. V. Hartland, *The Journal of Physical Chemistry B*, 1998, **102**, 6958-6967.
- 25 S. Logunov, T. Ahmadi, M. El-Sayed, J. Khoury and R. Whetten, *The Journal of Physical Chemistry B*, 1997, **101**, 3713-3719.
- 26 H. Elsayed-Ali, T. Juhasz, G. Smith and W. Bron, *Physical Review B*, 1991, **43**, 4488.
- 27 C. Sun, F. Vallée, L. Acioli, E. Ippen and J. Fujimoto, *Physical Review B*, 1994, **50**, 15337.
- 28 T. S. Ahmadi, S. L. Logunov and M. A. El-Sayed, *J. Phys. Chem.*, 1996, **100**, 8053-8056.
- 29 S. Link and M. A. El-Sayed, *The Journal of Physical Chemistry B*, 1999, **103**, 8410-8426.
- 30 C. Sun, F. Vallee, L. Acioli, E. Ippen and J. Fujimoto, *Physical Review B*, 1993, **48**, 12365.
- 31 S. Brorson, A. Kazeroonian, J. Moodera, D. Face, T. Cheng, E. Ippen, M. Dresselhaus and G. Dresselhaus, *Phys. Rev. Lett.*, 1990, **64**, 2172.
- 32 E. Heilweil and R. Hochstrasser, *J. Chem. Phys.*, 1985, **82**, 4762-4770.
- 33 B. Schrader, *Infrared and Raman spectroscopy: methods and applications*, John Wiley & Sons, 2008.
- 34 J. R. Ferraro, *Introductory raman spectroscopy*, Academic press, 2003.
- 35 K. Kneipp, H. Kneipp, I. Itzkan, R. R. Dasari and M. S. Feld, *Journal of Physics: Condensed Matter*, 2002, **14**, R597.
- 36 M. Kerker, D. Wang and H. Chew, *Appl. Opt.*, 1980, **19**, 3373-3388.
- 37 J. Gersten and A. Nitzan, *J. Chem. Phys.*, 1980, **73**, 3023-3037.
- 38 D. Weitz, S. Garoff, J. Gersten and A. Nitzan, *J. Chem. Phys.*, 1983, **78**, 5324-5338.
- 39 C. F. Bohren and D. R. Huffman, *Absorption and scattering of light by small particles*, John Wiley & Sons, 2008.
- 40 V. Amendola and M. Meneghetti, *Advanced Functional Materials*, 2012, **22**, 353-360.
- 41 S. A. Maier, *Optics Express*, 2006, **14**, 1957-1964.
- 42 V. Shubin, W. Kim, V. Safonov, A. Sarychev, R. Armstrong and V. M. Shalaev, *J. Lightwave Technol.*, 1999, **17**, 2183.
- 43 H. Xu, J. Aizpurua, M. Käll and P. Apell, *Physical Review E*, 2000, **62**, 4318.
- 44 M. D. Arnold and M. G. Blaber, *Optics express*, 2009, **17**, 3835-3847.
- 45 M. Cortie, A. Dowd, N. Harris and M. Ford, *Physical Review B*, 2007, **75**, 113405.
- 46 R. Ferrando, J. Jellinek and R. L. Johnston, *Chem. Rev.*, 2008, **108**, 845-910.
- 47 S. Tokonami, N. Morita, K. Takasaki and N. Toshima, *The Journal of Physical Chemistry C*, 2010, **114**, 10336-10341.
- 48 C. M. Gonzalez, Y. Liu and J. Scaiano, *The Journal of Physical Chemistry C*, 2009, **113**, 11861-11867.
- 49 M. J. Hostetler, C. Zhong, B. K. Yen, J. Anderegg, S. M. Gross, N. D. Evans, M. Porter and R. W. Murray, *J. Am. Chem. Soc.*, 1998, **120**, 9396-9397.
- 50 J. Murray, *ASM Materials International, Materials Park, OH*, 2002, .
- 51 M. Kim, H. Na, K. C. Lee, E. A. Yoo and M. Lee, *Journal of Materials Chemistry*, 2003, **13**, 1789-1792.
- 52 S. Link, Z. L. Wang and M. El-Sayed, *The Journal of Physical Chemistry B*, 1999, **103**, 3529-3533.
- 53 M. P. Mallin and C. J. Murphy, *Nano Letters*, 2002, **2**, 1235-1237.
- 54 K. Lee and M. A. El-Sayed, *The Journal of Physical Chemistry B*, 2006, **110**, 19220-19225.
- 55 M. Blaber, M. Arnold, N. Harris, M. Ford and M. Cortie, *Physica B: Condensed Matter*, 2007, **394**, 184-187.
- 56 J. H. Hodak, A. Henglein, M. Giersig and G. V. Hartland, *The Journal of Physical Chemistry B*, 2000, **104**, 11708-11718.
- 57 P. Mulvaney, M. Giersig and A. Henglein, *J. Phys. Chem.*, 1993, **97**, 7061-7064.
- 58 Q. Zhang, J. Xie, J. Y. Lee, J. Zhang and C. Boothroyd, *Small*, 2008, **4**, 1067-1071.
- 59 S. Bruzzone, M. Malvaldi, G. Arrighini and C. Guidotti, *The Journal of Physical Chemistry B*, 2006, **110**, 11050-11054.
- 60 Y. Sun and Y. Xia, *J. Am. Chem. Soc.*, 2004, **126**, 3892-3901.
- 61 J. Yan, X. Zhang, T. Akita, M. Haruta and Q. Xu, *J. Am. Chem. Soc.*, 2010, **132**, 5326-5327.
- 62 H. Yasuda and H. Mori, *Zeitschrift für Physik D Atoms, Molecules and Clusters*, 1996, **37**, 181-186.
- 63 K. Chatterjee, J. Howe, W. Johnson and M. Murayama, *Acta materialia*, 2004, **52**, 2923-2935.

## 2. Optical properties of plasmonic intermetallic nanoparticles and nanoalloys

- 64 E. Cattaruzza, G. Battaglin, F. Gonella, R. Polloni, B. Scremin, G. Mattei, P. Mazzoldi and C. Sada, *Appl. Surf. Sci.*, 2007, **254**, 1017-1021.
- 65 A. B. Smetana, K. J. Klabunde, C. M. Sorensen, A. A. Ponce and B. Mwale, *The Journal of Physical Chemistry B*, 2006, **110**, 2155-2158.
- 66 A. Henkel, A. Jakab, G. Brunklaus and C. Sönnichsen, *The Journal of Physical Chemistry C*, 2009, **113**, 2200-2204.
- 67 W. Scott and L. Muldrew, *Physical Review B*, 1974, **9**, 1115.
- 68 G. Meitzner, G. Via, F. Lytle and J. Sinfelt, *J. Chem. Phys.*, 1985, **83**, 4793-4799.
- 69 D. Manikandan, S. Mohan and K. Nair, *Physica B: Condensed Matter*, 2003, **337**, 64-68.
- 70 T. Anderson, R. Magruder III, J. Wittig, D. Kinser and R. Zuhr, *Nuclear Instruments and Methods in Physics Research Section B: Beam Interactions with Materials and Atoms*, 2000, **171**, 401-405.
- 71 M. Cortie, X. Xu and M. Ford, *Physical Chemistry Chemical Physics*, 2006, **8**, 3520-3527.
- 72 A. Henglein, *The Journal of Physical Chemistry B*, 2000, **104**, 2201-2203.
- 73 Y. Mizukoshi, T. Fujimoto, Y. Nagata, R. Oshima and Y. Maeda, *The Journal of Physical Chemistry B*, 2000, **104**, 6028-6032.
- 74 N. Toshima, M. Harada, Y. Yamazaki and K. Asakura, *J. Phys. Chem.*, 1992, **96**, 9927-9933.
- 75 A. F. Lee, C. J. Baddeley, C. Hardacre, R. M. Ormerod, R. M. Lambert, G. Schmid and H. West, *J. Phys. Chem.*, 1995, **99**, 6096-6102.
- 76 Y. Xiang, X. Wu, D. Liu, X. Jiang, W. Chu, Z. Li, Y. Ma, W. Zhou and S. Xie, *Nano Letters*, 2006, **6**, 2290-2294.
- 77 J. H. Song, F. Kim, D. Kim and P. Yang, *Chemistry-A European Journal*, 2005, **11**, 910-916.
- 78 N. Tabrizi, Q. Xu, N. van der Pers and A. Schmidt-Ott, *Journal of Nanoparticle Research*, 2010, **12**, 247-259.
- 79 S. Xiao, W. Hu, W. Luo, Y. Wu, X. Li and H. Deng, *The European Physical Journal B-Condensed Matter and Complex Systems*, 2006, **54**, 479-484.
- 80 G. C. Bond, *Platinum Metals Review*, 2007, **51**, 63-68.
- 81 M. Grzelczak, J. Pérez-Juste, B. Rodríguez-González and L. M. Liz-Marzán, *Journal of Materials Chemistry*, 2006, **16**, 3946-3951.
- 82 J. Belloni, M. Mostafavi, H. Remita, J. Marignier and M. Delcourt, *New Journal of Chemistry*, 1998, **22**, 1239-1255.
- 83 J. Zhang, M. Post, T. Veres, Z. J. Jakubek, J. Guan, D. Wang, F. Normandin, Y. Deslandes and B. Simard, *The Journal of Physical Chemistry B*, 2006, **110**, 7122-7128.
- 84 H. Wang, G. P. Goodrich, F. Tam, C. Oubre, P. Nordlander and N. J. Halas, *The Journal of Physical Chemistry B*, 2005, **109**, 11083-11087.
- 85 M. Cortie and M. Ford, *Nanotechnology*, 2007, **18**, 235704.
- 86 M. Gaudry, E. Cottancin, M. Pellarin, J. Lermé, L. Arnaud, J. Huntzinger, J. Vialle, M. Broyer, J. Rousset and M. Treilleux, *Physical Review B*, 2003, **67**, 155409.
- 87 C. Kim, C. Wang, Y. Yang, Y. Hwu, S. Seol, Y. Kwon, C. Chen, H. Liou, H. Lin and G. Margaritondo, *Mater. Chem. Phys.*, 2006, **100**, 292-295.
- 88 L. Vitos, A. Ruban, H. L. Skriver and J. Kollar, *Surf. Sci.*, 1998, **411**, 186-202.
- 89 W. Tyson and W. Miller, *Surf. Sci.*, 1977, **62**, 267-276.
- 90 F. De Boer, R. Boom, W. Mattens, A. Miedema and A. Niessen, *Cohesion in Metals*, North-Holland, Amsterdam, 1988.
- 91 C. de Julián Fernández, G. Mattei, E. Paz, R. Novak, L. Cavigli, L. Bogani, F. Palomares, P. Mazzoldi and A. Caneschi, *Nanotechnology*, 2010, **21**, 165701.



## 2. Optical properties of plasmonic intermetallic nanoparticles and nanoalloys

# Chapter 3

## Laser Ablation Synthesis of Nanoparticles in Liquid Solution

### 3.1 Introduction

Among the possible synthesis methods that can be used to obtain nanoparticles, Laser Ablation Synthesis in Solution provides several advantages: requires a relatively simple setup, allows a very large combination of liquid solvents and metal targets, does not produce or require dangerous or polluting chemicals, and gives nanoparticles with an easily accessible surface that can be functionalized immediately or at longer times.

The typical setup, in its simplest form, is shown in figure 3.1. The necessary elements are a pulsed laser, a mirror for deflecting the laser beam (when needed), a lens to focus the beam on the ablation target, a container filled with the solvent of choice, and the bulk material to be ablated.

Laser power, pulse duration and wavelength can influence the type of nanoparticles obtained, because of the different interaction with the target and the solvent.<sup>1</sup>

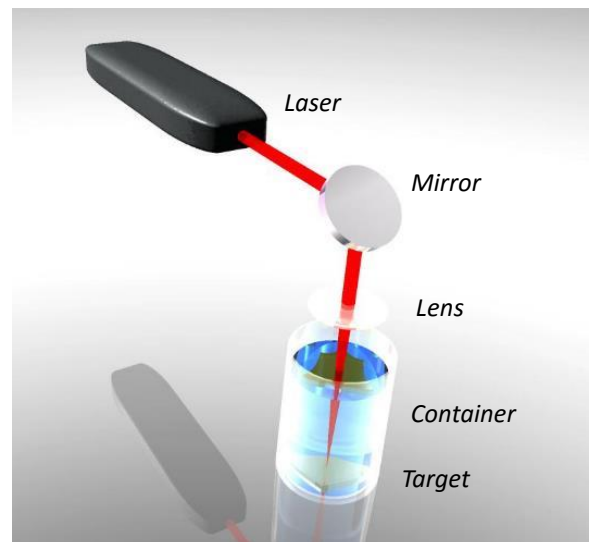


Figure 3.1 – Sketch of the typical setup for laser ablation

The number of possible metal and solvent combinations is very large. Indeed, it is possible to choose the best target for our needs, such as alloys with well defined composition, as

### 3. Laser Ablation Synthesis of Nanoparticles in Liquid Solution

well as to exploit the interaction of the liquid with the metal target during the ablation process to obtain different products.

Since no surfactants or stabilizing molecules are required on the surface of the nanoparticles during the synthesis, it is possible to add directly in the solvent as many ligands as it is necessary, allowing the immediate functionalization of the nanoparticles<sup>2</sup>.

## 3.2 Dynamics of Laser Ablation

It is possible to identify different stages in the laser ablation: the first step is the absorption of the laser pulse from the target, followed by the creation and expansion of a plasma plume containing the ablated material, which is accompanied by two shockwaves propagating in the solid and in the liquid phases. Successively, the ablated material cools down by heating up the surrounding liquid and creating a cavitation bubble, that collapses emitting a second shockwave after having reached the point of maximum expansion in the liquid<sup>3</sup>. After the first collapse, a second cavitation bubble with smaller size can expand and collapse again, depending on energy of the laser pulse and physical properties of the liquid<sup>3</sup>.

There are four parameters that contribute to define the final products of the laser ablation: temperature (T), pressure (P), concentration of the ablated material ( $C_M$ ), and concentration of the solution species ( $C_S$ ). Figure 3.2 shows a sketch of the ablation area, with the 4 gradients outlined<sup>3</sup>:

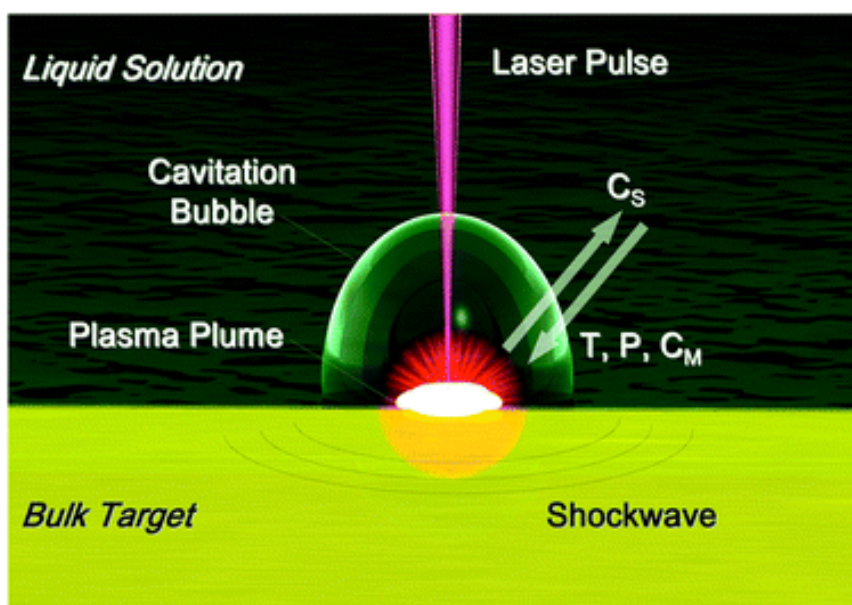


Figure 3.2 – Diagram of the ablation area. It is possible to see that, when we approach the ablation area, the temperature, pressure, and concentration of ablated material increase, while the concentration of solution species decreases. From reference 3.

### 3. Laser Ablation Synthesis of Nanoparticles in Liquid Solution

In table 3.1 the ablation sequence is broken in six different steps, to better track the parameters that bring to the final nanomaterials, considering  $t=0$  when the laser pulse hits the target:

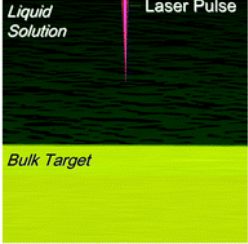
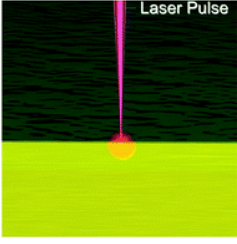
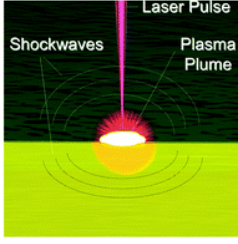
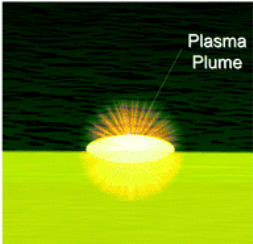
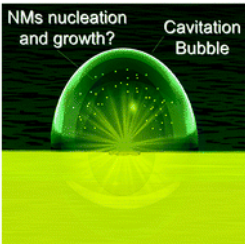
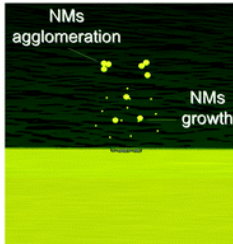
<p style="text-align: center;"><b><math>t &lt; 0</math></b></p>  <p style="text-align: center;"><u>Pulse penetration in the liquid</u></p>	<p style="text-align: center;"><b>From <math>t=0</math> to <math>\tau_{pulse}</math></b></p>  <p style="text-align: center;"><u>Pulse absorption</u></p>	<p style="text-align: center;"><b>From <math>t= 10^{-12}s</math> to <math>10^{-10}s</math></b></p>  <p style="text-align: center;"><u>Removal of ablated material</u></p>
<p style="text-align: center;"><b>From <math>t=10^{-10}s</math> to <math>10^{-7}s</math></b></p>  <p style="text-align: center;"><u>Expansion and cooling of the plasma plume</u></p>	<p style="text-align: center;"><b>From <math>t=10^{-6}s</math> to <math>10^{-4}s</math></b></p>  <p style="text-align: center;"><u>Expansion and collapse of the cavitation bubble</u></p>	<p style="text-align: center;"><b><math>t &gt; 10^{-4}s</math></b></p>  <p style="text-align: center;"><u>Growth of the nanoparticles</u></p>

Table 3.1 – Steps of the ablation process. From reference 3.

**Pulse penetration in the liquid.** Before hitting the target, the laser pulse must travel through the solution. This means that any energy absorption due to the liquid must be as low as possible. While completely removing solvent absorption is not feasible, care must be taken in choosing a solvent with negligible absorption even at the large fluence of LASiS.

A possible cause of energy loss is the creation of a parasitic plasma inside the solvent. Berthe et al. studied the pressure waves induced by parasitic plasma with varying power and wavelength, identifying a specific breakdown threshold that limits the maximum ablation power achievable for a specific combination of wavelength, pulse power, and laser pulse duration. The results of this study are reported in figure 3.3<sup>4</sup>. At low power density with all three used wavelengths (1064, 532, 355 nm), the shockwave pressure increases with laser intensity following the theoretical predictions. A power density level defined as *saturation intensity*,  $I_{sat}$  is reached, after which the shockwave power remains stable at a value defined as *saturation pressure*,  $P_{sat}$ . As the wavelength increases, the maximum value of  $I_{sat}$  and  $P_{sat}$  both increase. It is also possible to observe additional effects, such as reduced

### 3. Laser Ablation Synthesis of Nanoparticles in Liquid Solution

shockwave duration<sup>5</sup> and shortening of the laser pulse transmitted to the target<sup>6</sup>.

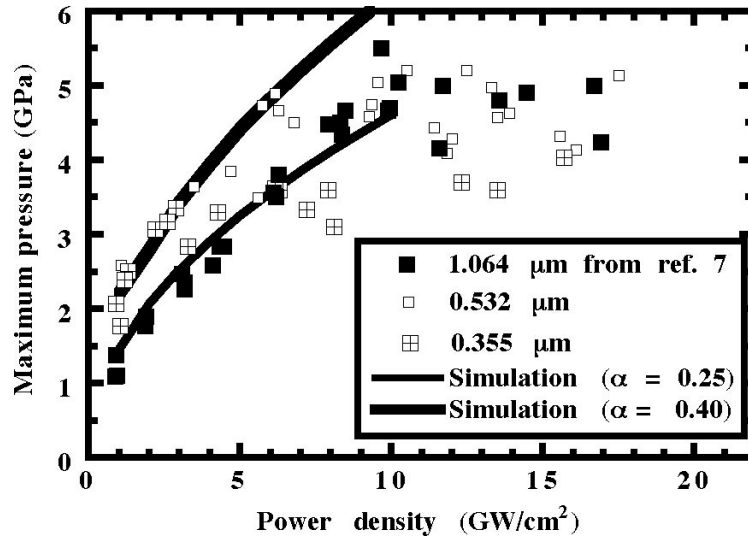


Figure 3.3 – Peak shockwave pressures obtained during the ablation experiments, carried out with nanosecond lasers (25–30 ns). The data for the 1064nm ablation were obtained by reference <sup>5</sup>, while the two simulations were obtained from Simulation Hydrodynamique Lagrangienne de Chocs (SHYLAC) data, from reference 7.

Following these studies, it has been possible to identify the parameter  $\alpha$ , defined as the efficiency of the confined laser interaction. This parameter contains the fraction of the plasma internal energy which contributes to the rise in plasma pressure, following the formula  $E_{th} = \alpha E_{int}$ , where  $E_{int}$  is the plasma internal energy and  $E_{th}$  is the fraction of  $E_{int}$  devoted to the pressure rise of the laser plasma. This parameter allows us to define  $E_{ioni} = (1 - \alpha)E_{int}$  as the fraction of internal energy that contributes fully to the plasma ionization.

The mechanisms that underlie the laser-induced breakdown of the solvent are two: multiphoton ionization (MPI) and avalanche ionization (AI)<sup>4</sup>.

MPI consists in the ionization of atoms (M) in the medium, with generation of free electrons, which occurs when the electromagnetic field is sufficiently large, i.e. when the number ( $m$ ) of photons per atom is above the threshold for ionization:



It is important to point out that, in this phenomenon, one of the determining parameters is the energy of the incoming photon, with the efficiency higher for shorter wavelengths. For water, with a laser wavelength of 1064nm  $m = 11$ , while for 355nm we have  $m = 5$ .

The AI mechanism is linked to the quick growth in the number of free electrons, due to the impact ionization of the medium via free-electron laser absorption, with a mechanism defined as *inverse bremsstrahlung* (IB). We can write down the process by considering it as a reaction:

### 3. Laser Ablation Synthesis of Nanoparticles in Liquid Solution



It is important to note that this phenomenon is more relevant at lower wavelengths, since  $IB \propto \lambda^2$  due to its scaling law<sup>8</sup>, and can start only when free electrons are present in the medium<sup>4</sup>.

Nichols et al., while studying the ablation of platinum targets, discovered that, working in defocused conditions and at high laser powers (70-120 J/cm<sup>2</sup>), breakdown in water can be caused by the focusing of the laser reflected from the target (about 25% of the incoming photons at 355 nm)<sup>9</sup>.

*Pulse absorption.* When the laser pulse hits the target, a fraction of its energy not lower than 50-60% is absorbed. What happens next is strongly influenced by the laser pulse duration.

With femtosecond laser pulses, the absorption is mainly due to free electrons, via inverse Bremsstrahlung<sup>10</sup>. In these conditions, the temperature of the electrons is higher than that of the lattice, while the only two contributions to cooling are the energy exchange with the lattice and the electron heat conduction (the latter smaller than the former)<sup>10</sup>. This behaviour is observable when the laser pulse duration  $\tau_L$  is shorter than the characteristic time  $\tau_E$  required by the electrons to reach a complete thermal equilibrium with the ions by phonon emission, which goes from 10<sup>-12</sup>s to 10<sup>-11</sup>s<sup>11, 12</sup>. In this instance, the ablation proceeds on the skin depth of the target via creation of plasma and vapour phases, without any form of thermal conduction into the target<sup>1, 13</sup>.

When laser pulses longer than  $\tau_E$  are used, the thermal conduction pathway takes place simultaneously to photon absorption. For instance, the presence of a melted zone in the ablation crater is observable, progressively more widespread the longer the laser pulse duration<sup>1</sup>.

*Removal of ablated material.* When laser pulses are shorter than  $\tau_E$ , the dynamics become more complex. In figure 3.4 are reported the data from a simulation (the dynamics of the atomic degrees of freedom are obtained with molecular dynamics, while the evolution of the carriers is treated with a Monte Carlo scheme) of temperature  $T$  versus density  $\sigma$  in case of ablation of a model material of atoms arranged in a triangular lattice with 200 fs pulses, developed by Perez et al.<sup>13</sup> in the hypothesis of Lennard-Jones hard spheres atoms<sup>14, 15</sup>.

From the plot of  $T$  versus  $\sigma$ , it is possible to see that the initial rapid heating of the ablated material is followed its expansion and melting, through a metastable liquid region (located under the liquid-vapour coexistence line), and relaxes again crossing the liquid-solid line.

### 3. Laser Ablation Synthesis of Nanoparticles in Liquid Solution

The material flow from the upper layers can be considered adiabatic, because it consists mainly of clusters surrounded by a dilute gas, a composition that strongly reduces the efficiency of the energy transfer. The large portion of the ablated material, on the other hand, is cooled down by unimpeded heat diffusion and then goes back to its original conditions.

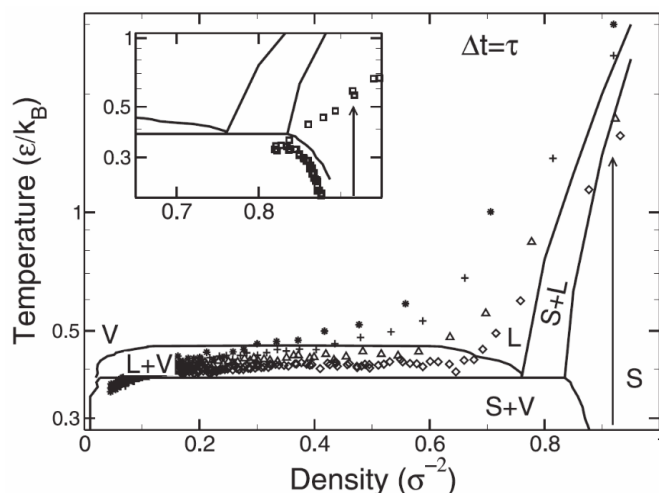


Figure 3.4 – Thermodynamic evolution of the ablated material (laser pulse 200 fs) for different depths under the surface. The symbol \* represents the data from a depth of  $-15\sigma$  ( $\sigma$  represents the Lennard-Jones hard-sphere diameter), + the data from a depth of  $-20\sigma$ ,  $\Delta$  for a depth of  $-50\sigma$ ,  $\diamond$  for a depth of  $-90\sigma$ . In the inset are reported the data for  $-300\sigma$ . S, L and V stand for Solid, Liquid, and Vapour. The arrow shows the path of the material during heating. From reference 13.

Experimental observations<sup>14, 15</sup> showed that, with femtosecond pulses, the ablation is caused by mechanical fragmentation for the upper layers (15-20  $\sigma$  from the surface, with  $\sigma$  being the Lennard-Jones hard-sphere diameter) and by phase expansion for the lower layers (50-90  $\sigma$  from the surface). The simulation also showed that by raising or lowering the power of the laser pulse, different ablation mechanisms are reported, such as rapid vaporization in the former case and spallation in the latter<sup>13</sup>.

When the laser pulse duration is increased up to the picosecond regime, the behaviour of the absorbing material changes significantly, as can be seen in figure 3.5, that reports the results for an ablation pulse length of 100ps<sup>13</sup>. The expansion of the material in these conditions is strongly dependent from its position in the solid. The heating can be no longer considered isochoric, so the material will more likely relax within the fluid than enter the metastable liquid region. The analysis excludes phase explosion, since it would require the system to pass through a metastable phase<sup>13</sup>. It is also possible to exclude the vaporization as a mechanism, since clusters of large dimensions (up to 100 atoms) are identifiable. These characteristics assimilate the ablated material to a supercritical fluid, since it adopts the same equilibrium structure during the expansion. Since this structure is usually strongly inhomogeneous at low densities<sup>16, 17</sup>, it is possible to define the ablation mechanism just as simple fragmentation<sup>18</sup>.

### 3. Laser Ablation Synthesis of Nanoparticles in Liquid Solution

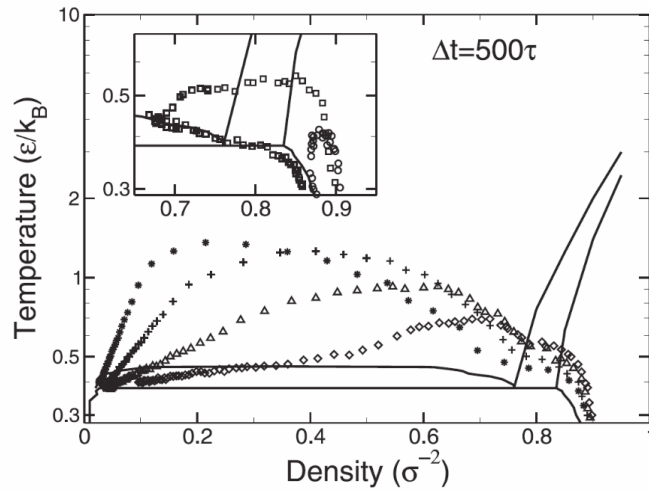


Figure 3.5 – Thermodynamic evolution of the ablated material (laser pulse 100 ps) for different depths under the surface. The symbol \* represents the data from a depth of  $-15\sigma$  ( $\sigma$  represents the Lennard-Jones hard-sphere diameter), + the data from a depth of  $-20\sigma$ ,  $\Delta$  for a depth of  $-50\sigma$ ,  $\diamond$  for a depth of  $-90\sigma$ . In the inset,  $\square$  signals the data from  $-180\sigma$ ,  $\circ$  for  $-250\sigma$ . The arrow shows the path of the material during heating. From reference 13.

The results of the simulation for even longer pulse durations (400 ps) are reported in picture 3.6<sup>13</sup>. With these parameters, the upper layers of the target expand very closely to the solid-vapour and liquid-vapour phase boundaries, and since there is enough time for heat diffusion inside the plume, the  $T, \sigma$  plot is similar for the different target depth considered in the calculation. The material ablated from the deepest part of the sample (as shown in the inset in figure 3.6) relaxes along the coexistence lines. Again, since no fraction of the material enters the metastable liquid region, it is possible to exclude phase explosion, and the mechanism is again fragmentation<sup>13</sup>.

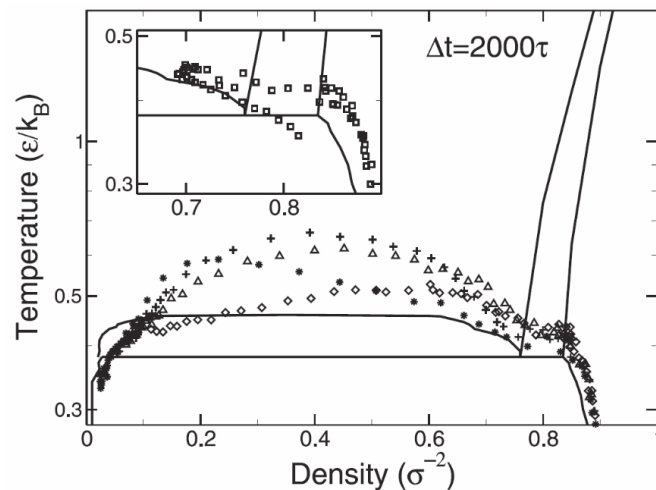


Figure 3.6 – Thermodynamic evolution of the ablated material (laser pulse 400 ps) for different depths under the surface. The symbol \* represents the data from a depth of  $-15\sigma$  ( $\sigma$  represents the Lennard-Jones hard-sphere diameter), + the data from a depth of  $-20\sigma$ ,  $\Delta$  for a depth of  $-50\sigma$ ,  $\diamond$  for a depth of  $-90\sigma$ . In the inset are reported the data from  $-170\sigma$ . The arrow shows the path of the material during heating. From reference 13.

The differences between different pulse lengths can be seen in simulations reported in figure 3.7<sup>12</sup>. For nanosecond ablation pulses, when  $\tau_L > \tau_E$ , the process is considered a quasi-equilibrium one, and it is possible to identify three main processes: fragmentation, explosive



### 3. Laser Ablation Synthesis of Nanoparticles in Liquid Solution

boiling, and heterogeneous nucleation. Perez et al.<sup>19</sup> have carried out simulation of the ablation mechanism, and the results are reported in figure 3.7. It is possible to identify three different zones inside the ablation volume: in the upper region (I) there are mainly rapidly expanding liquid drops and gases; in the second region (II), the content of gas is lower, but the area is still mainly melted; lastly, in the depths of the sample (III) there are cavities in a solid-liquid region.

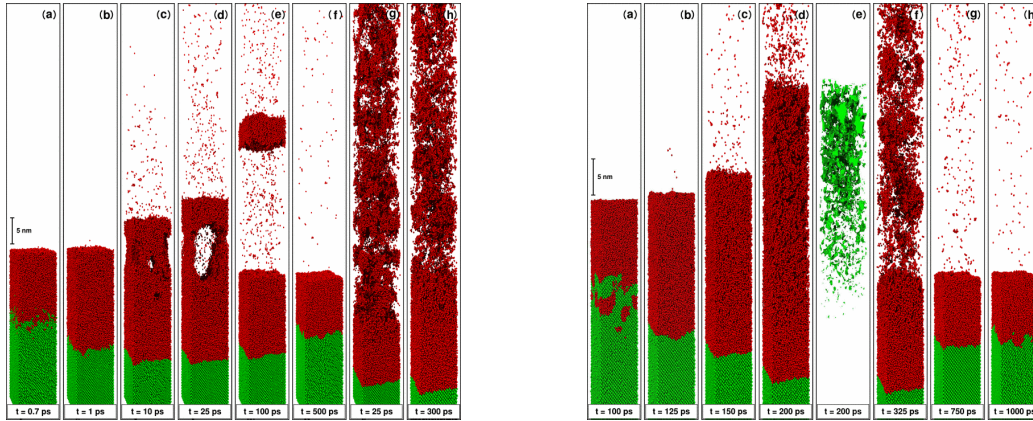


Figure 3.7 - Snapshot of the structural changes induced in a Si(100) substrate by a laser with  $\lambda=266$  nm and pulse length of 500fs (left) and 100 ps (right). In red, the molten material; in green, the solid material. On the right, (e) represents a detail of the voids in the expanding molten layer. From reference 12.

In the  $\rho$ - $T$  graphs it is possible to follow the temporal evolution of the system (using the arrows). The black dots show the data for the “dense” (intended as solid/liquid) phase of the system; the white dots show the data for the “average” phase (mixture of dense/gas), while the gas phase is out of range from the graphs.

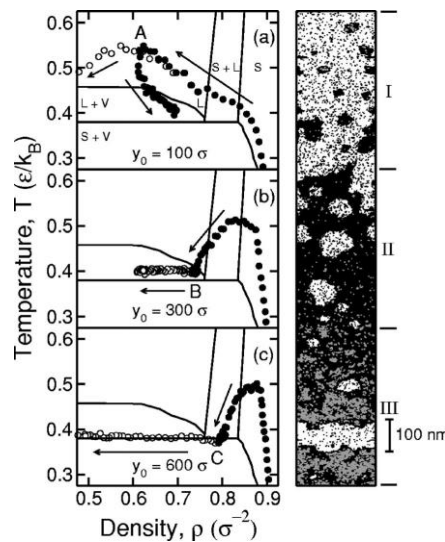


Figure 3.8 – On the left, time evolution of the  $\rho$ - $T$  systems for the different areas of the ablated zone. On the right, a simulation of the ablated area at time  $t=2500\tau$ . From reference 13.

Since for times shorter than  $10^{-12}$  s the material is inertially confined to the surface of the target, excess energy absorbed on this timescale is released in form of two shockwaves. One is emitted in the solid, another in the liquid where it changes the refraction index and

### 3. Laser Ablation Synthesis of Nanoparticles in Liquid Solution

can be directly measured by shadowgraphy<sup>20</sup>. In figure 3.9 we report the data regarding the dimension and position of a shockwave linked to laser ablation of silver in water<sup>21</sup>.

In the experiment of Figure 3.9, the speed of the shockwave front was estimated at around 2600 m/s. From the comparison with data regarding laser focusing in liquid nitrogen<sup>22</sup>, it was estimated that energy converted in the generation of the shockwave is of ~30% of total absorbed energy.

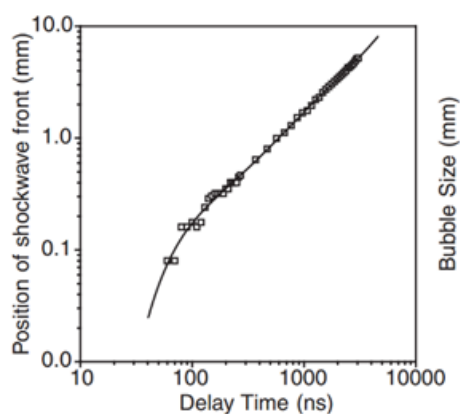


Figure 3.9 – Time profiles of the position of the shockwave front obtained during laser ablation (1064 nm, 8ns, 20 mJ/pulse) of silver in water. From reference 21.

The ablated species are highly ionized due to the extreme temperature and direct photoionization from the laser pulse, and are generally considered to leave the ablation crater in the form of a “plasma plume”. An example of the optical emission from plasma generated in laser ablation of graphene in water is reported in figure 3.10<sup>23</sup>, where one can appreciate the characteristic plasma emission composed of a continuous emission spectrum lasting up to 100 ns after the ablation, due to bremsstrahlung and radiative recombination. After that period the dominating contribution is that of discrete emissions from excited atomic and molecular species<sup>23, 24</sup>.

The plasma plume is localized over the target, but for shorter pulses ( $T_L < 10^{-12}$  s) this does not constitute a problem, since the liquid-vapour equilibration time is  $\geq 10^{-12}$  s<sup>12, 25</sup>. For lasers with longer pulses, especially nanoseconds, the ablation plume is an absorption source, and even at power near the ablation threshold can cause ionization of the ablated material<sup>26, 27</sup>, sensibly raising the temperature of the plasma and lengthening its lifetime<sup>10, 28</sup>.

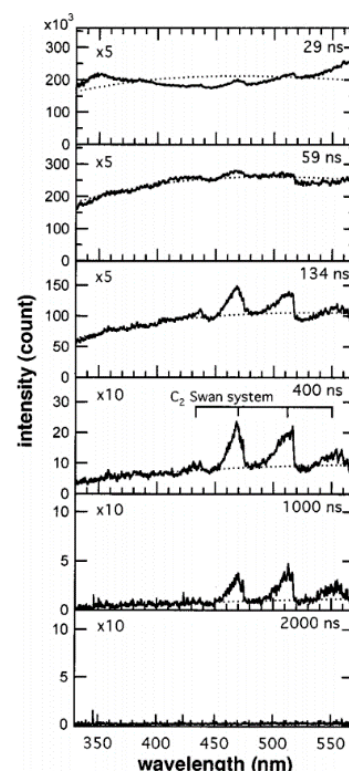


Figure 3.10 – Emission spectra from the graphite ablation in water. The dotted line is a curve fitting. From reference 23.

### 3. Laser Ablation Synthesis of Nanoparticles in Liquid Solution

*Expansion and cooling of the plasma plume.* Independently from pulse duration, the liquid confines the ablated material immediately over the target, slowing its expansion in the liquid<sup>29</sup> and, consequently, its cooling. Besides, the liquid keeps the heated plasma over the target, supplying the latter with an additional energy source with a lifetime potentially longer than that of the laser pulse (several nanoseconds). The final result is that a larger portion of the target arrives to the ablation threshold, and the ablation yield increases compared to laser ablation in gaseous environment<sup>30-34</sup>. For very short times from the ablation ( $t < 10^{-10}$  s) the gradients of the parameters  $T$ ,  $P$ ,  $C_M$ , and  $C_S$  are very sharp and only three zones are clearly distinguishable: the target, the plasma plume, and the solvent. After that period is possible to observe the smoothing of these sharp gradients, due to the heating of both solvent and target from the plasma plume<sup>23, 24</sup>. From this moment, nucleation of nanoparticles is possible. Several details of the process are poorly understood to date, with some authors placing the beginning of nucleation at  $10^{-9}$  s<sup>35</sup>, while other around  $10^{-5}$  s<sup>20, 33</sup>. A particularly important factor that needs to be clarified is the possibility of mixing of the ablated species and solvent ones before that nucleation starts. Some studies have shown that it may actually occur already inside the plasma plume, but further information on the entity of this phenomenon is missing at the moment<sup>23, 24</sup>.

*Expansion and cooling of the cavitation bubble.* The formation of bubbles at the solid-liquid interface is a characteristic of the laser ablation<sup>36</sup>. In general, bubbles can be formed by explosive boiling when the liquid is heated up to the limit of superheating  $\Delta T_C$ , or by cavitation when the pressure of the liquid falls below the tension strength of the liquid by an amount  $\Delta P_C$ . Indeed, both mechanisms are quite similar, since  $\Delta P_C$  and  $\Delta T_C$  can be related by the equation of Clausius–Clapeyron (equation 3.1)<sup>36</sup>:

$$\frac{dP}{dT} = \frac{L}{T\Delta V} \quad (3.3)$$

In laser ablation, the layer close to the heated target almost inevitably boils. The bubbles can nucleate heterogeneously at the interface between the solid and the liquid, or in the superheated liquid, and then aggregate in the foamy layer following the expansion of the ablation plume<sup>36</sup>.

The heterogeneous nucleation rate  $J$  of the bubble can be calculated with the following formula:

$$J = \frac{\rho_{N,l}^{2/3} (1 + \cos \theta)}{2F} \sqrt{\left(\frac{3F\sigma}{\pi m}\right)} \exp \left\{ \frac{-16F\pi\sigma^3}{3k_B T_l [\eta P_{sat}(T_l) - P_l]^2} \right\} \quad (3.4)$$

In this equation,  $\rho_{N,l}$  is the number of liquid molecules/atoms per unit volume,  $\sigma$  is the surface

### 3. Laser Ablation Synthesis of Nanoparticles in Liquid Solution

tension,  $m$  is the mass of one molecule/atom,  $k_B$  is the Boltzmann constant,  $T_l$  is the temperature of the liquid,  $P_{SAT}(T_l)$  is the saturation vapour pressure at  $T_l$ ,  $P_l$  is the ambient liquid pressure, and the value of  $\eta$  and  $F$  is determined by the following expression<sup>37</sup>:

$$\eta = \exp \left[ \frac{P_l - P_{sat}(T_l)}{\rho_l R T_l} \right] \quad (3.5)$$

$$F = \frac{1}{2} + \frac{3}{4} \cos \sigma - \frac{1}{4} (\cos \sigma)^3 \quad (3.6)$$

In these expressions,  $\rho_l$  is the density of the liquid, and  $\theta$  is the liquid-solid contact angle.

On the other hand, spontaneous generation can happen in the metastable region of the superheated liquid, following the equation<sup>37</sup>:

$$J = \rho_{N,L} \sqrt{\left( \frac{3\sigma}{\pi m} \right)} \exp \left\{ \frac{-16\pi\sigma^3}{3k_B T_l [\eta P_{SAT}(T_l) - P_l]^2} \right\} \quad (3.7)$$

The contributions from equation 3.3 and 3.5 vary depending on the value of  $\theta$ , since for  $\theta > 70^\circ$  the heterogeneous nucleation rate (3.5) is higher than the spontaneous generation rate (3.5), while it becomes smaller for  $\theta < 65^\circ$ <sup>37</sup>. Since water has contact angles  $\sim 20^\circ$  on metal and  $30-40^\circ$  on oxides, the dominant nucleation mode is the homogeneous mode.

After bubble formation, it grows up to its maximum dimension, while the internal pressure and temperature decreases up to a point where internal and external pressures are equal, after that the bubble collapses to a minimum. An example of this behaviour can be found in figure 3.11<sup>38</sup>. In most cases, the process proceeds cyclically by repeated pressure and temperature growth and gas expansion, but every time up to a lower dimension because of energy dissipation during the process, until complete transfer of bubble energy to the environment.

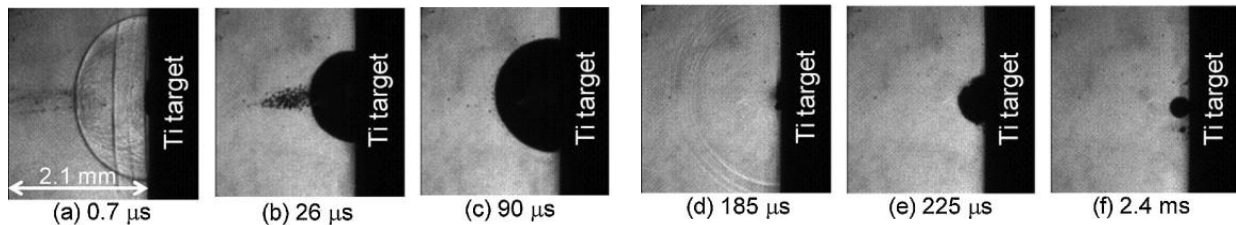


Figure 3.11 – Time-resolved shadowgraph of cavitation bubbles produced by laser ablation of a Ti target in water. From reference 38.

A factor that can increase the stability of the bubble is the availability of gas, as shown by Zijie in his analysis of ablation of Mg in water<sup>39</sup>. The author discovered that the formation of atomic or molecular hydrogen as byproduct of the formation of MgO in water, could increase the bubble lifetime duration from  $0.9\mu\text{s}$  to  $1.2\text{ s}$ , since when the bubble contains gas its

### 3. Laser Ablation Synthesis of Nanoparticles in Liquid Solution

lifetime is largely determined by the mass diffusion of the gas from the bubble to the liquid. The bubbles containing the gas might also collapse in microscopic foam, serving as seeds for the formation of further cavitation<sup>40</sup>. Other factors that can prolong the lifetime of the bubble are impurities, such as nanoparticles<sup>40</sup>, due to their adsorption on the bubble interface sterically impeding its movement. A similar effect is linked to the alteration in the viscosity of the liquid<sup>41</sup>: its increase lowers the rate of bubble oscillation, and prolongs its lifetime. Each collapse of the bubble can cause cavitation damage to the target and remove further material from the surface<sup>42</sup>. However, bubble collapse occurs after times of the order of hundreds of  $\mu\text{s}$  to  $\text{ms}$ , when target temperature is comparable to room temperature, hence material removal occurs only by a purely mechanical effect.

The growth of the bubble in a superheated liquid usually shows two stages: it is initially inertially-controlled and  $R(t)$  grows proportionally to  $t$ , and then becomes heat-transfer controlled and the growth of  $R(t)$  becomes proportional to  $\sqrt{t}$ . If the growth takes place near to an heated surface, it is more difficult that the bubble will follow the theoretical trend, since the symmetry is not spherical and there are temperature gradients, but still shows stages of inertia and thermal effects<sup>36, 37</sup>.

*Growth of the nanoparticles.* During the expansion phase of the laser-induced plasma plume, its temperature decreases quickly,<sup>36</sup> ions and electrons recombine, and vapour condensation starts<sup>36</sup>. Condensation proceeds in two steps: first the critical cluster nucleation, then growth of the nuclei. The availability of ions inside the ablation plume is important for the average cluster size: ions lower the clustering energy barrier due to dielectric attraction with surrounding vapour neutral atoms, thus increasing the nucleation rate and lowering the average cluster size<sup>43</sup>.

Nucleation time depends on the pressure of buffer medium, as shown by table 3.2 for the gas phase<sup>36</sup>. From the values reported, one can see that increasing the confinement of the ablation plume will decrease the nucleation time<sup>36</sup>. It is therefore expected that at the typical pressure used in LASiS (atmospheric pressure, 760 Torr) the time will be longer than the isothermal nucleation time (calculated by Wang et al. in  $10^{-10}$ - $10^{-9}$  s<sup>35</sup>) but shorter than the typical time of the first oscillation for a laser-induced bubble. Then, clustering and growth of the nanoparticles will start inside the bubble, and this means that modification to the bubble dynamics will strongly influence the final result.

Nanocluster formation time in 10 Torr He	Nanocluster formation time in 1 Torr Ar	Clustering time in 10 Torr He	Clustering time in 10 Torr Ne	Clustering time in 10 Torr Ar	Clustering time in 10 Torr N <sub>2</sub>
150-200 $\mu$ s	3 ms	200 $\mu$ s	250 $\mu$ s	300 $\mu$ s	800 $\mu$ s

Table 3.2 – Onset time of nanocluster formation and clustering time for Si ablation in gas. From reference 44-46.

A good example of this behaviour is the experiment carried out by Yan et al.<sup>47</sup>, where organic molecules such as Triton X-100 were added in water and caused significant increase in the obtained nanoparticles' size.

After the collapse of the bubble, the material is dissolved in the liquid, where chemical reaction with solution species may occur, such as the formation of reactive metal oxides (like the formation of ZnO from the ablation of zinc targets in water<sup>48</sup>).

### 3.3 Investigation techniques

To study the ablation process, information should be collected from beneath the liquid layer, or even from the plasma. However, each one of these layers also interfere with the analysis. Moreover, the temporal resolution of the investigation techniques need to be extremely high, since the mechanism itself has a very short time span and the amount of material obtained by each ablation pulse is very low ( $10^{-1}$ - $10^{-3}$   $\mu$ g per pulse<sup>49</sup>). A scheme of the possible analysis methods is displayed in figure 3.12:

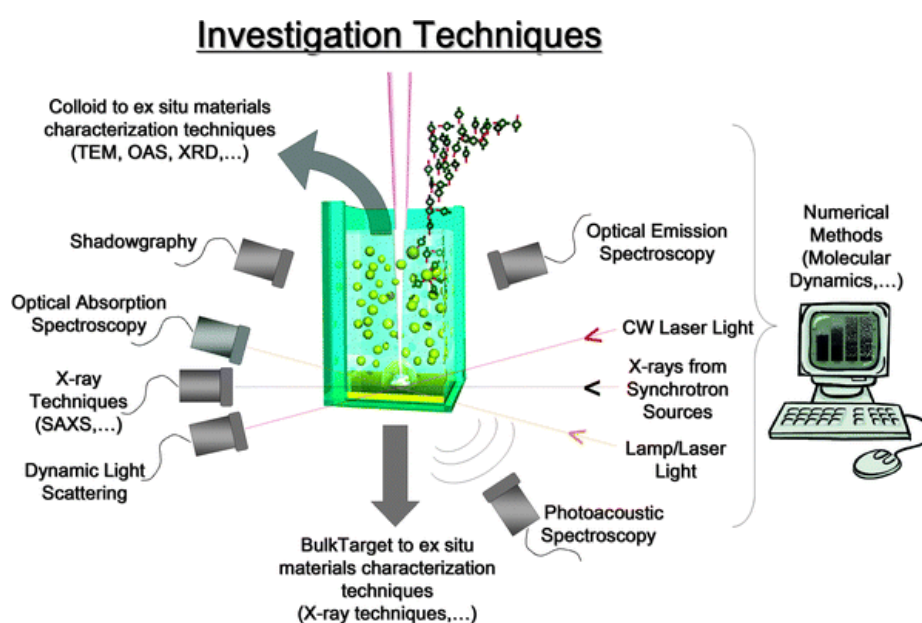


Figure 3.12 – Possible analysis techniques for the LASiS. From reference 3.

**Optical emission spectroscopy.** This technique, also known as Laser-Induced Breakdown Spectroscopy (LIBS), has been used in the last decades as an analytical tool to determine

### 3. Laser Ablation Synthesis of Nanoparticles in Liquid Solution

the elemental composition of solid samples<sup>50</sup> due to its high sensitivity and fast response time<sup>51</sup>. Other advantages of this method are the possibility to use it with many materials and without surface preparation, and the degree of flexibility in the experimental setup<sup>52-55</sup>. Recent developments of this technique include the Double Pulse LIBS, allowing a signal up to two orders of magnitude greater than that obtained in the standard LIBS<sup>51</sup>. This technique is particularly interesting for analysis in liquid environment, since the second laser pulse induces plasma expansion in a hot vapour bubble and not in the liquid environment<sup>56, 57</sup>.

The setup of this technique is usually composed from a pulsed laser source, powerful enough to ablate the target surface, and a spectrograph capable of detecting the emission signal<sup>51</sup>, like the one shown in figure 3.13:

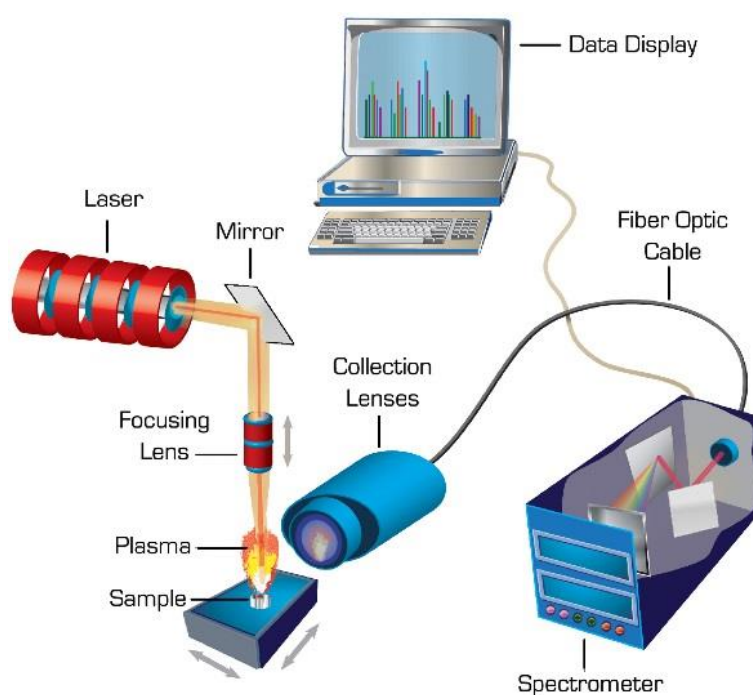


Figure 3.13 – Setup for a typical bench LIBS. From reference 58.

The emission from the plasma can be performed in different geometries, depending on the desired data. Transverse acquisition requires a simple setup, but caution is needed to avoid problems with the reproducibility in plasma emission detection<sup>59, 60</sup>. Collinear acquisition allows higher sensitivity, is less affected by the changes in target morphology caused by drilling and allows longer acquisition of plasma emission, but has no spatial plasma resolution<sup>61, 62</sup>. The orthogonal configuration gives the most accurate measurements for studying plasma evolution<sup>56, 63</sup>.

**Shadowgraphy.** This technique is similar in principle to the one described above, but works by illuminating the ablation area with an external lamp in a transversal setup. In figure 3.14 the typical setup for this technique is shown<sup>64</sup>:



### 3. Laser Ablation Synthesis of Nanoparticles in Liquid Solution

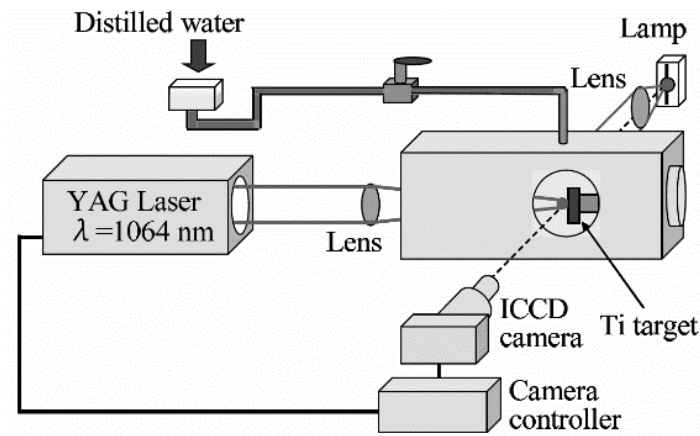


Figure 3.14 – Setup for a typical shadowgraphy instrument. From reference 64.

Useful information can be collected about the plasma plume, the dynamics of the laser-induced bubbles and of the shockwaves<sup>32, 33, 65, 66</sup>.

*Photoacoustic spectroscopy.* With this technique the sound emitted when the laser pulse is absorbed by the target is acquired with the help of a microphone, and analysed in detail. A typical setup is shown in figure 3.15:

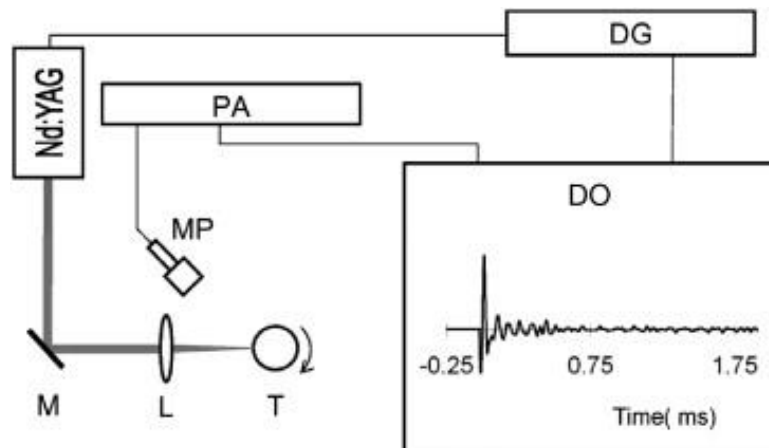


Figure 3.15 – Setup of the measurement system used in the analysis of the acoustic signal generated in pulsed laser ablation. From reference 67.

The photoacoustic signal shows dependence on many parameters, like laser energy<sup>68</sup> and sample type<sup>69</sup>. In some materials, like aluminium, calculation of the amount of ablated material from the acoustic data is even possible<sup>70</sup>.

*Optical absorption spectroscopy.* This technique allows the collection of a wide amount of data, depending from the acquired wavelengths and the time resolution of the instrument. In figure 3.16 a multi-spectrometer setup is shown:



### 3. Laser Ablation Synthesis of Nanoparticles in Liquid Solution

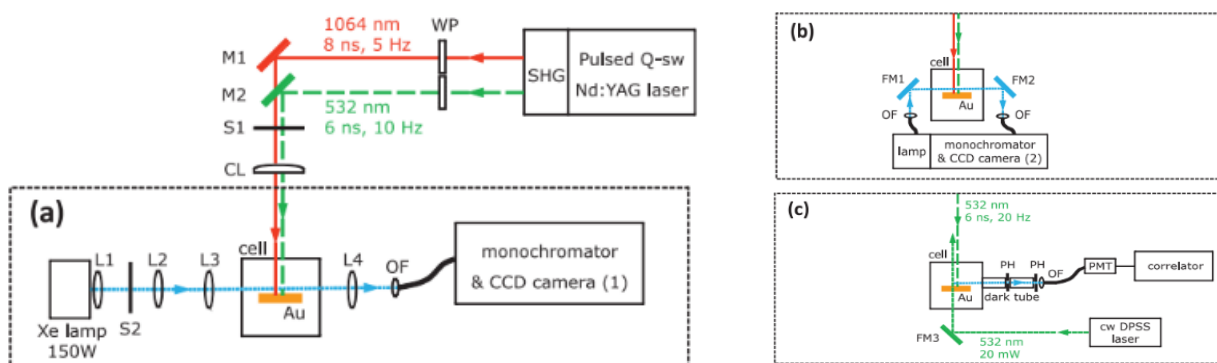


Figure 3.16 – Optical configuration for a three-spectrometer setup. (a) shows the transient absorption spectrometer, (b) the absorption spectrometer for long delay times and (c) the Dynamic Light Scattering Spectrometer. WP is a half-wave plate, M are reflecting mirrors, FM are flipping mirrors, S are shutters, CL are cylindrical lenses, L are lenses, OF are optical fibres, PH are pinholes. From reference <sup>71</sup>.

This kind of setup allows the collection of data from nanoseconds to hours after the ablation<sup>71</sup>.

**X-ray analysis.** This class of techniques, including principally small angle x-ray scattering (SAXS), provide detail on the condensed phase and high atomic weight materials<sup>3</sup>. The main problem is the necessity of extremely bright time-resolved sources, like synchrotron radiation<sup>3</sup>. The experimental setup for this technique is sketched in figure 3.17:

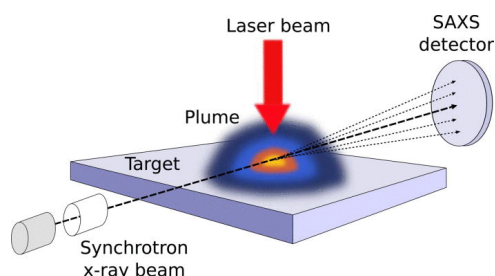


Figure 3.17 – Experimental setup for this technique. From reference <sup>72</sup>.

This analysis can give profound insights in the ablation mechanism, from providing information about bubble dynamics, to spatiotemporal particle distribution in the cavitation bubble, to temporal evolution of particle size, allowing detailed studies about the correlation of cavitation bubble dynamics and particle formation<sup>73, 74</sup>.

## 3.4 Parameters of Laser Ablation

**Laser pulse wavelength.** The effect of the wavelength in laser ablation is well documented<sup>64</sup>. The analysis of the phenomenon is by Jeon and Yeh<sup>75</sup>, who studied the ablation of silver nanoparticles in water and isopropanol with a Nd:YAG laser operating with an unfocused beam at 532 and 1064 nm. In their study, they found that at shorter wavelengths the nanoparticles were produced with an higher yield and were significantly bigger. They also

### 3. Laser Ablation Synthesis of Nanoparticles in Liquid Solution

found that focusing the laser, even using lower power and longer wavelength, gave higher yields and bigger nanoparticles. In table 3.3 are reported some of the data:

Wavelength (nm)	Laser intensity (mJ/cm <sup>2</sup> )	Solvent	Diameter (nm)	$\sigma$ (nm)
532	397	H <sub>2</sub> O	25.7	± 6.8
1064	397	H <sub>2</sub> O	16.3	± 21.7
1064 (focused)	247	H <sub>2</sub> O	32.9	± 9.6

Table 3.3 – Information regarding silver nanoparticles obtained varying wavelength and focalization. From reference 75.

However, further experiments by Tsuji et al, carried out by focusing the beam, proved the opposite<sup>30, 31, 76</sup>. The explanation to this apparent contradiction has been found by considering the absorption linked to the newly formed nanoparticles which form over the metal target: where these nanoparticles absorb more, less energy gets to the target and actually ablates it<sup>64</sup>. Besides, the absorption of silver NPs around 532 nm is larger than at 1064 nm, and the freshly obtained nanoparticles absorb a greater fraction of energy from the incoming laser beam, while being photofragmented<sup>77</sup>. Once we remove this disturbance from the analysis, the ablation efficiency is again increased by moving to shorter wavelength, due to the increased absorption efficiency of the metal target itself<sup>64</sup>.

There are two possible processes for this “colloidal self-absorption” process. In the first process, defined as *interpulse*, nanoparticles obtained from previous pulses absorb a portion of the following pulse. The second process, called *intrapulse*, considers the nanoparticles obtained during the same pulse as the source of this absorption, and it is considered a feasible process only for relatively long pulses, such as those of nanosecond, microsecond or millisecond lasers. A graphical explanation of these possible processes is reported in figure 3.18<sup>64</sup>:

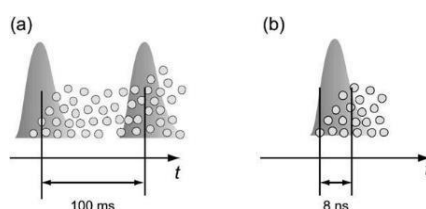


Figure 3.18: Possible laser light absorption mechanisms due to ablated nanoparticles in (a) interpulse and (b) intrapulse colloidal absorption processes. From reference 64.

An important effect is also played by the absorption coefficient of the material, since it determines the skin depth of the target. At shorter wavelengths the solids usually present an high absorption coefficient, and so it is possible to observe UV radiation absorbed with a good efficiency and in an uniform manner<sup>78</sup>, while IR radiation is usually absorbed by

### 3. Laser Ablation Synthesis of Nanoparticles in Liquid Solution

impurities and surface defects of the target<sup>78, 79</sup>. This means that the surface of the ablated area will be quite different: regularly eroded when subjected to UV ablation, with a more rugged surface when subjected to IR ablation<sup>3</sup>.

*Laser pulse duration.* The duration of the laser pulse, defined as  $\tau_L$ , has a noticeable influence on the ablation mechanism. Longer pulses favour thermal mechanisms of ablation over photoionization, as we have already shown in section 3.2<sup>12, 15, 29, 80, 81</sup>. To understand the differences among these regimes, it is important to look at the ablation craters. Figure 3.19 reports the images of ablation craters obtained with ablation pulses of different length<sup>1</sup>.

The first image shows the femtosecond crater where no trace of molten material are noticeable around the hole, excluding a dust ring. This kind of behaviour is explained considering the ablation as dominated by direct photoionization processes (see Section 3.2).

In the picosecond phase, the ablation borders are still visible, however the inner part of the ablation crater is not clean, and rings appear around the crater. In this ablation regime we have coexistence of photoionization processes and thermal ablation processes, like ejection of droplets or vaporization of the material.

In the nanosecond pulse, the material appears deposited around the borders, and an extensive “corona” linked to the pressure exerted by the inner part of the ablation plume is visible. In this regime the photoionization coexist with thermal ejection processes.

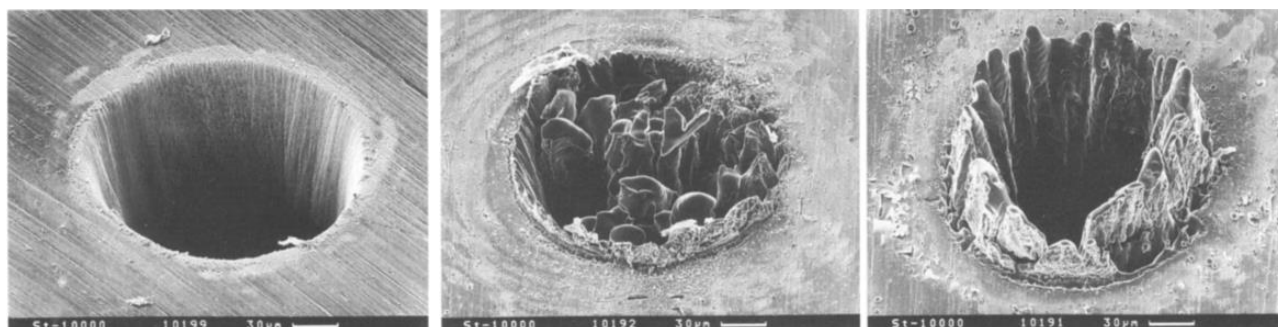


Figure 3.19 – Ablation spots obtained on 100  $\mu\text{m}$  steel foils with a 780nm  $\lambda$  laser, using different pulse lengths. (left) spot obtained with a 120 $\mu\text{J}$ , 200fs laser, (middle) image 900 $\mu\text{J}$ , 80ps, (right) 1mJ, 3.3ns. From reference 1.

*Laser Spot area.* Experimental measurements have shown that by increasing the ablation spot the nanoparticles size is larger, and the size distribution also increases<sup>82, 83</sup>. Explanation of this phenomenon has been attributed to the increase of energy on the target, causing the coexistence of different ablation mechanisms, which are associated to nanoparticles with a different size distribution<sup>78</sup>.

Data regarding the ablation yield as a function of spot size are shown in figure 3.20. From these data, it is possible to see that the nanoparticle yield is increased for larger spot sizes,

as a consequence of the increasing amount of laser energy delivered to the bulk target.

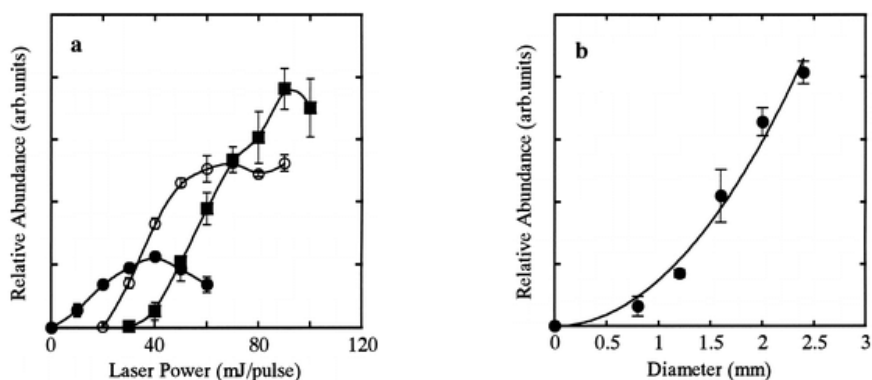


Figure 3.20 – (a) Relative abundance of silver nanoparticles obtained with different laser spot sizes (1.2 nm solid circle, 1.6 nm open circle, 2.4 nm solid square) with increasing power; (b) relative abundance of silver nanoparticles at different diameters with increasing laser spot size and constant fluence. From reference 82.

**Laser repetition rate.** Increasing the repetition rate of the laser is an easy way to improve the productivity of the ablation. The total quantity of removed material increases with the repetition rate, and since the average target temperature raises, the quantity of material that reaches the ablation threshold is increased as well<sup>84, 85</sup>. However this improvement only stands if the delay between two following laser pulses remains higher than the average bubble lifetime ( $10^{-3}$ - $10^{-4}$  s<sup>84</sup>). If this condition is not met, the efficiency of the ablation is lower than expected. This happens because the interface of the cavitation bubble introduces a discontinuity in the refractive index, and scatters the incoming laser light. Furthermore, the target surface is in contact with an hot vapour phase (the inner of the cavitation bubble), so the confining effect of the liquid on the plasma is not available. Besides, the presence of the previously ablated material inside the bubble reduces the laser power and favours the aggregation of the newly formed nanoparticles<sup>86</sup>. The effect of these conditions on productivity is shown in figure 3.21.

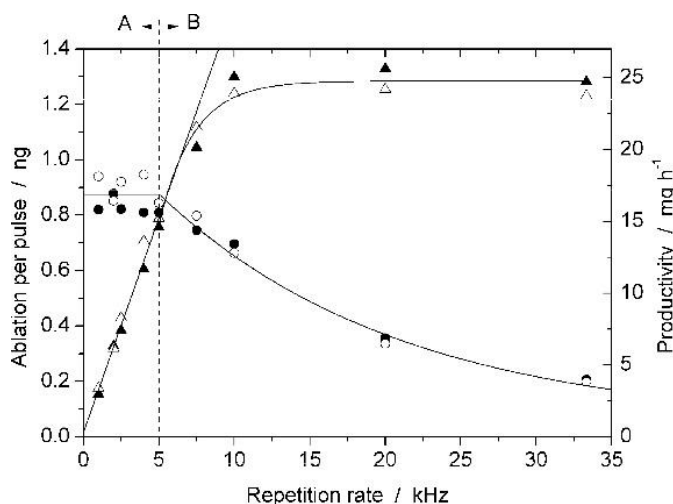


Figure 3.21 – Effect of the increase of repetition rate on the ablation yield for Zn in THF, with an energy pulse of 125  $\mu$ J.  $\circ$  reports the ablation yield per shot for 175  $\mu$ m spaced ablation pulses,  $\bullet$  for 125  $\mu$ m spaced pulses.  $\triangle$  reports the productivity for 175  $\mu$ m spaced ablation pulses,  $\blacktriangle$  for 125  $\mu$ m spaced ablation pulses. From reference 84.

### 3. Laser Ablation Synthesis of Nanoparticles in Liquid Solution

Increasing the ablation rate remains useful only until a certain threshold of the order of approximately 5 kHz. When this limit is surpassed, the increase in the ablation rate only compensates the reduced yield per shot.

*Number of laser shots.* This parameter is seldom considered, but aside from the obvious increase in productivity, there are several possible effects related to it. The sustained ablation on a single spot can induce modifications on the bulk target, both of chemical (formation of new compounds by interaction with the solvent or for thermodynamic reasons due to the high temperature and pressure) or physical (detachment of material and morphological changes) type<sup>9</sup>. In alloy targets, segregation of the components is theoretically possible due to the extreme conditions of the ablated area<sup>87</sup>.

*Effects of solute molecules.* Solutes can affect the solvent, the newly formed nanoparticles, or both. In the first case, one should consider the possibility of changes in solvent viscosity and density due to the addition of solutes at appreciably high concentration. These modifications can enhance the confinement of the plasma on the surface of the target, increasing the ablation yield<sup>33</sup>. An example of this effect is shown in figure 3.22, where it is possible to observe an increase in the ablation yield of Ag nanoparticles by increasing PVP concentration. The nanoparticles also showed a decrease in dimensions, due to surface coating with PVP.

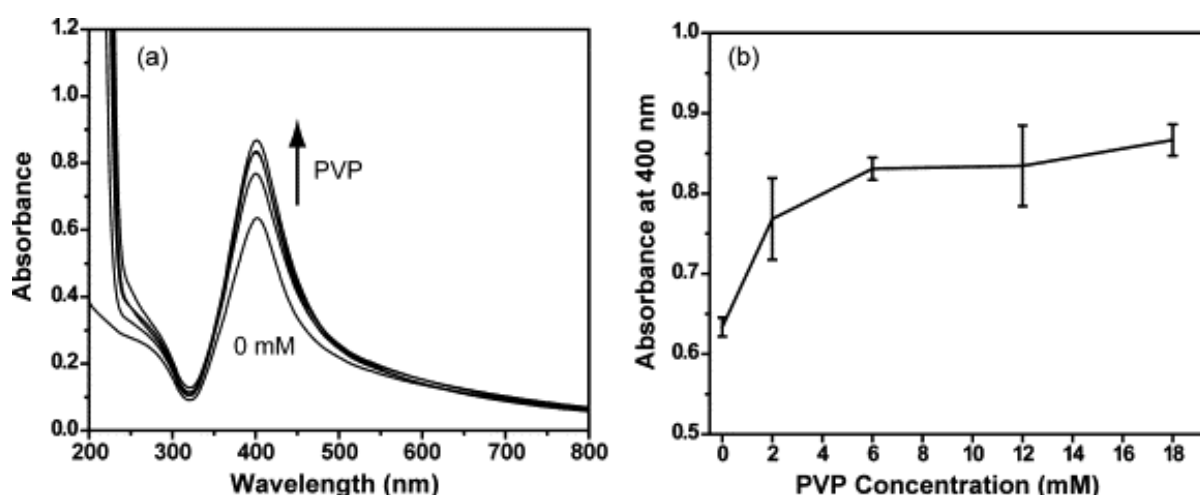


Figure 3.22 – (a) UV-Visible absorption spectra of silver nanoparticles obtained in water-polyvinylpyrrolidone solutions at growing concentrations (b) Change in ablation efficiency at different concentrations of PVP. From reference 33.

In fact, the most frequent effect of the solute molecules on the nanoparticles is the covering of the newly formed nanoparticle with a molecular layer functioning as a capping and stabilising agent, as shown in Figure 3.23a.

### 3. Laser Ablation Synthesis of Nanoparticles in Liquid Solution

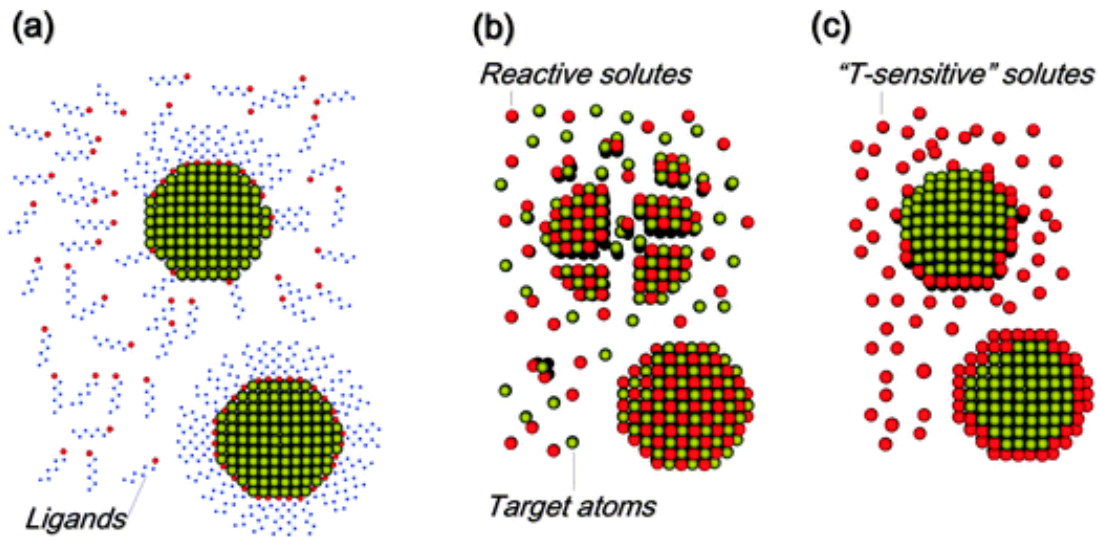


Figure 3.23 – (a) ligands are adsorbed on the surface of the nanoparticles, preventing growth and aggregation; (b) solute molecules react with the ablated material, to obtain nanoparticles with a composition different from the starting target; (c) the solute, sensitive to temperature, reacts on the extremely hot surface of the newly formed nanoparticles to give new materials. From reference 3.

An example of this interaction is the addition of organic molecules to gold solutions, to promote the aggregation of nanoparticles in different fashions, as shown in figure 3.24, where is reported the strong effect of different concentrations of dextran on the dimensional distribution of the nanoparticles, effectively preventing their size growth.

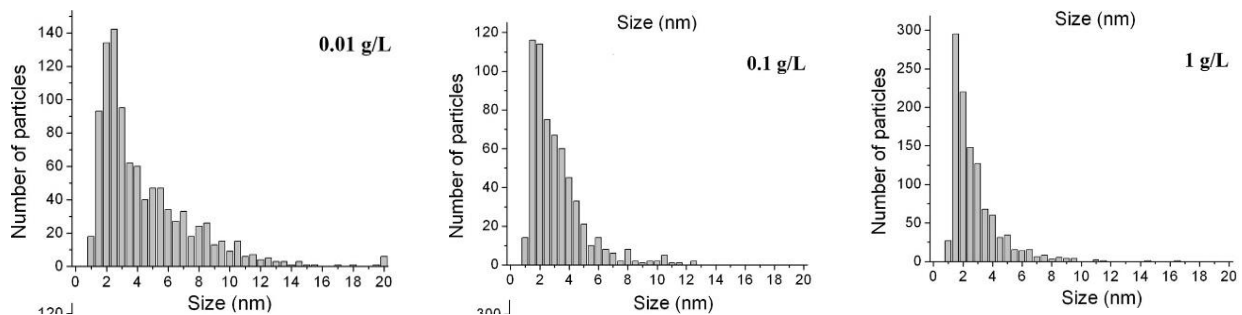


Figure 3.24 – Dimensional distribution of gold nanoparticles obtained by femtosecond ablation in a solution of water/dextran at differing concentrations. From reference 88.

A different possibility is having solutes that can actually interact with the ablated material to form new compounds (Figure 3.23b). An example of this behaviour is the ablation of gold nanoparticles in water with the addition of chloride salts such as KCl and NaCl. Nanoparticles obtained in this way have an enhanced  $\zeta$ -potential due to the creation of Au-Cl bonds with concomitant breakage of the surface Au-O-Au bonds into Au-O<sup>-</sup>, and thus result in more stable nanoparticles<sup>34</sup>.

The last possibility is to use temperature-sensitive compounds, such as metal salts, that spontaneously react with the nanoparticle due to their higher temperature compared to ambient conditions (Figure 3.23c). Interestingly, this has been used to promote the creation

### 3. Laser Ablation Synthesis of Nanoparticles in Liquid Solution

of core-shell structures with Au-Ag alloy core and silica shell such as that shown in figure 3.25.<sup>89</sup>

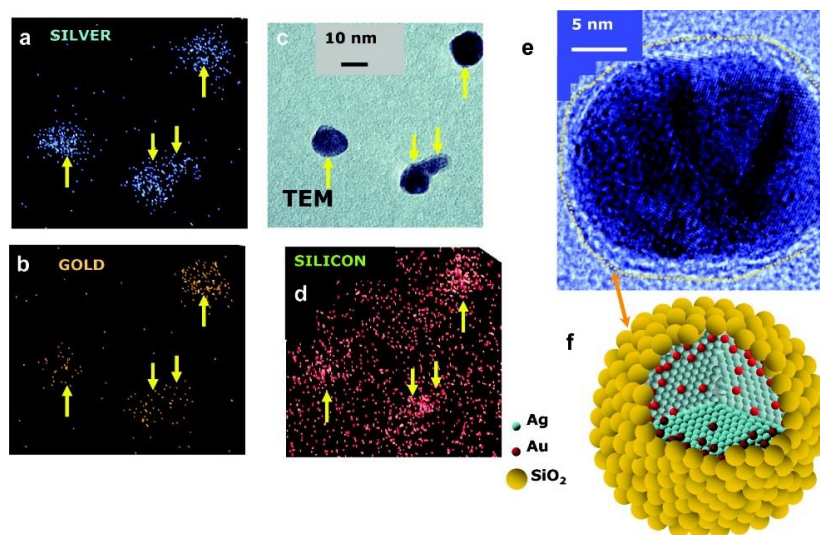


Figure 3.25 – (a,b,d) EDX images of nanoparticles obtained via ablation of a silver target in water with  $\text{AgNO}_3$  and  $\text{HAuCl}_4$ . (c,e) TEM image of the nanoparticles, showing the silica shell. (f) Graphical representation of the nanoparticle. From reference 89.

**Effect of temperature and pressure.** Liquid temperature may have effects on viscosity, density, refractive index, surface tension and compressibility, possibly modifying efficiency of laser irradiation, plasma plume confinement and the dynamics of the cavitation bubble<sup>90-93</sup>. Menéndez-Manjón et al. have shown that varying the temperature can have important effects on the hydrodynamic size of gold nanoparticles aggregates, due to variation of the liquid compressibility<sup>93</sup>. However, due to the huge temperatures and pressures reached during the ablation process, it is expected that only minor effects on nanoparticles formation will derive from liquid temperature and pressure.

Ablation in extremely high pressures can be achieved by using specialized setup. Gold and silicon ablations have been carried out at high pressures in supercritical fluids such as  $\text{CO}_2$  and  $\text{CHF}_3$  but the only significant difference discovered is an average larger size of the nanoparticles, probably due to a more effective ablation efficiency linked to the more effective confinement of the plasma on the crater<sup>94-96</sup>. The nanoparticles obtained at high pressure are more efficiently cooled<sup>96</sup> and the duration and maximum dimension of the bubble decrease<sup>97</sup>, but how these effects may influence the final result is unclear.

**Effects of solvent and target.** The solvent has a strong effect on the composition and structure of laser generated nanoparticles. Amendola et al.<sup>3</sup> carried out laser ablation of various combinations of targets and solvents with a 1064nm nanosecond laser with a pulse



power of 10 J/cm<sup>2</sup>. TEM images of the results are shown in figure 3.26:

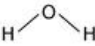

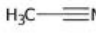
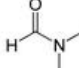

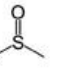
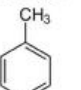
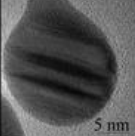
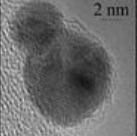
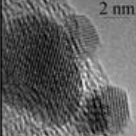
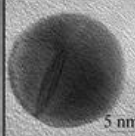
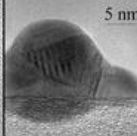
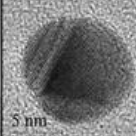
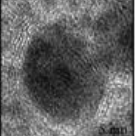
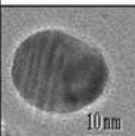
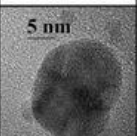
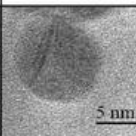
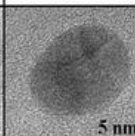
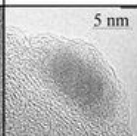
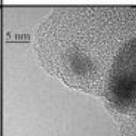

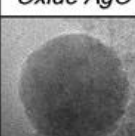
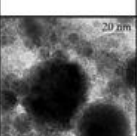
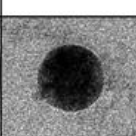
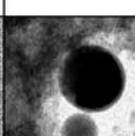
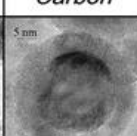
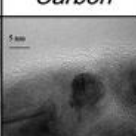
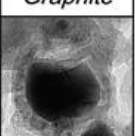
Target ↓ Solvent ↑	Water 	Ethanol 	Acetonitrile 	Dimethyl- formamide 	Tetra- hydrofuran 	Dimethyl- sulfoxide 	Toluene 
<b>Au</b>	 5 nm <i>Metal Au</i>	 2 nm <i>Metal Au</i>	 2 nm <i>Metal Au</i>	 5 nm <i>Metal Au</i>	 5 nm <i>Metal Au</i>	 5 nm <i>Metal Au</i>	 5 nm <i>Metal Au/ Graphite</i>
<b>Ag</b>	 10 nm <i>Metal Ag/ Oxide AgO</i>	 5 nm <i>Metal Ag</i>	 5 nm <i>Metal Ag</i>	 5 nm <i>Metal Ag</i>	 5 nm <i>Metal Ag/ Carbon</i>	 5 nm <i>Metal Ag/ Carbon</i>	 5 nm <i>Metal Ag/ Graphite</i>
<b>Fe</b>	 10 nm <i>Fe<sub>3</sub>O<sub>4</sub>, Fe<sub>2</sub>O<sub>3</sub>, Fe(OOH)<sub>2</sub></i>	 20 nm <i>Fe<sub>3</sub>O<sub>4</sub>, FeC<sub>3</sub></i>	 10 nm <i>Fe<sub>3</sub>O<sub>4</sub>, Carbon</i>	 20 nm <i>Fe<sub>3</sub>O<sub>4</sub>, Carbon</i>	 5 nm <i>Metal Fe/ Fe<sub>3</sub>O<sub>4</sub></i>	 5 nm <i>Metal Fe/ Carbon</i>	 10 nm <i>Fe-Carbide/ Graphite</i>

Figure 3.26 – TEM images of the nanoparticles obtained by laser ablation of three bulk materials in different solvents. From reference 3.

Gold is one of the best known materials in laser ablation. Its characteristic colour and stability have prompted many researchers to probe the reasons for its peculiar properties, finding Au-O bonds on the surface<sup>34, 98</sup>. Surface oxidation, visible as Au(I) atoms, has been detected on the surface of the nanoparticle, so the conditions during the ablation are probably strongly oxidizing. It has also been found that fluxing the ablation solutions with nitrogen or argon has a stabilizing effect on the nanoparticles solution, therefore atmospheric CO<sub>2</sub> or O<sub>2</sub> might possibly have a negative effect on the oxidization process of the nanoparticle during the ablation, possibly due to electron scavenging<sup>99</sup>.

Ablation carried out in ethanol, tetrahydrofuran (THF), dimethylsulphoxide (DMSO), acetonitrile, and dimethylformamide (DMF) gives as result crystalline nanoparticles, but the average size is smaller than those of the nanoparticles obtained in water and there is an higher fraction of aggregated or otherwise non-spherical nanoparticles<sup>100, 101</sup>. Furthermore, gold nanoparticles obtained in organic solvents are usually less stable on the long term than the ones obtained in water<sup>100, 101</sup>. This effect could be attributed to the reduced ablation efficiency in organic solvents or to the capping effect of organic by-products generated during the ablation. The first hypothesis can be discarded because the yield in organic solvents is equal or even slightly superior to the one in water. Furthermore, Raman analysis



### 3. Laser Ablation Synthesis of Nanoparticles in Liquid Solution

by Compagnini et al. has shown that laser ablation in organic solvents can produce polyynes, that are adsorbed on the surface of the nanoparticles<sup>102, 103</sup>. The formation of non-spherical particles is probably the best confirmation of this behaviour, since these molecules cannot interfere with the formation of the gold lattice, but can prevent its growth by preferential adsorption along certain crystallographic directions. Another negative factor substantially impacting the stability of these nanoparticles is their dielectric constant, significantly lower compared to the one of water<sup>104</sup>.

Nanoparticles obtained in acetone and ethanol behave differently, because formation of enolates in the former case<sup>105</sup> and alcoholates in the latter was reported<sup>106</sup>. These molecules are negatively charged and may improve the stability of the nanoparticles if they form complexes on the surface of the metal.

The products of laser ablation in toluene show nanoparticles that are very small (average size is 1 nm) and embedded in an extended carbon matrix. Since there is no reactivity between carbon and gold, the nanoparticles probably act as starting sites for the graphitization process of the solvent, and this produces a graphitic matrix that rapidly stops nanoparticles growth.

Chloroform has a different effect, since the only ablation result is gold chloride ( $\text{AuCl}_3$ ), and no nanoparticles are observed<sup>107</sup>. This means that temperature and pressure in the reaction environment are above the Au-Cl reaction threshold.

*Silver* is a particularly interesting metal for laser ablation in different solvents, since it is a noble metal with very scarce reactivity with carbon, but has standard reduction potential for  $\text{Ag}/\text{Ag}^+$  0.8 eV, quite low when compared to the 1.69 eV of  $\text{Au}/\text{Au}^+$ . This higher reactivity produces appreciable effects even when the ablation takes place in water, since the resulting nanoparticles are crystalline silver with a thin shell of  $\text{Ag}_2\text{O}$ , that slowly increases in thickness with ageing<sup>49</sup>.

When the ablation is carried out in ethanol, acetonitrile, and DMF, the final results are similar to those obtained for gold: nanoparticles with reduced dimensions and an higher percentage of non-spherical or aggregate nanoparticles<sup>2, 99, 102</sup>.

Ablation of silver in THF results in nanoparticles with amorphous carbon shells. The dimension of the nanoparticles, however, remains consistent with that of silver nanoparticles obtained in other organic media. This means that the nanoparticles immediately after the formation and growth of the nuclei are still hot enough to enact pyrolysis of the solvent<sup>2, 108</sup>. In DMSO the results is similar, but an extended carbon matrix is visible, not a simple shell.

### 3. Laser Ablation Synthesis of Nanoparticles in Liquid Solution

This means that solvent degradation takes place while the nanoparticles are still forming, and not after their coalescence<sup>2</sup>. The substantial differences of the ablation results from gold might be due to the lower content of free oxygen available in the ablation area (an higher amount of oxygen would react with silver to give silver oxide), promoting the growth of amorphous carbon networks instead of the isolated oxidised by-products found in the gold syntheses. This observation is substantiated by experiments carried out ablating silver with ps pulses in fluxed tetrahydrofuran, which produced nanoparticles without amorphous shell<sup>109</sup>. This means that the ablation by-products probably accumulate in the solution liquid and not on the nanoparticles, allowing the formation of the amorphous structures seen in some samples; furthermore the use of ultrashort pulses helps in avoiding pyrolysis of the solvent, since the ablation mechanisms are different and the plasma plume does not overlap with the laser pulse.

Ablation in toluene and chloroform gives the same results obtained with gold<sup>107, 110</sup>.

*Iron* can react with oxygen and carbon to form (respectively) various oxides and carbides, and its reduction potentials are -0.41 V for the  $\text{Fe}^{2+}/\text{Fe}^+$  couple and 0.77 V for the  $\text{Fe}^{3+}/\text{Fe}^{2+}$  couple. In water, hydroxide or mixed oxide/hydroxide phases can be obtained (both crystalline and amorphous). In fact, when the ablation takes place in water, the obtained nanoparticles are composed of polycrystalline iron oxide, embedded in an amorphous hydroxide matrix<sup>111, 112</sup>. The composition of nanoparticles obtained in this medium has been shown to be (in weight) 75%  $\text{Fe}_3\text{O}_4$ , 22%  $\alpha\text{-Fe}_2\text{O}_3$ , ~2% of FeO and ~1% of Fe<sup>111</sup>, but variations are possible when local temperature and pressure change. Studying the obtained nanoparticles is an excellent way to understand the dynamics of ablation: the amorphous iron hydroxide network is created by direct reaction of extracted atoms with excess water and oxygen. However, heating Fe hydroxides above 250K yields iron oxides of various structures<sup>112-114</sup>, so this external phase must be formed in less extreme conditions than those of the plasma bubble, for example when the nanoparticles is cooling down by moving towards the solution. Another interesting information can be gained from the higher content of  $\text{Fe}_3\text{O}_4$  compared to the  $\alpha\text{-Fe}_2\text{O}_3$ , since this means that the concentration of iron and oxygen is very similar but the formation conditions are less extreme ( $\alpha\text{-Fe}_2\text{O}_3$  forms at higher temperature and in more oxidizing environments). If we consider that the metal Fe phases that are discovered in the nanoparticles are often hundreds of nm big while the iron oxide domains are 3-10 nm large, we can hypothesize that the metal iron domains derives from the detachment of particularly large fragments while the smaller iron oxide domains result from nucleation and growth of vaporized material.

### 3. Laser Ablation Synthesis of Nanoparticles in Liquid Solution

If the ablation is carried out in ethanol, there are two types of visible nanoparticles:  $\text{Fe}_3\text{O}_4$  smaller than 5 nm, and  $\text{FeC}_3$  bigger than 10 nm. The origins of the latter are debated: the target might be modified during the ablation process to iron carbide and so the  $\text{FeC}_3$  nanoparticle might be the result of direct ablation of the modified target, or they might form in areas of the plasma plume where the temperature and concentration of pyrolysed ethanol molecules are high enough to warrant their formation<sup>115</sup>.

The ablation in acetonitrile and DMF produces mainly  $\text{Fe}_3\text{O}_4$  nanoparticles, but hydroxide is not found, due to the trace amount of water available in the solvent<sup>116</sup>. On the other hand, amorphous carbon can be found as a by-product of ablation, although it does not contain nanoparticles on the inside. It is also important to point out that no iron carbides have been found, probably due to a larger reactivity of carbon with oxygen than with the iron atoms.

In tetrahydrofuran about a 20% of  $\text{Fe}_3\text{O}_4$  nanoparticles are obtained, but the remaining 80% of nanoparticles is composed of  $\text{Fe}@Fe_3\text{O}_4$  structures<sup>116</sup>. The reduced thickness of the iron oxide shell may be due to the extremely quick reaction of the solvent molecules with free carbon and oxygen atoms. Alternatively, the core may be formed by ejected droplets from the target, probably due to a different behaviour of the ablation in THF. However the properties of THF are not different enough to warrant this kind of difference, and in the other metals there is no such difference, so this hypothesis is more difficult to explain.

In DMSO the result is similar to silver: metal iron nanoparticle in an amorphous carbon matrix<sup>116</sup>. This result suggests that to have this kind of final structure it is necessary to have metal with low reduction potentials.

Laser ablation of iron in toluene results in graphitic matrix containing amorphous iron carbide nanoparticles<sup>116</sup>, probably because the reaction by-products are more reactive than the ones obtained in DMSO.

## 3.5 Bibliography

- 1 B. Chichkov, C. Momma, S. Nolte, F. Von Alvensleben and A. Tünnermann, *Applied Physics A*, 1996, **63**, 109-115.
- 2 V. Amendola, S. Polizzi and M. Meneghetti, *Langmuir*, 2007, **23**, 6766-6770.
- 3 V. Amendola and M. Meneghetti, *Physical Chemistry Chemical Physics*, 2013, **15**, 3027-3046.
- 4 L. Berthe, R. Fabbro, P. Peyre and E. Bartnicki, *J. Appl. Phys.*, 1999, **85**, 7552-7555.
- 5 L. Berthe, R. Fabbro, P. Peyre, L. Tollier and E. Bartnicki, *J. Appl. Phys.*, 1997, **82**, 2826-2832.
- 6 L. Berthe, R. Fabbro, P. Peyre and E. Bartnicki, *The European Physical Journal Applied Physics*, 1998, **3**, 215-218.
- 7 F. Cottet and M. Boustie, *J. Appl. Phys.*, 1989, **66**, 4067-4073.
- 8 L. J. Radziemski and D. A. Cremers, 1989, .
- 9 W. T. Nichols, T. Sasaki and N. Koshizaki, *J. Appl. Phys.*, 2006, **100**, 114913.

### 3. Laser Ablation Synthesis of Nanoparticles in Liquid Solution

- 10 C. Momma, B. N. Chichkov, S. Nolte, F. von Alvensleben, A. Tünnermann, H. Welling and B. Wellegehausen, *Opt. Commun.*, 1996, **129**, 134-142.
- 11 D. Von der Linde, K. Sokolowski-Tinten and J. Bialkowski, *Appl. Surf. Sci.*, 1997, **109**, 1-10.
- 12 P. Lorazo, L. J. Lewis and M. Meunier, *Physical Review B*, 2006, **73**, 134108.
- 13 D. Perez and L. Lewis, *Applied Physics A*, 2004, **79**, 987-990.
- 14 D. Perez and L. J. Lewis, *Phys. Rev. Lett.*, 2002, **89**, 255504.
- 15 D. Perez and L. J. Lewis, *Physical Review B*, 2003, **67**, 184102.
- 16 H. Luo, G. Ciccotti, M. Mareschal, M. Meyer and B. Zappoli, *Physical Review E*, 1995, **51**, 2013.
- 17 M. W. Maddox, G. Goodyear and S. C. Tucker, *The Journal of Physical Chemistry B*, 2000, **104**, 6248-6257.
- 18 S. Toxvaerd, *Physical Review E*, 1998, **58**, 704.
- 19 D. Perez, L. J. Lewis, P. Lorazo and M. Meunier, *Appl. Phys. Lett.*, 2006, **89**, 141907.
- 20 T. E. Itina, *The Journal of Physical Chemistry C*, 2010, **115**, 5044-5048.
- 21 T. Tsuji, Y. Okazaki, Y. Tsuboi and M. Tsuji, *Japanese journal of applied physics*, 2007, **46**, 1533.
- 22 Y. Tomita, M. Tsubota and N. An-Naka, *J. Appl. Phys.*, 2003, **93**, 3039-3048.
- 23 T. Sakka, S. Iwanaga, Y. H. Ogata, A. Matsunawa and T. Takemoto, *J. Chem. Phys.*, 2000, **112**, 8645-8653.
- 24 T. Sakka, K. Takatani, Y. H. Ogata and M. Mabuchi, *J. Phys. D*, 2002, **35**, 65.
- 25 N. Bulgakova and A. Bulgakov, *Applied Physics A*, 2001, **73**, 199-208.
- 26 Z. Zhang and G. Gogos, *Physical Review B*, 2004, **69**, 235403.
- 27 B. Toftmann, J. Schou and J. Lunney, *Physical Review B*, 2003, **67**, 104101.
- 28 J. Yoo, S. Jeong, X. Mao, R. Greif and R. Russo, *Appl. Phys. Lett.*, 2000, **76**, 783-785.
- 29 D. Perez, L. K. Béland, D. Deryng, L. J. Lewis and M. Meunier, *Physical Review B*, 2008, **77**, 014108.
- 30 T. Tsuji, K. Iryo, H. Ohta and Y. Nishimura, *Japanese Journal of Applied Physics*, 2000, **39**, L981.
- 31 T. Tsuji, K. Iryo, N. Watanabe and M. Tsuji, *Appl. Surf. Sci.*, 2002, **202**, 80-85.
- 32 T. Tsuji, Y. Tsuboi, N. Kitamura and M. Tsuji, *Appl. Surf. Sci.*, 2004, **229**, 365-371.
- 33 T. Tsuji, D. Thang, Y. Okazaki, M. Nakanishi, Y. Tsuboi and M. Tsuji, *Appl. Surf. Sci.*, 2008, **254**, 5224-5230.
- 34 J. Sylvestre, S. Poulin, A. V. Kabashin, E. Sacher, M. Meunier and J. H. Luong, *The Journal of Physical Chemistry B*, 2004, **108**, 16864-16869.
- 35 C. Wang, P. Liu, H. Cui and G. Yang, *Appl. Phys. Lett.*, 2005, **87**, 201913.
- 36 Z. Yan and D. B. Chrisey, *Journal of Photochemistry and Photobiology C: Photochemistry Reviews*, 2012, **13**, 204-223.
- 37 V. Carey, *Vapor-Liquid Phase Change Phenomena: An Introduction to the Thermophysics of Vaporization and Condensation Processes in Heat Transfer Equipment*, Taylor & Francis, New York, 2008.
- 38 K. Sasaki and N. Takada, *Pure and Applied Chemistry*, 2010, **82**, 1317-1327.
- 39 Z. Yan, R. Bao, C. M. Busta and D. B. Chrisey, *Nanotechnology*, 2011, **22**, 265610.
- 40 C. E. Brennen, *Cavitation and bubble dynamics*, Cambridge University Press, 2013.
- 41 W. Lauterborn, T. Kurz, R. Mettin and C. Ohl, *Advances in chemical physics*, 1999, **110**, 295-380.
- 42 N. Takada, T. Nakano and K. Sasaki, *Applied Physics A*, 2010, **101**, 255-258.
- 43 M. Tillack, D. Blair and S. Harilal, *Nanotechnology*, 2004, **15**, 390.
- 44 Y. Nakata, J. Muramoto, T. Okada and M. Maeda, *J. Appl. Phys.*, 2002, **91**, 1640-1643.
- 45 J. Muramoto, T. Inmaru, Y. Nakata, T. Okada and M. Maeda, *Appl. Phys. Lett.*, 2000, **77**, 2334-2336.
- 46 D. B. Geohegan, A. A. Puretzky, G. Duscher and S. J. Pennycook, *Appl. Phys. Lett.*, 1998, **72**, 2987-2989.
- 47 Z. Yan, R. Bao and D. B. Chrisey, *Langmuir*, 2010, **27**, 851-855.
- 48 H. Zeng, W. Cai, Y. Li, J. Hu and P. Liu, *The Journal of Physical Chemistry B*, 2005, **109**, 18260-18266.
- 49 V. Amendola and M. Meneghetti, *Physical chemistry chemical physics*, 2009, **11**, 3805-3821.
- 50 L. J. Radziemski and D. A. Cremers, in *Laser-induced plasmas and applications*, ed. anonymous, 1989.
- 51 A. De Giacomo, M. Dell'Aglio, O. De Pascale and M. Capitelli, *Spectrochimica Acta Part B: Atomic Spectroscopy*, 2007, **62**, 721-738.
- 52 N. Omenetto, *J. Anal. At. Spectrom.*, 1998, **13**, 385-399.
- 53 E. Tognoni, V. Palleschi, M. Corsi and G. Cristoforetti, *Spectrochimica Acta Part B: Atomic Spectroscopy*, 2002, **57**, 1115-1130.
- 54 D. Rusak, B. Castle, B. Smith and J. Winefordner, *TrAC Trends in Analytical Chemistry*, 1998, **17**, 453-461.
- 55 M. Corsi, G. Cristoforetti, M. Hidalgo, S. Legnaioli, V. Palleschi, A. Salvetti, E. Tognoni and C. Vallebona, *Appl. Geochem.*, 2006, **21**, 748-755.
- 56 A. Casavola, A. De Giacomo, M. Dell'Aglio, F. Taccogna, G. Colonna, O. De Pascale and S. Longo, *Spectrochimica Acta Part B: Atomic Spectroscopy*, 2005, **60**, 975-985.
- 57 A. Pichahchy, D. Cremers and M. Ferris, *Spectrochimica Acta Part B: Atomic Spectroscopy*, 1997, **52**, 25-39.
- 58 A. A. Bol'Shakov, J. H. Yoo, C. Liu, J. R. Plumer and R. E. Russo, *Appl. Opt.*, 2010, **49**, C132-C142.
- 59 S. Klein, J. Hildenhausen, K. Dickmann, T. Stratoudaki and V. Zafirooulos, *Journal of Cultural Heritage*, 2000, **1**, S287-S292.

### 3. Laser Ablation Synthesis of Nanoparticles in Liquid Solution

- 60 V. Lazic, F. Colao, R. Fantoni and V. Spizzicchino, *Spectrochimica Acta Part B: Atomic Spectroscopy*, 2005, **60**, 1014-1024.
- 61 A. Bogaerts and Z. Chen, *Spectrochimica Acta Part B: Atomic Spectroscopy*, 2005, **60**, 1280-1307.
- 62 B. Sallé, D. A. Cremers, S. Maurice, R. C. Wiens and P. Fichet, *Spectrochimica Acta Part B: Atomic Spectroscopy*, 2005, **60**, 805-815.
- 63 A. Casavola, G. Colonna, A. D. Giacomo and M. Capitelli, *J. Thermophys. Heat Transfer*, 2003, **17**, 225-231.
- 64 G. Yang, *Laser ablation in liquids: principles and applications in the preparation of nanomaterials*, CRC Press, 2012.
- 65 S. Heiroth, J. Koch, T. Lippert, A. Wokaun, D. Günther, F. Garrelie and M. Guillermin, *J. Appl. Phys.*, 2010, **107**, 014908.
- 66 W. Soliman, N. Takada and K. Sasaki, *Applied physics express*, 2010, **3**, 035201.
- 67 Y. Cai and N. Cheung, *Microchemical Journal*, 2011, **97**, 109-112.
- 68 N. Cheung and E. S. Yeung, *Appl. Spectrosc.*, 1993, **47**, 882-886.
- 69 K. Nahen and A. Vogel, *Lasers Surg. Med.*, 1999, **25**, 69-78.
- 70 S. L. Lui, *Spectrochemical analysis of solid samples using resonance-enhanced laser-induced plasma spectroscopy*, Hong Kong Baptist University, 2005.
- 71 S. Wei and K. Saitow, *Rev. Sci. Instrum.*, 2012, **83**, 073110.
- 72 L. Lavisse, J. Le Garrec, L. Hallo, J. Jouvard, S. Carles, J. Perez, J. Mitchell, J. Decloux, M. Girault and V. Potin, *Appl. Phys. Lett.*, 2012, **100**, 164103.
- 73 P. Wagener, S. Ibrahimkutty, A. Menzel, A. Plech and S. Barcikowski, *Physical Chemistry Chemical Physics*, 2013, **15**, 3068-3074.
- 74 S. Ibrahimkutty, P. Wagener, A. Menzel, A. Plech and S. Barcikowski, *Appl. Phys. Lett.*, 2012, **101**, 103104.
- 75 J. Jeon and C. Yeh, *J. Chin. Chem. Soc.*, 1998, **45**, 721-726.
- 76 T. Tsuji, K. Iryo, Y. Nishimura and M. Tsuji, *J. Photochem. Photobiol. A.*, 2001, **145**, 201-207.
- 77 P. V. Kamat, M. Flumiani and G. V. Hartland, *The Journal of Physical Chemistry B*, 1998, **102**, 3123-3128.
- 78 W. T. Nichols, T. Sasaki and N. Koshizaki, *J. Appl. Phys.*, 2006, **100**, 114911.
- 79 Z. Lin, E. Leveugle, E. M. Bringa and L. V. Zhigilei, *The Journal of Physical Chemistry C*, 2009, **114**, 5686-5699.
- 80 L. V. Zhigilei, Z. Lin and D. S. Ivanov, *The Journal of Physical Chemistry C*, 2009, **113**, 11892-11906.
- 81 P. Lorazo, L. J. Lewis and M. Meunier, *Phys. Rev. Lett.*, 2003, **91**, 225502.
- 82 F. Mafuné, J. Kohno, Y. Takeda, T. Kondow and H. Sawabe, *The Journal of Physical Chemistry B*, 2000, **104**, 9111-9117.
- 83 M. A. Sobhan, M. Ams, M. J. Withford and E. M. Goldys, *Journal of Nanoparticle Research*, 2010, **12**, 2831-2842.
- 84 P. Wagener, A. Schwenke, B. N. Chichkov and S. Barcikowski, *The Journal of Physical Chemistry C*, 2010, **114**, 7618-7625.
- 85 C. L. Sajti, R. Sattari, B. N. Chichkov and S. Barcikowski, *The Journal of Physical Chemistry C*, 2010, **114**, 2421-2427.
- 86 Z. Yan, R. Bao, Y. Huang, A. Caruso, S. B. Qadri, C. Z. Dinu and D. B. Chrisey, *The Journal of Physical Chemistry C*, 2010, **114**, 3869-3873.
- 87 L. Rehn, P. Okamoto, D. Potter and H. Wiedersich, *J. Nucl. Mater.*, 1978, **74**, 242-251.
- 88 S. Besner, A. V. Kabashin, F. M. Winnik and M. Meunier, *The Journal of Physical Chemistry C*, 2009, **113**, 9526-9531.
- 89 E. Jiménez, K. Abderrafi, R. Abargues, J. L. Valdés and J. P. Martínez-Pastor, *Langmuir*, 2010, **26**, 7458-7463.
- 90 D. G. Shchukin and H. Möhwald, *Physical Chemistry Chemical Physics*, 2006, **8**, 3496-3506.
- 91 Z. Yan, R. Bao, Y. Huang and D. B. Chrisey, *The Journal of Physical Chemistry C*, 2010, **114**, 11370-11374.
- 92 R. Zhao, R. Xu, Z. Shen, J. Lu and X. Ni, *Optics & Laser Technology*, 2007, **39**, 968-972.
- 93 A. Menéndez-Manjón, B. N. Chichkov and S. Barcikowski, *The Journal of Physical Chemistry C*, 2010, **114**, 2499-2504.
- 94 K. Saitow, Y. Okamoto and Y. F. Yano, *The Journal of Physical Chemistry C*, 2012, **116**, 17252-17258.
- 95 K. Saitow, T. Yamamura and T. Minami, *The Journal of Physical Chemistry C*, 2008, **112**, 18340-18349.
- 96 K. Saitow, *The Journal of Physical Chemistry B*, 2005, **109**, 3731-3733.
- 97 K. Sasaki, T. Nakano, W. Soliman and N. Takada, *Applied Physics Express*, 2009, **2**, 046501.
- 98 H. Muto, K. Yamada, K. Miyajima and F. Mafuné, *The Journal of Physical Chemistry C*, 2007, **111**, 17221-17226.
- 99 D. Werner, S. Hashimoto, T. Tomita, S. Matsuo and Y. Makita, *The Journal of Physical Chemistry C*, 2008, **112**, 1321-1329.
- 100 V. Amendola, S. Polizzi and M. Meneghetti, *The Journal of Physical Chemistry B*, 2006, **110**, 7232-7237.
- 101 G. Compagnini, A. Scalisi and O. Puglisi, *J. Appl. Phys.*, 2003, **94**, 7874-7877.

### 3. Laser Ablation Synthesis of Nanoparticles in Liquid Solution

- 102 G. Compagnini, G. Patane, L. D'Urso, O. Puglisi, R. S. Cataliotti and B. Pignataro, *The Journal of Physical Chemistry C*, 2008, **112**, 20301-20306.
- 103 L. D'Urso, G. Grasso, E. Messina, C. Bongiorno, V. Scuderi, S. Scalese, O. Puglisi, G. Spoto and G. Compagnini, *The Journal of Physical Chemistry C*, 2009, **114**, 907-915.
- 104 P. Boyer and M. Meunier, *The Journal of Physical Chemistry C*, 2012, **116**, 8014-8019.
- 105 E. Giorgetti, M. Muniz-Miranda, P. Marsili, D. Scarpellini and F. Giammanco, *Journal of Nanoparticle Research*, 2012, **14**, 1-13.
- 106 G. Cristoforetti, E. Pitzalis, R. Spiniello, R. Ishak, F. Giammanco, M. Muniz-Miranda and S. Caporali, *Appl. Surf. Sci.*, 2012, **258**, 3289-3297.
- 107 G. Compagnini, A. A. Scalisi and O. Puglisi, *Phys.Chem.Chem.Phys.*, 2002, **4**, 2787-2791.
- 108 V. Amendola, O. M. Bakr and F. Stellacci, *Plasmonics*, 2010, **5**, 85-97.
- 109 A. Schwenke, P. Wagener, S. Nolte and S. Barcikowski, *Applied Physics A*, 2011, **104**, 77-82.
- 110 V. Amendola, S. Polizzi and M. Meneghetti, *Science of Advanced Materials*, 2012, **4**, 497-500.
- 111 V. Amendola, M. Meneghetti, G. Granozzi, S. Agnoli, S. Polizzi, P. Riello, A. Boscaini, C. Anselmi, G. Fracasso and M. Colombatti, *Journal of Materials Chemistry*, 2011, **21**, 3803-3813.
- 112 V. Amendola, P. Riello, S. Polizzi, S. Fiameni, C. Innocenti, C. Sangregorio and M. Meneghetti, *Journal of Materials Chemistry*, 2011, **21**, 18665-18673.
- 113 T. Sugimoto and E. Matijević, *J. Colloid Interface Sci.*, 1980, **74**, 227-243.
- 114 H. Yokoi and T. Kantoh, *Bull. Chem. Soc. Jpn.*, 1993, **66**, 1536-1541.
- 115 R. Sergienko, E. Shibata, Z. Akase, H. Suwa, T. Nakamura and D. Shindo, *Mater. Chem. Phys.*, 2006, **98**, 34-38.
- 116 V. Amendola, P. Riello and M. Meneghetti, *The Journal of Physical Chemistry C*, 2010, **115**, 5140-5146.

### 3. Laser Ablation Synthesis of Nanoparticles in Liquid Solution

# Chapter 4

## Gold-Iron alloy nanoparticles

### 4.1 Abstract

In literature there are no reliable evidences that gold-iron alloys were synthesized in liquid environment by wet chemistry methods, as well as by other methods. However, an alloy composed of these two metals presents several useful characteristics exploitable for nanomedicine, photonics or catalysis, which are due not only to the combination of plasmonic and magnetic response, but also to the mixing at the nanoscale of elements with different chemical reactivity.

LASiS of Au-Fe nanoalloys evidenced a series of singular challenges and the influence of the synthesis environment on the composition of nanoparticles was especially important in this case. Therefore, we found that a way to control the composition of the alloy is the synthesis of Au-Fe nanoparticles in mixtures of water and ethanol. The most interesting nanoalloys then have been cleaned from undesired ablation by-products and functionalized with different thiolated ligands, to study their structure, properties and biocompatibility. The possible use of the nanoparticles for SERS and as multimodal contrast agents were also investigated.



## 4.2 Nanoparticle synthesis

We carried out the synthesis of our gold-iron alloy nanoparticles by ablating a bulk Au-Fe alloy target with atomic composition of 73% gold and 27% iron, provided by MaTeck GmbH. We used the 1064 nm Nd:YAG laser with pulses of 9 ns, frequency of 10 Hz and power of 30 J/cm<sup>2</sup>. Results were compared to gold nanoparticles obtained by LASiS in ethanol (see Table 4.1):

Sample	Target	Solvent
A	Gold	Ethanol
B	Au <sub>73</sub> Fe <sub>27</sub>	Water
C	Au <sub>73</sub> Fe <sub>27</sub>	Water-ethanol 12:1
D	Au <sub>73</sub> Fe <sub>27</sub>	Water-ethanol 1:1
E	Au <sub>73</sub> Fe <sub>27</sub>	Ethanol

Table 4.1 – Samples obtained from the ablation of alloy targets.

The UV-visible absorption spectra of the nanoparticles as obtained after the laser ablation process are reported in figure 4.1, where a strong dependence of the optical properties on the synthesis environment is clearly visible. In fact, the alloy nanoparticles (samples B-E) show a marked decrease in surface plasmon absorption peak intensity when the quantity of ethanol in the synthesis environment increases.

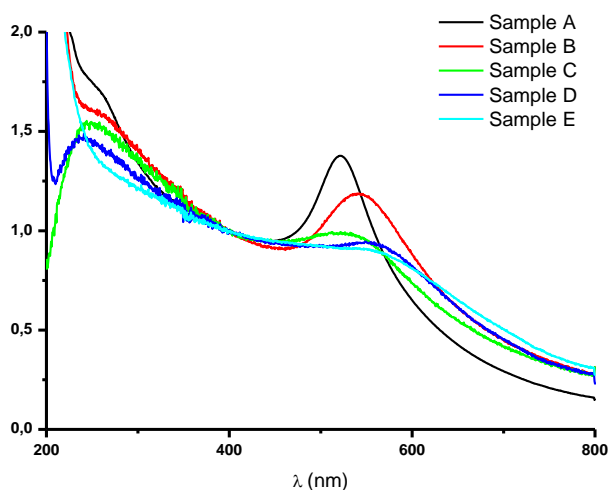


Figure 4.1 – UV- Visible absorption spectra of the gold and gold-iron nanoparticles reported in Table 4.1. The absorption spectra have been normalized at 400 nm for an easier visualization, and were acquired with a water reference.

In the next step, poly ethylene glycol (PEG) with average molecular weight of 5000 Dalton, hosting a thiol group at one end, was added to the samples. The addition of thiolated PEG is routinely performed with gold and silver nanoparticles when nanoparticle stability and protection in aqueous and organic solvents are desired<sup>RW.ERROR - Unable to find reference:688</sup>. Importantly, PEG coating also increases the biocompatibility of the nanoparticles<sup>RW.ERROR - Unable to find reference:689</sup>. In principle, for Au-Fe alloy nanoparticles, the formation of a metal-sulphur bond equivalent to the one that forms on noble metal is possible by reaction with surface Au atoms. In the typical procedure, a large excess of PEG was added to the colloidal dispersion. Then, the treatment of the nanoparticles dispersion prosecuted with the addition of ethylenediaminetetraacetic acid (EDTA). EDTA is very effective for the removal of amorphous iron hydroxides and other iron byproducts that eventually form during the synthesis, thus restoring the surface availability of the nanoparticles. The solution containing nanoparticles, PEG and EDTA was kept at 60° C for not less than 1 hour, and then filtered with a 10000 Dalton membrane, which is crucial for the complete separation of PEG-coated Au-Fe nanoalloys from other synthesis byproducts. Finally, all the samples from B to E were resuspended in distilled water. For homogeneity of treatment, also sample A (pure Au) was subjected to the same procedure.

Accurate comparison of nanoparticles optical/plasmonic properties requires that size and shape is the same among all samples and that nanoparticles are well dispersed in solution (e.g. non aggregated). To this purpose, the nanoparticles were further processed by a selective sedimentation-based-separation (SBS)<sup>RW.ERROR - Unable to find reference:690</sup>, which removes bigger or aggregated nanoparticles and gives samples with similar dimensions.

In figure 4.2 are shown the UV-visible absorption spectra from the five samples at the end of the whole preparation. The spectra shows in a more reliable way the dependence of the SPA from the synthesis environment, and in particular that the intensity and the position of the SPA change as the liquid solution becomes richer in ethanol (moving from B to E). It is interesting to note that, in comparison with the same samples before the treatment with PEG and EDTA, the SPA peaks of all the samples is blue-shifted and looks sharper than before, because one of the effects of the PEG/EDTA is to break up many aggregates that form after the synthesis, and removing the coating of iron hydroxides around the nanoparticles. In any case, the results confirm that samples from B to E have lower plasmon absorption than A.

#### 4. Gold-Iron alloy nanoparticles

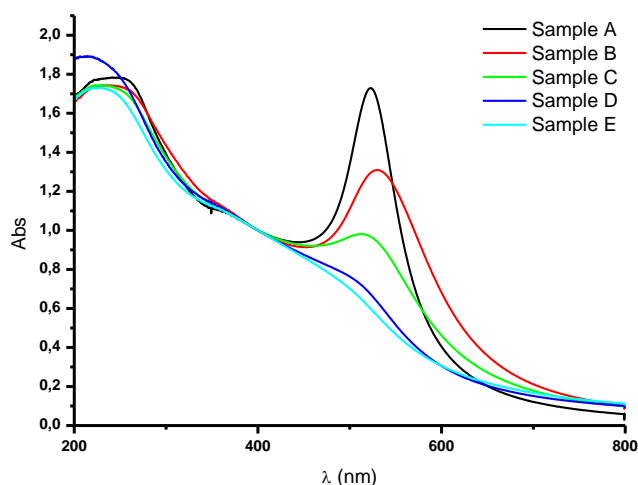


Figure 4.2 – UV-visible absorption spectra of the gold and gold-iron nanoparticles reported in table 4.1 after the treatment with PEG and EDTA, and the SBS. the absorption spectra have been normalized at 400 nm for an easier visualization.

The peak positions of the different samples, and the ratio of absorbance at 400 nm compared to that at SPA, are shown in table 4.2:

Sample	SPA Position (nm)	Abs@400nm/Abs@SPA
A	525	0.51
B	530	0.76
C	513	1.02
D	510	1.45
E	504	1.53

Table 4.2 – SPA data for the samples.

For the last two samples, the SPA is strongly damped, and it becomes difficult to easily identify the peak position, but the trend shows a decrease in the SPA intensity and a blue shift of its position.

In figure 4.3 are shown the images of the nanoparticles solutions, where it is possible to see at a glance the effect of liquid environment during the synthesis in the optical properties of the nanoparticles.

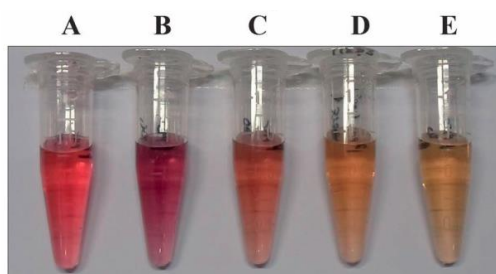


Figure 4.3 – Images of nanoparticles solution after the preparation procedure. It is possible to see how the damping of the SPA (visible in figure 4.2) is reflected in a change in colour from red to brown. From Reference 1.

These nano-objects remain stable in solution for prolonged time. In figure 4.4 are reported the UV-Visible absorption spectra of the nanoparticles after being filtered and after two weeks of storage at room temperature. This is not trivial, since we expect the presence of metal iron in the Au-Fe alloy, which may undergo to oxidation in water at room temperature. Besides, Au-Fe alloys are not thermodynamically stable. The reason for this excellent stability are investigated in the following section.

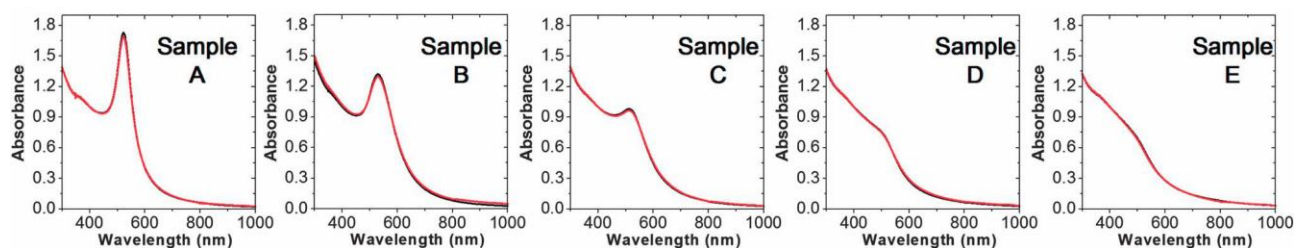


Figure 4.4 – UV-Visible absorption spectra of nanoparticles aqueous solutions after being filtered (in black) and after two weeks (in red). From reference 1.

### 4.3 Nanoparticle characterization

To assess the elemental composition of the nanoparticles, we initially performed EDS analysis, and we exploited the relative intensity of Fe  $K\alpha_2$  and Au  $L\alpha_1$  peaks to estimate the relative quantity of the two elements in each sample. The EDS peaks are reported in Figure 4.5, where one can see that the relative amount of iron in the samples clearly increases when the amount of ethanol in the synthetic environment was larger.

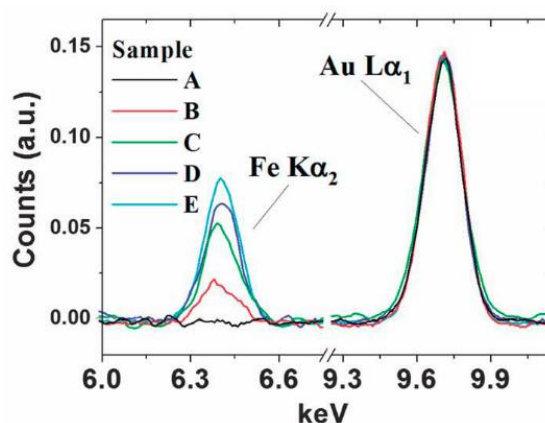


Figure 4.5 – EDS spectra of the Fe  $K\alpha_2$  and Au  $L\alpha_1$ . The spectra are normalized at the gold peak for an easier visualization. From reference 1.

Further investigation on the structure of the nanoparticles was carried out using TEM, and the results are shown in Figure 4.6. The nanoparticles shown in the TEM images are all in the 24-28 nm range, with polycrystalline structure and spherical shape. It is interesting to

#### 4. Gold-Iron alloy nanoparticles

point out that the nanoparticles deposited on the TEM platelets were exposed to the air, but no iron oxide shell is visible.

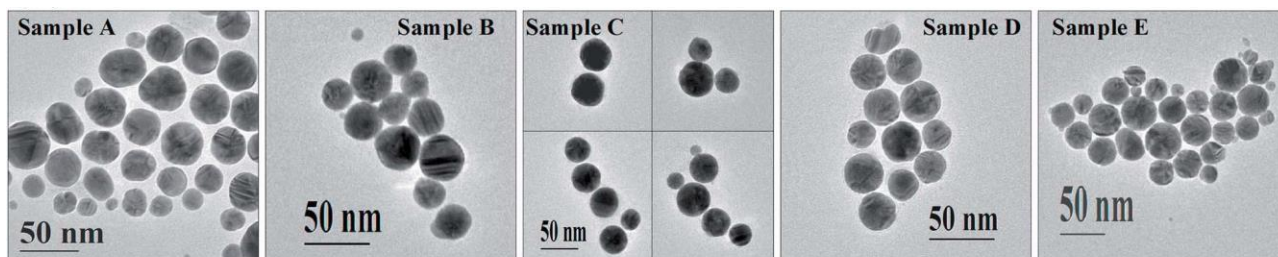


Figure 4.6 – TEM images of the samples A-E. From reference 1.

A statistic analysis of the dimensions of samples A-E is shown in figure 4.7, with numerical data resumed in Table 4.3. The size distribution is centred at 24 - 28 nm, with standard deviation of the order of 35%, as we expected after the SBS procedure.

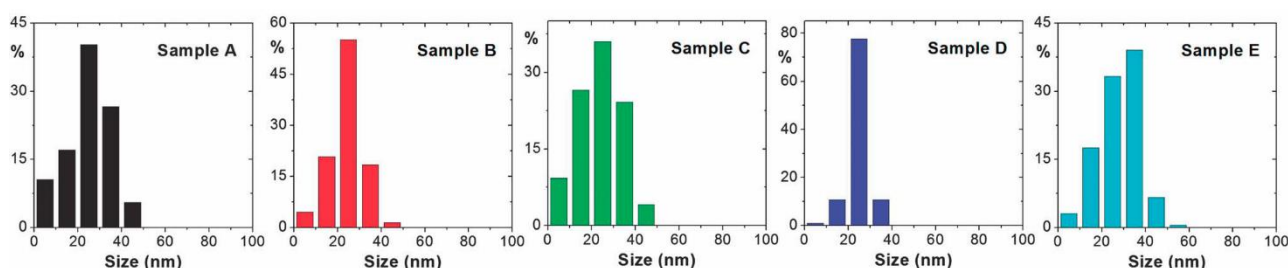


Figure 4.7 – Histograms of the size distribution of samples A-E. From reference 1.

Sample	Avg. Size (nm)
A	26 ± 10 nm
B	25 ± 7 nm
C	24 ± 9 nm
D	26 ± 5 nm
E	28 ± 10 nm

Table 4.3 – Data regarding the size distribution of the samples. From reference 1.

To better define the crystalline structure of the nanoparticles, Selected Area Electron Diffraction (SAED) analysis was carried out. The analysis evidenced that nanoparticles have an *fcc* structure, which is typical of pure gold nanoparticles. The (111) interplanar spacing, measured from the SAED pattern and also from High Resolution TEM (HRTEM) images, show a decrement of the spacing from sample A to E (figure 4.8). This behaviour can be explained thanks to Vegard's law (see Chapter 1), due to the presence of Fe atoms as random substitutional impurities in the Au lattice, with consequent reduction of the cell size in the nanocrystalline alloy.

#### 4. Gold-Iron Alloy nanoparticles

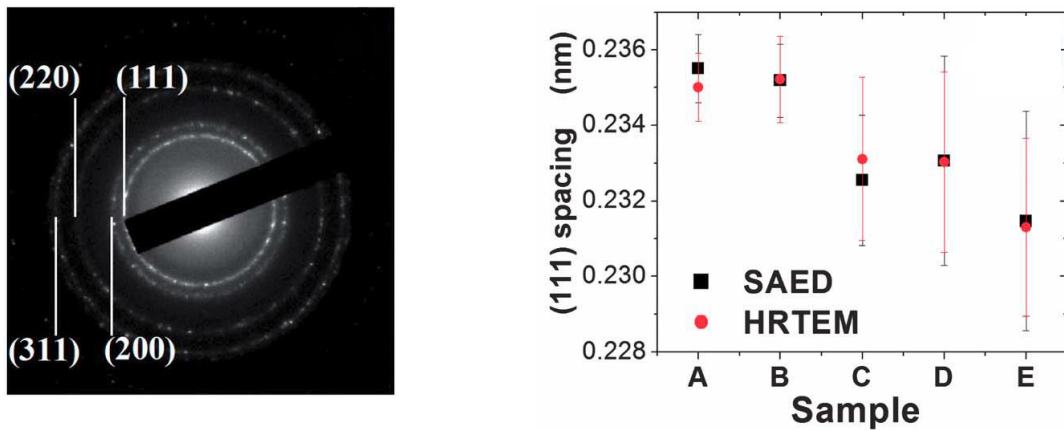


Figure 4.8 – (Left) fcc SAED pattern from sample E. (Right) (111) interplanar spacing obtained from SAED and HRTEM data. From reference 1.

Scanning transmission electron microscopy (STEM) analysis were carried out on alloy nanoparticles obtained in pure ethanol (sample E), to assess composition homogeneity and exclude segregation or core-shell structures (see Figure 4.9 and table 4.4).

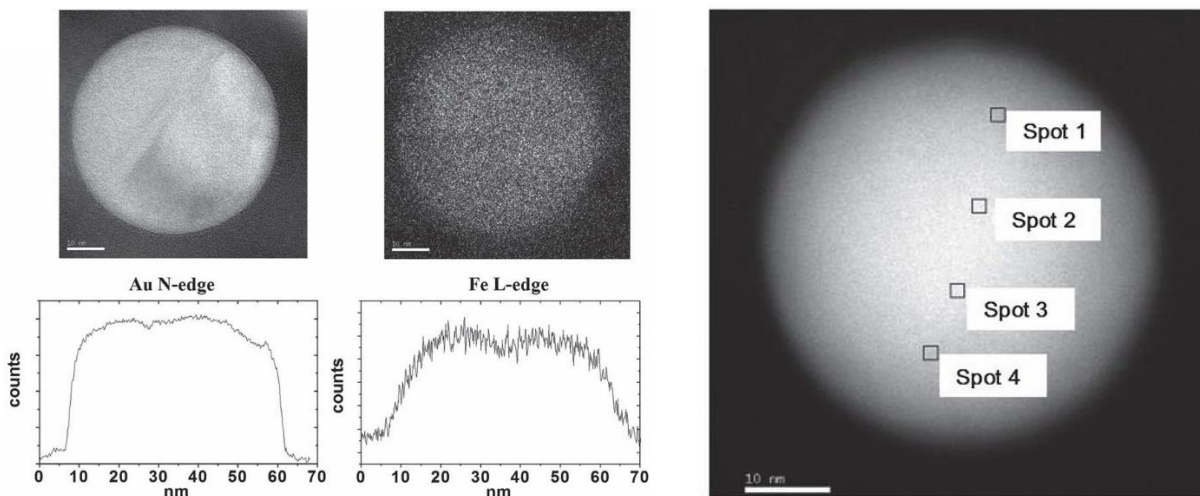


Figure 4.9 – STEM single elemental maps for the Au N-edge (83 eV) and Fe L-edge (708 eV) showing overlap for both elements (Left). STEM image of a single nanoparticle, for composition analysis. From reference 1.

Spot #	Au atomic content	Fe atomic content
1	89±11%	11±3 %
2	90±7%	10±2 %
3	89±8%	11±2 %
4	89±8%	11±2 %

Table 4.4 – EDX Composition data of the nanoparticle in Figure 4.9. From reference 2.

To obtain more information about the chemical nature of Fe and Au in these alloys, X-Ray photoelectron spectroscopy (XPS) analysis was performed on samples from A to E, drop casted on the surface of a copper substrate. In figure 4.10 are shown the data regarding the



#### 4. Gold-Iron alloy nanoparticles

Fe 2p and Au 4f peaks. The gold signals are quite consistent in all the samples, showing a single Au 4f<sub>7/2</sub> peak at 84 eV, the energy expected for metallic gold. This means that in the analysed samples the main form of gold is the metallic one, as was expected from the SAED analysis.

The iron signals are visible in all the Au-Fe alloy nanoparticles. However, the signals at lower binding energies, typical of more reduced species (Fe peak is at 707-708 eV, while Fe<sup>2+</sup> signal is at 709 eV), are found only in the samples with an higher content of iron (especially in sample E). Instead, in all cases the signal from Fe(III) dominates, clearly indicating that the surface of alloy nanoparticles actually is rich of oxidised iron.

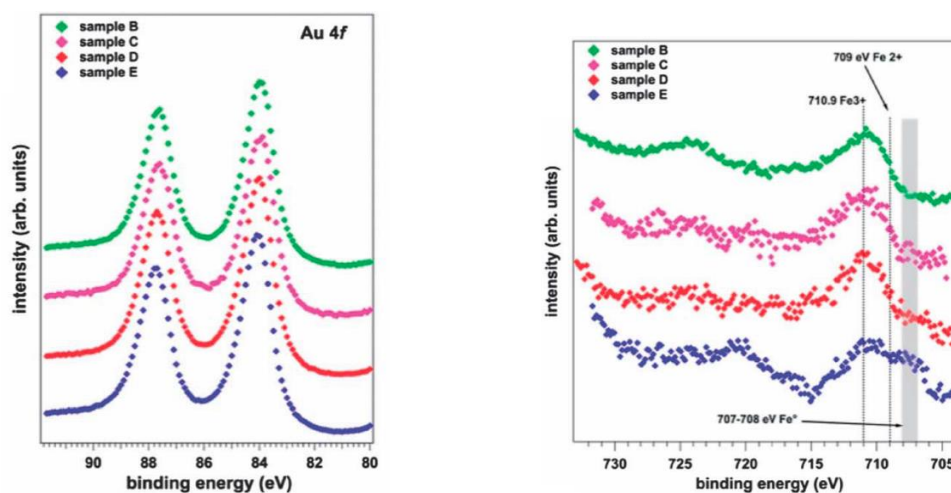


Figure 4.10 – XPS data regarding the Fe 2p (left) and Au 4f (right) peaks. The spectra are stacked for an easier visualization. From reference 1.

We performed a more in deep study of iron signal in sample E by comparing the bare nanoparticles with those covered with PEG and with the base nanoparticles sputtered for 10 minutes with Ar<sup>+</sup> atoms. The results are shown in figure 4.11, where one can see that the relative intensity of oxidised and reduced iron species changes going from the sputtered to the bare and PEG-coated sample. This clearly implies that reduced iron atoms are located below the surface of the nanoparticles. It is remarkable the increase in the relative intensity of the reduced iron signal of the sputtered sample, as expected for a metal Au-Fe alloy.

An analysis on the formation of thiol bonds in PEG coated particles of sample E was also carried out by analysing the S 2p photoemission peak. For the sulphur peak, after removing the background (dotted line) fitting reveals two Gaussian functions with a spin-orbit separation of 1.6 eV, one located at 162.7 eV (position of the S 2p<sub>3/2</sub>) and the other at 164.3 eV. In literature<sup>3,4</sup> the splitting of the single peak in these two components (the former representing the S-Au bond and the latter the S-H bond) has been previously observed on thiolated gold

nanoparticles, and clearly point out to the formation of S-metal bonds. Since Fe on nanoalloy surface is oxidised, it is expected that thiols reacted with free surface Au atoms.

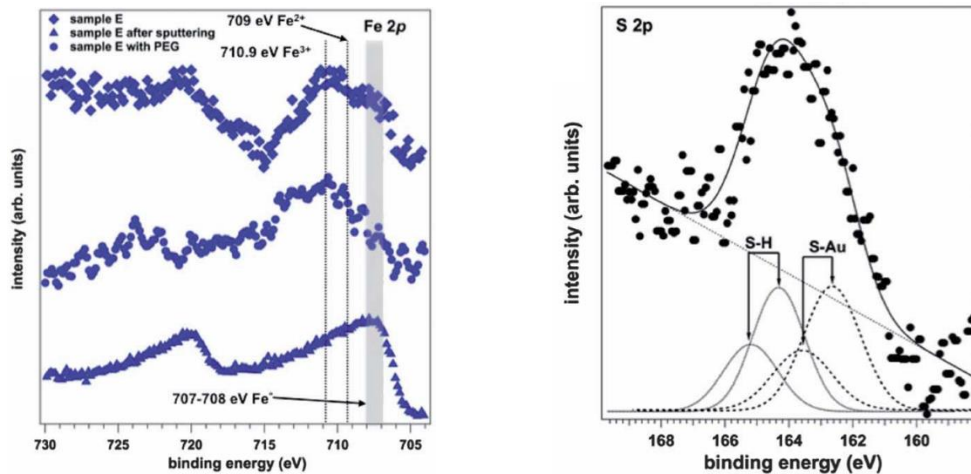


Figure 4.11 – XPS data of sample E for the Fe (left) and S (right) peaks. The spectra are stacked for an easier visualization. From reference 1.

From these measurements, we can assume that the iron in the nanoparticles is available in its reduced form due to the protection of the coating composed of gold and iron oxide on the outer layers of the nanoparticles. The availability of gold on the surface also gives the nanoparticles the same kind of reactivity of pure gold nanoparticles (for example, Au-S bonding).

## 4.4 Optical properties

It is possible to assess the change in the optical properties of spherical nanoparticles by using the Mie model (see Chapter 2). For instance, calculation of the UV-Visible absorption spectrum of for a given alloy composition ( $\text{Au}_{89}\text{Fe}_{11}$ ) with the Mie model was possible<sup>1,2</sup> by using the dielectric constant resulting from the weighted average of the optical constants taken from pure gold and from the closest alloy available in literature ( $\text{Au}_{84}\text{Fe}_{16}$ <sup>5</sup>). It is very instructive when the result is compared with the same spectrum obtained for a pure gold nanoparticle with same shape and size, as shown in Figure 4.12, where the damping of the plasmon resonance due to the presence of iron is evident. It is interesting also the comparison with the optical properties obtained by the average of pure Au and pure metal Fe, also shown in Figure 4.12, because it shows that plasmon resonance is sharper also in this case and, therefore, that the band structure of the Fe-Au alloy is modified compared to the pure metals. Moreover, the alloy also shows a blue shift of the plasmon peak, which is not visible in the other cases.



#### 4. Gold-Iron alloy nanoparticles

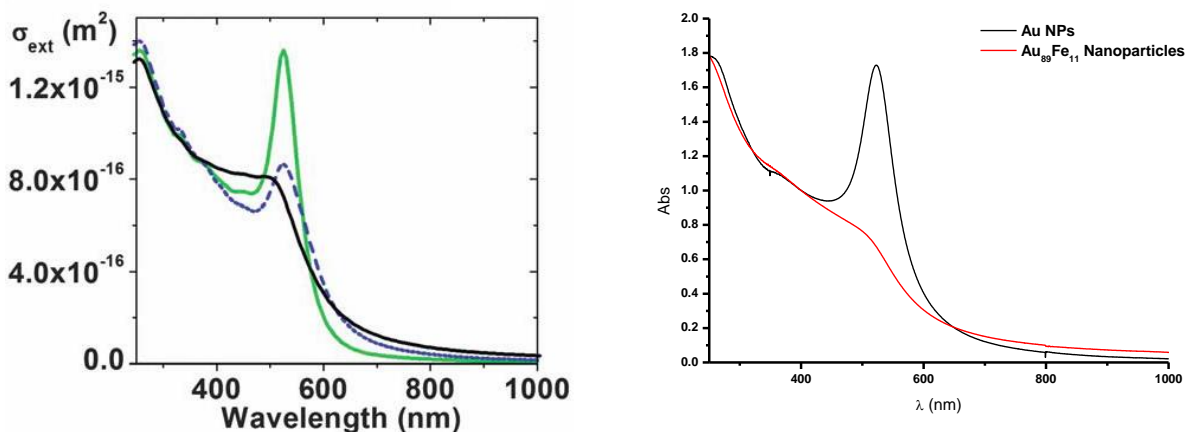


Figure 4.12 – (Left) Calculated extinction cross section  $\sigma_{ext}$  (from the Mie model) for 30 nm diameter nanoparticles with composition  $Au_{89}Fe_{11}$  (black line), pure gold (green), and with the weighted optical constant (see text above). From reference 2. (Right) UV-Visible absorption spectra of pure gold and  $Au_{89}Fe_{11}$  nanoparticles.

We can therefore deduce that the dependence of the damping is non-linear with iron content. In literature<sup>5</sup> the modification of the optical constants of alloys is attributed to single electron transitions from iron  $d$  states located below the Fermi surface of the alloy<sup>2</sup>. This behaviour is not exclusive to gold-iron alloys, but it is frequently observed in alloys of noble and transition metals with partially occupied  $d$  states<sup>6-8</sup>.

This means that by studying the UV-Visible absorption spectra it is possible to accurately model the composition of the nanoparticles, detect aggregates (due to the red shift and broadening of the SPA) and the formation of gold-oxides (due to the red shift and intensity increase of the SPA caused by the high refractive index of nearby iron oxides<sup>9</sup>). Besides, for accurate description of the optical properties, it is important to know the size of the nanoparticles and the dielectric constant of the alloy<sup>5</sup>. Since these information are available from our experimental data (size) or from literature data (optical constants for various Au-Fe alloy compositions), the Mie model can be used for the least square fitting of the experimental spectra of samples from A to E, leaving the composition as the fitting parameter. In this way, we obtained further information on the composition of the nanoparticles directly from their optical properties. The results of this fitting are shown in Figure 4.13. It is remarkable to see that even low concentrations of iron in the nanoparticles are sufficient to damp the SPA. The ratio of scattering to absorption is less influenced by the composition, while it is mostly dominated by size of nanoalloys, similar to the case of pure Au.

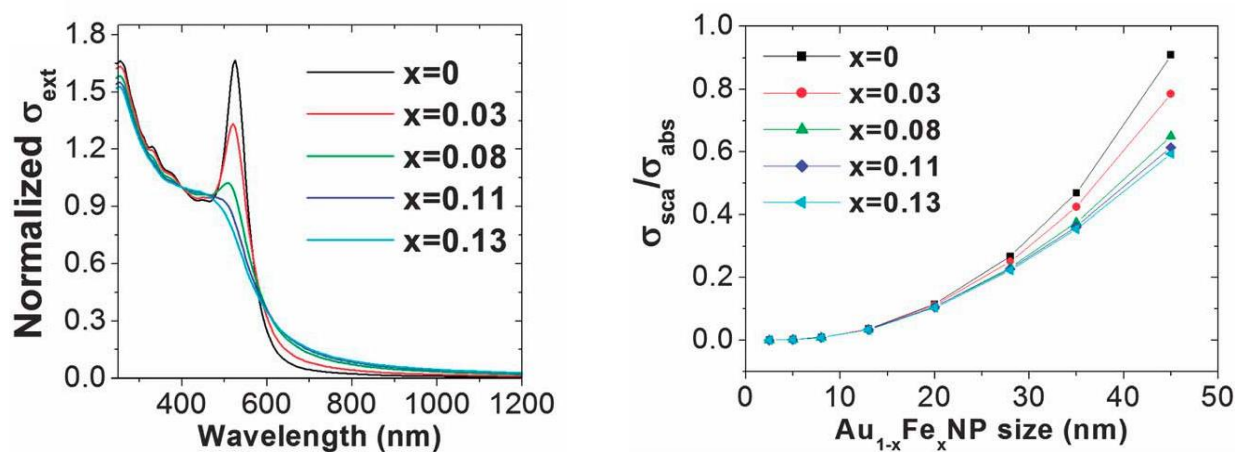


Figure 4.13 – (Left) Extinction cross-section  $\sigma_{ext}$  for  $Au_{1-x}Fe_x$  alloy spheres in water, normalized at 400nm for an easier visualization. (Right) Ratio between the Scattering Cross Section  $\sigma_{sca}$  and the Absorption Cross Section  $\sigma_{abs}$  calculated with the Mie model as a function of nanoparticle diameter and composition. From reference 1.

In table 4.5 we summarize the atomic % of iron as obtained from the Mie fitting of the experimental UV-Visible, and we compare it with the results of the EDS analysis:

Sample	Target composition	Solvent	% Composition of Iron	
			From EDS	From Mie
A	Au	EtOH	$0 \pm 2$	0
B	$Au_{73}Fe_{27}$	$H_2O$	$5 \pm 2$	3
C	$Au_{73}Fe_{27}$	$H_2O:EtOH$ 12:1	$9 \pm 2$	8
D	$Au_{73}Fe_{27}$	$H_2O:EtOH$ 1:1	$10 \pm 2$	11
E	$Au_{73}Fe_{27}$	EtOH	$15 \pm 2$	13

Table 4.5 – Data on sample synthesis and composition, inferred from Mie and EDS data. From reference 1.

To further exclude the occurrence of clustering of iron or iron oxide domains inside a gold matrix, as an alternative to the formation of Au-Fe alloy, we used the Discrete Dipole Approximation (DDA)<sup>10, 11</sup>. In this instance we considered spherical gold nanoparticles (26 nm of diameter) with 6 grains of iron (in either metallic or oxide form), occupying the six vertices of an octahedron. To better assess different structures, grains tangent or under the surface were considered<sup>1</sup>. The results of the calculation are shown in Figure 4.14. For segregated grains only a small damping of the SPA is visible, even with quantities of iron superior to those available in our nanoparticles. Furthermore a red-shift is seen at increasing iron concentrations, contrary to what is observed in our samples. This is another argument suggesting that the nanoparticles obtained by LASiS do not have phase segregation, but they are real alloys.

#### 4. Gold-Iron alloy nanoparticles

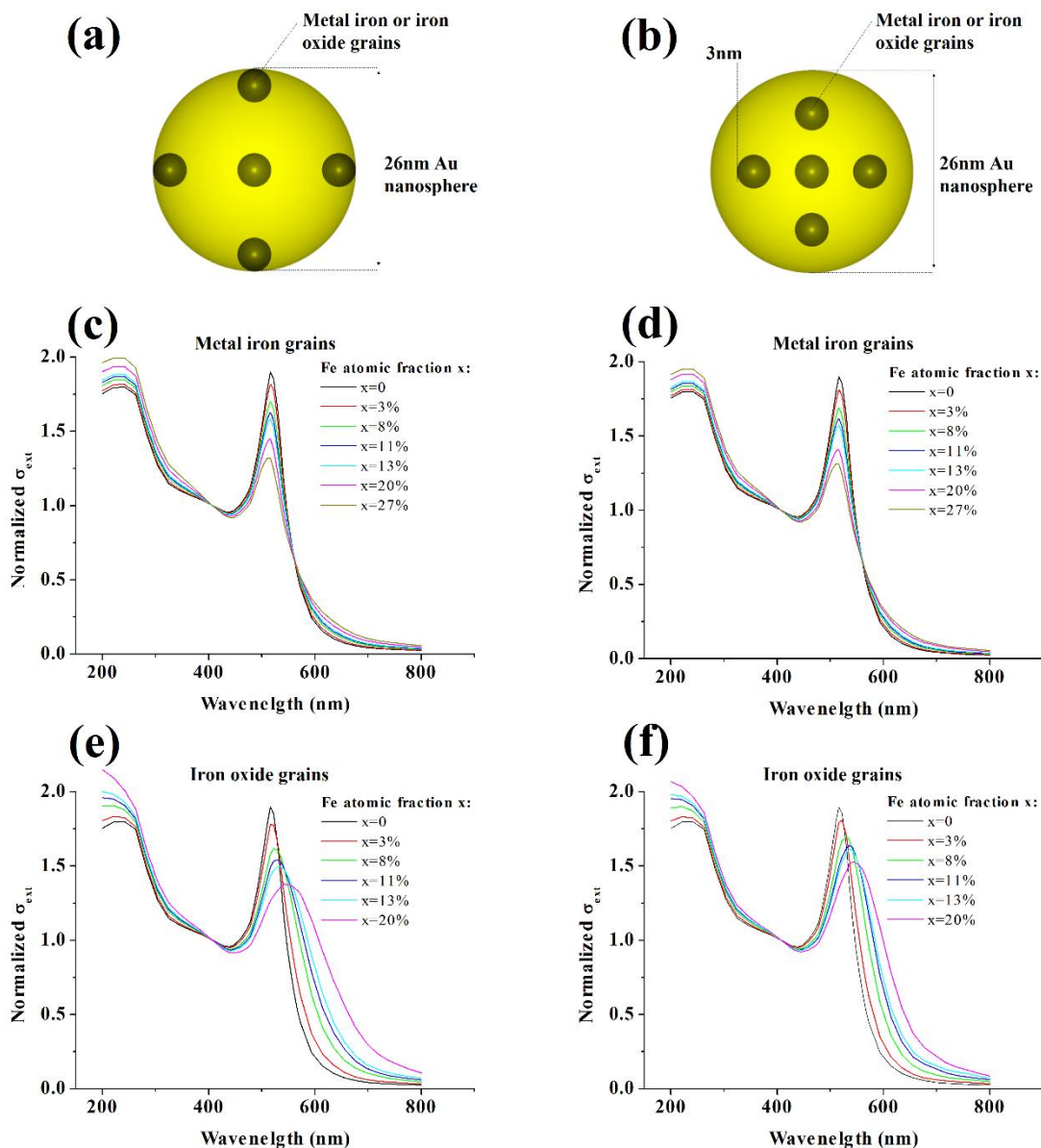


Figure 4.14 – Numerical DDA calculations of the normalized scattering cross sections of 26 nm gold nanospheres with 6 grains of iron embedded tangent (a) or 3 nm below (b) the surface. The calculations are carried out for metal iron (c,d) or iron(II, III) oxide (e, f) grains, whose size is progressively increased to change the total fraction of iron in the nanoparticles. The extinction cross section are then normalized at 400 nm for ease of visualization. From reference 1.

We also investigated the SERS response of the nanoalloy versus their composition. The SERS response of the nanoparticles was studied by adding an equal amount of Malachite Green (4-[[4-(Dimethylamino)phenyl](phenyl)methylene]-N,N-dimethyl-2,5-cyclohexadien-1-iminium chloride), an organic dye often used in SERS experiments. Raman analysis was carried out on the bare dye and on the five nanoparticles sample with the addition of the same quantity of dye. The samples were drop casted on a Teflon substrate and then dried. The results are shown in Figure 4.15. When the bare dye is analysed no Raman signal is visible, and only fluorescence is detected. The five samples containing nanoparticles show

strong Raman signals, and it is possible to discern a dependence of the signal intensity from the quantity of iron.

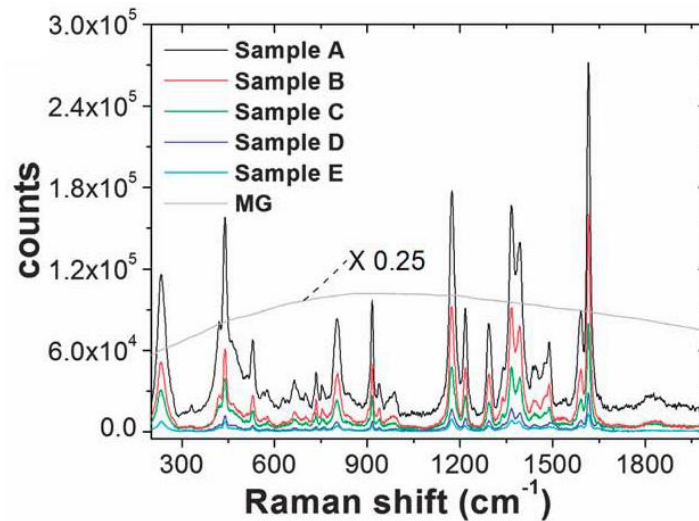


Figure 4.15 – Raman signals from the dye and the samples, acquired with a 633 nm continuous laser wave excitation. From reference 1.

To better show this trend, in Figure 4.16 are reported the intensities of the  $1617 \text{ cm}^{-1}$  peak for each sample. The intensity of the SERS peaks decreases more than 20 times from sample A (pure gold) to sample E (15% iron), so we can infer that, despite the iron content influences the optical properties of the alloy nanoparticles, SERS is still observable with comparable performances than in pure Au NPs.

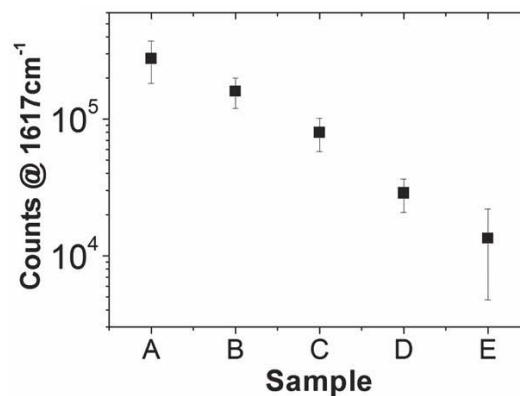


Figure 4.16 – Intensities of the Raman peaks at  $1617 \text{ cm}^{-1}$  for samples A-E. From reference 1.

Using DDA calculations, the electromagnetic field enhancement  $G_{SERS}$  at 633nm was calculated varying the quantity of iron in the  $\text{Au}_{1-x}\text{Fe}_x$  26 nm diameters nanoparticles. The calculation was further expanded to take into consideration single nanoparticles, dimers separated by 1 nm gaps, and fractal aggregates of 25 nanoparticles obtained with diffusion limited

#### 4. Gold-Iron alloy nanoparticles

aggregation growth processes (DLA)<sup>12</sup>. These processes effectively simulate the aggregation of nanoparticles and their growth into clusters following evaporation of solvents after their deposition of substrates<sup>12, 13</sup>. In figure 4.17 are shown the  $G_{SERS}$  of single nanoparticles, dimers and aggregates with  $x = 0.13$ . It is possible to see that  $G_{SERS}$  is strongly enhanced in the hot-spots that form between two nanoparticles. The enhancement values go from  $10^2$  for a single sphere, to  $10^6$  in the dimer and fractal aggregate.

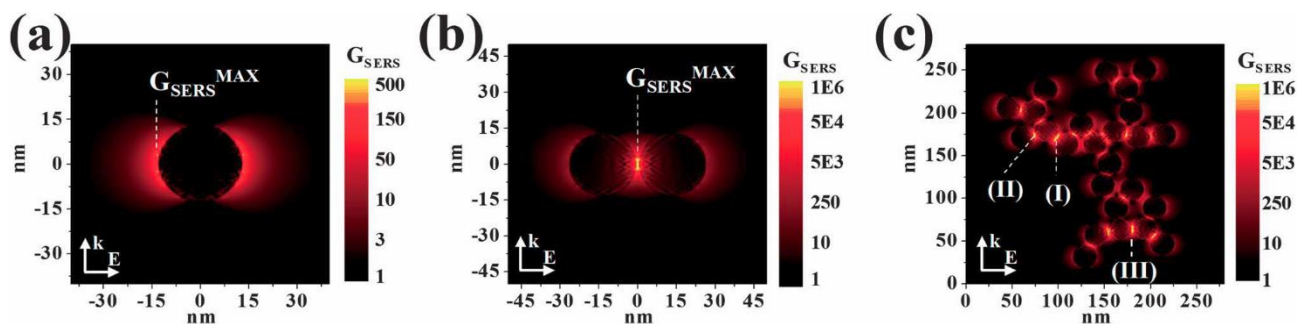


Figure 4.17 -  $G_{SERS}$  values for  $Au_{87}-Fe_{13}$  nanoparticles of 26 nm diameter monomers (a), dimers (b) or aggregates (c). The spots evidenced show the maximum  $G_{SERS}$  found in the simulations. From reference 1.

In figure 4.18 are reported the hot spot intensities for the structures shown above when the composition is varied. As expected from the Raman analysis of Malachite Green reported in Figure 4.15 (see above), there is a strong decrease in  $G_{SERS}$  for alloy nanoparticles, as long as the iron content increases. The 20-fold decrease in the entity of  $G_{SERS}$  for aggregates is in agreement with what found above, and indicates that the loss in  $G_{SERS}$  is linked to the same phenomenon that influences SPA damping, namely overlap of plasmon resonance with the single electron interband transitions due to iron atoms in the alloy<sup>1</sup>.

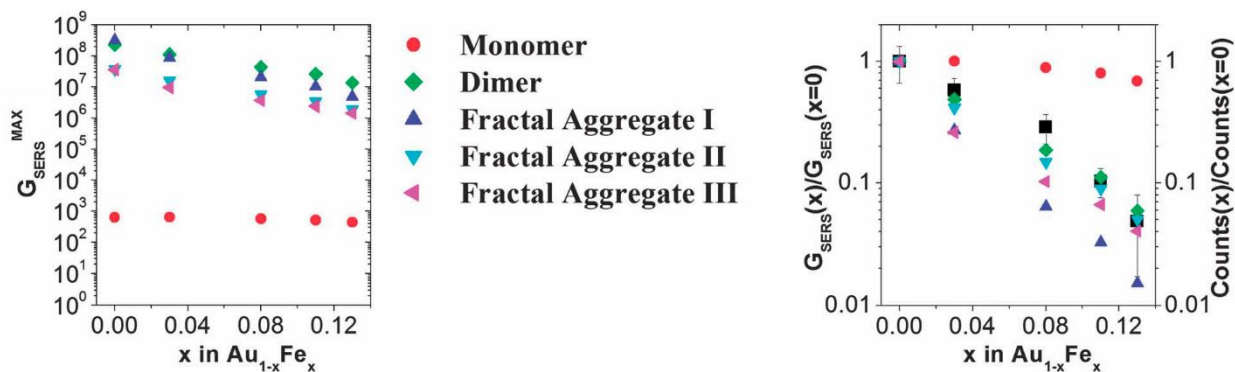


Figure 4.18 – (left) Values of maximum  $G_{SERS}$  for the structures reported in Figure 4.17 and (b) ratio of maximum  $G_{SERS}$  of each sample compared to pure gold structures. The single points reported for the aggregates correspond to the one in Figure 4.17. From reference 1.

## 4.5 Effect of solution on LASiS of Au-Fe

### Nanoalloys

Further studies on the effect of the liquid environment on the ablation results were carried out by modifying solutes dissolved in water and ethanol. These solvents were brought to boiling and then fluxed with different gases ( $N_2$ , Ar,  $CO_2$ ) for 30 minutes, and then left to cool for another 30 minutes under flux of the same gases. Another sets of ablations were carried out with water and ethanol with the 0.3% addition of hydrogen peroxide ( $H_2O_2$ ) 35% in volume. The modified solvents were then used for the ablation. In figure 4.19 are shown the UV-Visible absorption spectra of the samples obtained in water. The absorption spectra are compatible with those of Au-Fe alloys with a low iron concentration, like those we saw for ablation in water in Section 4.2. Two spectra differ: the first is from the nanoparticles obtained in water with carbon dioxide, that show an increase in the absorption in the region with  $\lambda > 600$  nm, and the one obtained in water and hydrogen peroxide, with a red-shifted broader SPA and increased absorbance at  $\lambda > 600$  nm.

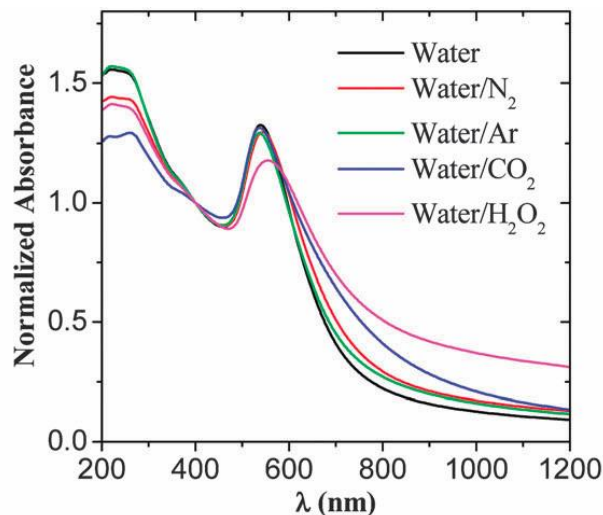


Figure 4.19 – UV-Visible absorption spectra of alloy nanoparticles obtained in water modified with different gases and with hydrogen peroxide. The spectra are normalized at 400 nm for an easier visualization. From reference 14.

The characteristics of the latter sample are compatible with core@shell structure with a dielectric shell, so TEM analysis of the sample were carried out. An image acquired by TEM and the size distribution histogram are shown in Figure 4.20. The TEM images show nanoparticles with a dark inner region, with a higher content of gold, and a less dense shell,



#### 4. Gold-Iron alloy nanoparticles

typical of low-Z elements such as iron oxide. The size distribution histogram shows a bimodal population distribution, not found in the usual ablation distribution (commonly monomodal and lognormal) and indicative of two different formation mechanisms.

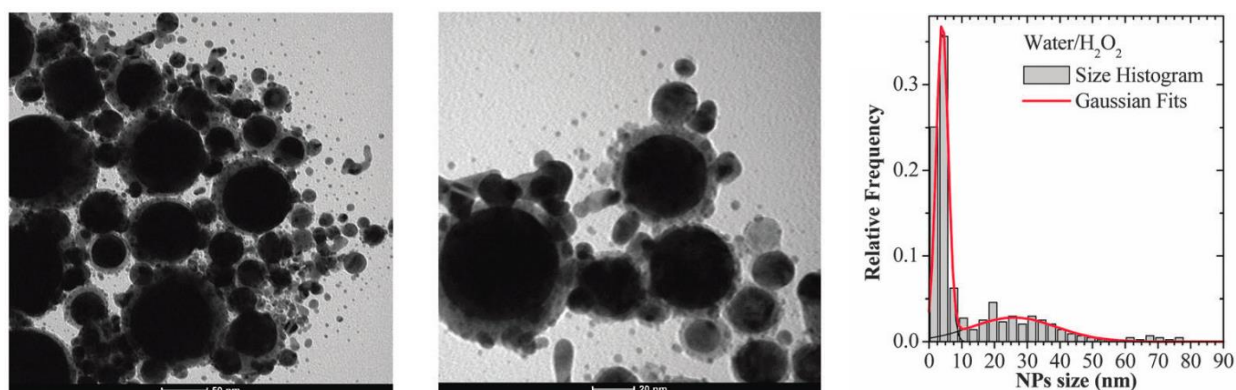


Figure 4.20 – (Left, Center) TEM images of AuFe nanoparticles obtained in water with 0.1 %  $H_2O_2$ . (Right) Size distribution histogram of the nanoparticles. From reference 14.

To evaluate the composition of the nanoparticles, the UV-Visible absorption spectrum was fitted with the Mie model for a nanosphere covered by a dielectric shell of iron oxide. In Figure 4.21 are reported the data of the simulation. The best result is given for a gold-rich (96% gold, 4% iron) alloy core nanoparticle, with some differences in the area where  $\lambda > 600$  nm due to the absorbance of coral-like and aggregated nanoparticles. The simulated spectrum for a gold nanosphere core does not correctly model the experimental data, due to the superior intensity of the SPR compared to the interband transitions.

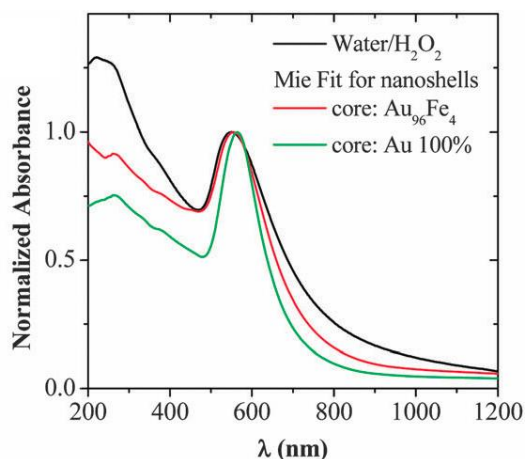


Figure 4.21 – UV-Visible absorption spectra of experimental data (black) and simulations (red and green) for AuFe nanoparticles obtained in water with 0.3% of  $H_2O_2$ . From reference 14.

For what concerns LASiS in ethanol, it was treated with gases such as nitrogen, argon and carbon dioxide, and with 0.3% addition of hydrogen peroxide 35% in volume. Since the hydrogen peroxide contains the 65% in volume of water, a further test was carried out, with

ethanol with the addition of 0.2% water. The UV-visible absorption spectra of the obtained samples are shown in Figure 4.22. As we saw in Section 4.2, the nanoparticles obtained in ethanol show a strongly damped SPA. The resulting samples can be divided in three main groups: the first comprises the nanoparticles obtained in ethanol with and without fluxing with gases, the second is the sample obtained in ethanol with hydrogen peroxide, and the third is the sample obtained in ethanol with water.

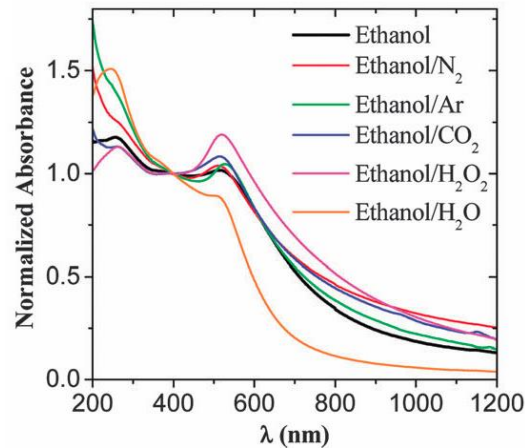


Figure 4.22 – UV-Visible absorption spectra of alloy nanoparticles obtained in ethanol modified with different gases, hydrogen peroxide, and water. The spectra are normalized at 400 nm for an easier visualization. From reference 14.

The sample obtained in ethanol fluxed with water is a good example of the first group. A TEM image, the size distribution histogram, and the fitting for the UV-Visible absorption spectrum are reported in Figure 4.23. The obtained nanoparticles show an homogeneous contrast in their TEM images. Considering their size distribution, that can be well fitted with a lognormal size distribution, and the UV-Visible absorption spectrum, correctly approximated by alloy nanoparticles with about 10% iron content, we can assume that the obtained nanoparticles are equivalent to those of Sample E in Section 4.2.

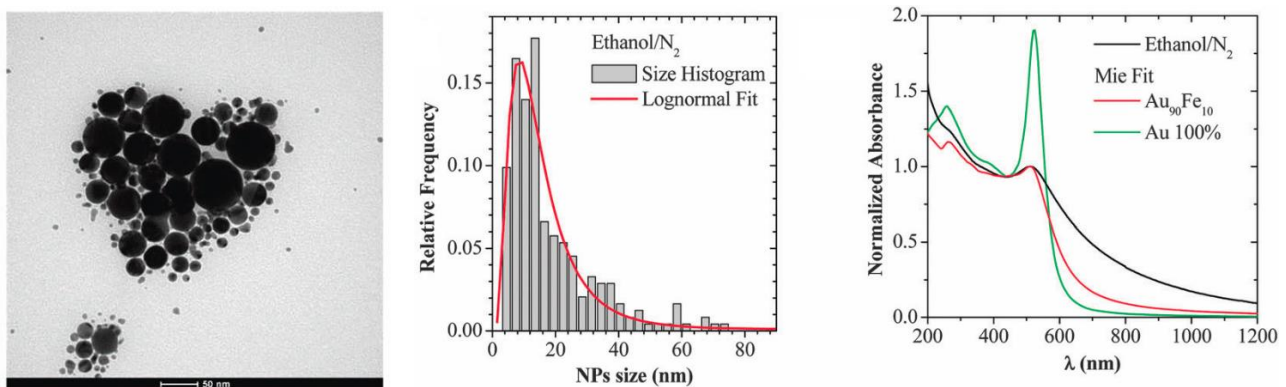


Figure 4.23 – (Left) TEM Image of the nanoparticles obtained in ethanol fluxed with nitrogen. (Center) Size distribution histogram for the nanoparticles. (Right) UV-Visible absorption spectra of the nanoparticles (black) and the Mie fits for two different compositions (red and green). From reference 14.



#### 4. Gold-Iron alloy nanoparticles

The TEM image, size distribution histogram, and fitting for the UV-Visible absorption spectrum of AuFe nanoparticles obtained in water with hydrogen peroxide are reported in Figure 4.24. In this sample, the UV visible absorption spectrum is compatible with that of alloy nanoparticles, and no red-shift or plasmon broadening are visible for the nanoparticles. To further confirm this hypothesis, the size distribution is lognormal as those of standard alloy nanoparticles (even if shifted at a size almost double of those obtained in pure ethanol) and the TEM images do not show an oxide shell.

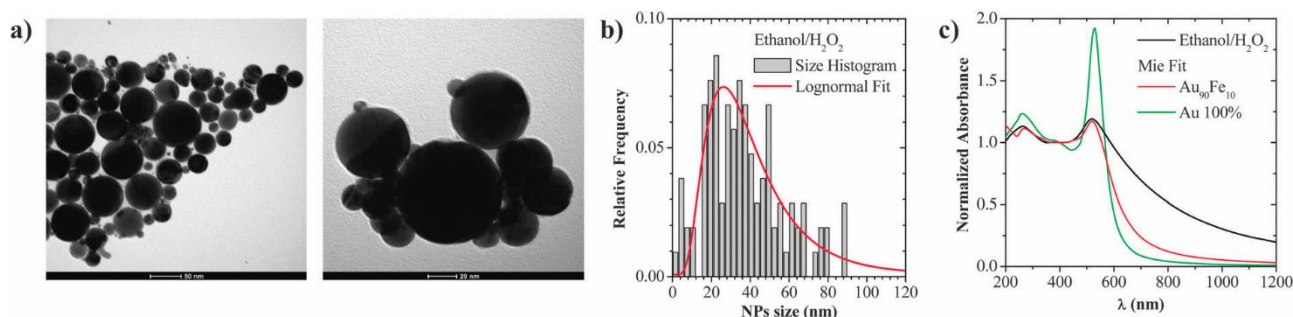


Figure 4.24 – (a) TEM Image of the nanoparticles obtained in ethanol with hydrogen peroxide 0.3%. (b) Size distribution histogram for the nanoparticles. (c) UV-Visible absorption spectra of the nanoparticles (black) and two Mie fits with different composition (red and green). From reference 14.

The nanoparticles obtained in ethanol with 0.2% of water, on the other hand, show some interesting differences. The TEM image, size distribution histogram, and fitting for the UV-Visible absorption spectrum of AuFe nanoparticles obtained in water with hydrogen peroxide are reported in Figure 4.25. The UV-Visible absorption spectra shows the characteristics of alloy nanoparticles, but the interband transitions are particularly intense when compared to the SPA peak, probably due to a large number of small nanoparticles (too small to show an appreciable SPA). The analysis of the TEM images supports this interpretation, showing a large number of nanoparticles with dimensions lower than 5 nm, and a much smaller number of nanoparticles over 20 nm. The large nanospheres also show an iron oxide nanocrescent with a thickness of about 1-4 nm, conferring asymmetric properties to the nanoparticles. The fitting of the absorption spectrum gave results that are halfway between those of alloy nanoparticles with a composition of 89% gold and 11% iron and nanoshells with a core composition of 88% gold and 12% iron, and a shell with a thickness of 0.05 times the core diameter.

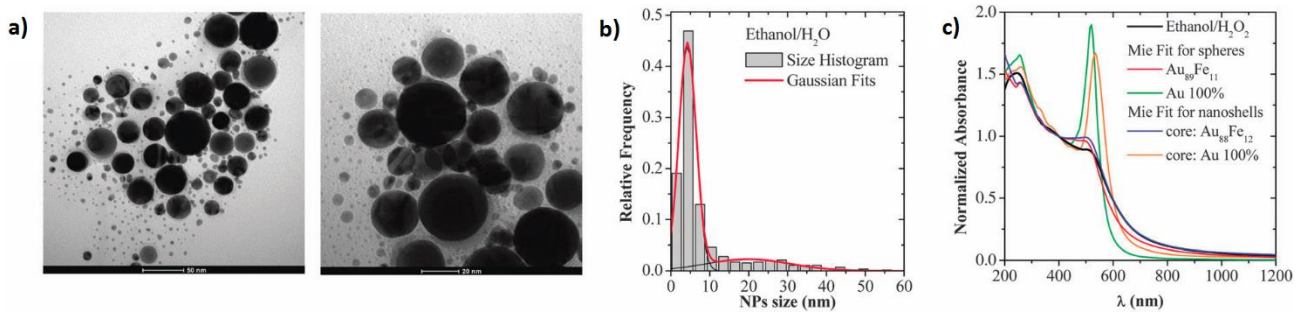


Figure 4.25 – (a) TEM Image of the nanoparticles obtained in ethanol with hydrogen peroxide 0.3%. (b) Size distribution histogram for the nanoparticles. (c) UV-Visible absorption spectra of the nanoparticles (black) and two Mie fits with different composition (red and green). From reference 14.

The differences in oxidation among the various samples prompted us to carry out XPS analysis. The results for this analysis are shown in Figure 4.26. The gold peak (Au 4f) show that metal gold is available on the surface of our samples, and no iron carbide signal is visible on the carbon C 1s peak. The iron peak (Fe 2p) is similar in all three samples and multiple contributions can be found for the binding energies of metal iron (707 eV), iron(II) oxide (709.5 eV), and iron(III) oxide (711 eV). Particularly interesting is the presence of metal iron and the small increase in the iron oxide signals available on the surface of the ethanol/H<sub>2</sub>O sample.

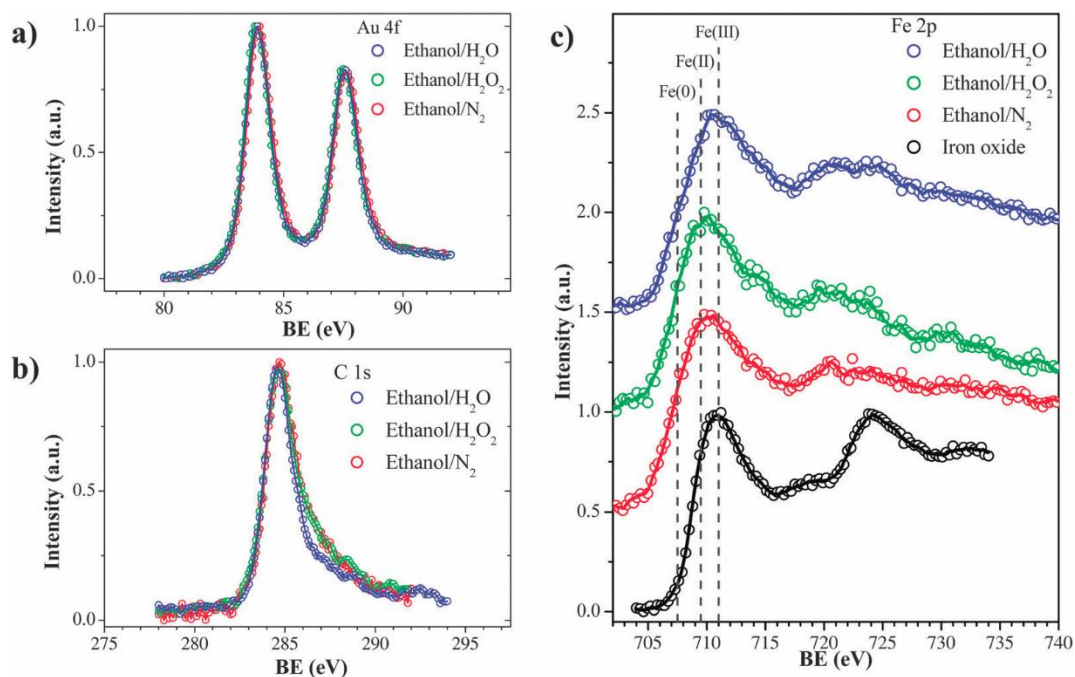


Figure 4.26 – XPS spectra for Au 4f (a), C 1s (b) and Fe 2p (c) peaks. The iron signals are vertically shifted for an easier visualization. From reference 14.

Furthermore, we also observed a large improvement in yield for the nanoparticles obtained in ethanol with 0.2% water, compared to the other synthesis environment, as can be seen in Figure 4.27:

#### 4. Gold-Iron alloy nanoparticles

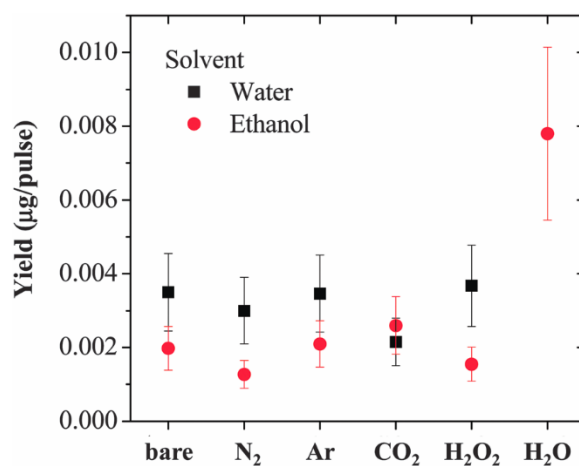


Figure 4.27 – Yield of ablation in water and ethanol modified by fluxing or reagent addition. From reference 14.

Based on the experimental evidences reported above, we can infer some information on the laser ablation synthesis mechanisms.

For ethanol with the addition of hydrogen peroxide, due to the extreme temperature of the laser generated plasma plume (well above the decomposition temperature of hydrogen peroxide) we can expect thermal decomposition of this compound in H<sub>2</sub>O and O<sub>2</sub> in the hot area around the ablation site<sup>15</sup>. The extra vapour pressure contributes to the formation of a larger cavitation bubble, and the ablated material has a larger probability to be found inside the vapour bubble. Since in the bubble the concentration of solute oxidizing species is lower, the iron oxidation happens with a lower frequency, and surface oxidation and cooling happen more slowly. This also means that the final size of the nanoparticles is larger, since they can coalesce for a longer period. The surface oxide also passivates the surface, avoiding the formation of further oxide inside the nanoparticle.

Nanoparticles obtained in ethanol fluxed with nitrogen grow in an ablation bubble with “standard” dynamics, because there is no addition of gas from decomposing compounds. This means that the ratio between nanoparticles formed inside and outside the cavitation bubble will be less oriented in favour of the former, as can be found in literature<sup>16, 17</sup>. The nanoparticles formed inside the cavitation bubble will cool more slowly, and the final dimensions will be bigger. On the other hand, the nanoparticles growing outside will be cooled more quickly, and will be more in contact with oxidizing species and contaminants, leading to a surface where iron oxides appear with higher abundance. However the size distribution is lognormal and not bimodal, suggesting that there are no macroscopic differences in the ablation mechanism.

When the nanoparticles are obtained in ethanol with 0.2% water, the solvent thermodynamic properties are not modified enough to make a substantial difference. However the nanoparticles that after formation are moved into the liquid are in contact with an higher concentration of oxidizing species. This means that the nanoparticles get oxidized with increasing frequency, and this can happen either to the newly formed nuclei (giving the very small nanoparticles seen in the size distribution) or to already grown nanoparticles (giving larger nanoparticles with crescent-sized oxide shells). Since a bimodal size distribution is observed, two different formation regimes are hypothesized.

Water with hydrogen peroxide is the most oxidizing environment in the performed tests, and the results can be seen in the obtained results. A considerable amount of nanoparticles, even of relatively small dimensions, shows an iron oxide shell. Furthermore, the density, surface tension, heat capacity and viscosity are higher than those of ethanol, and the cavitation bubble remains smaller, and contains less nanoparticles. The end result is that nanoparticles formed outside the bubble are immediately stopped in their growth, while those that grow inside the bubble form an oxide shell when they get in contact with the highly oxidizing environment.

A summary of the possible mechanisms is shown in the scheme of Figure 4.28:

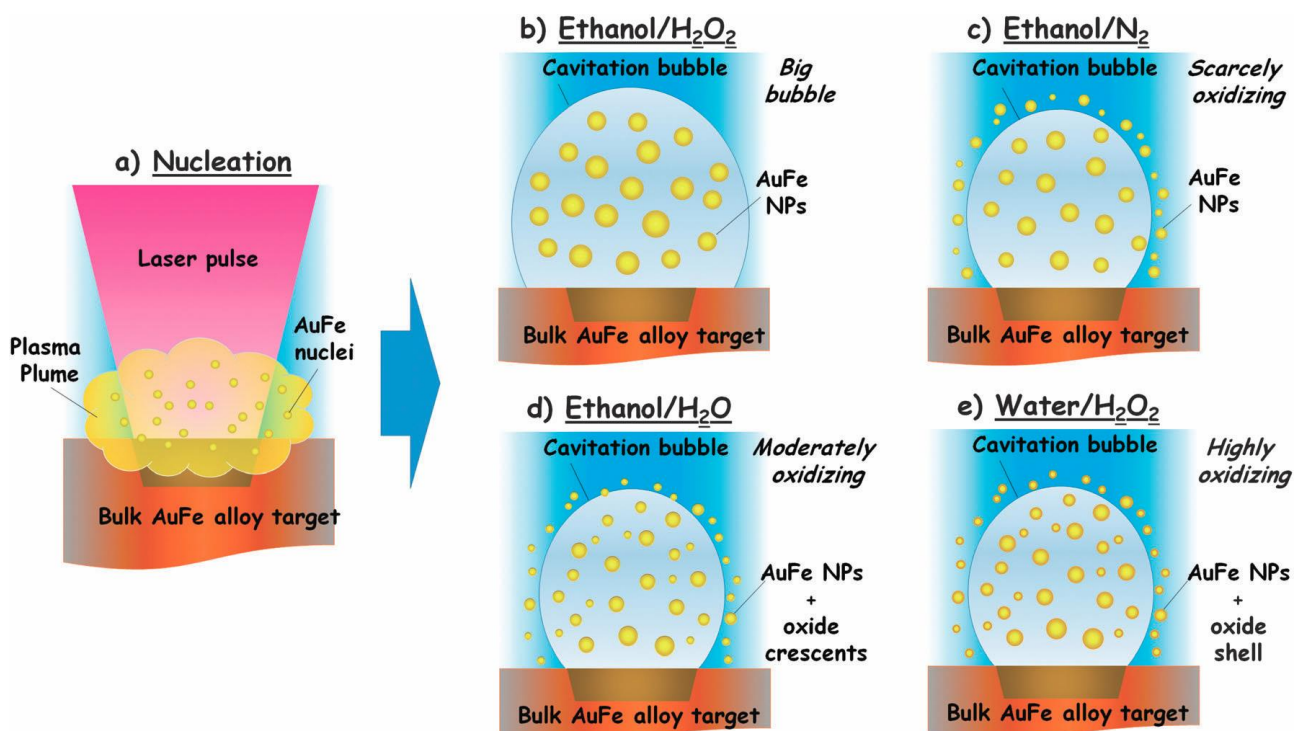


Figure 4.28 – Graphical representation of the possible ablation mechanisms that occur when the solvent is modified. From reference 14.

## 4.6 Magnetic properties

The dependence of the magnetization ( $M$ ) from the magnetic field for a sample with composition  $\text{Au}_{89}\text{Fe}_{11}$  was tested at 3 and 300 K<sup>2</sup>. The magnetization curves for the sample are shown in Figure 4.29. At 300K, the magnetization  $M$  follows linearly the strength of the applied field. This behaviour is compatible with a diamagnetic host (gold host) incorporating paramagnetic impurities (iron atoms)<sup>18</sup>. At 3K the sample shows collective magnetic correlations, visible due to the magnetic irreversibility when the system is cycled between +5T and -5T. When the measuring field was set at -5 T, the hysteresis loop was open, with a coercive field  $\mu_0 H_C = 121$  mT and a reduced remnant magnetization  $M_{0T}/M_{5T} = 0.3$ . When the field was set at +5 T, the analysis showed values of magnetization up to  $9.9 \text{ A}\cdot\text{m}^2\cdot\text{kg}^{-1}$ , five times larger than the one at 300K but still far from saturation<sup>2</sup>.

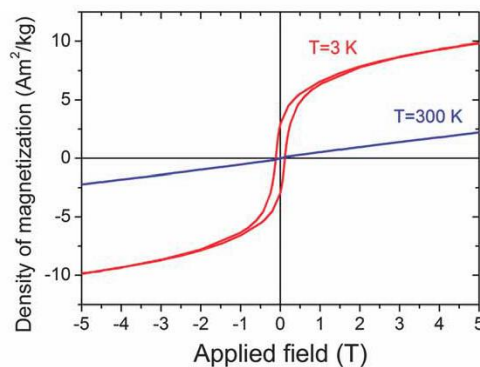


Figure 4.29 – Hysteresis loops at 3K and 300K for an  $\text{Au}_{89}\text{Fe}_{11}$  sample. From reference 2.

Field Cooled (FC) and Zero Field Cooled (ZFC) measurements were carried out, displaying a thermal irreversibility compatible with a spin freezing process<sup>2</sup>. The results are shown in Figure 4.30. The FC magnetization decreases from 3K to 15K, shows a maximum located from 50K to 75K, and then decreases quickly. The ZFC increases quickly, up to a maximum at around 75K, and then decreases sharply mimicking the FC.

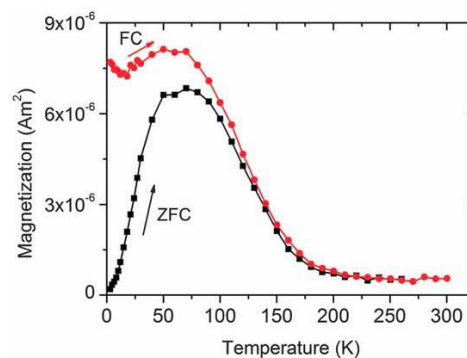


Figure 4.30 – Temperature dependence of FC and ZFC magnetizations. From reference 2.



To better understand the nature of this spin freezing process, the temperature dependence of the AC magnetic susceptibility ( $\chi = \chi' + i\chi''$ ) was analysed in the range from 1 Hz to 1 kHz. The results are shown in Figure 4.31. The in-phase component  $\chi'$  moves from 70K to 76K when the frequency is increased, while the out-of-phase component shows a peak at around 40K, but shows a much less clear trend. Considering the shift in the maximum  $\chi'$  ( $T_{max}$ ) with a decade change in frequency and applying the formula proposed by Midosh and Barrett<sup>19</sup>, it becomes possible to calculate  $\Delta T_{max}/[T_{max}\Delta \log(2\pi\nu)]$ . The calculated values ( $\sim 0.01$ - $0.02$ ) agree with those expected of a spin-glass ( $10^{-2}$  to  $10^{-3}$ )<sup>2, 19</sup>.

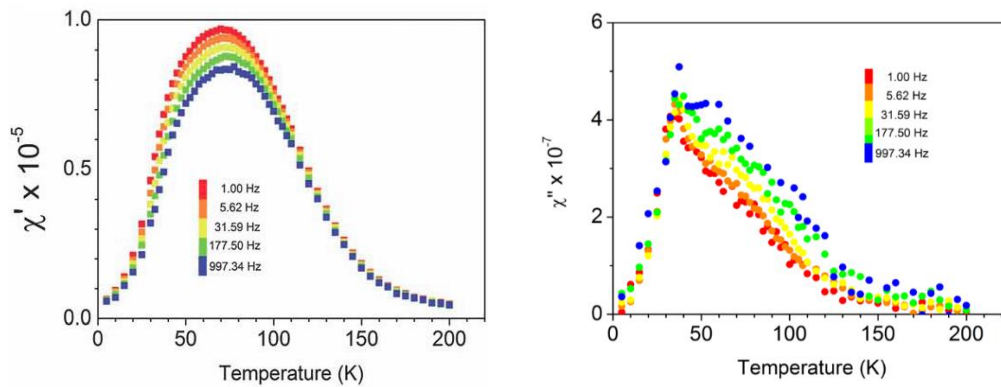


Figure 4.31 – (Left) Values of the in-phase component  $\chi'$  of the AC magnetic susceptibility in function of the frequency. (Right) Values of the out-of-phase component  $\chi''$  of the AC magnetic susceptibility in function of the frequency. From reference 2.

This happens because  $\text{Au}_{1-x}\text{Fe}_x$  alloys with an iron content lower than the percolation threshold ( $x = 0.155$ ) show a transition from paramagnetic to spin-glass behaviour at a temperature  $T_g$  that increases with  $x$ , arriving up to  $50\text{K}$ <sup>20</sup>. The spin-glass behaviour has its origins in the random distribution of the iron atoms in the gold matrix and the competing ferromagnetic-antiferromagnetic (FM-AFM) exchange interactions that take place between iron atoms via the gold conduction band (a mechanism known as Ruderman-Kittle-Kasuya-Yosida)<sup>21-23</sup>.

The density of magnetization at 5T,  $9.9 \text{ A}\cdot\text{m}^2\cdot\text{kg}^{-1}$ , corresponds to a magnetic moment of  $0.32 \mu_B$  per atom. If only the iron atoms contribute to the total magnetization, the net magnetization of the iron atoms can be calculated as  $292 \pm 30 \text{ A}\cdot\text{m}^2\cdot\text{kg}^{-1}$ , giving a magnetic moment of  $2.92 \pm 0.3 \mu_B$  per iron atom. This value is particularly interesting when compared to the bulk value of  $2.2 \mu_B$  per iron atom found in bulk bcc Fe, and is in agreement with previously reported calculated<sup>24</sup> and experimental<sup>25</sup> values for bulk gold-iron alloys. In these structures the iron atoms in the fcc structure are in the high spin state due to the stabilizing effect conferred by the lattice expansion<sup>26</sup>. In the alloy, the magnetization contribution of the

#### 4. Gold-Iron alloy nanoparticles

gold atoms is usually considered negligible<sup>24, 27</sup>. In the end, both the spin-glass behaviour at low temperature and the large magnetization value for Fe atoms support the hypothesis of a randomized structure of iron atoms, where large clusters are absent<sup>2</sup>.

The relaxivity of the nanoparticles was tested with <sup>1</sup>H NMR measurements with a frequency from 10 KHz to 60 MHz<sup>28</sup>, to better cover the range used in typical clinical and research MRI tomographs. The relaxivities  $r_1$  and  $r_2$  weighted by the magnetic centre concentration (the inverse of transverse <sup>1</sup>H nuclear relaxation times  $T_1$  and  $T_2$ ) are shown in Figure 4.32. The differences in behaviour of  $r_1(\nu)$  are attributable to the two different contributing mechanisms<sup>29-31</sup>. When  $\nu$  is lower than 1-5 MHz the mechanism that drives the nuclear relaxation is the Néel relaxation of the particle magnetization, that gives a correlation time related to the magnetic anisotropy barrier, giving a flattening of  $r_1(\nu)$ <sup>29-31</sup>. For higher frequencies the dominant mechanism is the Curie relaxation, that considers the diffusion of water molecules near magnetic centers, and gives a maximum of  $r_1(\nu)$  at higher frequencies<sup>29-31</sup>. Furthermore, when the distance between the hydrogen nuclei and the magnetic core is bigger than 5 nm, there is a noticeable dispersion in intermediate frequencies<sup>29-31</sup>. In the sample of Au-Fe nanoparticles, the high- and low-frequencies contribution are absent, thanks to the high magnetic anisotropy<sup>32, 33</sup> and the considerable thickness of the PEG shell, that in water can reach up to 10-15 nm<sup>34</sup>.

The values of  $r_2(\nu)$  rapidly rise when the frequencies surpass 7 MHz ( $64 \text{ s}^{-1}\cdot\text{mM}^{-1}$ ), reaching values comparable to those of commercial contrast agents such as Endorem ( $99 \text{ s}^{-1}\cdot\text{mM}^{-1}$ ). This is already a good result for a contrast agent, but the values of the  $r_1/r_2$  ratio, reaching up to 100 and never getting under 5 (whereas for the majority of contrast agents the threshold value is 2)<sup>30, 32, 33</sup>. The image reported below, obtained with a Spin Echo sequence, shows the promises of the nanoparticles as contrast agents.

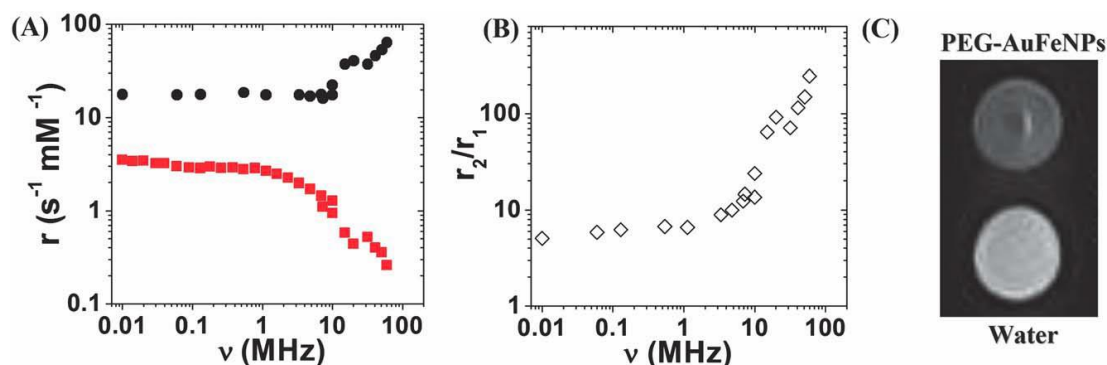


Figure 4.32 – Relaxivity properties of PEG-Au<sub>89</sub>Fe<sub>11</sub> nanoparticles. (A)  $r_1$  longitudinal (red squares) and  $r_2$  transversal relaxation rates (black dots). (B)  $r_2/r_1$  ratio. (C) Low frequency (8.5 MHz) shadows of nanoparticles (above) and water (below). From reference 2.

## 4.7 Au-Fe NPs as Multimodal Contrast Agents

The interesting properties of these alloy nanoparticles suggest their potential use as multimodal contrast agents (MCAs). Indeed we have shown in Section 4.3 that these nanoparticles are also capable of SERS, and in Section 4.2 that the structure (and avenues of functionalization) are those of gold nanoparticles. This also suggested the potential use of the AuFe nanoalloys as x-ray absorption computerized tomography (CT) contrast agents, since gold has a very high X-ray linear coefficient, almost 50 times greater than that of iron<sup>35</sup>.

An efficient multimodal contrast agent needs to show the best efficiency in each of the modes it is used. However, perfect multimodality in nanoalloys is not achievable in reality, because the gain in a mode is always balanced by the loss in a different mode (as we have seen in Section 4.2, talking about the loss of SERS enhancement with the increasing iron content). A graph reporting the efficiency of these MCAs is shown in Figure 4.33. The SERS and CT efficiency of the nanoparticles increase with the gold content, while the MRI efficiency is proportional to the iron content. A “sweet spot”, where the three systems coexist at the top of the efficiency is found with an iron content close to 10%.

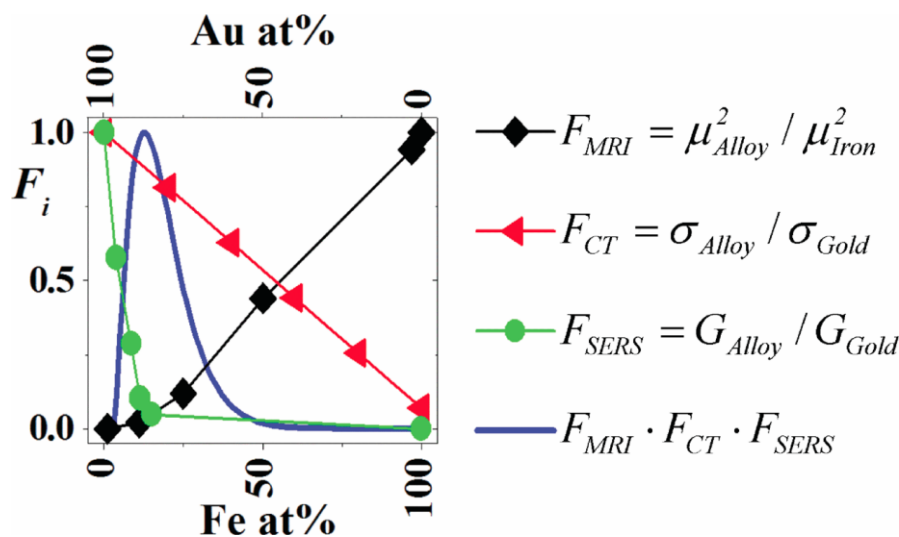


Figure 4.33 – Efficiencies of the imaging modes for the alloy nanoparticles as a function of Iron content. From reference <sup>36</sup>

MRI measurements, carried out in a 200 MHz instrument operating at 4.7 T with different concentrations of nanoparticles gave a value of relaxivity of  $60 \text{ mM}^{-1} \cdot \text{s}^{-1}$ , in agreement with the values found in Section 4.4, and not too far from  $100 \text{ mM}^{-1} \cdot \text{s}^{-1}$ , the value of Endorem™, a commercial contrast agent used as a benchmark. Similar tests were carried out for CT imaging with MCAs at different concentrations compared to pure gold nanoparticles. The value of absorption for nanoparticles with a concentration of 5.5 mg/mL was found to be 225



#### 4. Gold-Iron alloy nanoparticles

Hounsfield Units (HU), a value compatible with that of gold nanoparticles with similar concentration<sup>37</sup>. The absorption value also remained good (above 60 HU) for nanoparticles with a concentration below 1 mg/mL<sup>36</sup>. The results for both tests are shown in Figure 4.34, where it is possible to see that the MCAs compare favourably to both our reference contrast agents.

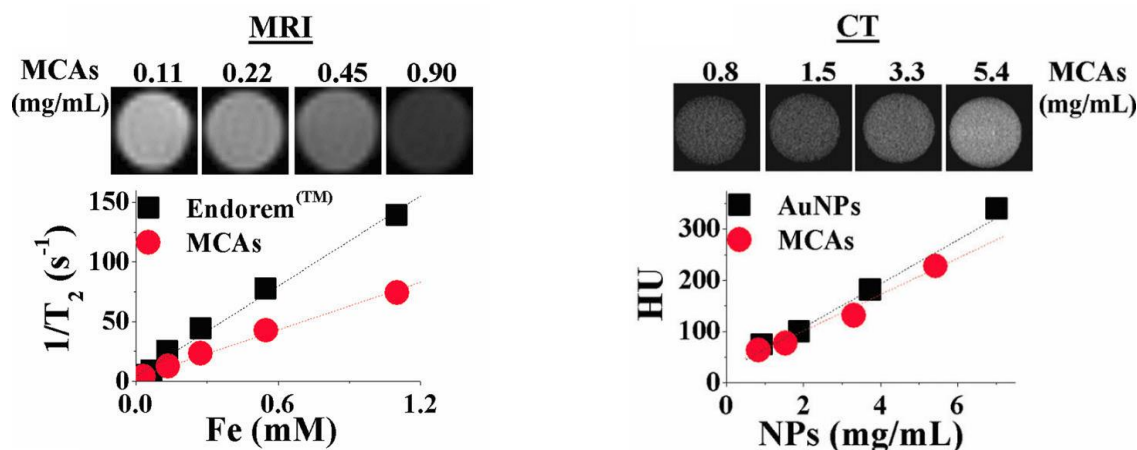


Figure 4.34 – (Left) MRI phantoms of samples loaded with different concentrations of nanoparticles, and relaxivity plot as a function of iron concentration for the alloy nanoparticles and Endorem<sup>TM</sup>. (Right) CT phantoms of samples loaded with different concentrations of nanoparticles, and plot of X-ray attenuation as a function of concentration for the alloy nanoparticles and gold nanoparticles. From reference <sup>36</sup>

An important parameter for the functionality of the nanoparticles as MCAs is the biocompatibility. This means that the contrast agent must not damage the host in any way. The cytotoxicity of the alloy nanoparticles was tested in an XTT assay on mouse mammary tumour cells (4T1) and on human histiocytic tumour cells (U397). The ability of the cell to proliferate indefinitely was also tested with a clonogenic assay, to document possible damages on the cell reproductive ability after incubation with the MCAs. The results of the tests are reported in Figure 4.35:

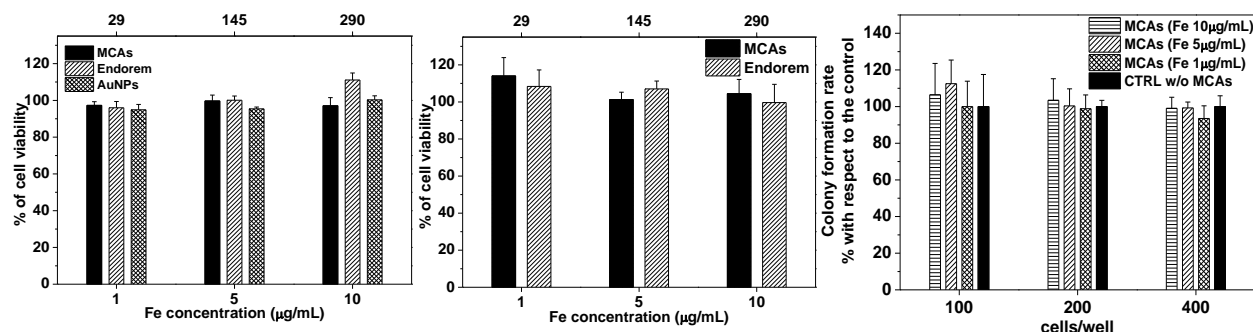


Figure 4.35 – (left) XTT Assay on 4T1 cells to evaluate cell viability after treatment with MCAs, Endorem<sup>TM</sup>, and AuNPs. The amount of Endorem<sup>TM</sup> and AuNPs was normalized to the quantity of (respectively) iron and gold available in the MCAs. (center) XTT Assay on PMA differentiated U937 cells after 24 hours treatment with different concentrations of MCAs and Endorem<sup>TM</sup>. (right) Soft agar clonogenic assay performed on 4T1 cells to evaluate the effects of MCAs on the clonogenic potential. The percentage of colony formation was calculated with respect to a mock-treated control. From reference <sup>36</sup>.

The nanoparticles did not induce appreciable modification in the cell viability when compared with Endorem™ of pure gold nanoparticles, even with the maximum concentration of nanoparticles (Fe = 10 µg/mL) surpassing the maximum concentration of Endorem™ used in analysis (Fe = 5.5 ±0.6 µg/mL, 0.56 mg/Kg). Further tests were carried out on two primary cell lines (human fibroblasts and myoblasts) and an additional tumour cell line (LNCaP), and in Annexin V assay on the human primary normal cells and two tumour cell lines (4T1 and U937). The results of these tests are reported in Table 4.6. From the tests it is possible to see that these nanoparticles show the same kind of biocompatibility of PEG-coated gold nanoparticles<sup>38</sup> or dextran coated iron oxides<sup>39, 40</sup>.

Cell type	Untreated	With MCAs, Fe = 10 µg/mL	Positive control
4T1	0.5 %	0.5 %	5.6 % *
U937 PMA differentiated	1.3 %	1.9 %	30.9 % *
Human Fibroblast	5.1 %	3.4 %	55.4 % **
Human Myoblast	1.2 %	1.4 %	13 % **

Table 4.6 – Percentage of apoptosis revealed by Annexin V assay after the treatment with MCAs for 24 hours. The positive control cells were treated with Taxol 2 µM or at 56° C in water for 30'. From reference 36.

The next step in evaluating the viability of the MCAs was an in-vivo test with a syngeneic mouse model. Balb/c mice with subcutaneous 4T1 tumour were intravenously injected with MCAs with an iron concentration of 1.2 mg/kg. MR images of the specimens were then acquired at 4.7 T over 24 hours. MR images of the liver and the tumour, and data of the ratio between T<sub>2</sub> relaxation times before and after MCAs addition are reported in Figure 4.36. The trend in the liver signals suggests that the nanoparticles quickly accumulate in the organ, showing a decrease in the T<sub>2</sub> only after ~20 hours. The signal from the tumour does not show great changes for similar amount of time, after whom there is a decrease in T<sub>2</sub> times of about 10%, suggesting that the nanoparticles have spread in the tissue interstices and do not move due to the absence of drainage effect (EPR effect)<sup>41-43</sup>.

#### 4. Gold-Iron alloy nanoparticles

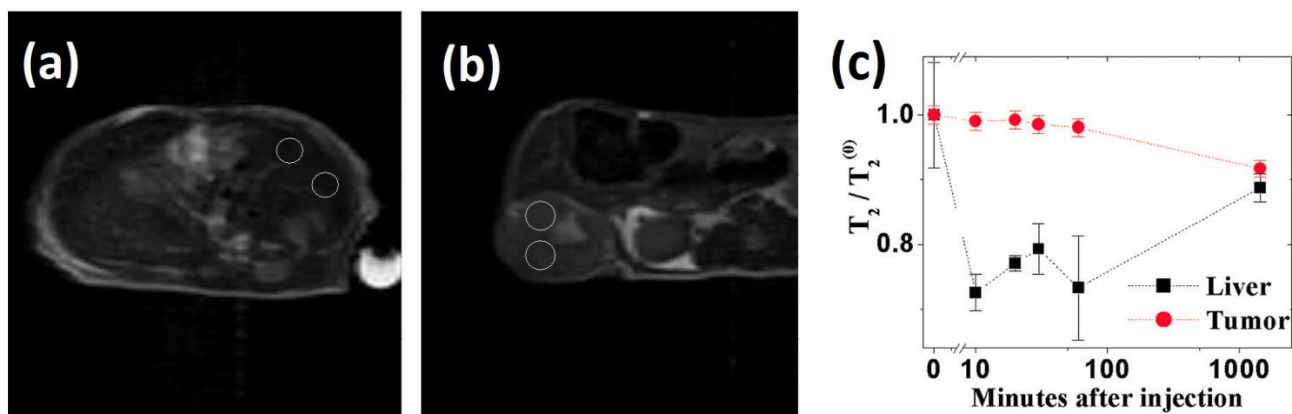


Figure 4.36 –  $T_2$ -weighted images of the liver (a) and tumour (b) of a representative mouse treated with the MCAs 24 hours after the injection. The increased negative contrast (due to the decreased  $T_2$  times) is quantitatively confirmed by the measurement in the white circled areas before and after the MCAs injection. (c) Quantitative data reporting the ratio before and after MCAs injection for the white circled areas in figure a and b. From reference 36.

Tests carried out ex vivo by Raman spectroscopy on the same tissues showed retention of the MCAs localized mainly on liver, spleen and kidneys, while the signals from lung and blood are negligible. The retention of MCAs is visible even to the naked eye, when looking to pellets obtained from the centrifugation of lysates from the target organs. The results of the Raman analysis and pictures from the pellets are reported in Figure 4.37. The retention reported in the graph is confirmed by the images.

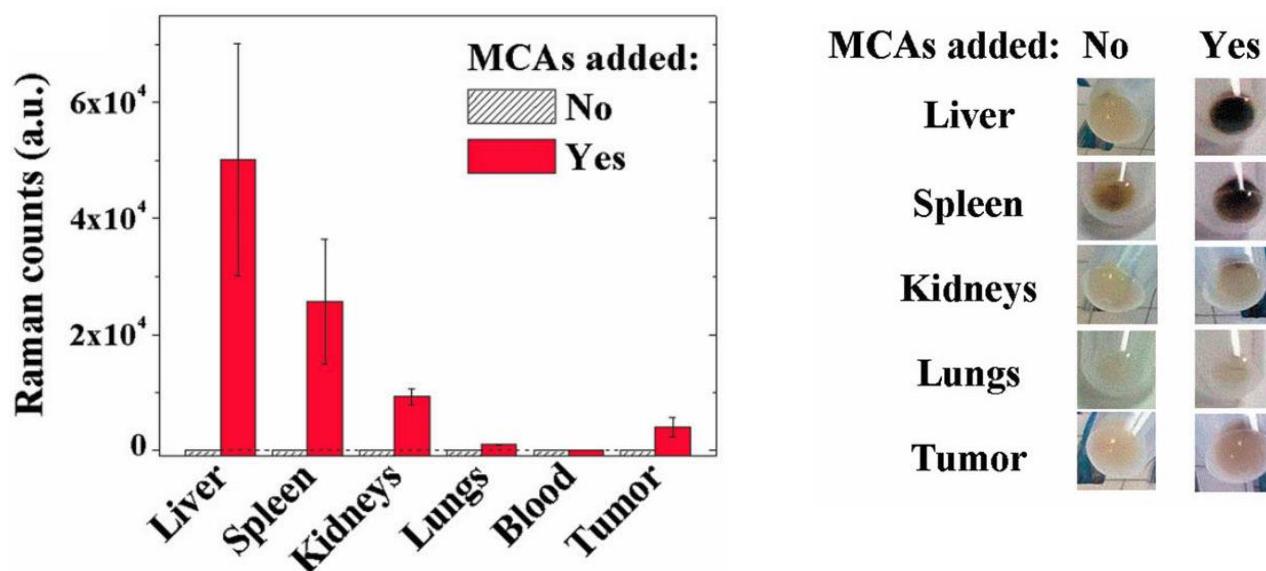


Figure 4.37 – (Left) Plot of Raman Intensity at 1505  $cm^{-1}$  for different organs. (Right) Images of pellets obtained by centrifugation of the lysates from mice treated with MCAs and mock-treated. From reference 36.

CT analysis were also carried out on the lysates of liver and tumour, to confirm the good results given by the bare nanoparticles. The data from this analysis are shown in Table 4.7:

Mouse	Sample	HU	mg/mL of sample	(HU)/(mg/mL of sample)
Treated with MCAs	Liver	160	156	1.03
	Tumour	65	36	1.82
Control	Liver	110	229	0.48
	Tumour	110	97	1.22

Table 4.7 – CT data from lysates of tumour and liver tissue from a specimen injected with MCAs and a control specimen. From reference 36.

The last test carried out was a histopathological evaluation of the tissues from liver and kidneys from a mouse treated with MCAs and from a control specimen. The results are shown in Figure 4.38:

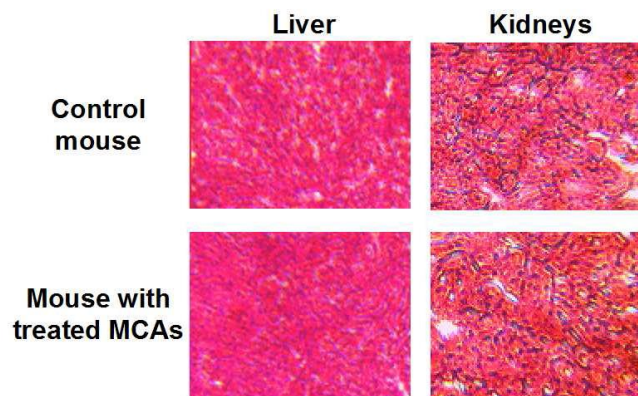


Figure 4.38 – Microscope Images (100X magnification) of liver and kidney tissue obtained from a mouse treated with MCAs and a control mouse. Samples stained with hematoxylin and eosin (H&E). From reference 36.

The evaluation did not find any abnormalities in the tissue, further demonstrating the biocompatibility of these alloy nanoparticles.

## 4.8 Ablation of multilayer targets

A different approach to synthesize gold-iron nanoparticles was attempted by ablating multilayer targets obtained in collaboration with Ca' Foscari University of Venice. Multilayers were prepared according to the well established procedures of the Cà Foscari University, at room temperature by radiofrequency magnetron multitarget sputtering deposition of iron and gold, in pure Ar atmosphere at a working pressure of  $40 \cdot 10^{-4}$  mbar, by alternate use of two different 13.56 MHz radiofrequency sources for iron and gold, respectively. Substrate were soda-lime glass slides. Before deposition, the soda-lime substrates were RF-biased at 20 W for 20 min, for removing possible surface contaminations (removed layer thickness around 10 nm). During deposition, the sample holder was rotating at 10 Hz. The rf power to the 2 inches

#### 4. Gold-Iron alloy nanoparticles

diameter targets was 40 W for iron and 20 W for gold. Different deposition times were used to obtain layers of the prescribed thickness. The final thickness of the different layers was measured by Rutherford Backscattering spectrometry (RBS), by using a 2.2 MeV  $4\text{He}^+$  beam. The incident direction was normal to the sample surface, and scattered particles were detected at the angle of  $160^\circ$ .

Different film thicknesses were used, as shown in Table 4.8:

Sample	Composition
286	Fe 34 nm + Au 95 nm
287	Fe 34 nm + Au 175 nm
288	Fe 56 nm + Au 95 nm
289	Fe 56 nm + Au 175 nm
314	Fe 95nm + Au 56nm
315	Fe 175nm + Au 56nm
316	Au 56nm + Fe 56nm
317	Fe 56nm + Au 56nm
318	Fe/Au/Fe/Au (each layer 20 nm)
319	Fe/Au/Fe/Au (each layer 37 nm)

Table 4.8 – Composition of the multilayer targets. Substrate is silica glass.

The obtained targets were ablated with a 1064 nm laser operating with 6 ns pulses at 32 mJ power, at two different frequencies, 0.5 Hz and 10 Hz. The cell was mounted on a motorized translating stage moving at constant speed. When the frequency is 0.5 Hz, the ablation craters are far enough to avoid thermal damage to the interface between the two metals, which typically takes place by thermal or mechanical effects. Conversely, when the ablation frequency is 10 Hz, each pulse hits an area that was in the influence zone of the previous ablation. To have a clear idea of the differences, in Figure 4.39 are reported the pictures of two targets:

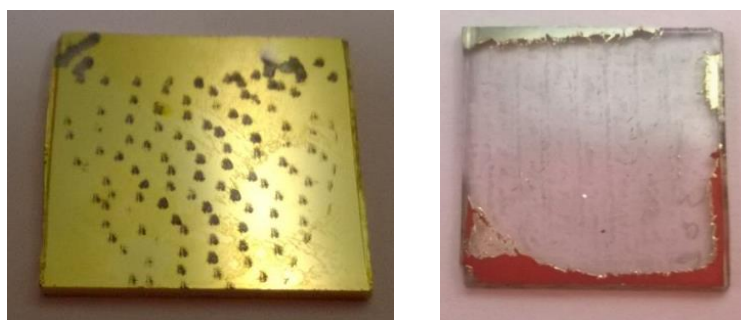


Figure 4.39 – Pictures of the target ablated at 0.5 Hz (left) and 10 Hz (right)



The second parameter that was altered is the solvent. we used again water and ethanol, with the objective to find different trends, in a manner similar to what happened with AuFe bulk targets (see Section 4.2). We immediately noticed an appreciable effect from the combination of solvent and frequency: in Figure 4.40 are reported the effects of the ablation frequency and solvent type for Sample 288. The optical properties of nanoparticles generated by ablation at very low laser repetition rate do not seem to be influenced in a significant way from the ablation environment. At 10 Hz the difference between water and ethanol is much more similar to the one discovered for bulk alloy targets, with a stronger SPA for NPs obtained in water (probably due to an higher gold content) and a more damped one for NPs obtained in ethanol (likely with an higher content of iron).

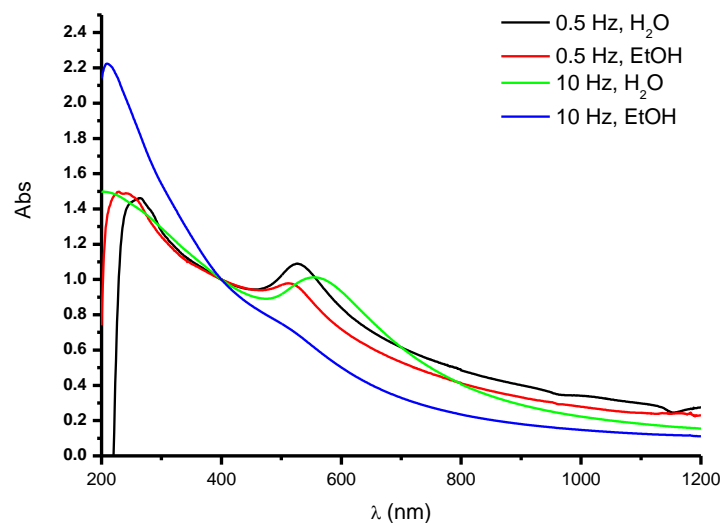


Figure 4.40 – UV-Visible absorption spectra of the nanoparticles obtained by ablation of the multilayer substrates by varying the frequency and the solvent. The spectra are normalized at 400 nm for an easier visualization.

Comparing the TEM images of the samples, the hypothesis formulated by observing the UV spectra is confirmed. As can be seen in Figure 4.41, the samples obtained in water and ethanol at low laser repetition rates appear very similar.

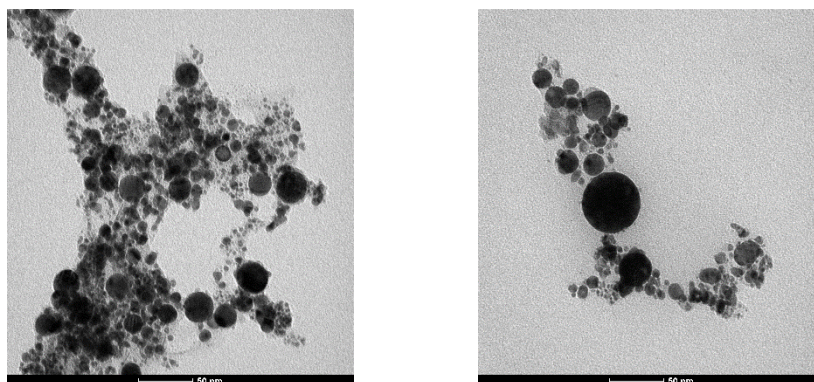


Figure 4.41 – TEM images of nanoparticles obtained from substrate 288 in H<sub>2</sub>O (left) and EtOH (right) at 0,5 Hz.

#### 4. Gold-Iron alloy nanoparticles

On the other hand, the nanoparticles obtained at higher laser repetition rate show interesting differences. Nanoparticles obtained in water often show an oxide shell, and higher polydispersity in dimensions. On the other hand, the nanoparticles obtained in EtOH do not show this shell, suggesting an alloyed structure. The stronger SPA shown in the sample obtained in water may be also influenced by the higher number of gold-rich small NPs in the sample.

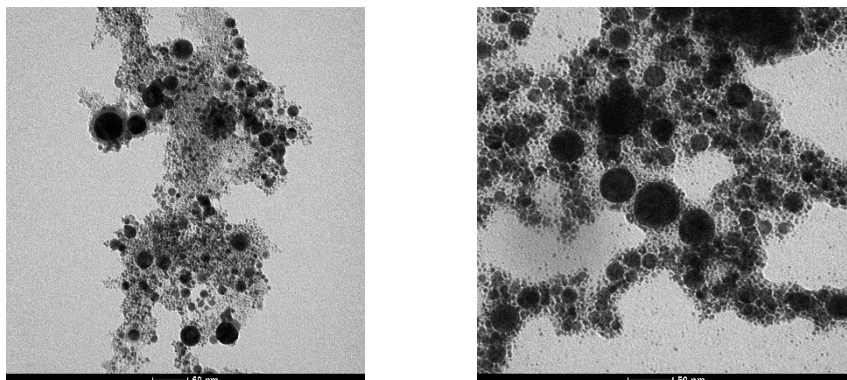


Figure 4.42 – TEM images of nanoparticles obtained from substrate 288 in H<sub>2</sub>O (left) and EtOH (right) at 10 Hz.

We carried out similar experiments on the other available samples, aiming to determine the effect of the ratio of gold to iron, and of the different order of deposition.

Comparing samples obtained from substrates 286 and 315 in EtOH it is possible to see the effect of increasing the iron content in the starting substrate. The results are shown in Figure 4.43, and it is possible to see that by inverting the proportions of gold and iron (from ~1:3 Fe:Au in substrate 286 to ~3:1 in substrate 315) the obtained nanoparticles show a much more damped SPA in the iron-rich sample.

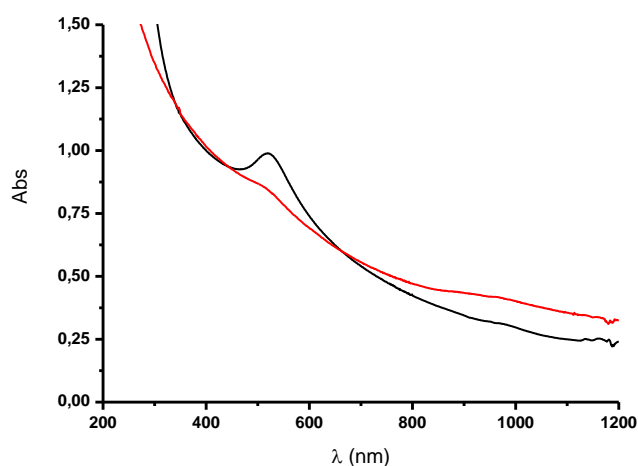


Figure 4.43 – UV-Visible absorption spectra of the nanoparticles obtained by substrate 286 (black) and 315 (red) in EtOH at 0,5 Hz. The spectra are normalized at 400 nm for an easier visualization.

We also studied the effect of the order of deposition of the sample by comparing NPs from substrate 316 to substrate 317. These substrates are identical in composition, but the order of deposition is inverted. The absorption spectra of the NPs obtained from these substrates in H<sub>2</sub>O and EtOH at 0.5 Hz are shown in Figure 4.44. Absorption spectra from samples obtained in water show important differences, with stronger SPA for sample 317. A similar trend can be observed in the samples obtained in EtOH.

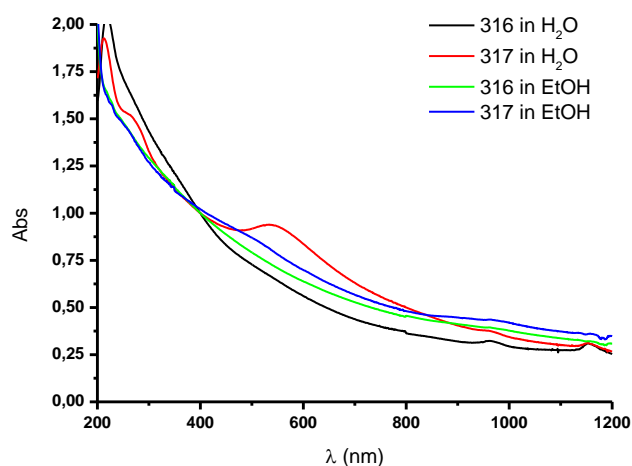


Figure 4.44 – UV-Visible absorption spectra of the nanoparticles obtained at 0,5 Hz. The spectra are normalized at 400 nm for an easier visualization.

TEM analysis shows peculiar core@shell structures in the samples obtained in water, shown in Figure 4.45, like those found in sample 288 when ablated in water (see figure 4.42).

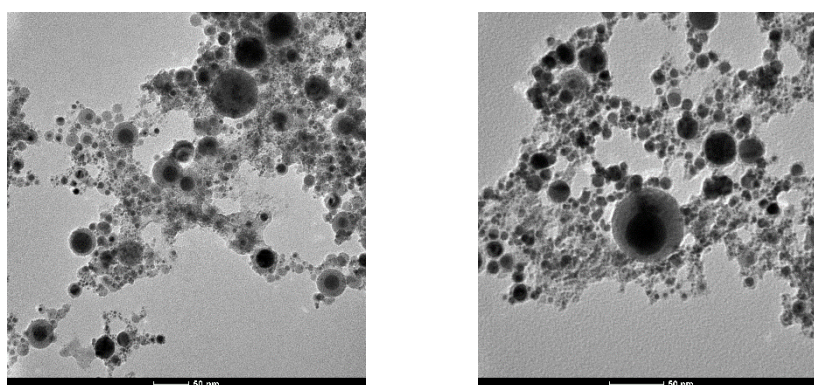


Figure 4.45 – TEM images of nanoparticles from sample 316 (left) and 317 in H<sub>2</sub>O (right).

However in samples obtained in ethanol no similar structures are visible, suggesting an alloy composition, as shown in Figure 4.46:



#### 4. Gold-Iron alloy nanoparticles

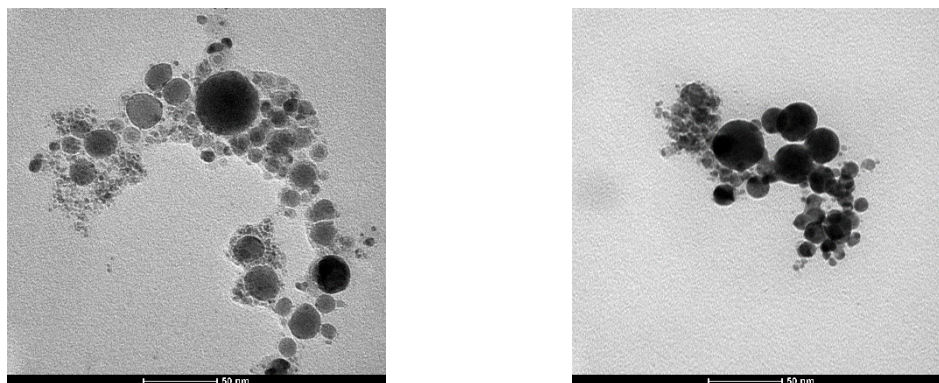


Figure 4.46 – TEM images of nanoparticles from sample 317 (left) and 318 in EtOH (right).

The main effect seems again to be linked to the synthesis environment, since in water appeared core@shell structures.

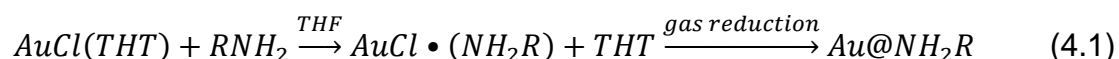
Further analysis on the effects of these parameters are ongoing. Overall, this type of experiments seems to hold big promises for the fabrication of complex nanostructures as well as , but also to better understand the dynamics of laser ablation.

## 4.9 Magnetic-Plasmonic NPs by LASiS and chemical reduction synthesis

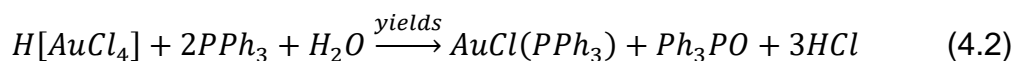
These experiments were carried during a short period of studies abroad (March-April 2014) under the supervision of Professor Catherine Amiens, with the financial support of COST Action MP0903 Nanoalloy.

The objective of this research period was to create a gold shell on the surface of iron nanoparticles obtained via LASiS of a pure metal target (>99.99%).

To obtain this kind of reaction, we looked to the reaction proposed by Debouttière<sup>44</sup>, who uses gas reduction of Chloro(tetrahydrothiophene)gold(I) (AuCl(THT)) after a ligand exchange reaction with amines:



Our objective was the substitution of the gas reduction with reduction due to Borane tert-butylamine complex (TBAB), a reducing agent used in similar reactions. More precisely, Zheng et al.<sup>45</sup> have used this reagent to reduce Chloro(Triphenylphosphine)gold (CTPP), a gold precursor more stable than AuCl(THT), that has degradation problems when exposed to UV-lights. To obtain CTPP, we used this reaction<sup>46</sup>:



The first step in the synthesis was obtaining iron nanoparticles in ethanol, with HDA dissolved inside. Synthesis of iron in ethanol has been shown in ref.<sup>47</sup>, and in our case we added 30 mg/mL of HDA. We then dried the sample and solubilized it again after arriving at the LCC. We then synthesized CTPP following the reaction shown in equation 4.2, obtaining a sample with a good degree of purity. Analysis results for the sample are reported in Table 4.9. The results are very close with the expected composition, and the sample purity is confirmed.

Elements	% theoretical	% 1 <sup>st</sup> test	% 2 <sup>nd</sup> test
C	43.6	44.31	44.3
H	3.1	2.74	2.55

Table 4.9 – Theoretical and actual composition of the Chloro(Triphenylphosphine)gold sample.

The following tests were test synthesis in toluene and THF, obtained by adding the iron nanoparticles obtained at our laboratory in liquid form (HDA melts at 44-48 °C) to the solvent, and subsequently adding the gold precursor and then the reducing agent. In both tests the reaction develops quickly, and the sample turns to red. Both samples show appreciable SPA, but the magnetic fractions are hardly separable, and the bigger fraction of gold remains confined in the non-magnetic fraction, leading us to think that the gold nanoparticles nucleate separately from the iron ones.

To avoid this problem, we used a less powerful reducing agent, ascorbic acid. We carried out the syntheses in THF and toluene, and this time we were able to separate the magnetic fraction. UV-Visible absorption spectra and size distribution of the obtained nanoparticles (from TEM data) are shown in Figure 4.47, and it is possible to see that the magnetic fractions retain an appreciable SPA, and the size distribution is compatible for both samples.

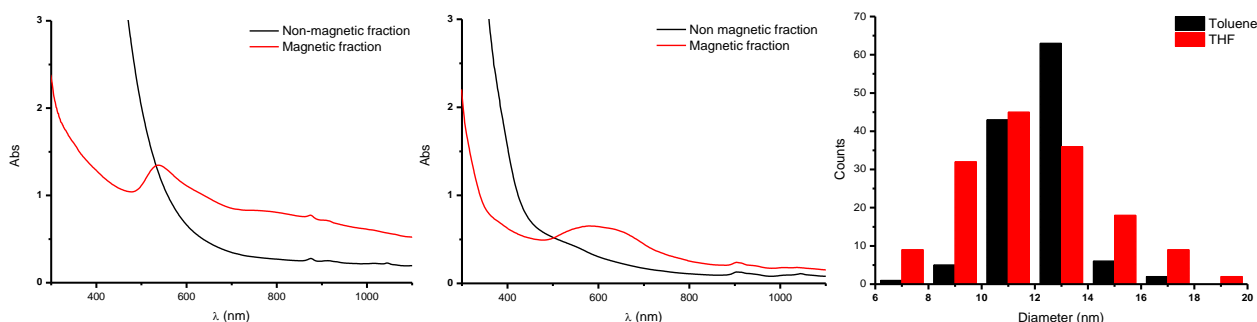


Figure 4.47 – UV-Visible absorption spectra of the magnetic and non-magnetic fractions from the sample obtained in toluene (left) and in THF (centre). On the right, size distribution of the two samples.

#### 4. Gold-Iron alloy nanoparticles

We then proceeded to carry out HRTEM-EDX analysis of the nanoparticles obtained above, to ascertain the composition. A sample image is shown in Figure 4.48, without and with EDX data. From this image it is possible to see that there is no formation of an uniform gold shell on the nanoparticles. On the contrary, many separate gold nanoparticles have formed, probably trapped in the HDA matrix around the iron nanoparticles.

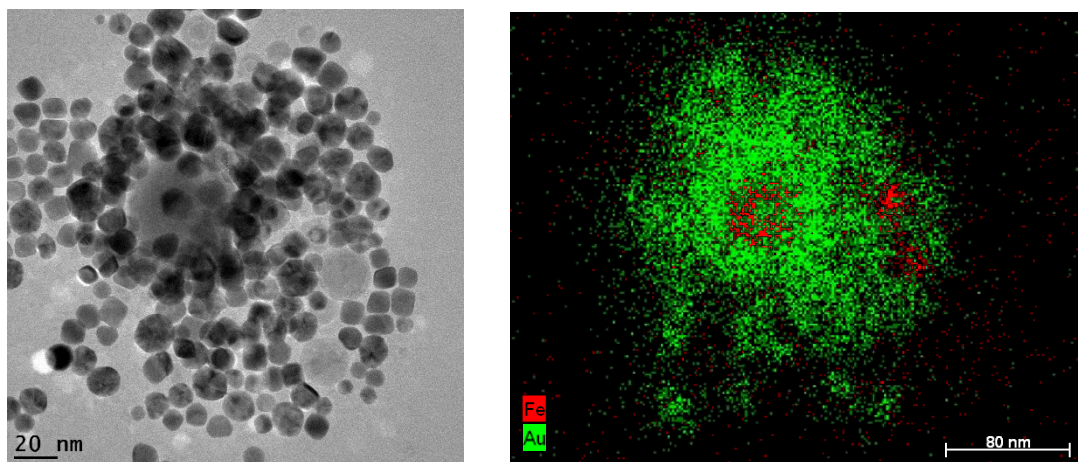


Figure 4.48 – HRTEM (left) and EDX data from the same image (right) of the sample obtained in THF.

Since this first approach has not worked out as expected, further work will have to be carried on this avenue of research to avoid this problem.

## 4.10 Bibliography

- 1 V. Amendola, S. Scaramuzza, S. Agnoli, S. Polizzi and M. Meneghetti, *Nanoscale*, 2014, **6**, 1423-1433.
- 2 V. Amendola, M. Meneghetti, O. M. Bakr, P. Riello, S. Polizzi, D. H. Anjum, S. Fiameni, P. Arosio, T. Orlando and C. de Julian Fernandez, *Nanoscale*, 2013, **5**, 5611-5619.
- 3 E. Pensa, E. Cortés, G. Corthey, P. Carro, C. Vericat, M. H. Fonticelli, G. Benítez, A. A. Rubert and R. C. Salvarezza, *Acc. Chem. Res.*, 2012, **45**, 1183-1192.
- 4 S. Sun, P. Mendes, K. Critchley, S. Diegoli, M. Hanwell, S. D. Evans, G. J. Leggett, J. A. Preece and T. H. Richardson, *Nano letters*, 2006, **6**, 345-350.
- 5 Y. Lee, Y. Kudryavtsev, V. Nemoskalkenko, R. Gontarz and J. Rhee, *Physical Review B*, 2003, **67**, 104424.
- 6 M. G. Blaber, M. D. Arnold and M. J. Ford, *Journal of Physics: Condensed Matter*, 2010, **22**, 143201.
- 7 H. Koike, S. Yamaguchi and T. Hanyu, *Journal of the Physical Society of Japan*, 1976, **40**, 219-225.
- 8 O. Hunderi, *Appl. Opt.*, 1972, **11**, 1572-1578.
- 9 A. Mezni, I. Balti, A. Mlayah, N. Jouini and L. S. Smiri, *The Journal of Physical Chemistry C*, 2013, **117**, 16166-16174.
- 10 J. Goodman, B. T. Draine and P. J. Flatau, *Opt. Lett.*, 1991, **16**, 1198-1200.
- 11 B. T. Draine and P. J. Flatau, *JOSA A*, 1994, **11**, 1491-1499.
- 12 T. A. Witten and L. M. Sander, *Physical Review B*, 1983, **27**, 5686.
- 13 A. J. Hurd and D. W. Schaefer, *Phys. Rev. Lett.*, 1985, **54**, 1043.
- 14 S. Scaramuzza, S. Agnoli and V. Amendola, *Phys. Chem. Chem. Phys.*, 2015, **17**, 28076.
- 15 P. A. Giguère and I. Liu, *Canadian Journal of Chemistry*, 1957, **35**, 283-293.
- 16 S. Ibrahimkutty, P. Wagener, A. Menzel, A. Plech and S. Barcikowski, *Appl. Phys. Lett.*, 2012, **101**, 103104.
- 17 P. Wagener, S. Ibrahimkutty, A. Menzel, A. Plech and S. Barcikowski, *Physical Chemistry Chemical Physics*, 2013, **15**, 3068-3074.

- 18 V. Cannella and J. Mydosh, *Physical Review B*, 1972, **6**, 4220.
- 19 J. Mydosh and T. W. Barrett, *J. Biol. Phys.*, 1993, **19**, 310-312.
- 20 B. Verbeek and J. Mydosh, *Journal of Physics F: Metal Physics*, 1978, **8**, L109.
- 21 A. Chakrabarti and C. Dasgupta, *Phys. Rev. Lett.*, 1986, **56**, 1404.
- 22 I. Campbell, S. Senoussi, F. Varret, J. Teillet and A. Hamzić, *Phys. Rev. Lett.*, 1983, **50**, 1615.
- 23 A. Prokhorov, V. Anzin, D. Vitukhnovskii, E. Zhukova, I. Spektor, B. Gorshunov, S. Vongtragool, M. Hesselberth, J. Aarts and G. Nieuwenhuys, *Journal of Experimental and Theoretical Physics*, 2006, **103**, 887-896.
- 24 F. Wilhelm, P. Pouloupoulos, V. Kapaklis, J. Kappler, N. Jaouen, A. Rogalev, A. Yaresko and C. Politis, *Physical Review B*, 2008, **77**, 224414.
- 25 S. Khmelevskiy, J. Kudrnovský, B. Gyorffy, P. Mohn, V. Drchal and P. Weinberger, *Physical Review B*, 2004, **70**, 224432.
- 26 V. Moruzzi, P. Marcus, K. Schwarz and P. Mohn, *Physical Review B*, 1986, **34**, 1784.
- 27 J. Cable and E. Wollan, *Physical Review B*, 1973, **7**, 2005.
- 28 G. Ferrante and S. Sykora, *Advances in inorganic chemistry*, 2005, **57**, 405-470.
- 29 A. Roch, R. N. Muller and P. Gillis, *J. Chem. Phys.*, 1999, **110**, 5403-5411.
- 30 P. Gillis, F. Moiny and R. A. Brooks, *Magnetic Resonance in Medicine*, 2002, **47**, 257-263.
- 31 S. Laurent, D. Forge, M. Port, A. Roch, C. Robic, L. Vander Elst and R. N. Muller, *Chem. Rev.*, 2008, **108**, 2064-2110.
- 32 L. Lartigue, C. Innocenti, T. Kalaivani, A. Awwad, Sanchez Duque, Maria del Mar, Y. Guari, J. Larionova, C. Guérin, J. G. Montero and V. Barragan-Montero, *J. Am. Chem. Soc.*, 2011, **133**, 10459-10472.
- 33 H. Amiri, R. Bustamante, A. Millán, N. J. Silva, R. Pinol, L. Gabilondo, F. Palacio, P. Arosio, M. Corti and A. Lascialfari, *Magnetic Resonance in Medicine*, 2011, **66**, 1715-1721.
- 34 T. L. Doane, C. Chuang, R. J. Hill and C. Burda, *Acc. Chem. Res.*, 2011, **45**, 317-326.
- 35 M. Hossain and M. Su, *The Journal of Physical Chemistry C*, 2012, **116**, 23047-23052.
- 36 V. Amendola, S. Scaramuzza, L. Litti, M. Meneghetti, G. Zuccolotto, A. Rosato, E. Nicolato, P. Marzola, G. Fracasso and C. Anselmi, *Small*, 2014, .
- 37 D. Kim, S. Park, J. H. Lee, Y. Y. Jeong and S. Jon, *J. Am. Chem. Soc.*, 2007, **129**, 7661-7665.
- 38 A. Thakor, J. Jokerst, C. Zavaleta, T. Massoud and S. Gambhir, *Nano letters*, 2011, **11**, 4029-4036.
- 39 D. Ling and T. Hyeon, *Small*, 2013, **9**, 1450-1466.
- 40 J. T. Jenkins, D. L. Halaney, K. V. Sokolov, L. L. Ma, H. J. Shipley, S. Mahajan, C. L. Loudon, R. Asmis, T. E. Milner and K. P. Johnston, *Nanomedicine: Nanotechnology, Biology and Medicine*, 2013, **9**, 356-365.
- 41 K. Cho, X. Wang, S. Nie, Z. G. Chen and D. M. Shin, *Clin. Cancer Res.*, 2008, **14**, 1310-1316 (DOI:10.1158/1078-0432.CCR-07-1441 [doi]).
- 42 K. Greish, *J. Drug Target.*, 2007, **15**, 457-464.
- 43 H. Meng, M. Xue, T. Xia, Z. Ji, D. Y. Tarn, J. I. Zink and A. E. Nel, *ACS nano*, 2011, **5**, 4131-4144.
- 44 P. Debouttière, Y. Coppel, P. Behra, B. Chaudret and K. Fajerweg, *Gold Bulletin*, 2013, **46**, 291-298.
- 45 N. Zheng, J. Fan and G. D. Stucky, *J. Am. Chem. Soc.*, 2006, **128**, 6550-6551.
- 46 M. Bruce, B. Nicholson, O. B. Shawkataly, J. Shapley and T. Henly, *Inorganic Syntheses, Volume 26*, 1989, , 324-328.
- 47 V. Amendola, P. Riello and M. Meneghetti, *The Journal of Physical Chemistry C*, 2010, **115**, 5140-5146.

#### 4. Gold-Iron alloy nanoparticles

# Chapter 5

## Iron-doped Ag nanoparticles

### 5.1 Abstract

Silver and iron are two elements used to obtain nanoparticles with various useful functions: silver nanoparticles have antimicrobial and optical characteristics<sup>1,2</sup>, while iron nanoparticles have appreciable magnetic properties<sup>3,4</sup>. As shown in Chapter 4, obtaining alloy nanoparticles from an alloy target via laser ablation is feasible and the composition of products can be tuned by varying the liquid environment for the synthesis.

We applied the same methodology for obtaining Fe-doped Ag nanoparticles, starting from metal targets with two different proportions of Ag and Fe. We studied the process and characterized optical and magnetic properties of the obtained nanoparticles.

### 5.2 Nanoparticles Synthesis

LASiS was performed on alloy targets composed of bimetallic iron-silver solid solution with a composition of 50%-50% or 34%-66% (provided from MaTeck). The ablations were carried out in ethanol and water, using a 1064 nm laser with pulse duration of 6 ns, a power of 80 mJ/cm<sup>2</sup> per pulse, and a frequency of 50 Hz. The UV-vis absorption spectra of the colloidal solutions resulting from laser ablation are reported in Figure 5.1. These spectra show a huge difference in SPA intensity of the silver nanoparticles when compared to the Ag-Fe ones. Among the samples obtained from the two alloy targets the difference in SPA relative intensity is surprisingly in favour of the iron-rich target. However there are no major

## 5. Iron-doped Ag Nanoparticles

differences between samples obtained in water and in ethanol. Since iron is easily oxidized in water, and no obvious advantage comes from choosing this solvent, the following ablations were carried out in ethanol.

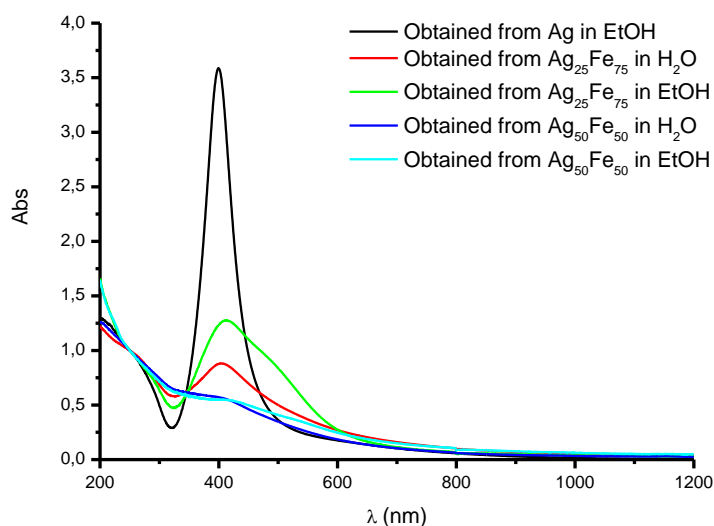


Figure 5.1 – UV-Visible absorption spectra of the Ag-Fe nanoparticles obtained immediately after laser ablation in water and ethanol, and of Ag obtained in ethanol. The spectra are normalized at 250 nm for an easier visualization.

The following step was the investigation of the effect of a post-production treatment usually carried out on the ablated nanoparticles with thiolated PEG and EDTA, followed by centrifugation washing cycles, to remove amorphous iron compounds often observed during LASiS of iron-containing targets<sup>5-7</sup>. The thiolated PEG binds to the surface of the silver nanoparticles via a sulphur-silver bond, and provides stability to the nanoparticles. The EDTA removes unwanted by-products from the surface of the nanoparticles such as amorphous or crystalline iron oxides, which are removed in the last step of centrifugation of the nanoparticles. Since we expected more oxidized species to form on the surface of the nanoparticles, we studied the effect on optical properties of the final products after heating of the solutions for 1-2 hours at different temperatures (30°, 60° and 90° C). The effects on the optical properties of the samples are shown in Figure 5.2. The nanoparticles obtained after the ablation are strongly aggregated, as suggested by the lack of a clearly defined SPA and the progressive decline in absorption (visible as a “shoulder”) at longer wavelengths. The addition of PEG and EDTA in all our samples substantially lowers the aggregation, and the UV spectra after treatment loose optical density in the shoulder region. It appears that the main difference can be found in varying the temperature, more than the treatment time,



since the treatment at higher temperatures gives nanoparticles with a more intense SPA.

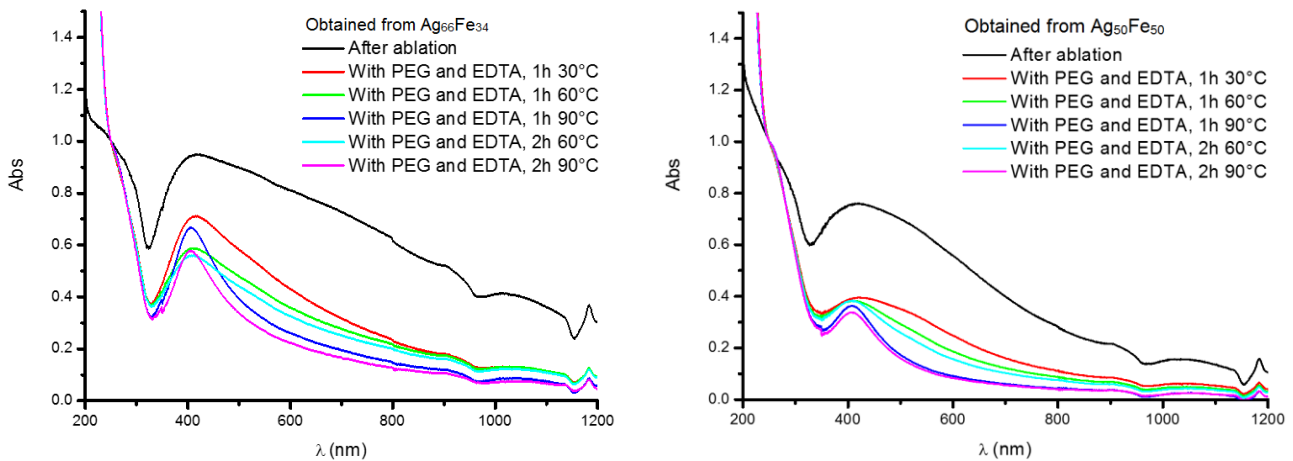


Figure 5.2 – UV-Visible absorption spectra of  $Ag_{75}Fe_{25}$  (left) and  $Ag_{50}Fe_{50}$  (right) silver-iron nanoparticles, treated at different temperatures for 1 or two hours. All the spectra are normalized at 250 nm for an easier visualization.

We chose to continue our studies on the nanoparticles treated at 30°C because we saw in Chapter 4 that a more intense SPA is usually associated with nanoparticles with less iron, and the objective of the synthesis is obtaining nanoparticles that present appreciable magnetic properties.

Finally, we qualitatively evaluated the magnetic response of the synthesized nanoparticles. We placed a magnet in contact with the vial containing the samples to separate the magnetic and non-magnetic fraction. The UV-Visible absorption spectra of the fractions are reported in Figure 5.3. The non-magnetic fractions show sharp plasmon absorptions similar to those of silver nanoparticles, probably indicating a lower amount of iron, and this is in agreement with the observed low sensitivity to magnetic fields. The magnetic fractions, on the other hand, show a broader SPA peak, probably due to bigger sizes and nonspherical shape, similar to what was observed in Au-Fe nanoparticles richer in iron (Chapter 4).

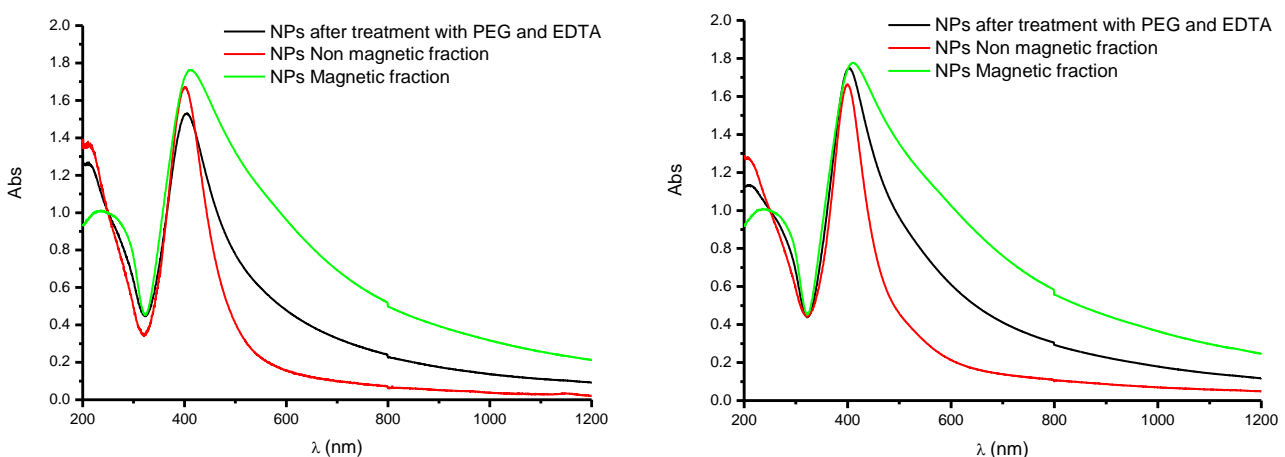


Figure 5.3 – UV-Visible absorption spectra of nanoparticles obtained from  $Ag_{50}Fe_{50}$  (left) and  $Ag_{66}Fe_{34}$  (right) silver-iron, before and after separation of the magnetic and non-magnetic phase. The spectra are normalized at 250 nm for an easier visualization.



## 5. Iron-doped Ag Nanoparticles

The main difference between the two compositions, however, is the yield of the two fractions. Yield data, obtained by multiplying Absorbance and volume of each sample, are shown in Figure 5.4. The quantity of magnetic nanoparticles from the  $\text{Ag}_{66}\text{Fe}_{34}$  target is significantly larger than that of the nanoparticles obtained from the  $\text{Ag}_{50}\text{Fe}_{50}$  target.

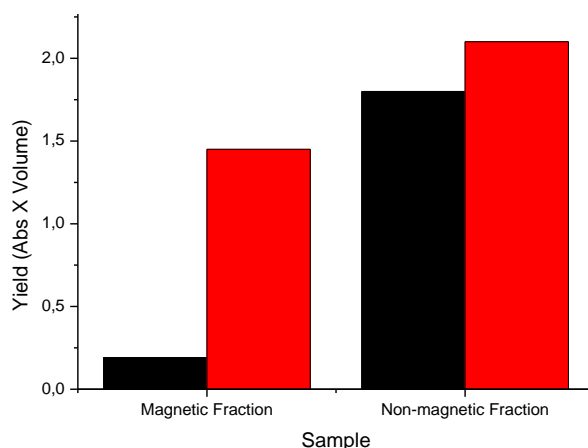


Figure 5.4 – Yield data for nanoparticles obtained from the  $\text{Ag}_{50}\text{Fe}_{50}$  (black) and  $\text{Ag}_{66}\text{Fe}_{34}$  (red) targets, reporting both the magnetic and non-magnetic fraction.

Since obtaining nanoparticles with an appreciable answer to the magnetic field is our objective, the  $\text{Ag}_{75}\text{Fe}_{25}$  target was preferred in the following tests.

### 5.3 Nanoparticles Characterization

Nanoparticles from both the magnetic and non-magnetic fractions, obtained from the ablation of an  $\text{Ag}_{75}\text{Fe}_{25}$  target, were studied with Transmission Electron Microscopy. Some representative pictures of both fractions are shown in Figure 5.5. The nanoparticles in the two different samples are quite different: in the magnetic fraction the nanoparticles have an irregular form, and are considerably larger (>50 nm), than those of the non-magnetic fraction. These nanoparticles are probably originated from the fusion of agglomerated clusters. The non-magnetic fraction instead is formed from much smaller and heterogeneous nanoparticles and it is possible to see very small nanoparticles (<10 nm).

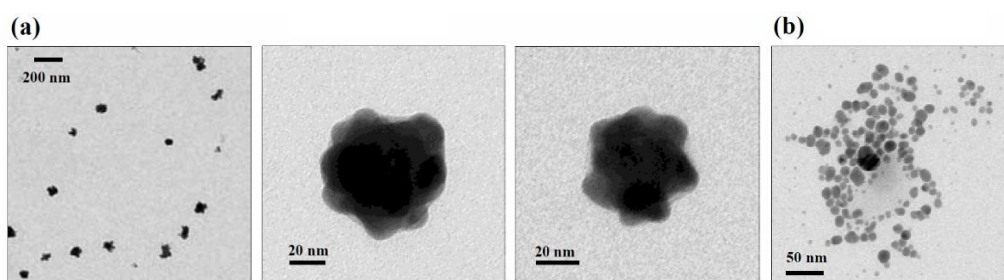


Figure 5.5 – TEM images of nanoparticles obtained by the ablation of a  $\text{Ag}_{75}\text{Fe}_{25}$  target. (a) Magnetic fraction (b) Non-magnetic fraction. From reference 8.

The size distribution of the two fractions are shown in Figure 5.6:

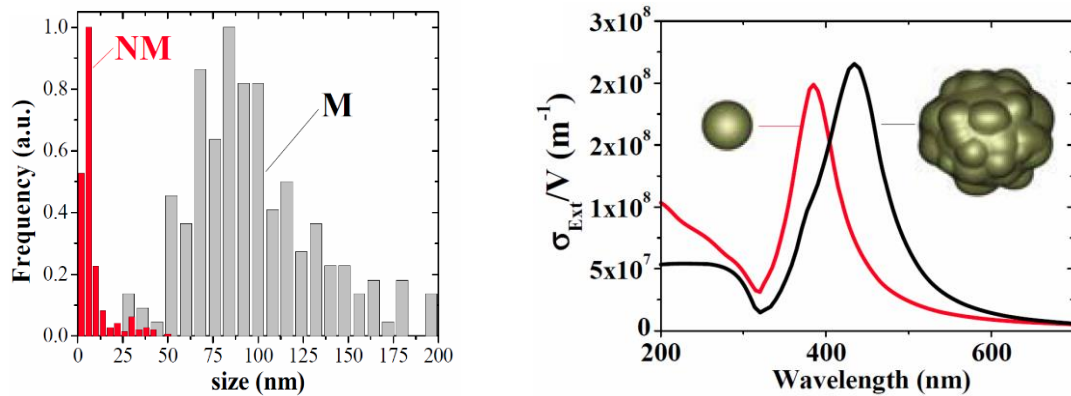


Figure 5.6 – Size distribution of the magnetic and non-magnetic fractions of the nanoparticle obtained from the ablation of a  $Ag_{75}Fe_{25}$  target (left) and numerical simulation of the extinction cross-section of the fractions (right). From reference 8.

The non-magnetic fraction is significantly smaller than the magnetic fraction, and furthermore the size distribution is bimodal. The nanoparticles of the magnetic fraction, on the other hand, are significantly larger and the distribution is lognormal. The calculated extinction cross section of the nanoparticles is compatible with the UV-Visible absorption spectra shown above, showing an appreciable red shift and broadening of the SPA for the larger nanoparticles.

XPS and EDS analysis of nanoparticles from both fractions were carried out to accurately assess the composition of the nanoparticles. The results of the EDS analysis on the magnetic fraction are shown in Figure 5.7. The EDS analysis on a cluster of magnetic nanoparticles not only shows that both the signal from iron ( $Fe\ K\alpha$ , 6.4 keV) and from silver ( $Ag\ L\alpha$ , 3.0 keV) are visible, but they are also overlapped on the same region, confirming the presence of both elements in the clusters of nanoparticles.

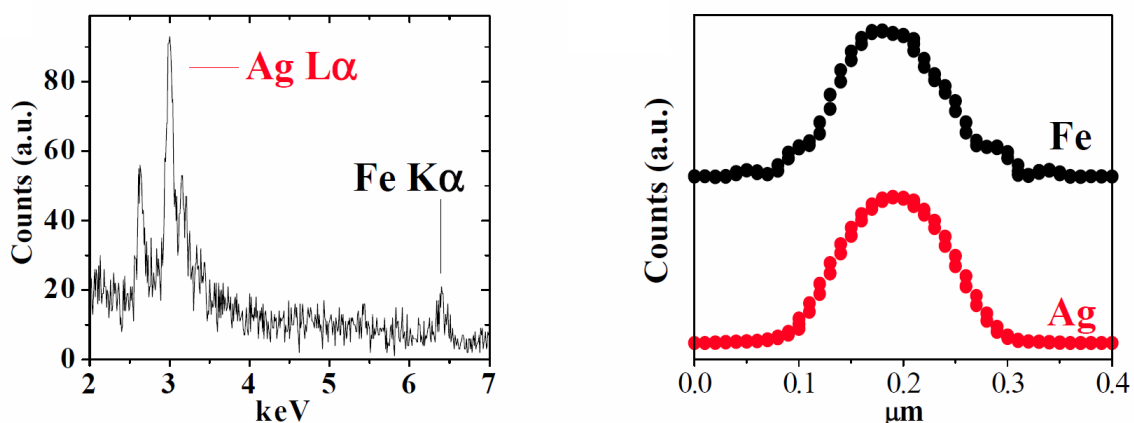


Figure 5.7 – EDS spectrum (left) and line intensity dependence (right) analysis of the magnetic fraction of nanoparticles obtained from the  $Ag_{75}Fe_{25}$  target. From reference 8.

XPS analysis showed the presence of sulphur, carbon, silver, oxygen and iron photoemission signals. In Figure 5.8 are shown the XPS peaks. The peaks from sulphur (S

## 5. Iron-doped Ag Nanoparticles

2p) and carbon (C 1s) are due to the PEG ligand shell that covers the nanoparticles, confirming the presence of the polymeric coating on the surface of the nanoparticles.

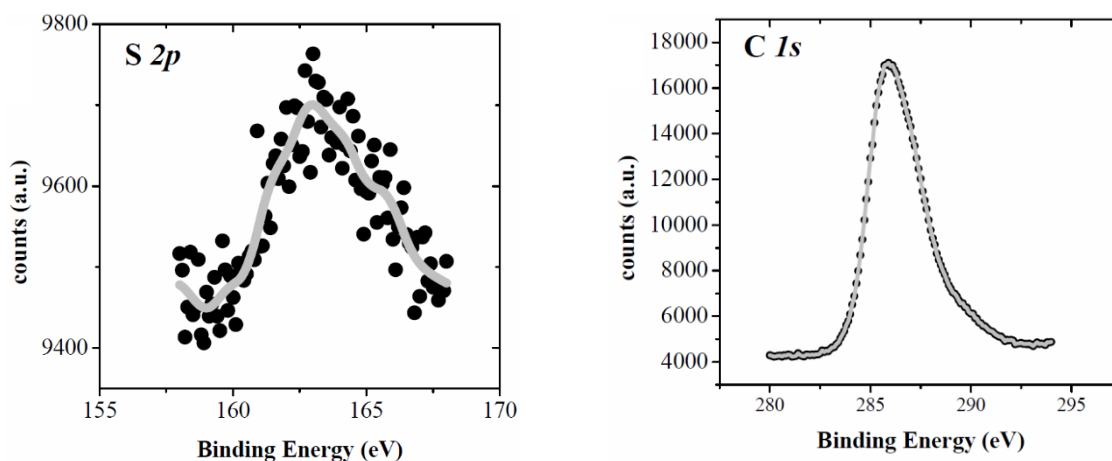


Figure 5.8 - S 2p (left), C 1s (right) XPS photoemission spectra, from nanoparticles obtained from the  $Ag_{75}Fe_{25}$  target. From reference 8.

The silver signal has a main component from Ag(0) at a binding energy of 368.4 eV, expected from a system where the SPA of silver is visible. The iron signal has a complex multiplet structure, which makes identification of the single components impossible. However, the Fe 2p<sub>3/2</sub> peak is located at the typical binding energy of oxides (709-714 eV), and has a visible tail at lower binding energies (708 eV) that is usually visible when metal iron is alloyed with noble metals<sup>7</sup>.

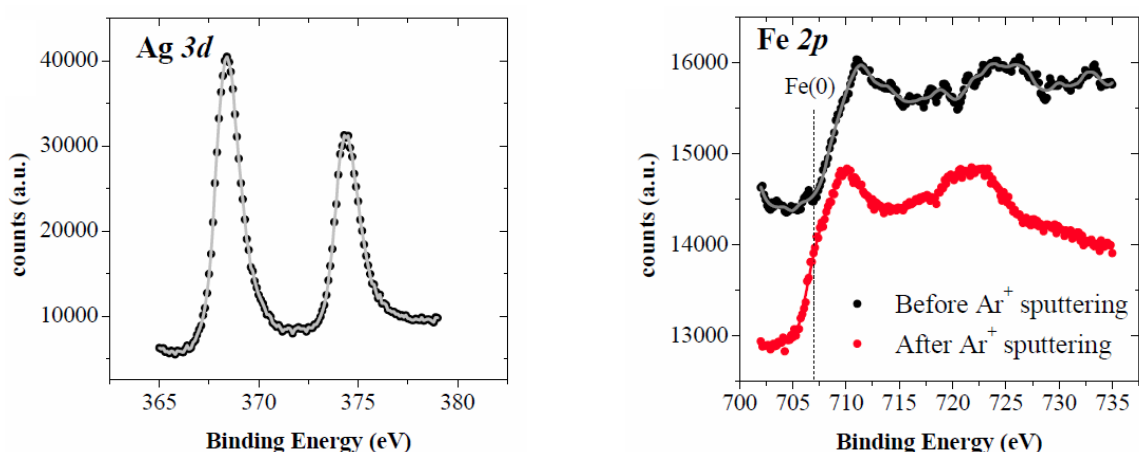


Figure 5.9 – Ag 3d (lower left) and Fe 2p (lower right) XPS photoemission spectra, from nanoparticles obtained from the  $Ag_{75}Fe_{25}$  target. For an easier visualization, the Fe 2p spectra have been stacked. From reference 8.

To assess the internal structure, the nanoparticles were sputtered for 10 minutes with Ar<sup>+</sup> ions (at 1 keV). We then observed an increase in the metal iron signal (708 eV), while the structure of Ag 3d peaks remained unchanged. This is compatible with Fe-Ag NPs in which an outer shell of oxidized iron and metal Ag protect the internal metal Ag and both metal and

oxidised Fe atoms.

We then assessed the composition of the nanoparticles by Inductively Coupled Plasma Mass Spectrometry (ICP-MS) and EDS, and found an iron content of about 15% in atoms, which is lower than the 34% of the bulk target. A similar behaviour during the ablation was discovered also for gold-iron alloys (see Chapter 4) and is connected to the fact that Fe can readily react with oxygen atoms formed from solvent molecules in the ablation plume.

X-Ray analysis of NPs structure and of the starting target was also carried out. The results are shown in Figure 5.10. The signal from fcc silver is clearly visible in both cases, but no signal from bcc iron is visible in the particles, while in target it is clearly present.

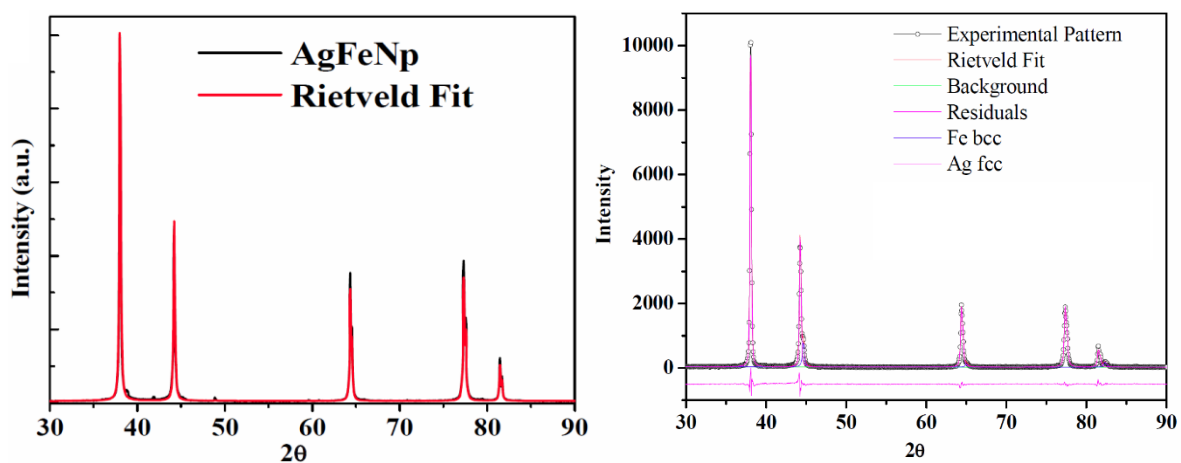


Figure 5.10 – XRD spectra of AgFe nanoparticles with its Rietveld fit (left), and  $Ag_{75}Fe_{25}$  bulk target (right) used for the ablation. From reference 8.

The detection limits of metal iron or ordered iron oxide phases are about ten times lower than the content of iron detected from EDS and ICP-MS, but no signals from ordered iron grains (with dimensions larger than 5-10 nm) can be detected from XRD. Also from FT-IR and Raman analysis we have not detected vibrational fingerprints typical of iron oxide phases. This kind of behaviour has been documented in literature for bimetallic Fe-Ag solid solutions, and is attributed to the presence of disordered or very small crystalline domains (with a very large surface-volume ratio) of silver-iron alloy<sup>9, 10</sup>.

To assess more efficiently the structure of the nanoparticles, we used Mössbauer spectroscopy to probe the surroundings of the iron atoms. The results of this analysis are reported in Figure 5.11. The stronger peak is at 0 mm/s, with a broad magnetically split component. To fit as best as possible the spectrum, three different elements, each one simulating a different environment of the iron atoms, were used:

- 40% superparamagnetic iron atoms in bcc lattice with grain size below 10 nm
- 30% paramagnetic iron atoms in sites lacking magnetic coupling, probably

## 5. Iron-doped Ag Nanoparticles

exclusively surrounded by silver atoms

- 30% iron atoms in two different sites showing coupling, compatible with an environment of silver and iron atoms

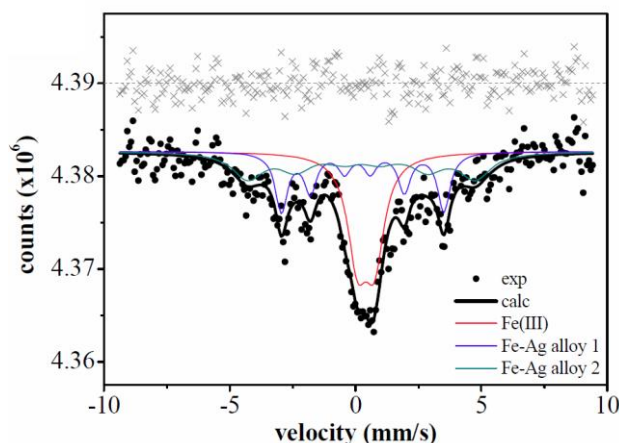


Figure 5.11 – Mössbauer spectrum of AgFe nanoparticles fitted with three elements (see text for explanation). Grey crosses are fit residuals. From reference 8.

The Mössbauer analysis does not show the presence of ordered iron oxide phases large enough to be detected, meaning that they probably are mainly amorphous and contribute only to the background. Data for the simulation are shown in Table 5.1:

Site	$\delta$ (mm/s)	$\Delta\epsilon$ (mm/s)	$\Gamma_{1/2}$ (mm/s)	B (T)	A (%)	Attribution
Doublet 1	0.41	0.67	0.47	/	40	Superparamagnetic Fe(III)
Sextet 1	0.179	0.106	0.30	20.03	30	Magnetically ordered Fe(III) in AgFe alloy regions
Sextet 2	0.24	0.00	0.75	28.1	30	Magnetically ordered Fe(III) in AgFe alloy regions (Fe-rich)

Table 5.1 – Fitting parameters for the Mössbauer analysis. From reference 8.

To obtain more information about the average symmetry of the atoms surrounding Fe centers in the Fe-doped Ag NPs, X-Ray Absorption Spectroscopy analysis was carried out. In figure 5.12 are shown the XANES and EXAFS spectra collected on our sample. The edge position and shape in XANES measurements (on the left) are particularly susceptible to the electronic and physical structure of the photoabsorber. For our purpose, the lower edge energy in the spectrum of our sample, when compared to the iron oxide spectrum, indicates the availability of metal iron in the former, as verified by the appearance of a Fermi level in the pre-edge region (where the  $1s \rightarrow 3d$  transition can be found). When compared to the bulk iron spectrum however, there is a slight but noticeable shift of the edge, suggesting the presence of oxidized atoms, and the damping of the oscillations after the edge suggests a disordered environment. The best results are obtained with a spectrum given by the linear

combination of 70% iron and 30% iron oxide.

The EXAFS spectrum has been fitted by a model containing two clusters, a disordered Fe(III) oxide with a relative weight of 30%, and a disordered Ag-Fe alloy with a structure derived from the Fe bcc. To obtain the best results the silver atoms were made available as random substituents of iron atoms in the bcc Ag-Fe alloy (that has a 1-1 ratio of Ag:Fe), while the iron oxide is coordinated with four iron atoms. The large values of the Debye Waller for all the shells of the fit confirms the overall structural inhomogeneity.

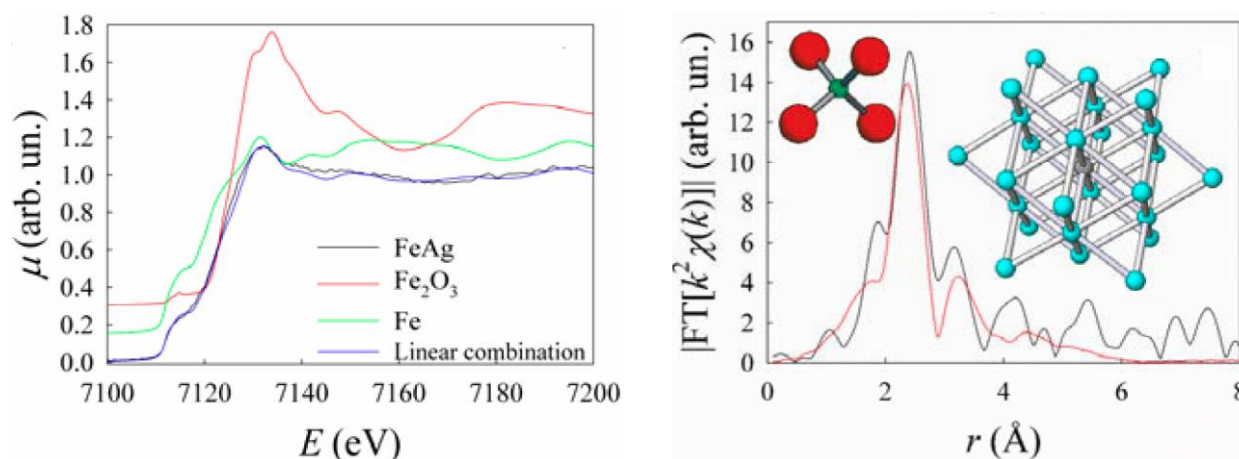


Figure 5.12 – (Left) XANES edge spectrum of the Fe-K, compared to bulk iron and iron oxide ( $\text{Fe}_2\text{O}_3$ ) spectra, stacked for an easier visualization. (Right) EXAFS Fourier transformed modulus (black) and its fit (in red), with models of the two structures used in the fit. In green: Fe(III), in grey: Fe(0), in cyan: mixed Fe/Ag (1-1), in red: oxide ions. From reference 8.

The EXAFS fit data are shown in Table 5.2:

Shell	N	Atom	r (Å)	$\sigma^2$ (Å <sup>2</sup> )	$r_0$ (Å)
1	4	O	1.78	$17 \cdot 10^{-3}$	1.881
<b>Fe fraction 0.3</b>					
1	8	Fe/Ag	2.50	$7 \cdot 10^{-3}$	2.483
2	6	Fe/Ag	2.89	$5 \cdot 10^{-3}$	2.868
3	12	Fe/Ag	3.99	$2 \cdot 10^{-3}$	4.056
<b>Fe fraction 0.7</b>					

Table 5.2 – Fitting parameters for the EXAFS fit of Figure 5.X. From reference 8.

The formation of these nanoparticles must follow a complex route, as can be assumed considering that silver and iron are insoluble both in solid and liquid phase<sup>11</sup>, and also because their shape suggests a formation pathway different from that of “standard” nanoparticles. Recent studies<sup>12</sup> have shown that nucleation of a thermodynamically favourable crystalline phase can form from a less favoured phase when in environments where atomic mobility is limited, obtaining a disordered structure. This means that



## 5. Iron-doped Ag Nanoparticles

disordered Fe-Ag domains can be formed if atomic mobility is sufficiently limited and the formation of interfaces among different separated crystalline Ag and Fe phases has a higher energetic cost.

The shape of the nanoparticles is probably due to the low miscibility between the iron and silver phases, causing formation of new interfaces between amorphous Ag-Fe and crystalline Ag in a single nanoparticle. Furthermore, the diffusivity is hampered due to presence of multiple obstacles such as grains with different structures or dislocations. The final shape is almost truffle-like, an ideal middle step between a sphere and a fractal cluster obtained by diffusion limited aggregation of nanometer-sized clusters.

It is also interesting to note that the difference in yield obtained from nanoparticles ablated in water and ethanol is probably linked to the particular formation mechanism of these nanoparticles: if the concentration of oxidizing species is higher (such as in water), nuclei formed from the coalescence of iron atoms will have an higher probability to form oxides. These oxidized nuclei will stick to the silver atom or nuclei with a greater difficulty, explaining the difference in yield of magnetic nuclei from ethanol (lower formation of oxides) to water (higher formation of oxides).

The formation mechanism of these nanoparticles can thus be summed in three steps:

*Nucleation*, with the formation of Ag, Fe or AgFe nuclei. The probability to be oxidized for these nuclei will be proportional to the reactivity of the environment.

*Coalescence*, with the formation of aggregates formed from single nuclei. The formation of these aggregates is possible only if their structure and composition allows it (see above).

*Passivation*, with the formation of an oxide layer where not already in place, and its growth elsewhere.

A scheme of this process is shown in Figure 5.13<sup>8</sup>:

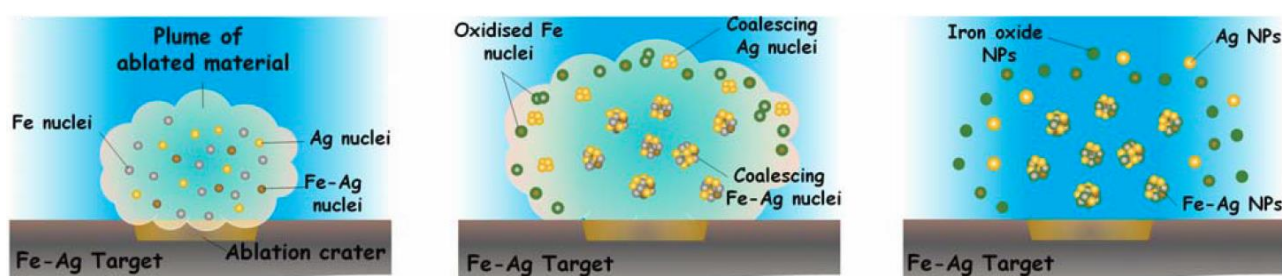


Figure 5.13 – Nucleation (left), coalescence (center) and passivation (right) of the nanoparticles. From reference 8.

## 5.4 Magnetic properties

Due to the response to magnetic fields shown by the magnetic fraction of the sample, and to the peculiar structure, we performed SQUID magnetometry analysis of the Fe-doped Ag NPs. The results of this analysis carried out on the magnetic fraction are shown in Figure 5.14. Near-full reversibility of the hysteresis loop at ambient temperature is achieved, and the maximum magnetization with the most powerful field is  $33 \text{ A}\cdot\text{m}^2/\text{kg}$  of iron. At low temperature the hysteresis loop is open, with a coercive field of 28 mT, a saturation magnetization of  $50 \text{ A}\cdot\text{m}^2/\text{kg}$ , and a reduced remnant magnetization of 0.11. The behaviour is compatible with those of single domain magnetic nanoparticles, with magnetic moments blocked at low temperature but entering the superparamagnetic state at room temperature.

The ZFC-FC measurements support this behaviour. The hysteresis loop at lower temperature does not saturate at the lowest measuring temperature, probably due to a certain amount of weakly coupled/disordered magnetic moments in the sample.

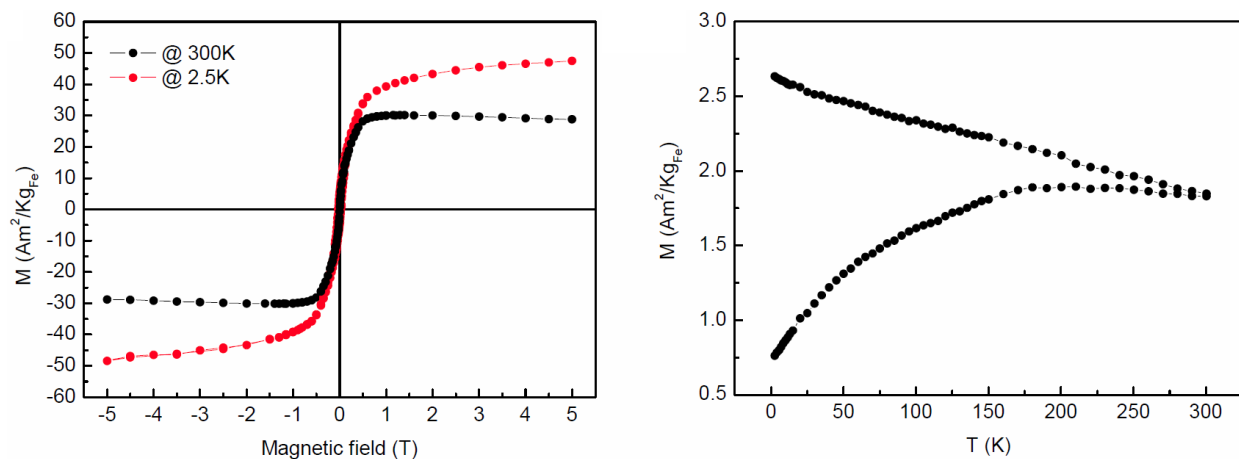


Figure 5.14 – Characterization of the magnetic properties of AgFe nanoparticles. (Left) Hysteresis loop at 2.5K and 300K. (Right) Temperature dependence of the ZFC-FC magnetization measured with a 5 mT probe field. From reference 8.

The appreciable decrease of the magnetization at 5T supports this hypothesis, as can be seen in Figure 5.15. The saturation magnetization measured at 2.5 K is 0.5 B per iron atom, lower than expected but explainable due to the presence of a consistent quantity of amorphous iron oxide and of spin disorder, strongly decreasing the magnetization. For example, the presence of a surface iron oxide shell is indirectly confirmed by 5T shift of the hysteresis loop along the field axis after sample cooling. This detail is typical of the exchange bias, due to the presence of interface between different structures, such as metal@oxide ones.



## 5. Iron-doped Ag Nanoparticles

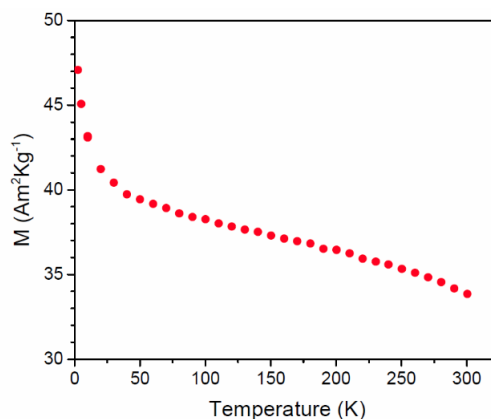


Figure 5.15 – Temperature dependence of the magnetization measured with an applied field of 5T. From reference 8.

## 5.5 Magnetic amplification of optical properties

We have already shown in Section 5.2 that the obtained nanoparticles show an absorption spectrum with an appreciable SPA, due to silver content.

Since magnetophoretic accumulation of nanoparticles was positively used to separate the magnetic from the non-magnetic fractions, the same procedure is applicable to collect the magnetic fraction in one spot to improve optical response such as SERS and photothermal heating. The magnet used for this experiment is NdFeB with a 2 mm diameter. Figure 5.16 shows the images relative to the magnetic collection of NPs for photothermal experiments at 785 nm (with a 300 mW diode laser). The magnetic accumulation of nanoparticles is visible to the naked eye, and is completed in a time of about 20 minutes. The beneficial effect of magnetic accumulation on photothermal heating is evident from thermal imaging, since the final temperature of the nanoparticles arrives up to 38° C, with an increase almost double than before the magnetic collection.

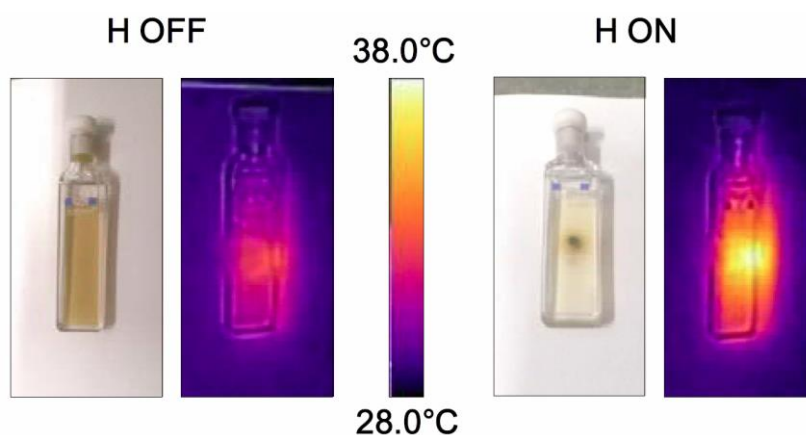


Figure 5.16 – Photothermal heating experiment on AgFe nanoparticles before (left) and after (right) magnetic collection. Irradiation by continuous wave laser at 785 nm. From reference 8.

The effect of the magnetophoretic accumulation on SERS signals were also investigated.

AgFe nanoparticles show SERS with various dyes, such as Malachite Green (MG) and HITC (2-[7-(1,3-dihydro-1,3,3-trimethyl-2H-indol-2-ylidene)-1,3,5-heptatrienyl]-1,3,3-trimethyl-3H-indolium iodide). The Raman spectra of nanoparticles dispersed in liquid solution containing these dyes are shown in Figure 5.17:

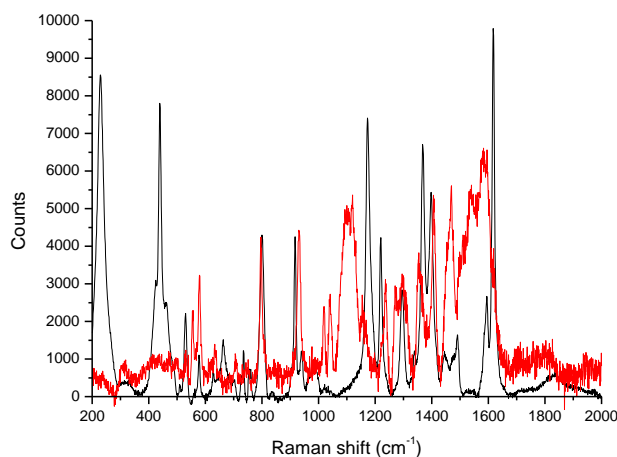


Figure 5.17 – Raman spectra of AgFe nanoparticles with MG (black) and HITC (red).

We collected Raman spectra of AgFe nanoparticles without dye, and with addition of MG before and after magnetic collection. The results are shown in Figure 5.18. The nanoparticles without dye show no Raman peaks, only some signals from 1200 to 1600  $\text{cm}^{-1}$  and from 400 to 500  $\text{cm}^{-1}$ . With dye, strong Raman signals appear, and after the collection the signal intensity increased of almost 25 times. This effect is due to the accumulation of the nanoparticles on the spot over the magnet.

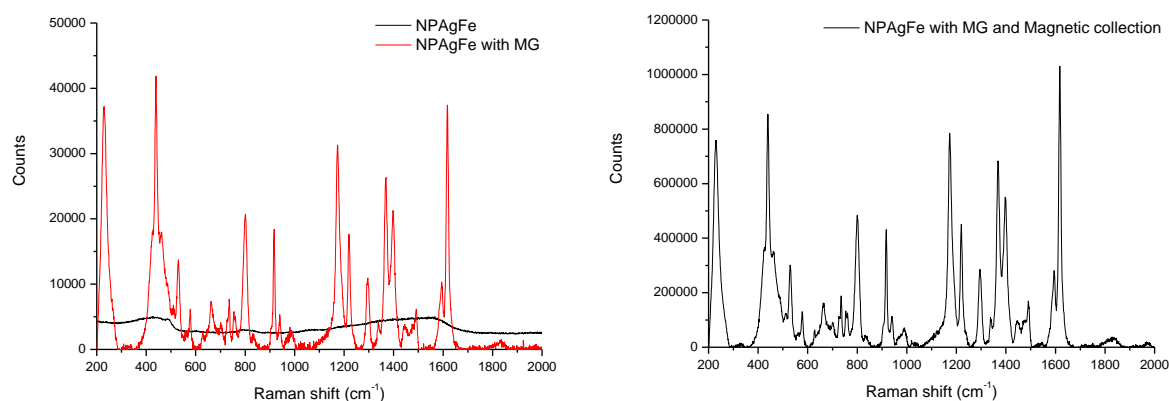


Figure 5.18 – Raman spectra of silver-iron nanoparticles without dye and with MG but not collected (left), and with MG after magnetic collection (right).

Since the distance of the dye molecule from the surface of the hot-spot of the nanoparticles can have a significant impact on the SERS enhancement, we tried to modify the surface ligand, using shorter chain lengths. We tested two different PEGs (with average molecular weight of 800 and 350 Dalton), 2-mercaptoethanol ( $\beta$ ME), Glutathione (GSH), and Sodium-3-mercapto-1-propanesulfonate (MPS). The nanoparticles were prepared with the

## 5. Iron-doped Ag Nanoparticles

standard method, discussed in Section 2, and their UV-Visible absorption spectra are shown in Figure 5.19. The sample obtained in  $\beta$ ME was discarded because after 24 hours we noticed lack of response to the magnetic field and a uniform opalescence in the container, suggesting dissolution of the nanoparticles. The other samples showed no such problems, and Raman analysis after accumulation of the nanoparticles with the addition of Malachite Green (20  $\mu$ L, 3  $\mu$ M) was carried out.

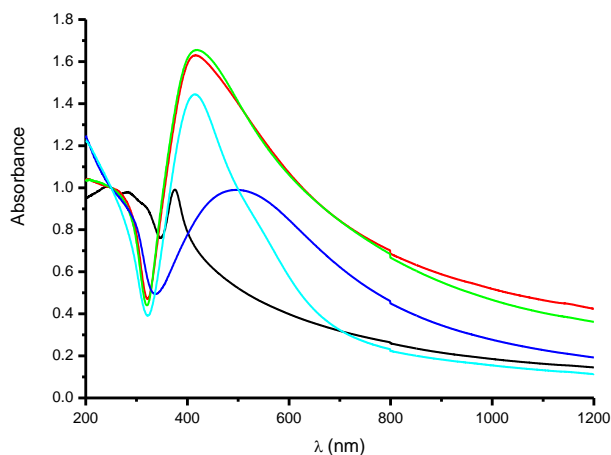


Figure 5.19 – UV-Visible absorption spectra of the AgFe nanoparticles with different surface ligands. In black  $\beta$ ME, in red with PEG350, in green with PEG800, in blue with GSH, in cyan with MPS. The spectra are normalized at 250 nm for an easier visualization.

Pictures of the arrays and Raman results are shown in Figure 5.20. The objective of the deposition was to obtain well defined spot as much as possible. Incomplete accumulation of the material, visible as a ring around the main spot, is visible in all the arrays excluding that obtained with MPS.

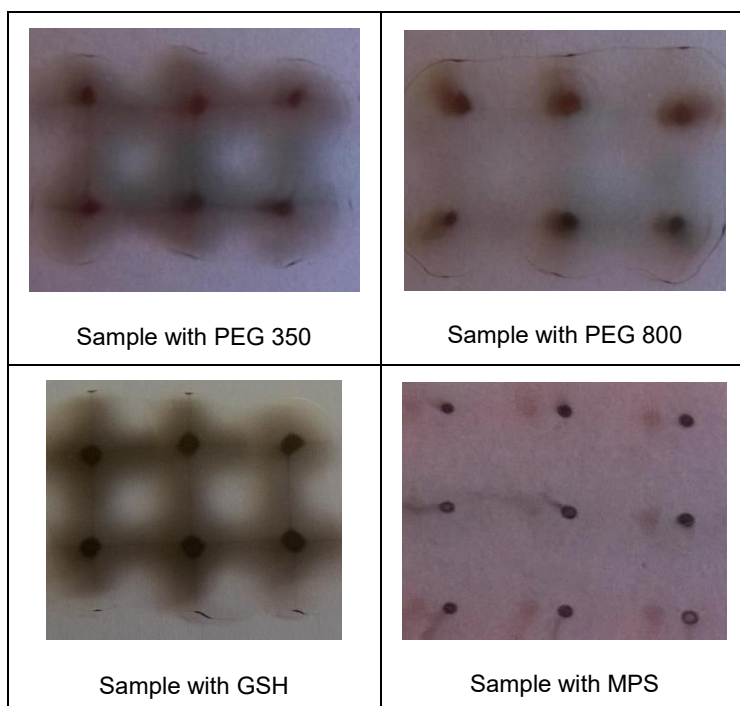


Figure 5.20 – Pictures of the nanoparticles array after magnetic accumulation

The Raman signals of the  $1600\text{ cm}^{-1}$  area, considered indicative of the whole SERS for this dye, show almost no peak for the two PEG-covered nanoparticles, while for MPS and GSH the signal is visible.

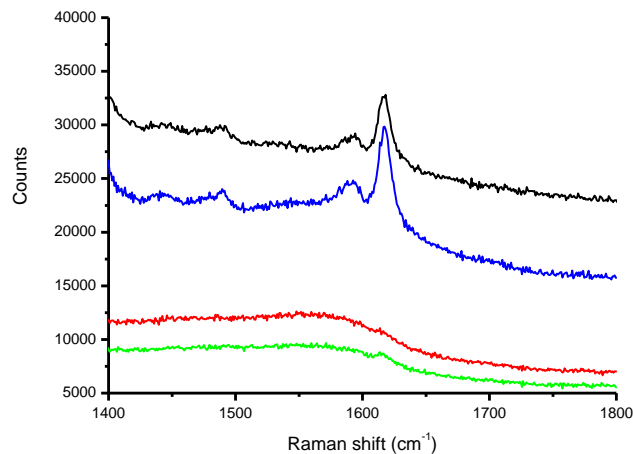


Figure 5.21 – Raman spectra of the  $1618\text{ cm}^{-1}$  peak (chosen for its intensity) for the samples with GSH (black), PEG 350 (red), PEG 800 (green) and MPS (blue).

We chose to continue the analysis only for the samples functionalized with GSH and MPS. A 2D map of the signals from the array spots was collected, and the intensity values for the  $1618\text{ cm}^{-1}$  peak for both samples after averaging are shown in Figure 5.22. The signal for the sample functionalized with MPS is almost double than the one with GSH, confirming the data we have seen in the Raman spectra above (Figure 5.21).

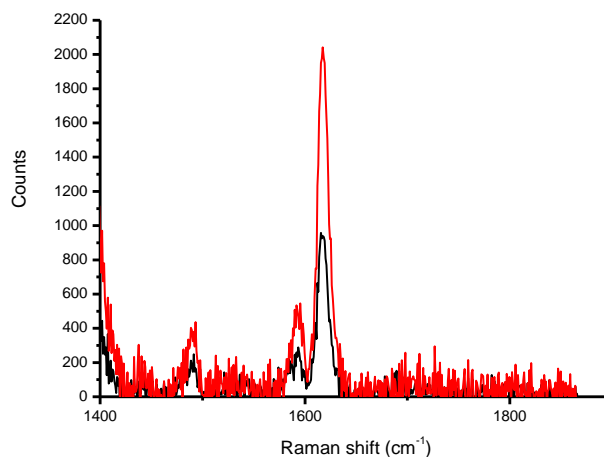


Figure 5.22 – Average Raman spectra of the  $1618\text{ cm}^{-1}$  peak for the sample with GSH (black) and MPS (red).

Further analysis, carried out on the whole surface of the array for the  $1618\text{ cm}^{-1}$  peak, is shown in Figure 5.23. The array obtained from nanoparticles functionalized with MPS has both more defined spots and signals very well contained to the same spots. The spots of the GSH array, on the other hand, show worse collection on the magnets, both of the particles and of the Raman signal.

## 5. Iron-doped Ag Nanoparticles

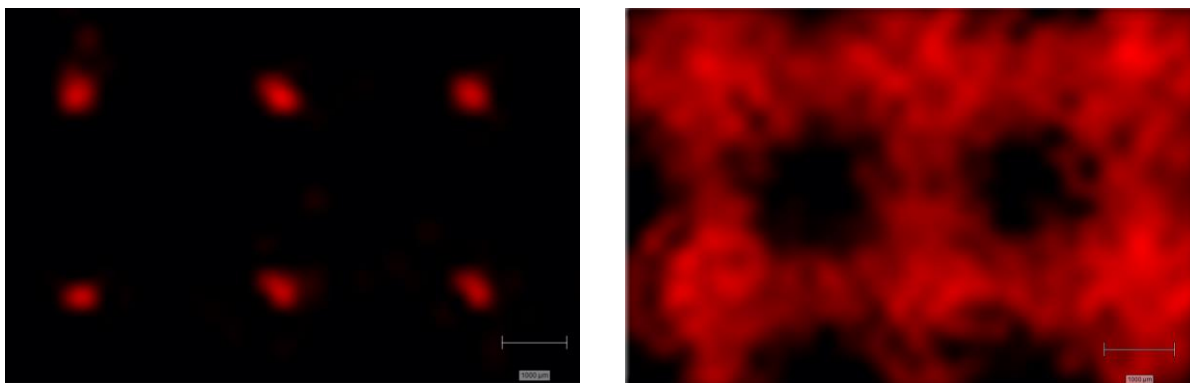


Figure 5.23 – Intensity of the Raman signal intensity at  $1618\text{ cm}^{-1}$  for the sample with MPS (left) and GSH (right). The maximum signal intensity are 2416 counts for the MPS sample and 1325 count for the GSH sample.

Therefore we chose to continue our experiments using MPS instead of PEG as surface coating for the nanoparticles when maximum SERS enhancement is required.

We then investigated the effect of the concentration of nanoparticles on the Raman signals. This investigation was carried out by diluting at different levels the original nanoparticles solution and dosing them with the MG used before (see above), to obtain the following final concentrations: 5C, 2C, C, C/2, C/4 (with C the concentration of nanoparticles used in previous experiment ( $\sim 6.5\text{ mg/mL}$ )). The signal intensity versus NPs concentration for the  $1618\text{ cm}^{-1}$  peak is shown in Figure 5.24. Increasing or lowering the nanoparticles concentration while keeping the dye quantity constant seems to have a negative effect on signal intensity, without significant trends in both directions.

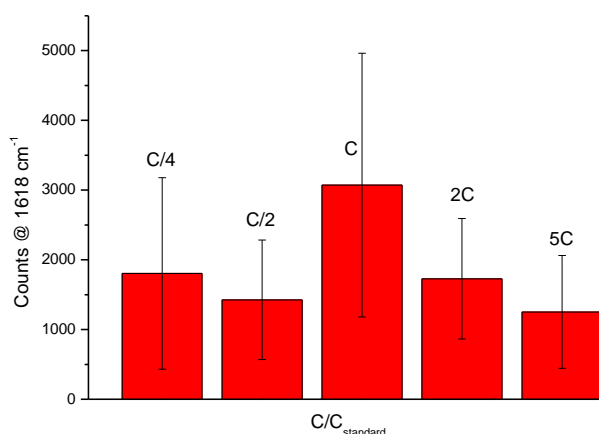


Figure 5.24 – Signal intensities for the  $1618\text{ cm}^{-1}$  peaks for nanoparticles arrays with different concentrations.

Therefore we decided to keep the nanoparticles concentration constant in the following experiments.

To test the effective detection limits for out-of-laboratory applications of the nanoparticles array we tested arrays with two different analytes: Sodium diethyldithiocarbamate trihydrate (DTC) and Tetramethylthiuram disulphide (Thiram). Both these molecules are commonly

used pesticides with negative effects on the environment. Having an array of nanoparticles where a potentially contaminated sample (for example, tap water) can be easily studied would be an interesting application. We tested the collected arrays with different concentrations of analytes, from mM to nM. The concentration used in the experiment are shown in Table 5.3, the results in Figure 5.25. SERS peaks are visible for mM concentrations of analytes

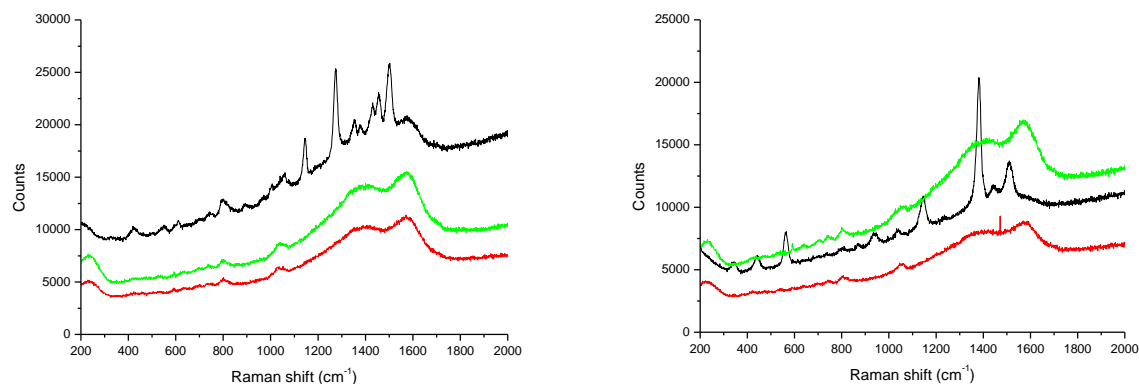


Figure 5.25 – Raman spectra of AgFe nanoparticle arrays with DTC (left) and Thiram (right) at different concentrations: mM (black),  $\mu\text{M}$  (red), nM (green).

Sample colour	DTC	Thiram
Black	3 mM	3 mM
Red	12 $\mu\text{M}$	4 $\mu\text{M}$
Green	48 nM	6 nM

Table 5.3 – Analyte additions for tests with nanoparticle arrays

## 5.6 Reusability of Arrays

The ease of preparation for the nanoparticles array primed us to test the reusability of the nanoparticles after a cleaning cycle to remove the previous analyte. Having a SERS array that can be used for analysis, cleaned from analytes, and then prepared again without signal loss or contamination is a feature that can greatly increase its usefulness in practical uses. For our tests we used arrays of silver-iron nanoparticles functionalized with MPS (as described in Section 5.4). The nanoparticles are deposited on a microscope glass placed on a magnet array (magnet diameter of 2mm), and then the liquid is allowed to dry on its own at ambient temperature. The deposition/drying sequence is shown in Figure 5.26:

## 5. Iron-doped Ag Nanoparticles

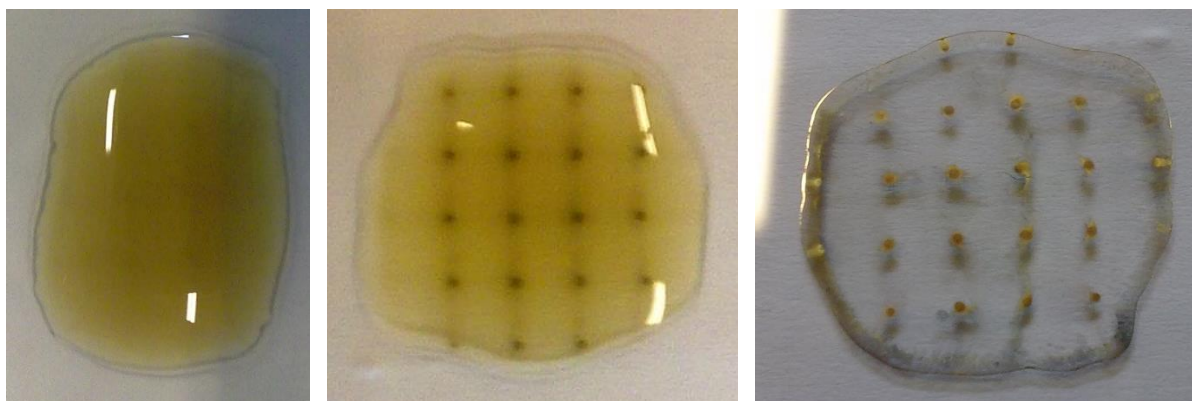


Figure 5.26 – Phases of the formation of nanoparticles array: deposition (left), magnetic collection of nanoparticles (centre), drying (right).

The deposition sequence shows a good degree of reproducibility, especially for the spots. On the periphery of the deposition area some material may give a “coffee ring” effect, especially if the solvent dries too quickly, but overall the array is well defined.

For the first step of the analysis, we premixed 100  $\mu\text{L}$  of nanoparticles with 20  $\mu\text{L}$  of Malachite Green 3  $\mu\text{M}$  concentration. Six spots were deposited, each one with 20  $\mu\text{L}$  of nanoparticles, collected with magnets, and allowed to dry. The intensity of the 1618  $\text{cm}^{-1}$  peak for the full area of each spot was collected and averaged after subtraction of the baseline. The results are shown in Figure 5.27. Although there are fluctuations in signal intensity up to 50% from one spot to the other, the Raman peaks are sharp and well distinguishable.

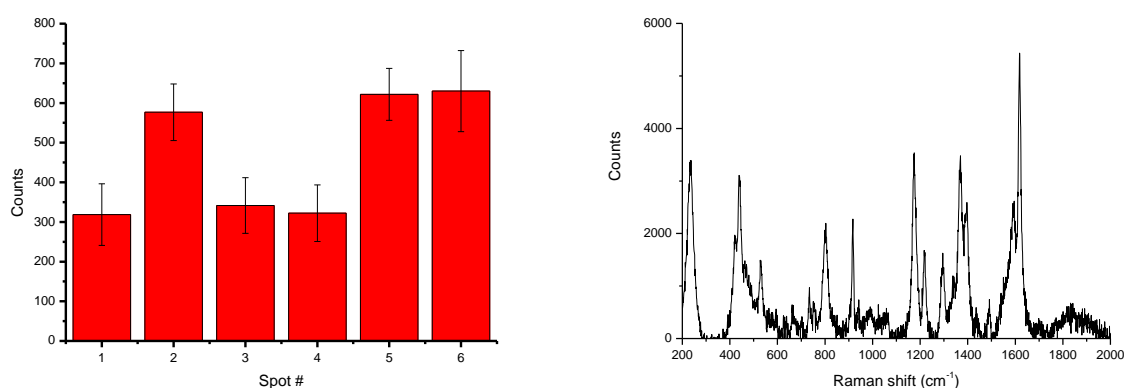


Figure 5.27 – Signal intensities for the 1618  $\text{cm}^{-1}$  peak for the single AgFe spots with MG (Left), and example Raman spectrum of these nanoparticles.

The substrate was then dissolved in water with  $10^{-4}$  NaCl and centrifuged two times for 10 minutes at 15000 g, each time removing the supernatants. The nanoparticles were then brought up to 100  $\mu\text{L}$  again and mixed with 20  $\mu\text{L}$  10mM DTC, to switch from a dye to a pesticide. We carried out again a map on the full surface for each spot, this time referencing to the 1266  $\text{cm}^{-1}$ . The results are shown in Figure 5.28. The peak intensities at 1266  $\text{cm}^{-1}$  clearly show the Raman fingerprint of DTC, although spot-to-spot signal intensity is more variable than in the MG case.



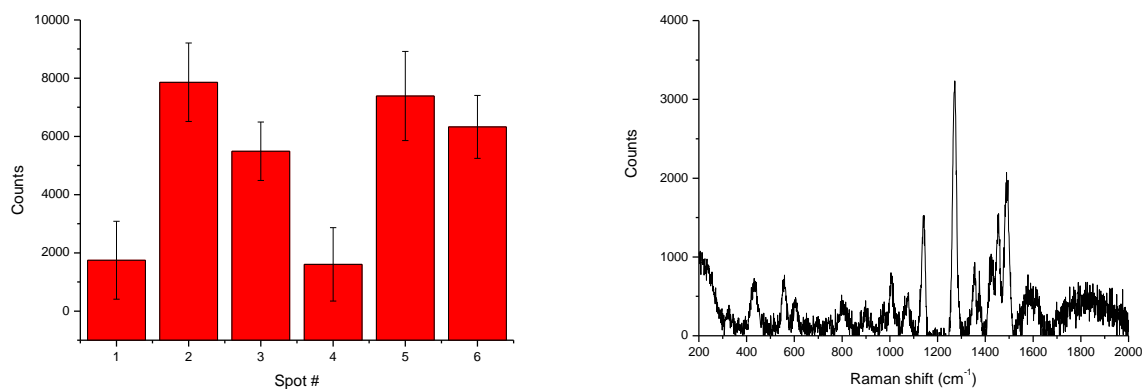


Figure 5.28 - Signal intensities for the  $1266\text{ cm}^{-1}$  peak for the single AgFe spots with MG (Left), and example Raman spectrum of these nanoparticles.

An alternative visualization of the cleaning and reusing process can be seen in Figure 5.29. It is possible to see that after the cleaning step the removal of the characteristic peaks is complete. Some of the areas underlining the characteristic peaks remains, but when further analytes are added the analysis is not significantly affected.

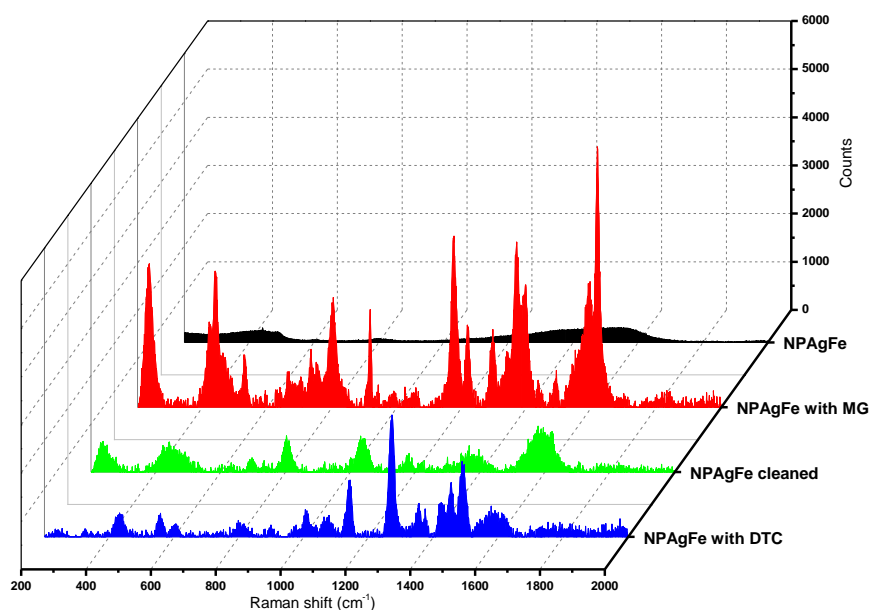


Figure 5.29 – Raman spectra of the nanoparticles without dye (black), with the addition of MG (red), after cleaning (green), and with DTC (blue).

A similar test, but more extended, was carried out by alternating Malachite Green and HITC in a sequence of four cleaning cycles. In figure 5.30 are reported the results, showing that after each centrifuge cycle the signal from the previous analyte was completely removed.



## 5. Iron-doped Ag Nanoparticles

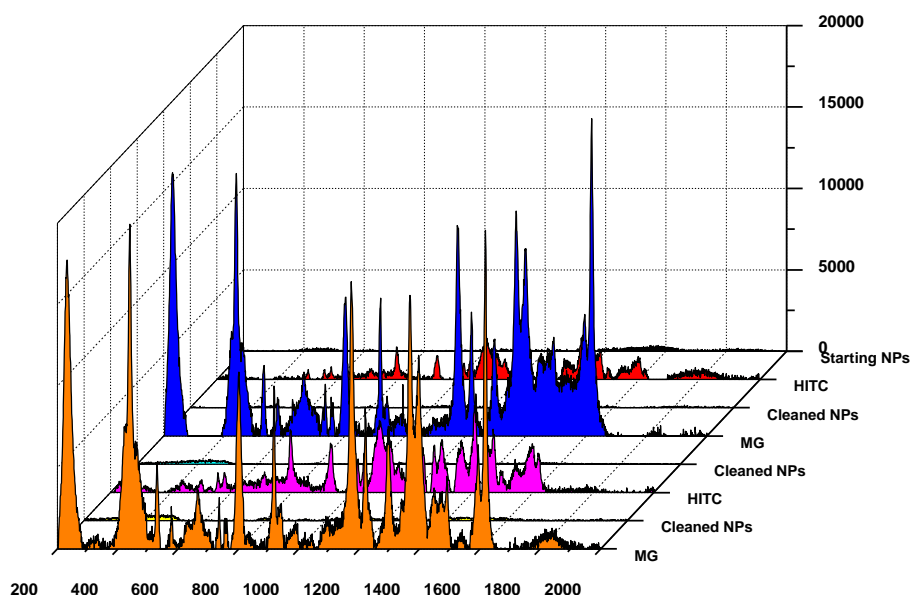


Figure 5.30 – Raman spectra of the nanoparticles without dye (black), with HITC (red and purple), and with Malachite Green (blue and orange).

Although the reusability of the arrays has been demonstrated, further work is needed to improve the detection limit with these nanoparticles.

## 5.7 Bibliography

- 1 M. Rai, A. Yadav and A. Gade, *Biotechnol. Adv.*, 2009, **27**, 76-83.
- 2 S. R. Emory and S. Nie, *Anal. Chem.*, 1997, **69**, 2631-2635.
- 3 E. E. Carpenter, *J Magn Magn Mater*, 2001, **225**, 17-20.
- 4 B. Chertok, B. A. Moffat, A. E. David, F. Yu, C. Bergemann, B. D. Ross and V. C. Yang, *Biomaterials*, 2008, **29**, 487-496.
- 5 V. Amendola, M. Meneghetti, G. Granozzi, S. Agnoli, S. Polizzi, P. Riello, A. Boscaini, C. Anselmi, G. Fracasso and M. Colombatti, *Journal of Materials Chemistry*, 2011, **21**, 3803-3813.
- 6 V. Amendola, S. Scaramuzza, L. Litti, M. Meneghetti, G. Zuccolotto, A. Rosato, E. Nicolato, P. Marzola, G. Fracasso and C. Anselmi, *Small*, 2014, .
- 7 V. Amendola, S. Scaramuzza, S. Agnoli, S. Polizzi and M. Meneghetti, *Nanoscale*, 2014, **6**, 1423-1433.
- 8 V. Amendola, S. Scaramuzza, S. Agnoli, G. Granozzi, M. Meneghetti, G. Campo, V. Bonanni, F. Pineider, C. Sangregorio, P. Ghigna, S. Polizzi, P. Riello, S. Fiameni and L. Nodari, *Nano Research*, 2015, (DOI:10.1007/s12274-015-0903-y).
- 9 J. Wang and G. Xiao, *Physical Review B*, 1994, **49**, 3982.
- 10 J. Alonso, M. Fdez-Gubieda, A. Svalov, C. Meneghini and I. Orue, *J. Alloys Compounds*, 2012, **536**, S271-S276.
- 11 L. Swartzendruber, *Journal of Phase Equilibria*, 1984, **5**, 560-564.
- 12 Y. Peng, F. Wang, Z. Wang, A. M. Alsayed, Z. Zhang, A. G. Yodh and Y. Han, *Nature materials*, 2015, **14**, 101-108.

# Conclusions

In this PhD thesis, the syntheses of alloy nanoparticles with magnetic and plasmonic properties was investigated, by exploiting Laser Ablation Synthesis in Solution (LASiS).

The synthesis of iron-gold alloy NPs started from an  $Au_{73}Fe_{27}$  target in water, ethanol or mixed water/ethanol environments. We have obtained contents of up to ~13% in composition. Optical properties and structural characterization data showed that iron atoms are located in the gold lattice as random substitutional dopants. Remarkably, the fraction of Fe in the alloys always exceeded the thermodynamic limit of ~2.5% at room temperature, meaning that metastable alloys were obtained. The surface plasmon absorption (SPA) of the obtained nanoparticles showed a strong dependence from the synthesis environment (i.e. from the iron content), with damping of the plasmon associated to increasing amount of iron. Further tests were carried out on the effect of solutes in the liquid environment, such as the addition of  $H_2O_2$  to ethanol or  $H_2O$ . This allowed the achievement of nanostructures with variable amounts of surface iron oxide, in some conditions even with asymmetric shape (nanocrescents) or core-shell structures.

Au-Fe nanoalloys obtained in pure ethanol were tested for in-vitro toxicity, without showing any negative effect on cell survival, in the same way of well established biocompatible nanomaterials such as Endorem™ (a commercially available contrast agent for MRI) and gold NPs. The NPs were tested against magnetic resonance imaging (MRI), computed x-ray absorption tomography (CT), and Raman imaging modalities, in conditions simulating their use as a diagnostic tools, showing results comparable with the reference nanomaterials for these applications. The NPs contrast ability was also tested in-vivo in mouse models for

MRI, and ex-vivo for CT and Raman imaging, showing promises for future development as multimodal contrast agents for cancer imaging.

The second main topic of the PhD work was the LASiS of silver-iron alloy nanoparticles, starting from targets with composition of  $\text{Ag}_{66}\text{Fe}_{34}$  or  $\text{Ag}_{50}\text{Fe}_{50}$ . The objective was the creation of NPs with an appreciable response to magnetic fields that could also work as SERS substrates. We discovered that the optimal setup for obtaining a higher yield of magnetic nanoparticles required the ablation in ethanol with the  $\text{Ag}_{66}\text{Fe}_{34}$  target. Ag-Fe NPs showed a very complex structure composed of disordered Fe-Ag alloy domains mixed with pure Ag crystals and a small component of defective iron oxides, all collected in NPs with a peculiar nanotruffle shape. The most striking property of these nanoparticles is the strong response to magnetic fields that allowed not only the easy separation of the magnetic from the non-magnetic fraction, but also the collection of the magnetic nanoparticles in the desired point.

An extensive series of tests was carried out to find the best surface ligand for the exploitation of NPs for the magnetophoretic amplification of SERS signals. Ligands are crucial for the stabilization of the NPs without compromising the analyte proximity to metal surface, as required in the SERS phenomenon. The best surface ligand, among those tested, was identified as sodium-3-mercaptopropylsulfonate. Ag-Fe NPs were then exploited for the realization of magnetically assembled SERS substrates and tested with different analytes such as dyes (Malachite Green, HITC) or pesticides (sodium diethyldithiocarbamate trihydrate - DTC - and tetramethylthiuram disulphide - Thiram). Furthermore, we tested the reusability of the arrays, by developing a short and simple procedure to remove, after the analysis, the analytes via sonication and centrifugation, and then depositing again the nanoparticles.

Overall, these results showed that LASiS is a viable technique for obtaining alloy nanoparticles, even with thermodynamically unfavoured structure, and that magnetic-plasmonic nanoalloys obtained in this way offer a series of interesting opportunities for the development of multifunctional nanotools for various fields such as photonics or nanomedicine.

# Publications

- V. Amendola, **S. Scaramuzza**, L. Litti, M. Meneghetti, G. Zuccolotto, A. Rosato, E. Nicolato, P. Marzola, G. Fracasso, C. Anselmi, M. Colombatti, *Small*, 2014, 10(12), 2476-2486.
- V. Amendola, **S. Scaramuzza**, S. Agnoli, S. Polizzi and M. Meneghetti, *Nanoscale*, 2014, 6, 1423-1433.
- **S. Scaramuzza**, S. Agnoli and V. Amendola, *Physical Chemistry Chemical Physics*, 2015, 17, 28076-28087.
- V. Amendola, **S. Scaramuzza**, S. Agnoli, G. Granozzi, M. Meneghetti, G. Campo, V. Bonanni, F. Pineider, C. Sangregorio, P. Ghigna, S. Polizzi, P. Riello, S. Fiameni and L. Nodari, *Nano Research*, 2015, 1-17
- D. Spadaro, M. A. Iatì, M. G. Donato, P. G. Gucciardi, R. Saija, A. R. Cherlakola, **S. Scaramuzza**, V. Amendola and O. M. Maragò, *RSC Advances*, 2015, 5, 93139-93146.
- E. Pizzolato, **S. Scaramuzza**, F. Carraro, A. Sartori, S. Agnoli, V. Amendola, M. Bonchio and A. Sartorel, *Journal of Energy Chemistry*, doi:10.1016/j.jechem.2015.12.004
- C. Sartorio, **S. Scaramuzza**, S. Cataldo, V. Vetri, M. Scopelliti, M. Leone, V. Amendola, and B. Pignataro, Submitted

# Acknowledgements

I would like to thank my supervisor, Professor Vincenzo Amendola, and all the personnel working in the Nanostructures and Optics Laboratory for the guidance and the counsel in these three years of PhD work.

Thanks go to our co-workers in University of Verona, University of Venice, and University of Padua.

Particular thanks go also to the COST action MP0903 NANOALLOY, and to Professor Catherine Amiens, for the hospitality and the guidance during my work at the LCC in Toulouse.